Elastic Electron and Muon Scattering Experiment Off the Proton at PSI

Steffen Strauch for the MUSE Collaboration
University of South Carolina, Columbia, SC 29208

DOI: http://dx.doi.org/10.3204/DESY-PROC-2014-04/76

While consistent results for the charge radius of the proton have been extracted from elastic electron-scattering data and through the spectroscopy of atomic hydrogen, recent high-precision studies of muonic hydrogen found notably smaller values for the charge radius. This so-called proton-radius puzzle raises questions ranging from experimental and methodological issues to physics beyond the Standard Model. The puzzle certainly calls for new measurements. The MUon Scattering Experiment (MUSE) at the Paul Scherrer Institute is being developed to provide elastic scattering data off the proton with electron and muon beams of positive and negative charge. Each of the four sets of data will allow the extraction of the proton charge radius; in combination, the data test possible differences of the electron and muon interactions and additionally two-photon exchange effects. The experiment will cover a four-momentum-transfer range from 0.002 to 0.07 GeV^2.

1 The Proton-Radius Puzzle

The electric and magnetic structure of the proton can be probed in electron-proton scattering experiments. In the one-photon exchange approximation, the experimental cross section depends on the electric and magnetic form factors, G_E and G_M, respectively. The form factors are functions of the four-momentum transfer squared, $-Q^2$, and can be determined in a Rosenbluth separation at fixed Q^2 in a series of measurements with varying electron scattering angles, θ. The slope of the electric form factor at $Q^2 = 0$ defines the proton charge radius, r_p,

$$r_p^2 = -6\hbar^2 \left. \frac{dG_E}{dQ^2} \right|_{Q^2=0} .$$

In a recent such measurement the A1 Collaboration in Mainz found a value of $r_p = 0.879 \pm 0.008$ fm [1]. The polarization transfer in electron-proton scattering experiments does not allow for a separation of the electric and magnetic form factors, but only depends on the form factor ratio, G_E/G_M. Polarization data, however, give independent constraints and a recent measurement and analysis of the LEDEX Collaboration at Jefferson Lab found a value of $r_p = 0.875 \pm 0.010$ fm [2]. An alternative method to determine the proton radius is the spectroscopy of atomic hydrogen. The electron wave function in the S states has overlap with the proton wave function and their interaction modifies the Lamb shift in hydrogen by an amount, which depends on the proton radius, $\Delta E \propto |\psi_S(0)|^2 r_p^2$. Radius extractions by CODATA from electronic hydrogen spectroscopy data give a value of $r_p = 0.8775 \pm 0.0051$ fm. Due to the larger muon mass, the overlap of the lepton wave function with the proton in muonic hydrogen is 8×10^6 times larger than in electronic hydrogen, making the spectroscopy of muonic hydrogen that much more sensitive. While the electronic data have been consistent, recent measurements of the Lamb shift in the muonic hydrogen atom obtained a significantly smaller value of the proton radius of 0.84087 ± 0.00039 fm [3, 4]. That these precise results differ by seven standard deviations from the combined results of all electronic data is the so called *proton radius puzzle.* Figure 1 shows this obvious disagreement.

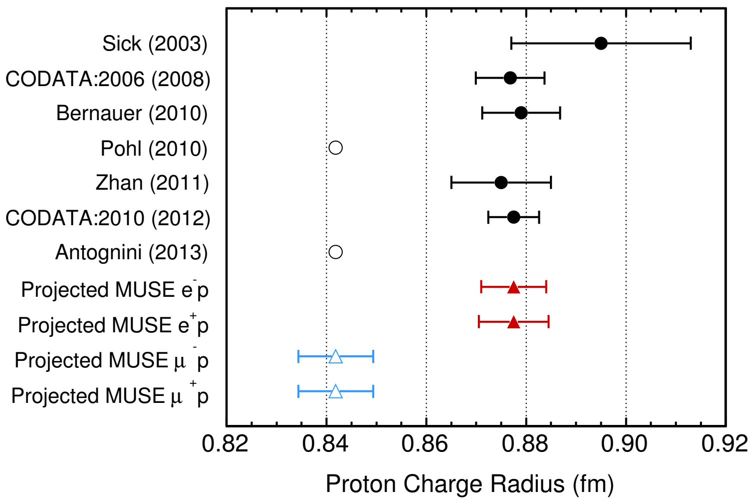

Figure 1: Previous results (circles) and projected MUSE results (triangles) of proton-radius measurements and extractions of electronic (full symbols) and muonic (open symbols) data [1, 2, 3, 4, 5, 6, 7].

This discrepancy has triggered a lively discussion. A recent review article [8] discusses many ideas, which were brought forward as possible solutions to the puzzle. The explanations can be grouped as follows. First, there may be problems with the experiment, including underestimation of uncertainties, difficulties in fitting the slope of the electric form factor for the radius extraction [9], or issues in QED calculations in the analysis of spectroscopy data. Second, novel hadronic physics may be important for μp but not for ep systems; suggested effects include proton polarizability effects proportional to m_ℓ^4 [10], off-shell corrections, and two-photon proton-structure corrections. Finally, the discrepancy may be an indication of the violation of μ/e universality and hint at physics beyond the standard model; *e.g.* [11]. Several ideas have been ruled out and none have gained universal acceptance.

Clearly, new data are needed. New spectroscopy measurements have been performed, including also experiments on deuterium and on helium [12]. New electron scattering experiments will try to improve on the precision of the form factor extraction and to reach lower values of Q^2 [12]. The proposed MUSE experiment [13] at the Paul Scherrer Institute (PSI), however, is unique. It is the only experiment, which will directly compare ep and μp in an elastic scattering experiment.

2 The MUSE Experiment at PSI

The MUSE experiment will measure $e^{\pm}p$ and $\mu^{\pm}p$ elastic scattering cross sections for lepton scattering angles between $\theta = 20^\circ$ and 100° and beam momenta of $p = 115, 153,$ and 210 MeV with a low beam flux of up to 5 MHz. The experiment will cover a range in Q^2 between 0.002 and 0.07 GeV^2. Measurements with both charges for the lepton allow for studies of possible two-photon exchange mechanisms. The use of both e and μ beams allows for a direct test of lepton-type dependent effects.

The experiment will be set up at PSI's πM1 secondary beam line. A schematic diagram of the proposed large-acceptance setup is shown in Fig. 2. In the absence of inelastic reactions off the proton, the determination of the lepton scattering angle at a given beam momentum completely determines the kinematics of the reaction. A magnetic spectrometer to determine the scattered particle momentum is not needed. The beam Čerenkov detector measures the beam particle time relative to the radio-frequency of the accelerator. Test measurements have shown that the particle types (e, μ, and π) can be well separated by their time-of-flight. The quite large emittance of the incident beam requires to track each incoming particle in a scintillator fiber detector and a set of three gas-electron multiplier (GEM) chambers. The scattered particles are tracked in a series of straw chambers and are detected in the fast scintillators, which are

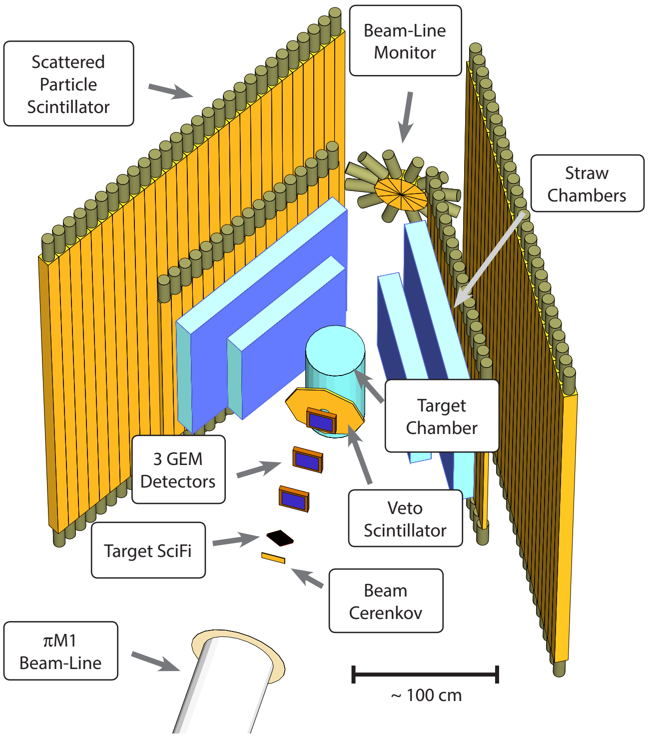

Figure 2: Schematic view of the planned detector setup for the MUSE experiment.

included in the trigger for the experiment. The veto scintillator, just upstream of the scattering chamber, allows a reduction of the trigger rate due to background tracks. The stability of the beam properties will be monitored with a downstream beam-line monitor. That detector also serves as an efficient veto for Møller scattering events.

Detailed Geant4 [14] based Monte-Carlo simulations of the experiment are underway to help optimize the detector setup and to study the parameters of the experiment. Items being studied include the resolution of the scattering-angle and vertex reconstructions, the muon decay-in-flight background, which is a source of electron tracks, and the Møller scattering background. Beam- and scattered-particle momentum distributions including radiative tails are necessary ingredients for radiative corrections of the experimental cross sections. These distributions are determined in full simulations of the experiment. The simulation results are being validated to the extent possible with experimental data.

Preliminary estimates of the total relative cross-section uncertainties for muon and electrons are 0.4% and 0.6%, respectively. The sensitivity of the experiment to differences in the extracted proton radius from e and μ scattering data is expected to be ±0.009 fm.

Acknowledgments

R&D work on the MUSE experiment is funded by the U.S. NSF and DOE. This work has also been supported in parts by NSF PHY-1205782.

References

[1] J.C. Bernauer *et al.*, Phys. Rev. Lett. **105**, 242001 (2010).

[2] X. Zhan *et al.*, Phys. Lett. **B705**, 59–64 (2011).

[3] R. Pohl *et al.* Nature **466**, 213–216 (2010).

[4] A. Antognini *et al.*, Science **339**, 417–420 (2013).

[5] I. Sick, Phys. Lett. **B576**, 62–67, (2003).

[6] P.J. Mohr, B.N. Taylor, and D.B. Newell, Rev. Mod. Phys. **84**, 1527–1605 (2012).

[7] P.J. Mohr, B.N. Taylor, and D.B. Newell, Rev. Mod. Phys. **80**, 633–730 (2008).

[8] R. Pohl, R. Gilman, G.A. Miller, and K. Pachucki, Ann. Rev. Nucl. Part. Sci. **63**, 175–204 (2013).

[9] E. Kraus, K.E. Mesick, A. White, R. Gilman, and S. Strauch, arXiv:1405.4735 [nucl-ex] (2014).

[10] G.A. Miller, Phys. Lett. **B718**, 1078–1082, (2013).

[11] C.E. Carlson and B.C. Rislow, Phys. Rev. **D86**, 035013 (2012).

[12] Mainz Institute for Theoretical Physics. Proton Radius Puzzle Workshop, (2014). `https://indico.mitp.uni-mainz.de/conferenceDisplay.py?ovw=True&confId=14`.

[13] R. Gilman *et al.*, arXiv:1303.2160 [nucl-ex] (2013).

[14] S. Agostinelli *et al.*, Nucl. Instrum. Meth. **A506**, 250–303 (2003).

Constraining Transversity and Nucleon Transverse-polarization Structure Through Polarized-proton Collisions at STAR

James L. Drachenberg for the STAR Collaboration

Valparaiso University, Valparaiso, IN 46383, United States of America

DOI: http://dx.doi.org/10.3204/DESY-PROC-2014-04/78

Studies of jet and di-hadron production from polarized-proton collisions can expand current knowledge of nucleon transverse-polarization structure. In data collected in 2006 at $\sqrt{s} =$ 200 GeV, STAR observes for the first time in $p^\uparrow + p$ nonzero asymmetries from transversity coupled to Collins and di-hadron fragmentation functions. Measurements at 500 GeV allow sensitivity to different mixes of partonic subprocesses; and comparisons of all measurements at 200 and 500 GeV may enlighten theoretical questions concerning evolution, universality, and factorization-breaking in non-collinear formulations of pQCD. Results from analyses of STAR data collected in 2011 at $\sqrt{s} = 500$ GeV are presented, including first-ever measurements offering constraints on models involving gluon linear polarization.

1 Introduction

Azimuthal transverse single-spin asymmetries, A_{UT}, from polarized-proton collisions present a challenge and an opportunity. To account for nonzero A_{UT} from high-p_T hadroproduction (e.g. Ref. [1]) one is challenged to understand pQCD beyond the collinear formulation at leading twist [2]. By so doing, one gains the opportunity for insight into the transverse polarization structure of the nucleon.

Two approaches that can generate nonzero A_{UT} in pQCD are to formulate collinear pQCD to account for higher twist multi-parton correlators (twist-3 formalism) [3, 4] or to formulate pQCD to account for intrinsic transverse momentum dependence (TMD formalism) [5, 6]. In the twist-3 formalism one can obtain asymmetries, in principle, from both the parton distribution functions or the fragmentation functions (e.g. Refs. [7, 8]). Similarly, in the TMD formalism one can obtain asymmetries, in principle, from both the parton distribution functions (the so-called "Sivers effect") [5, 6] and the fragmentation functions, e.g. the so-called "Collins effect" [9]. Furthermore, it has been shown that the intrinsic transverse momentum integrals of the TMD functions are closely related to the twist-3 functions (e.g. Ref. [10]).

One avenue to enrich understanding of nucleon spin structure is through jet production from high-energy polarized-proton collisions [11]. By measuring the spin-dependent, azimuthal asymmetry in the jet production ($A_{UT}^{\sin\phi_S}$), one can access the twist-3 parton distribution function, sensitive to the Sivers function. Additionally, by measuring different spin-dependent, azimuthal modulations in the distribution of hadrons within a jet ($A_{UT}^{\sin(\phi_S-\phi_H)}$ or $A_{UT}^{\sin(\phi_S-2\phi_H)}$), one can gain sensitivity to transversity or gluon linear polarization coupling to spin-dependent Collins or "Collins-like" [12] fragmentation functions, respectively. Similarly to the Collins effect, one can also access transversity coupled to polarized "interference fragmentation functions" (IFF) through spin-dependent, azimuthal asymmetries in the relative orientation of two hadrons from the same parton (e.g. Ref. [13]). While IFFs survive in the leading-twist, collinear formulation of pQCD with factorization expected to hold, the Collins effect depends upon TMD-factorization that is broken, in general, for high-p_T hadroproduction [14]. Thus, by studying both Collins and IFF asymmetries for overlapping kinematics, one opens the possibility to enlighten deep theoretical questions, such as TMD factorization-breaking and universality.

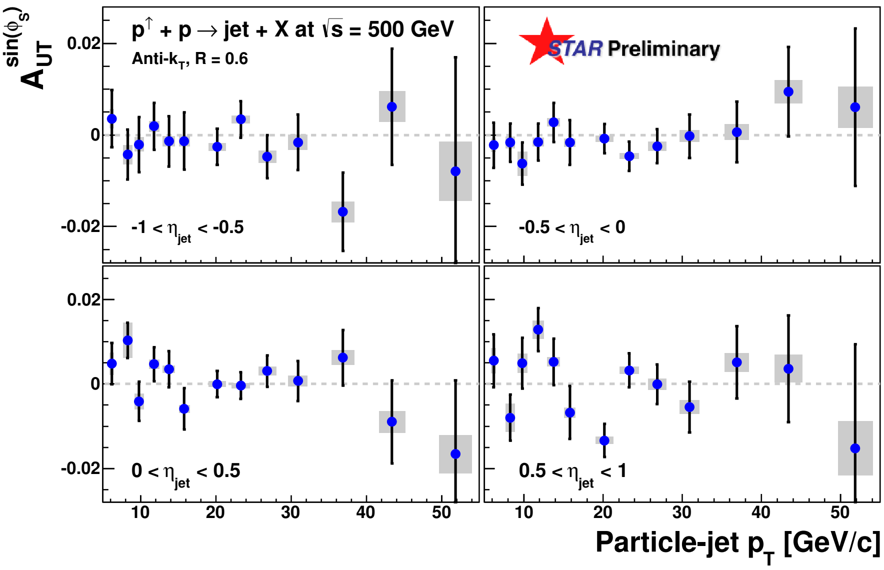

Figure 1: Inclusive jet azimuthal transverse single-spin asymmetries as a function of particle-jet transverse momentum for four bins of jet pseudorapidity relative to the polarized beam. Statistical uncertainties are shown by error bars and systematic uncertainties by error boxes. Measurements show no sign of large asymmetries and may suggest further constraints on the gluon Sivers function through the sensitivity of the twist-3 parton distribution function.

The STAR detector [15] at RHIC has seen the first signatures of transversity in polarized-proton collisions from charged-pion Collins [16] and IFF [17] asymmetries at $|\eta| < 1$ from 2.4 pb^{-1} at $\sqrt{s} = 200$ GeV collected in 2006. In 2011 STAR integrated 25 pb^{-1} of luminosity from $p^{\uparrow} + p$ at $\sqrt{s} = 500$ GeV with 53% polarization. This dataset allows the first measure of these asymmetries at $\sqrt{s} = 500$ GeV, including the first-ever measurement of the "Collins-like" asymmetry, with sensitivity to gluonic subprocesses enhanced relative to $\sqrt{s} = 200$ GeV. Comparison of all asymmetry modulations across $\sqrt{s} = 200$ and 500 GeV is expected to extend the current knowledge of these effects to broader kinematics as well as inform questions about the evolution of transversity and the TMD functions.

2 Analysis

The present data were collected with a minimum-bias trigger (VPDMB), requiring a coincidence in STAR's vertex position detector (VPD) [18], as well as with "jet-patch" triggers, requiring patches of energy in STAR's barrel (BEMC) and endcap (EEMC) electromagnetic calorimeters [15]. Jets are reconstructed using the "anti-k_T" algorithm [19] with a radius of 0.6 and utilize energy deposition in the BEMC and EEMC as well as charged-particle tracks from STAR's time projection chamber (TPC) [15].

Descriptions of the analysis techniques and simulation studies are given in Ref. [20]. The dominant systematic uncertainties arise from jets reconstructed at the detector level that fail to match to one at the parton-jet level. Additional systematic uncertainties come from the contamination of kaons, protons, and electrons to the charged-pion signal; trigger bias; the "leak-through" of competing effects coupling to non-uniform detector acceptance; uncertainties from calorimeter gains, efficiencies, and response to charged hadrons; tracking efficiency; and Monte Carlo simulation statistics. Measured asymmetries are corrected for smearing due to finite azimuthal-angle resolution.

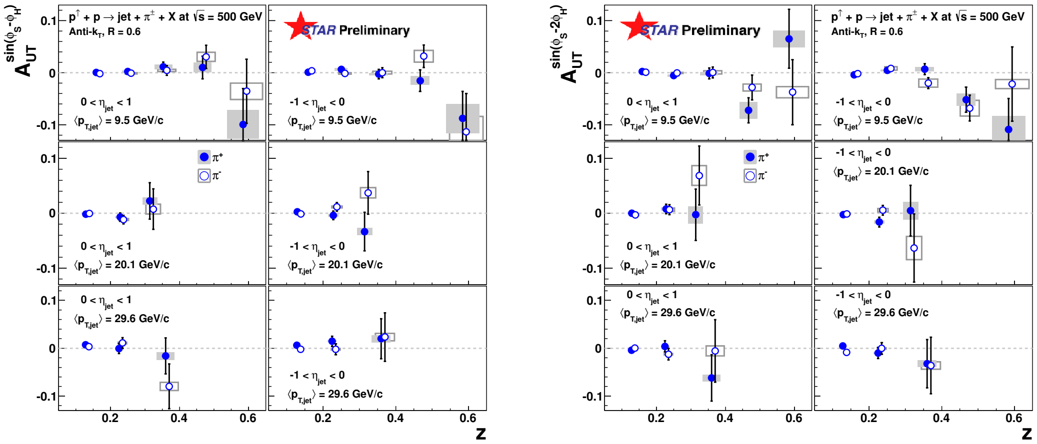

Figure 2: (left) Collins and (right) "Collins-like" asymmetries as a function of pion z for three bins of jet p_T and two bins of jet pseudorapidity relative to the polarized beam. Collins asymmetries are consistent with zero at low jet p_T, where gluonic subprocesses dominate, and are statistics limited at high jet p_T, where the best sensitivity to quark subprocesses is expected. The present "Collins-like" asymmetries should provide the first experimental constraints on model predictions utilizing linearly polarized gluons.

3 Results

In Fig. 1 the measured azimuthal asymmetries in the inclusive jet production are presented as a function of particle-jet p_T for four bins of jet pseudorapidity relative to the polarized beam. No large asymmetries are observed, consistent with expectation from measurements at $\sqrt{s}$ = 200 GeV [21, 22, 23] as well as model predictions [7]. The present data may suggest further constraints on the gluon Sivers function through the sensitivity of the twist-3 parton distribution function.

The left-hand panel of Fig. 2 shows Collins asymmetries as a function of $z = p_\pi/p_{jet}$ for three bins of jet p_T and two bins of jet psuedorapidity relative to the polarized beam. At low p_T, Collins asymmetries are expected to be quite small due to the prevalence of gluonic subprocesses [24], and this is consistent with the present measurement. For the higher two bins of jet p_T, quark-gluon scattering is expected to begin to dominate the underlying partonic cross section [24]. Thus, one may expect sensitivity to a nonzero Collins effect at higher p_T, however, the present data are statistics limited in this kinematic region. Analysis of STAR's high-statistics dataset at $\sqrt{s} = 200$ GeV, collected in 2012, will provide good sensitivity to effects from quark subprocesses in a region where nonzero signals are already observed [16, 25].

The right-hand panel of Fig. 2 shows the "Collins-like" asymmetries as a function of z for three bins of jet p_T and two bins of jet psuedorapidity relative to the polarized beam. Existing model predictions are unconstrained by measurement and suggest a maximum possible upper-limit of $\approx 2\%$ [11]. The present data fall well below this maximum with the best precision at lower values of z, where models suggest the largest effects may occur. Thus, the present data should allow for the first experimental constraints beyond the positivity bounds.

References

[1] B. I. Abelev et al. *Phys. Rev. Lett.*, 101:222001, 2008.

[2] G. Kane, J. Pumplin, and W. Repko. *Phys. Rev. Lett.*, 41:1689, 1978.

[3] A. Efremov and O. Teryaev. *Yad. Fiz.*, 36:242, 1982. [Sov. J. Nucl. Phys. 36, 140 (1982)].

[4] J. Qiu and G. Sterman. *Phys. Rev.*, D59:014004, 1998.

[5] D. Sivers. *Phys. Rev.*, D41:83, 1990.

[6] D. Sivers. *Phys. Rev.*, D43:261, 1991.

[7] K. Kanazawa and Y. Koike. *Phys. Lett.*, B720:161, 2013.

[8] K. Kanazawa, Y. Koike, A. Metz, and D. Pitonyak. *Phys. Rev.*, D89:111501, 2014.

[9] J. Collins. *Nucl. Phys.*, B396:161, 1993.

[10] D. Boer, P.J. Mulders, and F. Pijlman. *Nucl. Phys.*, B667:201, 2003.

[11] U. D'Alesio, F. Murgia, and C. Pisano. *Phys. Rev.*, D83:034021, 2011.

[12] M. Anselmino et al. *Phys. Rev.*, D73:014020, 2006.

[13] A. Bacchetta and M. Radici. *Phys. Rev.*, D70:094032, 2004.

[14] T.C. Rogers and P.J. Mulders. *Phys. Rev.*, D81:094006, 2010.

[15] K.H. Ackermann et al. *Nucl. Instr. Meth.*, A499:624, 2003. and references therein.

[16] R. Fatemi. *AIP Conf. Proc.*, 1441:233, 2012.

[17] A. Vossen. *AIP Conf. Proc.*, 1560:519, 2013.

[18] W.J. Llope et al. *Nucl. Instr. Meth.*, A759:23, 2014.

[19] M. Cacciari, G. P. Salam, and G. Soyez. *J. High Energy Phys.*, 04:063, 2008.

[20] J.L. Drachenberg. *EPJ Web Conf.*, 73:02009, 2014.

[21] B. Abelev et al. *Phys. Rev. Lett.*, 99:142003, October 2007.

[22] L. Adamczyk et al. *Phys. Rev.*, D86:032006, August 2012.

[23] A. Adare et al. arXiv:1312.1995.

[24] A. Mukherjee and W. Vogelsang. *Phys. Rev.*, D86:094009, 2012.

[25] E.C. Aschenauer et al. The RHIC Spin Program: Achievements and Future Opportunities. 2013. arXiv:1304.0079.

Partial Wave Analyses of the $\pi^+\pi^-\pi^-$ System at upgraded VES Setup

Igor Kachaev[1], *V. Dorofeev*[1], *A. Ekimov*[1], *V. Gotman*[1], *A. Ivashin*[1], *V. Kalendarev*[1], *Yu. Khokhlov*[1,2], *M. Kholodenko*[1], *V. Konstantinov*[1], *V. Matveev*[1], *M. Mikhasenko*[1], *V. Nikolaenko*[1], *A. Plekhanov*[1], *D. Ryabchikov*[1], *Yu. Salomatin*[1], *V.Sugonyaev*[1], *E. Volkov*[1], *A. Zaitsev*[1,2]

[1] IHEP, Pobedy street 1, 142280 Protvino, Russia
[2] MIPT, Kerchenskaya street 1A, 117303 Moscow, Russia

DOI: http://dx.doi.org/10.3204/DESY-PROC-2014-04/200

Partial Wave Analysis of the $\pi^+\pi^-\pi^-$ system produced by 29 GeV/c π^- beam on berillium target is presented. About $30 \cdot 10^6$ events in the wide $|t'|$ range $0 \ldots 0.8$ GeV^2/c^2 are collected with upgraded VES setup. The size of the data sample is 2.5 times larger than that previously analyzed by VES. Data are analyzed using formalism of density matrix with unlimited rank. We discuss status of the $a_1(1420)$, $a_2(1700)$, $a_3(1875)$ states, structure of exotic $\rho(770)\pi$ P-wave with $J^{PC} = 1^{-+}$.

1 VES setup and events selection

We present preliminary results of mass independent PWA of the $\pi^+\pi^-\pi^-$ system on the data obtained after VES upgrade. We compare them with data obtained before upgrade and discuss structures which can be considered resonant. Currently we do not claim any numerical results.

VES setup is full featured magnetic spectrometer which operates on mostly π^- beam (2% of K^-) with energy 37 GeV/c before upgrade and 29 GeV/c after upgrade. It is equipped with electromagnetic calorimeter and multicellular Cherenkov counter for particle identification. Description of VES setup before upgrade can be found in [1] and after upgrade in [2]. For charged 3π system net result of the upgrade is severely large acceptance (see Fig. 1) due to taking out of trigger hodoscope and severely large statistics due to upgraded DAQ.

Diffractive production of charged 3π final state dominates at VES energies, so data selection is simple and background is negligible. We require beam particle identified as π^-, 3 tracks with charges $+--$ (identification as π mesons is done for old data only), total energy for charged tracks 27–31 (36–38) GeV, free (not associated with tracks) energy in the electromagnetic calorimeter less than 0.5 GeV and vertex of interaction inside the target. Analysis is done for $M(3\pi) = 0.6$–2.6 GeV/c^2 in 20 MeV/c^2 bins and four $|t'|$ intervals 0–0.03–0.15–0.30–0.80 GeV^2/c^2. We have about $30 \cdot 10^6$ 3π events after upgrade and about $12 \cdot 10^6$ 3π events before upgrade.

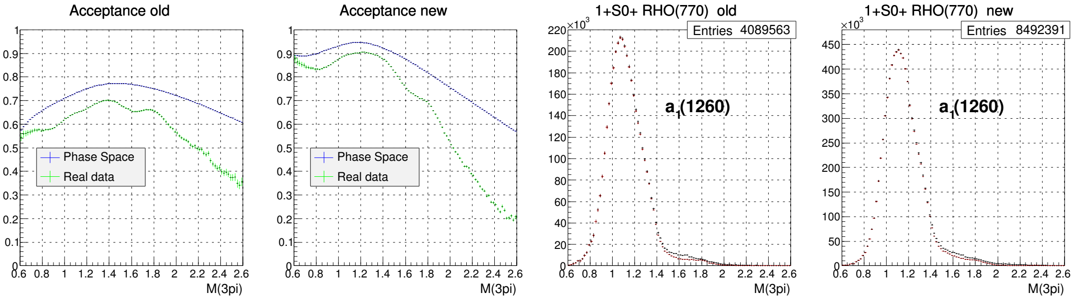

Figure 1: VES geometric acceptance before and after upgrade; largest wave $1^+S0^+\rho(770)$ for $|t'| < 0.03\ GeV^2/c^2$ in old and new data.

2 Method of the analysis

Our method of the analysis is based on Illinois PWA [3]. We are using extended likelihood event by event fit with positive definite density matrix as parameters. No restrictions are placed on the rank of the matrix. Amplitudes are constructed using isobar model, sequential decay of 3-particle system via $\pi\pi$ subsystem, with relativistic corrections according to [4]. Wave has quantum numbers $J^P LM^\eta$ R where J^P is spin-parity for 3π system, M^η is projection of spin and exchange naturality, R is the known resonance in $\pi\pi$ system and L is orbital momentum in Rπ decay. Isospin and G-parity $I^G = 1^-$ are the same for all 3π charged states. To describe broad part of $\pi\pi$ S-wave we use modified M solution from [5]. To make this amplitude broad we drop 4-th order terms and coupling to $K\bar{K}$. We name this pseudo state ε, it should describe among other things $f_0(1400)$ and possible $\sigma(600)$. Narrow $f_0(975)$ and $f_0(1500)$ are included separately. Purely geometric (not GEANT) model of the acceptance is used.

2.1 Coherent part of density matrix

Coherent part of the density matrix ρ is the largest part of the matrix which has rank one and behaves like vector of amplitudes. Let us decompose ρ with dimension d into its eigenvalues and eigenvectors:

$$\rho = \sum_{k=1}^{d} e_k V_k V_k^+ \quad \text{where} \quad \begin{cases} e_k \text{ is k-}th\text{ eigenvalue} \\ V_k \text{ is k-}th\text{ eigenvector} \end{cases}$$

Let $e_1 \gg e_2 > \ldots > e_d > 0$. This condition is often met for 3π system. Leading term $\rho_L = e_1 V_1 V_1^+$ is coherent part of density matrix and $\rho_S = \rho - \rho_L$ is the rest, incoherent part. This decomposition is stable with respect to variations of ρ matrix elements. Experience shows that resonances tend to concentrate in ρ_L while ρ_S can contain non-leading exchanges, albeit it often contains garbage. Results for full ρ are drawn below as black points with errors, for ρ_L as red one.

3 Fit results

In Fig. 1 one can see wave $1^+S0^+\rho(770)$ for low $|t'|$ region in both old $37\,GeV/c$ and new $29\,GeV/c$ data. The wave contains huge contribution from $a_1(1260)$ and a shoulder at $M(3\pi) \approx$

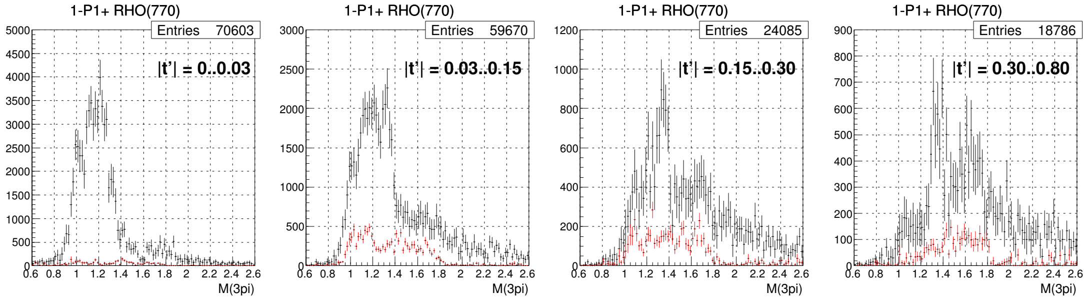

Figure 2: Exotic wave $1^- P1^+ \rho(770)$ in all four $|t'|$ regions, old 37 GeV/c data.

$1.7\,GeV/c^2$ which can correspond to $a_1(1700)$. Two conclusions can be drawn here — first, the structure of the wave is approximately the same in both old and new data; next, data for the coherent part of the density matrix fill the whole wave. The same is true for all other largest waves, like $0^- S0^+ \varepsilon$ and $2^- S0^+ f_2(1270)$ (not shown here).

Probably the wave with exotic quantum numbers $J^{PC} = 1^{-+}$ has the most controversial status in the whole 3π PWA. Corresponding objects $\pi_1(1300)$ and $\pi_1(1600)$ are long discussed. The wave $1^- P1^+ \rho(770)$ is shown in Fig. 2, 3 for all four $|t'|$ intervals both for old and new data. The wave is small — no more than 2–5% on the total number of events for old and new data in all $|t'|$ regions. This wave does not correspond to coherent part of density matrix — results for ρ_L are 2–10 times smaller than for the whole ρ. Prominent feature of the new data is that this wave is two times larger than in old data with respect to total number of events for $|t'| < 0.03$ GeV^2/c^2 and is slightly more structured in other $|t'|$ regions. We think that our model of the setup is still too crude. Given this data existence of both π_1 objects looks questionable.

Now we will discuss some other possibly resonant waves. To save space only new 29 GeV/c data are shown. As it was shown in the presentation new data have better quality although old data mostly lead us to the same conclusions. In Fig. 4 (a) one can see wave $2^+ D1^+ \rho(770)$ for medium $|t'| = 0.03 \ldots 0.15$ GeV^2/c^2 region with well known $a_2(1320)$. State $a_2(1700)$ is discussed in this wave. One can see that the state $a_2(1320)$ is in the coherent part of the density matrix ρ_L and there is nothing in this wave outside $a_2(1320)$ region, especially in its

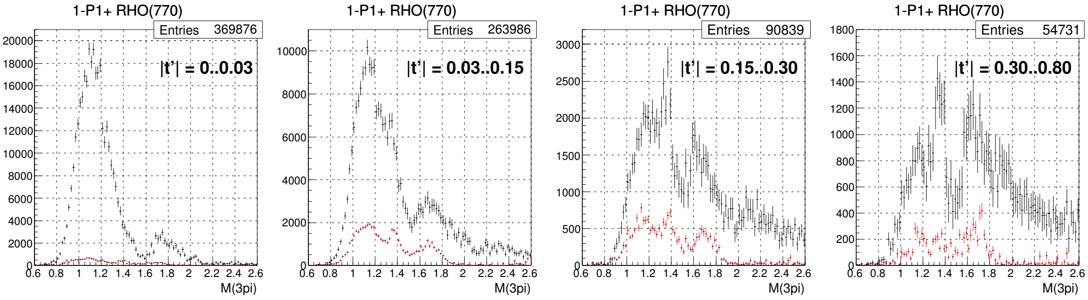

Figure 3: Exotic wave $1^- P1^+ \rho(770)$ in all four $|t'|$ regions, new 29 GeV/c data.

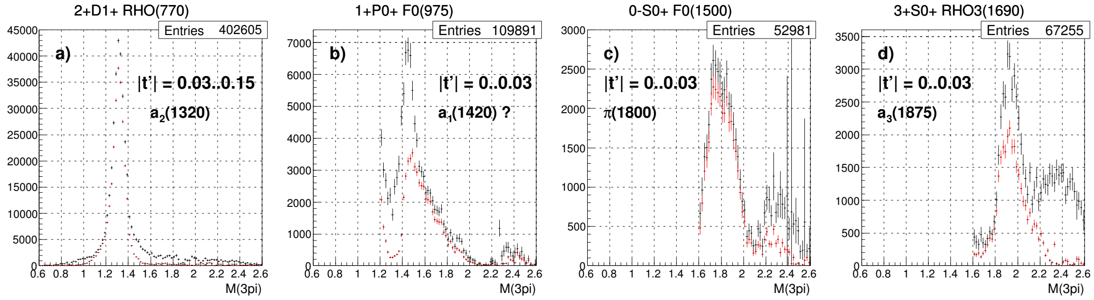

Figure 4: Waves $2^+D1^+\rho(770)$, $1^+P0^+f_0(975)$, $0^-S0^+f_0(1500)$, $3^+S0^+\rho_3(1690)$, new data.

coherent part. We can't see anything which can be interpreted as $a_2(1700)$.

Until the end of this section all waves are shown for $|t'| < 0.03\ GeV^2/c^2$. In Fig. 4 (b) the wave $1^+P0^+f_0(975)$ with discussed $a_1(1420)$ is shown. Good narrow resonant like structure can be seen at $M(3\pi) \approx 1.45\ GeV/c^2$. The same structure, albeit less prominent and never reported, can be seen in our old data. This structure has some peculiarities — its coherent and incoherent parts are approximately of the same magnitude; coherent part is severely wider than the peak itself. These features make difficult resonant interpretation of given structure.

In Fig. 4 (c) the wave $0^-S0^+f_0(1500)$ is shown. This is probably a decay mode $\pi(1800) \to f_0(1500)\pi$ which was studied before but is much more pronounced in new data. For this wave at $M(3\pi) \sim 1.8 GeV/c^2$ coherent part fills the whole wave which supports resonant interpretation of the peak. In Fig. 4 (d) one can see the wave $3^+S0^+\rho_3(1690)$. A peak at $M(3\pi) \sim 1.9\ GeV/c^2$ is clearly seen. The peak is even more pronounced in ρ_L. We think this is a decay mode $a_3(1875) \to \rho_3(1690)\pi$. The object $a_3(1875)$ is listed as "further states" in [6] and was last observed in [7]. Our analysis can be a ground to re-establish this state.

4 Conclusions

Mass-independent PWA is done for old 37 GeV and new 29 GeV $\pi^+\pi^-\pi^-$ data collected with VES setup. Preliminary results are shown. Large PWA waves look alike for 37 GeV and 29 GeV data. Some small waves are seen much better in new data. Decay modes $\pi(1800) \to f_0(1500)\pi$, $a_3(1875) \to \rho_3(1690)\pi$ are seen in 0^-S and 3^+S waves. State $a_2(1700)$ is not seen in $2^+D1^+\ \rho\pi$. Interpretation of $f_0(975)\pi$ in 1^+S wave at $M \sim 1.4\ GeV/c^2$ is controversial. The wave $1^-P1^+\rho(770)$ with $J^{PC} = 1^{-+}$ is small, no more than 2–4% from total number of events in all $|t'|$ regions both in old and new data. Its coherent part is 2–10 times smaller.

Acknowledgments

This research was supported in part by Presidential grant NSh-999.2014.2 and RFBR grant 13-02-00576.

References

[1] S.I. Bityukov *et al.*, Phys. Lett. **B268** 137 (1991)

[2] Yu. Khokhlov *et al.*, EPJ Web of Conferences **37**, 01029 (2012)
[3] J.D. Hansen *et al.*, Nucl. Phys. **B81** 403 (1974)
[4] S.U. Chung *et al.*, Phys. Rev. **D48**, N3 1225 (1993)
[5] Au, Morgan, Pennington, Phys. Rev. **D35** 1633 (1987)
[6] K. Nakamura *et al.*, Particle Data Group, **JP G** 37, 075021 (2010)
[7] S.U. Chung *et al.*, Phys. Rev. **D65** 07 (2001)

Chapter 3

Quarks and gluons in hot and dense matter

Upsilon Production at the STAR Experiment with a Focus on New U+U Results

Róbert Vértesi for the STAR Collaboration

Nuclear Physics Institute ASCR, 25 068 Řež, Czech Republic

DOI: http://dx.doi.org/10.3204/DESY-PROC-2014-04/91

We report recent Υ measurements in p+p, d+Au and Au+Au collisions at $\sqrt{s_{NN}} = 200$ GeV, and detail the analysis in U+U collisions at $\sqrt{s_{NN}} = 193$ GeV. Results on Υ production versus rapidity are consistent with pQCD predictions in p+p collisions. However, Υ production in mid-rapidity ($|y|<0.5$) d+Au collisions is suppressed with respect to p+p collisions beyond model predictions that take into account modification of parton distribution functions and initial parton energy loss inside nuclei. The nuclear modification factor R_{AA} shows a significant suppression in central Au+Au and U+U collisions, consistent with model calculations including color screening effects in a deconfined medium.

1 Introduction

Due to color screening, the production of quarkonia in high energy heavy ion collisions is expected to be sensitive to the energy density of the medium. Sequential suppression of different quarkonium states may therefore serve as a thermometer of the medium [1]. Although the suppression of charmonia was anticipated as a key signature of the Quark Gluon Plasma (QGP), the observed energy dependence of J/ψ suppression is rather weak [2]. This phenomenon is explained by J/ψ production via recombination (coalescence) of $c\bar{c}$ pairs in the QGP. Bottomonia, on the other hand, are less affected by recombination and can provide a cleaner probe of the strongly interacting medium. While p+p measurements provide a benchmark for pQCD and serve as a baseline for nuclear modification, d+Au collisions are generally considered as suitable to study cold nuclear matter (CNM) effects such as shadowing of the parton distribution functions and initial state parton energy loss. Central U+U data at $\sqrt{s_{NN}} = 193$ GeV, which is estimated to have a 20% higher average energy density than that of Au+Au [3], allow for further tests of the sequential suppression hypothesis.

2 Experiment and analysis

The STAR experiment at RHIC is a complex detector that provides a full azimuthal coverage at mid-rapidity ($|\eta|<1$). A detailed description of the STAR detector is in Ref. [4]. The $\Upsilon \rightarrow \mathrm{e}^-\mathrm{e}^+$ decay channel, with a branching ratio $B_{\mathrm{ee}} \approx 2.4$ %, was studied. Analysis of year 2012 $\sqrt{s_{NN}} =$ 193 GeV U+U data was done in a similar way to recently published Υ measurements in p+p, d+Au and Au+Au collisions at $\sqrt{s_{NN}} = 200$ GeV [5], with differences highlighted below. A total of 17.2 million *high-tower* triggered U+U events were collected requiring an energetic hit in the Barrel Electromagnetic Calorimeter (BEMC), corresponding to an integrated luminosity of 263.4 μb^{-1}. Momentum measurement and electron identification based on the energy loss dE/dx were done in the Time Projection Chamber (TPC). The projected position of the track is required to match the position of the hit in the BEMC to the extent $\Delta R = (\Delta\varphi^2 + \Delta\eta^2)^{1/2} < 0.04$ in the azimuth–pseudorapidity space. The three most energetic adjacent BEMC towers including the hit tower were combined into *cluster*s. Electron candidates were required to have similar cluster energy and momentum ($0.75 < E_{cluster}/p < 1.35$ c) with most of the energy in one tower ($E_{tower}/E_{cluster} > 0.7$ for those candidates that fired the trigger, $E_{tower}/E_{cluster} > 0.5$ for other candidates). They were then paired, and required to have an opening angle $\theta > 90°$. Fig. 1 shows the invariant mass distribution of the paired candidates. The combinatorial background was subtracted using like-sign combinations. In the peak region there is also a significant contribution from Drell-Yan and open $b\bar{b}$ processes. Templates of the $\Upsilon(nS)$ peaks and the Drell-Yan contributions obtained from simulations, and the $b\bar{b}$ contribution from pQCD model calculations were fitted simultaneously to determine their relative contributions. The reconstruction efficiency was determined using simulations and electron-enriched data samples as $\epsilon \approx 3\%$. The corrected p_{T}-spectrum is shown in Fig. 2. Bin-shift correction was done using a Boltzmann function with a slope $T = 1.16$ GeV, extracted from a parametrized interpolation over ISR, CDF and CMS data. A fit to the spectrum yiels a slope $T = 1.32{\pm}0.21$ GeV, consistent with the interpolation. The measured Υ cross section in U+U collisions is $B_{\mathrm{ee}} \left.\frac{d\sigma^{\Upsilon}_{\mathrm{AA}}}{dy}\right|_{|y|<1} = 4.37{\pm}1.09(stat){\pm}^{+0.65}_{-1.01}(syst)$ μb. The major systematic uncertainties are from signal extraction ($^{+4.8}_{-18}\%$), tracking efficiency (11.8%), electron identification in the TPC ($^{+4.0}_{-6.4}\%$) and in the BEMC (5.9%), TPC-BEMC matching (5.4%), trigger efficiency ($^{+1.1}_{-3.6}\%$), geometrical acceptance ($^{+1.7}_{-3.0}\%$) and input p_{T} and y spectrum in the simulations (2.1%).

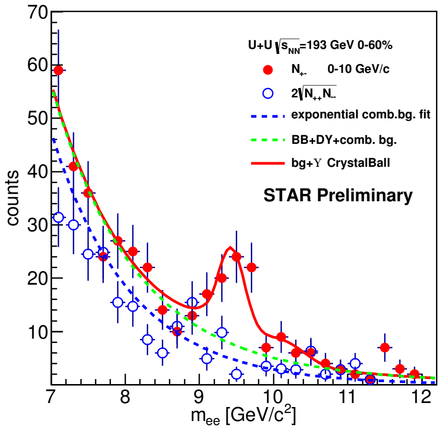

Figure 1: Invariant mass distribution of like-sign (filled dots) and unlike-sign (open points) electron pairs in $\sqrt{s_{NN}}$=193 GeV U+U collisions of 0–60% centrality at mid-rapidity, with background and peak fits.

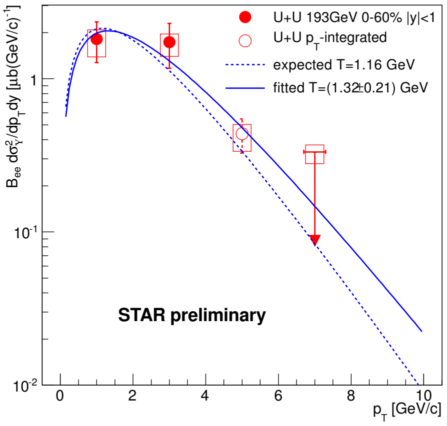

Figure 2: Υ p_{T}-spectrum in $\sqrt{s_{NN}}$=193 GeV U+U collisions of 0–60% centrality at mid-rapidity. The fit (solid line) to the data is compared to the expected slope (dashed).

3 Upsilon production in p+p and d+Au collisions

Fig. 3 shows the cross sections for Υ production in $\sqrt{s_{NN}}$=200 GeV p+p and d+Au collisions [5]. The data are compared to NLO pQCD color evaporation model predictions [6]. In Fig. 4 the nuclear modification factor in d+Au is compared to calculations including shadowing and/or parton energy loss [6, 7]. While the p+p data are consistent with pQCD, CNM effects alone may not be enough to explain the suppression in the d+Au mid-rapidity bin ($|y|<0.5$).

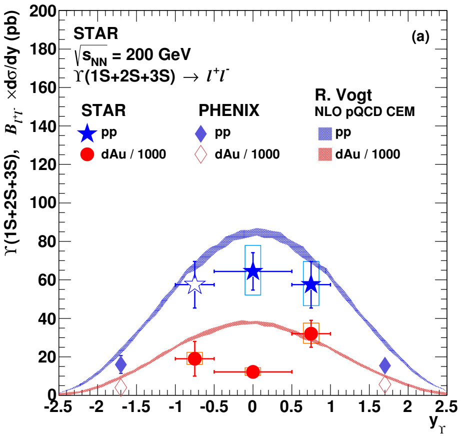

Figure 3: Υ yield $B_{\mathrm{ee}}\frac{d\sigma}{dy}$ for p+p and d+Au collisions [5] compared to a pQCD model [6].

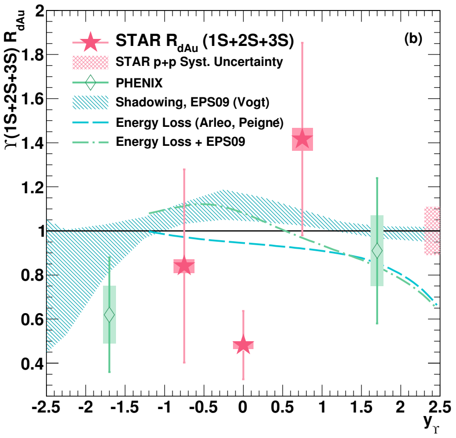

Figure 4: R_{dAu} versus y of Υ mesons [5] compared to theoretical calculations [6, 7].

4 Upsilon suppression in heavy ion collisions

Nuclear modification factors of the Υ(1S+2S+3S) in d+Au, Au+Au and U+U collisions are presented in Fig. 5 with respect to the number of participants, and compared to model calculations [8, 9], as well as $\sqrt{s_{NN}}$=2.76 TeV Pb+Pb data from the CMS experiment [10]. The trend observed in Au+Au is generally continued in the U+U data, with an $R_{\mathrm{AA}} = 0.35 \pm 0.17(stat.)^{+0.03}_{-0.13}(syst.)$ in the 10% most central U+U collisions. The model of Strickland and Bazow [8] incorporates lattice QCD results on screening and broadening of bottomonium, as well as the dynamical propagation of the Υ meson in the colored medium. The scenario with a potential based on heavy quark internal energy is consistent with the observations, while the free energy based scenario is disfavoured. The strong binding scenario in a model proposed by Emerick, Zhao, and Rapp [9], which includes possible CNM effects in addition, is also consistent with STAR results. The measured R_{AA} at RHIC and at LHC are consistent within the sizeable uncertainties. However, the LHC data, which corresponds to higher energy densities, shows a trend that differs from RHIC: a strong suppression is present at all but the lowest N_{part} values.

Fig. 6 shows Au+Au R_{AA} for the ground state Υ(1S) and the excited states Υ(2S+3S) separately, compared to the R_{AA} of high-p_{T} J/ψ mesons in $\sqrt{s_{NN}}$ = 200 GeV Au+Au collisions [11]. The Υ(1S) shows a suppression similar to that of high-p_{T} J/ψ mesons, more than if only cold nuclear matter effects were present [5]. The excited state yields are consistent with a complete suppression within the precision of the measurement.

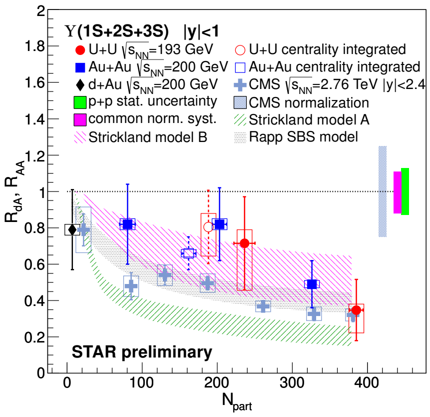

Figure 5: R_{AA} vs. N_{part} in $\sqrt{s_{NN}}$=200 GeV d+Au, Au+Au and 193 GeV U+U collisions, compared to models [8, 9] and LHC data [10].

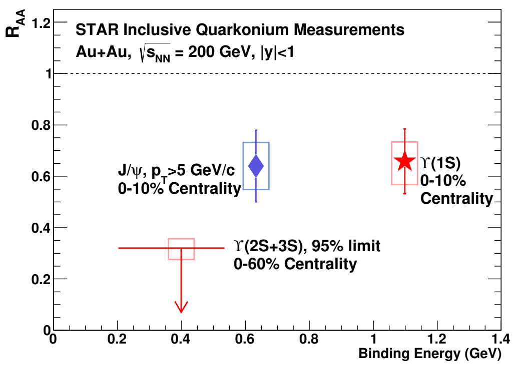

Figure 6: R_{AA} of the Υ(1S) and the Υ(2S+3S) states compared to high-p_{T} J/ψ R_{AA} [11], plotted against binding energy, in $\sqrt{s_{NN}}$=200 GeV Au+Au collisions.

5 Summary and outlook

We reported recent measurements of Υ production in p+p, d+Au and Au+A collisions at $\sqrt{s_{NN}}$ = 200 GeV, as well as U+U at 193 GeV. The slope of the p_{T}-spectrum in U+U collisions is consistent with interpolations from other experiments. We see a significant suppression in $|y|$<1 central Au+Au and U+U collisions, which attests to the presence of a deconfined medium and support the sequential melting hypothesis. However, the $|y|$<0.5 d+Au data also shows a suppression beyond model predictions, suggesting that CNM effects may also play an important role. The new Muon Telescope Detector has been completed by 2014, and will allow for a precise reconstruction of the three Υ states separately, through the dimuon channel. Future high-statistics p+Au collisions from 2015 will help us gain a deeper insight to the CNM effects.

This work has been supported by the grant 13-20841S of the Czech Science Foundation (GAČR), and by the MSMT grant CZ.1.07/2.3.00/20.0207 of the European Social Fund (ESF) in the Czech Republic: Education for Competitiveness Operational Programme (ECOP).

References

[1] A. Mócsy and P. Petreczky, Phys. Rev. Lett. **99**, 211602 (2007).
[2] A. Adare *et al.* [PHENIX Collaboration], Phys. Rev. Lett. **98**, 232301 (2007).
[3] D. Kikola, G. Odyniec and R. Vogt, Phys. Rev. C **84**, 054907 (2011).
[4] K. H. Ackermann *et al.* [STAR Collaboration], Nucl. Instrum. Meth. A **499**, 624 (2003).
[5] L. Adamczyk *et al.* [STAR Collaboration], Phys. Lett. B **735**, 127 (2014).
[6] R. Vogt, R. E. Nelson and A. D. Frawley, PoS ConfinementX, **203** (2012).
[7] F. Arleo and S. Peigne, JHEP **1303**, 122 (2013).
[8] M. Strickland and D. Bazow, Nucl. Phys. A **879**, 25 (2012).
[9] A. Emerick, X. Zhao and R. Rapp, Eur. Phys. J. A **48**, 72 (2012).
[10] S. Chatrchyan *et al.* [CMS Collaboration], Phys. Rev. Lett. **109**, 222301 (2012).
[11] L. Adamczyk *et al.* [STAR Collaboration], Phys. Lett. B **722**, 55 (2013).

Recent Highlights from the PHENIX Heavy-Ion Program at RHIC

Baldo Sahlmueller[1] for the PHENIX collaboration

[1] Goethe University, Max-von-Laue-Str. 1, 60438 Frankfurt, Germany

DOI: http://dx.doi.org/10.3204/DESY-PROC-2014-04/318

Over the last decade it has been established that a quark-gluon plasma (QGP) is formed in ultrarelativistic A+A collisions at RHIC energies. In recent years, detector upgrades have enabled the detailed study of this hot and dense matter. Important probes, among others, are direct photons and heavy flavor observables. Although the RHIC d+Au program was originally undertaken to study initial state and cold nuclear matter effects, recent measurements at both RHIC (d+Au) and the LHC (p+Pb) have found evidence for collective phenomena in these small systems.

1 Direct Photons

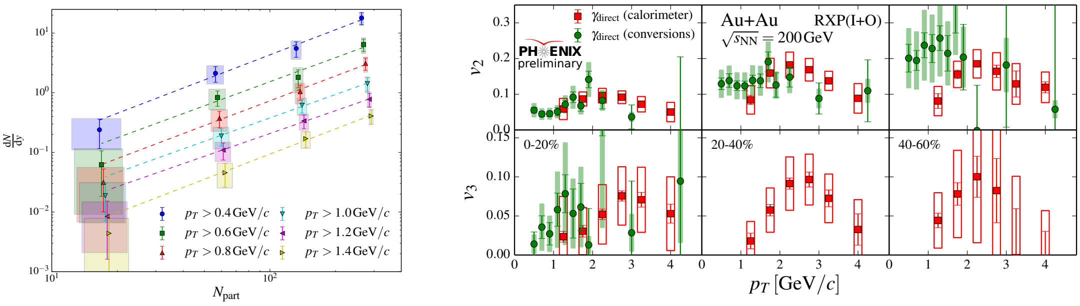

Figure 1: a) Integrated thermal photon yields as a function of N_{part} for different lower p_T integration limits. The dashed lines are independent fits to a power-law. b) Azimuthal anisotropy v_2 and v_3 of direct photons, for three different centrality selections.

Earlier PHENIX measurements established a surprising behavior of direct photon production and elliptic flow at low transverse momenta [1]. Current theoretical models cannot explain this so-called direct photon puzzle, a large excess of direct photon production over the $p+p$ baseline in Au+Au collisions at $\sqrt{s_{\rm NN}} = 200$ GeV, together with a large azimuthal anisotropy of direct photons.

A new measurement, using data taken in 2010, offers a significantly improved precision for both the direct photon spectra and the azimuthal anisotrop [2]. This new measurement uses the conversion of real photons in the detector material for the measurement, it confirms the previously published data and extends the transverse momentum range towards lower p_T. The new data furthermore allow the analysis in finer centrality bins than before. The thermal photon yield is extracted as the excess of the direct photon production over the binary-scaled $p+p$ baseline. It is fit with an exponential, the slopes of these functions are independent of the centrality selection within the uncertainties of the measurement, with an average slope of ∼240 MeV/c.

The integrated thermal photon yield has been calculated in four centrality bins for different p_T ranges, it is shown in Figure 1a as a function of N_{part}. We observe a scaling of the integrated yield with a power law function AN_{part}^{α}. The exponent α was found to be common for all p_T integration ranges, with $\alpha = 1.48 \pm 0.08(\text{stat.}) \pm 0.04(\text{syst.})$. This is in the range of recent theoretical models describing direct photon emission in Au+Au collisions at this energy (see references in [2]).

The new methods have also been used to measure the direct photon azimuthal anisotropy, for the first time, the triangular flow v_3 has also been measured. The p_T range and the precision of v_2 have been improved compared to the previously published data. The direct photon v_2 and v_3 are shown in Figure 1b. The result on both v_2 and v_3 puts strong new constraints on the modeling of the hydrodynamic time evolution and the modeling of radiation emission in heavy ion collisions.

2 Quarkonia and Heavy Flavor

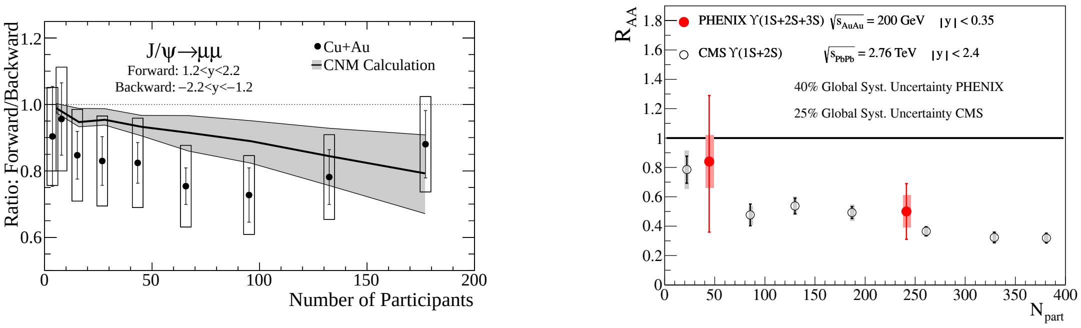

Figure 2: a) Ratio of forward- and backward-rapidity (Cu-going/Au-going) J/ψ yields measured in Cu+Au collisions, with a model calculation for the contributions from cold nuclear matter (see [3] and references therein). b) Υ nuclear modufication factor R_{AA} in Au+Au collisions at $\sqrt{s_{\mathrm{NN}}}$ = 200 GeV [4], compared to CMS results at LHC energies.

Heavy quarks are produced predominantly in hard scattering processes in the early phase of the collisions and hence can be used as a probe for the evolution of the medium. Quarkonia can be used like a thermometer for the medium, for example the Υ dissolves at a lower temperature than the J/ψ. PHENIX has excellent capabilities to measure heavy flavor production and quarkonia through leptonic channels.

One result of the J/ψ measurement in Cu+Au collisions at $\sqrt{s_{\mathrm{NN}}} = 200$ GeV is the ratio of the yields in the Cu-going direction and the Au-going direction [3]. This ratio is shown in Figure 2a as a function of centrality, represented by the number of participants. The suppression of the

J/ψ is stronger in the Cu-going direction which is consistent with more low-x shadowing in the Au nucleus than the Cu nucleus. The result is also consistent with observations in d+Au collisions at the same energy where the suppression is stronger in the d going direction.
The Υ has been measured in Au+Au collisions at the same energy [4]. The resulting R_{AA} is shown in Figure 2b, a suppression of the Υ is seen in more central collisions. The suppression is consistent with the disappearance of the $2s$ and $3s$ states of the meson. A similar suppression within uncertainties can be seen in Pb+Pb collisions at the LHC.

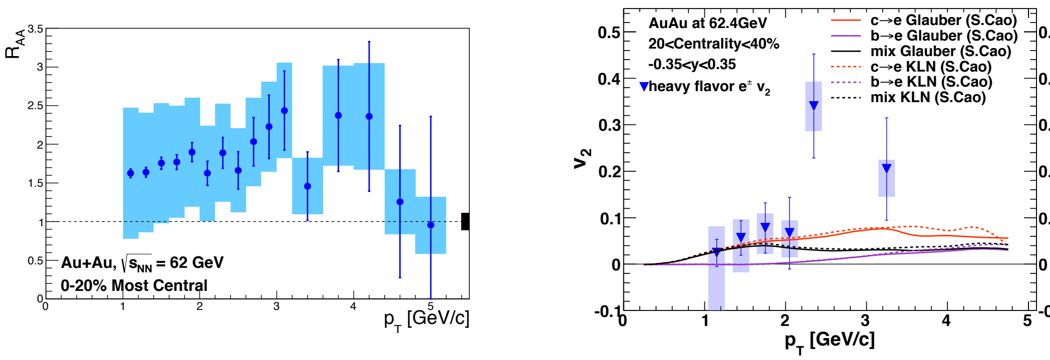

Figure 3: a) Nuclear modification factor R_{AA} of heavy-flavor electrons in 0-20% central Au+Au collisions at $\sqrt{s_{\mathrm{NN}}} = 62.4$ GeV. b) Heavy-flavor electron v_2, compared to model calculations, at the same energy (see [5] and references therein)
.

Heavy flavor production and its azimuthal anisotropy was measured via single electrons in Au+Au collisions at a lower energy of $\sqrt{s_{\mathrm{NN}}} = 62.4$ GeV. [5] Surprisingly, R_{AA} of these single electrons shows an enhancement over the $p+p$ reference at this energy, as seen in Figure 3a. This is opposite to the measurement of the same observable at $\sqrt{s_{\mathrm{NN}}} = 200$ GeV. The v_2 measurement, shown in Figure 3b, hints at a small but positive v_2 for heavy-flavor electrons which is also predicted by theoretical models. With the currently large uncertainties, no final conclusion can be drawn, hence it is important to improve the measurement with a new dataset that should be obtained in the future.

3 Initial State Effects

LHC analyses on p+Pb collisions at $\sqrt{s_{\mathrm{NN}}} = 5.02$ TeV have indicated strong azimuthal long-range correlations of hadron pairs, PHENIX has complemented these results with a measurement of the charged particle v_2 in d+Au collisions at $\sqrt{s_{\mathrm{NN}}} = 200$ GeV, using a small rapidity gap of $\Delta\eta = 0.47$ to 0.7 [6]. So far, the reason for these anisotropies is now known.
A new analysis of the azimuthal angular correlations between charged hadrons at central rapidity and the energy deposited in a calorimeter at forward (Au-going direction) rapidity, with a pseudorapidity gap of $\Delta\eta > 2.75$, shows an enhanced near-side angular correlation [7]. Figure 4a depicts this ridge-like correlation in central d+Au collisions. This result confirms the earlier PHENIX measurement with a smaller rapidity gap.
The azimuthal anisotropy v_2 has been measured as well with a large rapidity gap of $\Delta\eta > 2.75$

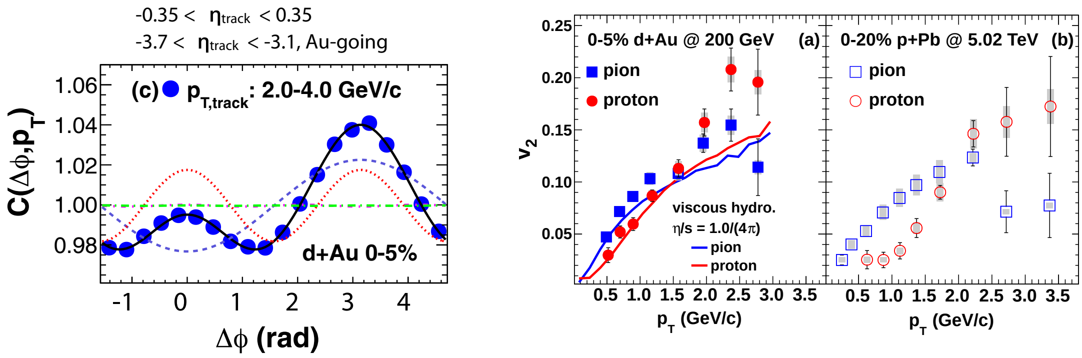

Figure 4: a) Azimuthal correlation function $C(\Delta\phi, p_T)$ for track-tower pairs in 0-5% central d+Au collisions at $\sqrt{s_{\mathrm{NN}}} = 200$ GeV, together with a four-term Fourier expansion fit. The individual components are drawn as well. b) v_2 of identified pions and (anti-)protons in the same collisions. The PHENIX data are compared with a hydrodynamic calculation in the left panel [9], and with LHC data for central p + Pb collisions in the right panel of the figure [8].

between the event plane and the observed particles. The measurement has been done with identified charged particles (pions and protons). The result of this measurement can be seen in Figure 4b, compared with results in p+Pb collisions at the LHC. At both energies, the same mass ordering as in heavy-ion collisions is observed. The PHENIX data are compared to a calculation with Glauber initial conditions for viscous hydrodynamics with $\eta/s = 1.0/(4\pi)$, starting at $\tau = 0.5$ fm/c, followed by a hadronic cascade [9]. The mass splitting at lower p_T is seen in the calculation as well, the mass splitting is larger at the LHC which might indicate a larger radial flow in the higher energy regime.

4 Future

Currently, the PHENIX collaboration is working on the construction of a new detector for future RHIC runs. It will cover 2π in azimuth and include excellent capabilities to measure jets with electromagnetic and hadronic calorimetry. It is described in more detail in [10].

References

[1] A. Adare *et al.*, Phys. Rev. Lett. **104**, 132301 (2010), Phys. Rev. Lett. **109**, 122302 (2012).
[2] A. Adare *et al.*, arXiv:1405.3940 (2014).
[3] C. Aidala *et al.*, arXiv:1404.1873 (2014).
[4] A. Adare *et al.*, arXiv:1404.2246 (2014).
[5] A. Adare *et al.*, arXiv:1405.3301
[6] A. Adare *et al.* Phys. Rev. Lett. **111**, 212301 (2013).
[7] A. Adare *et al.*, arXiv:1404.7461 (2014).
[8] B. B. Abelev *et al.* (ALICE Collaboration), Phys. Lett. **B 726**, 164 (2013).
[9] J. Nagle *et al.*, arXiv:1312.4565 (2013), M. Luzum, P. Romatschke, Phys. Rev. **C 78**, 034915 (2008).
[10] C. Aidala *et al.*, arXiv:1207.6378 (2012).

ALICE Results on Vector Meson Photoproduction in Ultra-peripheral p–Pb and Pb–Pb Collisions

Evgeny Kryshen for the ALICE Collaboration
CERN, 1211 Geneva 23, Switzerland

DOI: http://dx.doi.org/10.3204/DESY-PROC-2014-04/198

Lead nuclei, accelerated at the LHC, are sources of strong electromagnetic fields that can be used to measure photon-induced interactions in a new kinematic regime. These interactions can be studied in ultra-peripheral p–Pb and Pb–Pb collisions where impact parameters are larger than the sum of the nuclear radii and hadronic interactions are strongly suppressed. Heavy quarkonium photoproduction is of particular interest since it is sensitive to the gluon distribution in the target. The ALICE Collaboration has studied J/ψ and ψ(2S) photoproduction in ultra-peripheral Pb–Pb collisions and exclusive J/ψ photoproduction off protons in ultra-peripheral p–Pb collisions at the LHC. Implications for the study of gluon density distributions and nuclear gluon shadowing are discussed. Recent ALICE results on ρ^0 photoproduction are also presented.

1 Introduction

Lead nuclei, accelerated at the LHC, are sources of strong electromagnetic fields, which are equivalent to a flux of quasi-real photons, thus p–Pb and Pb–Pb collisions can be used to measure γp, γPb and $\gamma\gamma$ interactions in a new kinematic regime. These interactions are usually studied in ultra-peripheral collisions (UPC), characterised by impact parameters larger than the sum of the radii of the incoming hadrons, in which hadronic interactions are strongly suppressed. Heavy quarkonium photoproduction is of particular interest since, in leading order perturbative QCD, its cross section is proportional to the squared gluon density of the target. LHC kinematics corresponds to Bjorken-x ranging from $x \sim 10^{-2}$ down to $x \sim 10^{-5}$, while the heavy-quark mass requires a virtuality Q^2 larger than a few GeV^2, hence introducing a hard scale. Thus quarkonium photoproduction off protons in p–Pb UPC can be used to probe the behaviour of the gluon density at low x and to search for gluon saturation in the proton. On the other hand, quarkonium photoproduction in Pb–Pb UPC provides a direct tool to study nuclear gluon shadowing effects, which are poorly known and play a crucial role in the initial stages of heavy-ion collisions. Light vector meson photoproduction measurements would also help to shed light on underlying photoproduction mechanisms at a soft scale.

The ALICE experiment [1] measured J/ψ, ψ(2S) and ρ^0 photoproduction in Pb–Pb UPC at $\sqrt{s_{\mathrm{NN}}} = 2.76$ TeV and exclusive J/ψ photoproduction off protons in p–Pb UPC at $\sqrt{s_{\mathrm{NN}}} = 5.02$ TeV [2, 3, 4]. These results are briefly reviewed in the following sections.

2 J/ψ, ψ(2S) and ρ^0 photoproduction in Pb–Pb collisions

The ALICE detector consists of a central barrel covering the pseudorapidity range $|\eta| < 0.9$ and a muon spectrometer in the forward direction. Central barrel detectors, relevant for UPC measurements, include an Inner Tracking System (ITS), a Time Projection Chamber (TPC) and a Time-Of-Flight detector (TOF). The muon spectrometer consists of a set of absorbers, a dipole magnet, five tracking and two trigger stations used to detect muons in the range $-4 < \eta < -2.5$. The VZERO-A ($2.8 < \eta < 5.1$) and the VZERO-C ($-3.7 < \eta < -1.7$) scintillator arrays are used for triggering and multiplicity measurements. The Zero-Degree Calorimeters (ZDC), located at ±114 m from interaction point, are used to detect neutrons in the very forward regions.

ALICE measured J/ψ photoproduction in ultra-peripheral Pb–Pb collisions at forward rapidity in the dimuon channel [2] and at central rapidity both in the dimuon and dielectron channels [3]. The forward UPC trigger required a single muon with $p_{\mathrm{T}} > 1$ GeV/c in the muon spectrometer, at least one hit in VZERO-C and a veto on VZERO-A activity. For the measurement at central rapidity, the trigger required two back-to-back hits in TOF, two hits in a Silicon Pixel Detector (SPD, two innermost ITS layers) and vetoes on both VZERO detectors. Events with only two unlike sign dileptons and a neutron ZDC signal below 6 TeV were then selected in the offline analysis. The energy deposition in the TPC was used to separate dielectron and dimuon channels at mid-rapidity.

The reconstructed J/ψ signal includes contributions from coherent and incoherent production mechanisms. Coherent J/ψ photoproduction, when a photon interacts coherently with the whole nucleus, is characterized by a narrow transverse momentum distribution with $\langle p_{\mathrm{T}} \rangle \sim 60$ MeV/c. In the incoherent case the photon couples to a single nucleon so that the p_{T} distribution becomes much broader with $\langle p_{\mathrm{T}} \rangle \sim 400$ MeV/c. The transverse momentum distributions for dileptons with an invariant mass around the J/ψ mass were fitted with templates corresponding to different production mechanisms. Contributions from continuum dilepton production, feed-down from ψ(2S) decays and a possible contamination from hadronically produced J/ψ's were also taken into account in the fits. The results on the coherent J/ψ photoproduction cross section are compared with various model calculations in Fig. 1 (left). The best agreement was found for the model [5], which incorporates gluon shadowing according to EPS09 global fits [6]. A similar conclusion was obtained in Ref. [7] where the gluon shadowing factor $R_g(x \sim 10^{-3}, Q^2 \sim 2.4\ \mathrm{GeV}^2) = 0.61^{+0.05}_{-0.04}$ was extracted from the ALICE measurement at mid-rapidity.

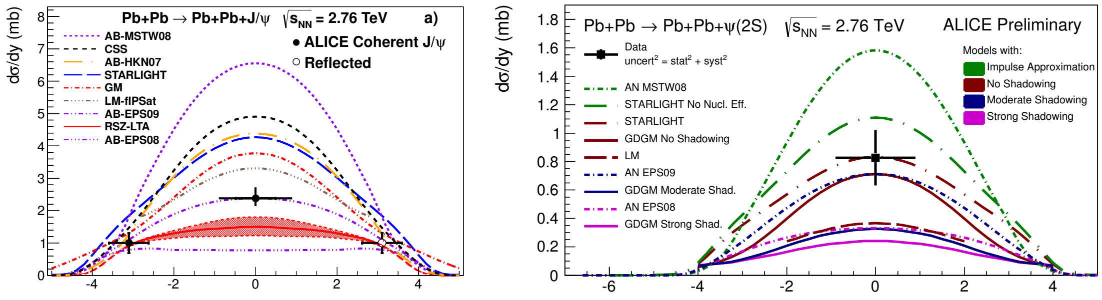

ALI-PUB-66209 ALI-PREL-68037

Figure 1: ALICE results on coherent J/ψ (left) and ψ(2S) (right) photoproduction cross section in Pb–Pb collisions at $\sqrt{s_{\mathrm{NN}}} = 2.76$ TeV in comparison with model predictions [2, 3].

ALICE also measured coherent $\psi(2\mathrm{S})$ cross section at mid-rapidity via the dilepton (l^+l^-) decay and in the channel $\psi(2\mathrm{S}) \to \mathrm{J}/\psi + \pi^+\pi^-$ followed by $\mathrm{J}/\psi \to l^+l^-$ decay. The measured cross section, shown in Fig. 1 (right), disfavours models with no nuclear effects and those with strong gluon shadowing, however different predictions rely on different reference $\gamma + \mathrm{p} \to \psi(2\mathrm{S}) + \mathrm{p}$ cross sections, thus preventing stronger conclusions. Many uncertainties on the measurement and on the $\gamma\mathrm{p}$ reference cancel in the ratio of the coherent $\psi(2\mathrm{S})$ and J/ψ cross sections. The measured ratio $\sigma^{\mathrm{coh}}_{\psi(2\mathrm{S})}/\sigma^{\mathrm{coh}}_{\mathrm{J}/\psi} = 0.344^{+0.076}_{-0.074}$ appears to be a factor two larger than in $\gamma\mathrm{p}$ measurements at HERA [8] indicating that nuclear effects may affect differently 1S and 2S charmonium states.

Measurement of the coherent ρ^0 photoproduction at the LHC is important for verification of ρ^0 photoproduction models, which differ by factor two in the predicted cross sections [9, 10, 11]. ALICE measured coherent ρ^0 photoproduction cross section in the $\pi^+\pi^-$ channel at mid-rapidity in ultra-peripheral Pb–Pb collisions at $\sqrt{s_{\mathrm{NN}}} = 2.76$ TeV. ALICE results, shown in Fig. 2 (left), disfavour the standard Glauber approach (GDL1 curve) [11], but appear to be in agreement with STARLIGHT, which is also based on the Glauber formalism, but neglects the elastic part of the total ρN cross section [9]. It is worth noting that a similar trend has been already revealed at lower energies by the STAR experiment [12]. The ALICE measurement is also consistent with the GM model [10] based on the colour-dipole approach and the Color Glass Condensate formalism.

3 Exclusive J/ψ photoproduction in p–Pb collisions

The large photon flux produced by the lead nucleus in p–Pb collisions at the LHC offers a possibility to measure exclusive J/ψ photoproduction off protons and to probe the gluon density distribution in the proton in a new kinematic regime. J/ψ photoproduction has been previously studied at HERA at $\gamma\mathrm{p}$ centre-of-mass energies $W_{\gamma\mathrm{p}}$ ranging from 20 to 305 GeV [13]. HERA cross sections are well described by a power law $\sigma(W_{\gamma\mathrm{p}}) \sim W^{\delta}_{\gamma\mathrm{p}}$, reflecting the fact that the underlying gluon distribution follows a power law in x down to $x \sim 10^{-4}$. A deviation from the power law for $\sigma(W_{\gamma\mathrm{p}})$ at higher energies could indicate a change in the evolution of the gluon density function at lower x, as expected at the onset of saturation.

ALICE utilized three options to trigger on J/ψ decays in ultra-peripheral p–Pb collisions:

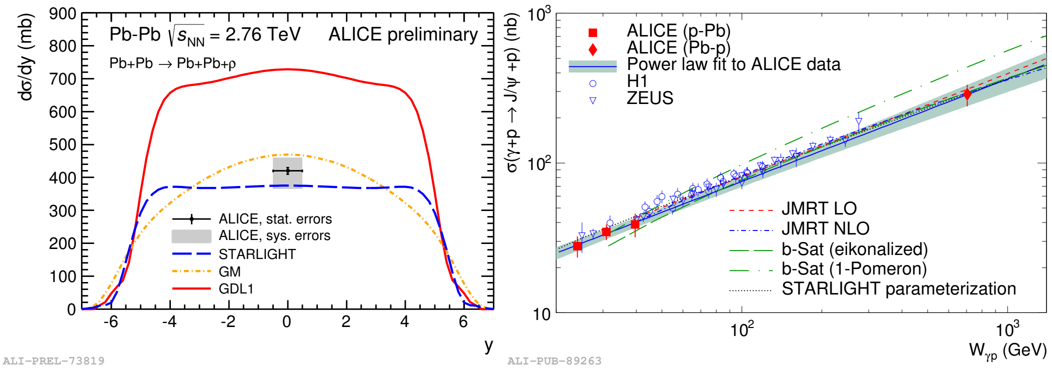

Figure 2: Left: ALICE results on coherent ρ^0 photoproduction cross section in Pb–Pb collisions at $\sqrt{s_{\mathrm{NN}}} = 2.76$ TeV. Right: exclusive J/ψ photoproduction cross section off protons measured by ALICE in comparison with HERA data and model predictions [4].

dimuon in the muon spectrometer ($-4.0 < \eta < -2.5$), dimuon or dielectron in the central barrel ($|\eta| < 0.9$) and intermediate case with a muon in the muon arm and another one in the barrel. In addition, the LHC provided collisions of protons on lead ions in two configurations: p–Pb (the proton moves towards the muon spectrometer) and Pb–p (the lead ion moves towards the muon spectrometer). This allowed ALICE to study exclusive J/ψ photoproduction in a rapidity range $-4 < y < 4$, extend accessible $W_{\gamma\mathrm{p}}$ energies up to almost 1 TeV and to probe Bjorken-x down to $x \sim 2 \times 10^{-5}$ where saturation effects might already play an important role.

The first ALICE results on exclusive J/ψ photoproduction off protons measured in p–Pb collisions via dimuon channel at forward rapidity were published in [4]. J/ψ decays were reconstructed in $2.5 < y < 4.0$ (p–Pb) and $-3.6 < y < -2.6$ (Pb–p) rapidity intervals, corresponding to γp centre-of-mass energies of $21 < W_{\gamma\mathrm{p}} < 45$ GeV and $577 < W_{\gamma\mathrm{p}} < 952$ GeV respectively. Exclusive J/ψ events were selected by vetoing activity in SPD, VZERO-A and ZDC. The remaining non-exclusive J/ψ, e.g. diffractive events accompanied by the proton dissociation, were subtracted out by fitting p_{T} distributions with templates corresponding to exclusive and non-exclusive event samples. Photoproduction cross sections $\sigma(W_{\gamma\mathrm{p}})$ were extracted from the exclusive cross sections $\frac{\mathrm{d}\sigma}{\mathrm{d}y}(\mathrm{p} + \mathrm{Pb} \to \mathrm{p} + \mathrm{Pb} + \mathrm{J}/\psi)$ at the corresponding rapidity intervals by dividing out the photon flux from Pb nuclei. ALICE results on $\sigma(W_{\gamma\mathrm{p}})$ are shown in Fig. 2 (right) in comparison with previous measurements and various theoretical models based on extrapolations of HERA data. ALICE photoproduction cross sections are consistent with a power law with $\delta = 0.68 \pm 0.06$ (stat + syst), similar to the trend obtained from HERA, thus indicating no significant change in the power-law x-dependence of the gluon density in the proton down to $x \sim 2 \times 10^{-5}$.

4 Conclusions

ALICE results on the coherent J/ψ photoproduction in ultra-peripheral Pb–Pb collisions are in good agreement with models based on the moderate gluon shadowing from the EPS09 global fit. The measured coherent $\psi(2\mathrm{S})$ photoproduction cross section disfavours models with no nuclear effects and those with strong gluon shadowing. Coherent ρ^0 photoproduction in Pb–Pb collisions at the LHC cannot be described in the standard Glauber formalism, but is in agreement with STARLIGHT and the colour-dipole approach. ALICE results on the exclusive J/ψ photoproduction off a proton measured in p–Pb collisions indicate no significant change in the power-law x-dependence of the gluon density in the proton between HERA and LHC energies.

References

[1] K. Aamodt *et al.* [ALICE Collaboration], J. Instrum. **3**, S08002 (2008).
[2] B. Abelev *et al.* [ALICE Collaboration], Phys. Let. **B718**, 1273 (2013).
[3] E. Abbas *et al.* [ALICE Collaboration], Eur. Phys. J. **C73**, 2617 (2013).
[4] B. Abelev *et al.* [ALICE Collaboration], arXiv:1406.7819 [nucl-ex] (2014).
[5] A. Adeluyi and C. A. Bertulani, Phys. Rev. **C85**, 044904 (2012).
[6] K. J. Eskola, H. Paukkunen and C. A. Salgado, JHEP **0904**, 065 (2009).
[7] V. Guzey, E. Kryshen, M. Strikman and M. Zhalov, Phys. Lett. **B726**, 290 (2013).
[8] C. Adloff *et al.* [H1 Collaboration], Phys. Lett. **B541**, 251 (2002).
[9] S. R. Klein and J. Nystrand, Phys. Rev. **C60**, 014903 (1999).
[10] V. P. Goncalves and M. V. T. Machado, Phys. Rev. **C84**, 011902 (2011).
[11] V. Rebyakova, M. Strikman and M. Zhalov, Phys. Lett. **B710**, 647 (2012).

[12] G. Agakishiev *et al.* [STAR Collaboration], Phys. Rev. **C85**, 014910 (2012).
[13] S. Chekanov *et al.* [ZEUS Collaboration], Eur. Phys. J. **C24**, 345 (2002).
C. Alexa *et al.* [H1 Collaboration], Eur. Phys. J. **C73**, 2466 (2013).

J/ψ production at the STAR experiment

Petr Chaloupka for the STAR collaboration

Czech Technical University in Prague, Zikova 1903/4, 16636, Praha 6, Czech Republic

DOI: http://dx.doi.org/10.3204/DESY-PROC-2014-04/89

This paper reports on STAR measurements of J/ψ production at mid-rapidity. We present results on the $\psi(2S)$ to J/ψ yield ratio in p+p collisions at $\sqrt{s}$=500 GeV. We also report results from Au+Au collisions at $\sqrt{s_{NN}} = 39$ GeV, 62.4 GeV, 200 GeV together with results from U+U collisions at $\sqrt{s_{NN}}$=193 GeV. Nuclear modification factors are presented as a function of centrality and p_T.

1 Introduction

Suppression of quarkonium production in heavy-ion collisions due to Debye color screening of quark and antiquark potential in the deconfined medium, has been proposed as a signature of quark-gluon plasma (QGP) formation. Since the Debye screening length depends on the temperature attained by the QGP medium, systematic measurements of production of various quarkonium states can provide insight into thermodynamic properties of the QGP. However, there are other effects that may alter the observed yields, such as cold nuclear matter effects (CNM) including shadowing/anti-shadowing of parton distribution functions and final state nuclear absorption, and statistical coalescence of quark-antiquark pairs in the QGP. Measurements of J/ψ yields at different collision energies, collision systems, and centralities help to disentangle the interplay of these effects on the J/ψ production.

2 Data analysis and results

The STAR experiment is a large-acceptance detector which excels at tracking and identification of charged particles at mid-rapidity ($|\eta| < 1$) with full azimuthal coverage. In the bellow discussed analyses J/ψ's are reconstructed at mid-rapidity in the di-electron decay channel, $J/\psi \to e^+ + e^-$ (branching ratio $B_{ee} = 5.9\%$). Electrons and positrons are reconstructed using the Time Projection Chamber (TPC) which also provides particle identification by measuring ionization energy loss (dE/dx). Furthermore, the particle identification is enhanced by the Time of Flight detector (TOF) in the low-p_T region and by the Barrel Electromagnetic Calorimeter (BEMC) in the high-p_T region.

In order to correctly interpret results from heavy-ion collisions we first need to understand the J/ψ production in elementary p+p collisions. STAR has measured production of J/ψ in p+p collisions at $\sqrt{s}$=500 GeV, the highest collision energy achievable in p+p collisions at RHIC. A p_T-dependent differential cross section for inclusive J/ψ production is shown in Fig. 1. The high precision results at the new collision energy reaching up to $p_T = 20$ GeV/c provide additional information that can be used to discriminate among different production models.

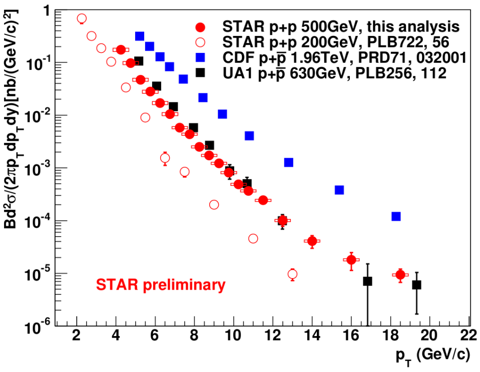

Figure 1: The J/ψ invariant cross section in p+p collisions at $\sqrt{s_{NN}}$=200 and 500 GeV, compared to results from other experiments.

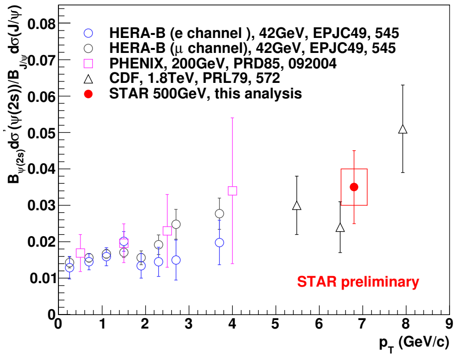

Figure 2: Ratio of $\psi(2\mathrm{S})$ to J/ψ yields in p+p at $\sqrt{s}$=500 GeV, compared to results from HERA-B, PHENIX and CDF experiments.

Moreover, the high statistics data recorded in year 2011 allowed to measure for the first time the production of $\psi(2\mathrm{S})$ state in p+p collisions at $\sqrt{s}$=500 GeV. The STAR result on the $\psi(2\mathrm{S})$ to J/ψ yield ratio at mid-rapidity presented in Fig. 2 is in agreement with results from other experiments which exhibit an increasing trend with p_T with no significant dependence on the collision energy.

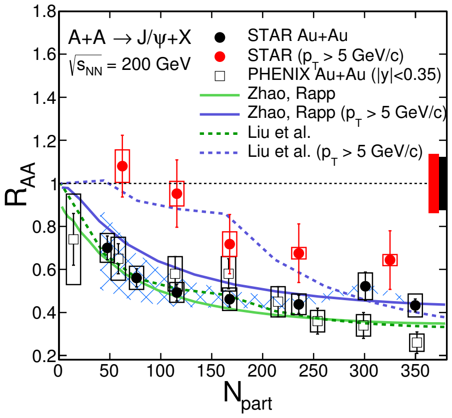

Figure 3: J/ψ R_{AA} as a function of centrality in Au+Au collisions at $\sqrt{s_{NN}}$=200 GeV from STAR [1, 2] and PHENIX [3], compared to model calculations [4, 5].

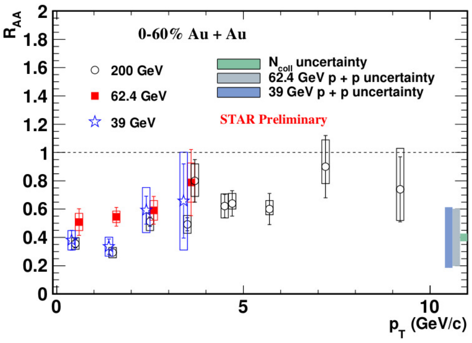

Figure 4: STAR results on J/ψ R_{AA} from 0-60% Au+Au collisions at $\sqrt{s_{NN}}$= 39, 62.4 and 200 GeV as a function of p_T. Open boxes represent systematic uncertainties. The boxes on the vertical axis represent uncertainties from CEM [6] baseline estimation for 39 and 62.4 GeV and $\langle N_{coll} \rangle$ uncertainties.

STAR results [1, 2] on modification of J/ψ production in Au+Au collisions at $\sqrt{s_{NN}}$=200 GeV are presented in Fig. 3. The nuclear modification factor R_{AA} is shown as a function of centrality (represented by number of participants, N_{part}) and compared to PHENIX [3] results. Strong suppression in the most central collisions is observed for both the low-p_T dominated result [1] (shown in black) and the high-p_T (p_T>5 GeV/c) results [2] (shown in red). R_{AA} at high-p_T are systematically higher than the low-p_T ones. For high-p_T J/ψ the suppression is observed only in central collisions (0-30%) while in peripheral and mid-peripheral collisions the R_{AA} is consistent with unity. Since d+Au results[7] indicate that at p_T> 5 GeV/c the CNM effects are negligible, the observed suppression in Au+Au collisions is likely to come from suppression in the QGP (due to color screening or other dynamical effects). However, it should be noted that the data are not corrected for B→J/ψ feed-down which can be, based on p+p data, as high as 15-25% in this p_T range. The data in Fig. 3 are compared to models of Zhao and Rapp [5] and Liu et al. [4]. These models contain not only suppression due to the color screening effect, but also secondary production of J/ψ via recombination of thermalized c and $\bar{c}$ quarks. The interplay between direct production and recombination can be studied by varying collision energy. Fig. 4 shows STAR results on p_T dependence of J/ψ R_{AA} in Au+Au collisions at $\sqrt{s_{NN}}$=200, 62.4 and 39 GeV. Centrality dependence of the low-p_T (p_T< 5 GeV/c) part of the data is shown in Fig. 5. At all three energies a similar suppression pattern is observed. The centrality dependence in Fig. 5 is compared to the model by Zhao and Rapp [5]. These calculations, in agreement with the data, predict rather small dependence of the suppression on the collision energy. In these models, the suppression of primordial J/ψ is more significant at a higher collision energy, but it is compensated by the increased contribution from regeneration due to larger charm quark production cross section.

It should be noted that STAR did not measure p+p data at 62.4 and 39 GeV and hence the Color Evaporation Model (CEM) [6] was used as a reference instead. The resulting uncertainties are shown as boxes in Fig. 4 and 5.

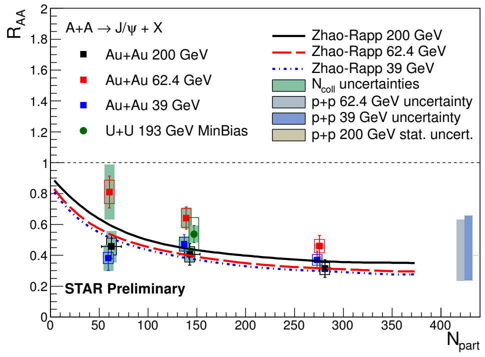

Figure 5: Centrality dependence of J/ψ R_{AA} for p_T<5 GeV/c in Au+Au collisions at different collision energies and U+U (p_T<6 GeV/c) at $\sqrt{s_{NN}}$=193 GeV.

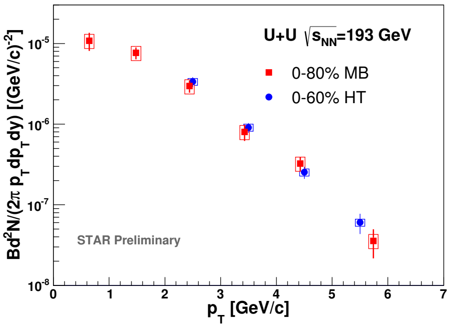

Figure 6: J/ψ invariant yield versus transverse momentum in U+U collisions at $\sqrt{s_{NN}}$=193 GeV from minimum bias (red) events and events triggered by high-p_T electron in BEMC (blue).

To further study the pattern of quarkonium suppression STAR recorded collisions of non-spherical Uranium nuclei at $\sqrt{s_{NN}}$=193 GeV in which an approximately 20% higher energy density can be reached. STAR results on J/ψ invariant yield at mid-rapidity in U+U collisions at $\sqrt{s_{NN}}$=193 GeV are shown in Fig. 6 with p_T reaching up to 6 GeV/c. The presented data are from 0-80% minimum bias (in red) and at high-p_T from events triggered by a signal from high-p_T electron in Electromagnetic Calorimeter (in blue). Spectra from p+p collisions at $\sqrt{s_{NN}}$=200 GeV are used to obtain J/ψ R_{AA} in U+U at $\sqrt{s_{NN}}$=193 GeV. The p_T dependence

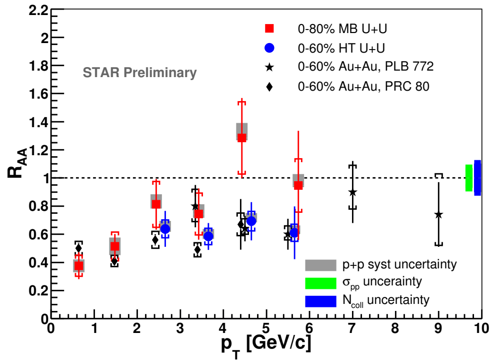

Figure 7: J/ψ nuclear modification factor in U+U collisions at $\sqrt{s_{NN}}$=193 GeV as a function of p_T, compared to results form Au+Au collisions at $\sqrt{s_{NN}}$=200 GeV.

of the R_{AA} shown in Fig. 7 is within uncertainties similar to Au+Au collisions. The data show a strong suppression at low-p_T with a non-negligible suppression remaining even in the high-p_T region. The R_{AA} obtained from the low-p_T dominated 0-80% minimum bias events are compared to the centrality (N_{part}) dependence of R_{AA} at different Au+Au collision energies in Fig. 5. The U+U results are consistent within uncertainties with the suppression pattern observed in Au+Au.

3 Summary

STAR has measured ratio of ψ(2S) to J/ψ in p+p collisions at $\sqrt{s}$=500 GeV and found it consistent with the results at other collision energies. The J/ψ suppression in Au+Au collisions at lower energies of $\sqrt{s_{NN}}$=39 and 62.4 GeV is similar to those at 200 GeV suggesting an important interplay of suppression of primordial J/ψ and regeneration. STAR has also measured J/ψ R_{AA} in U+U collisions at $\sqrt{s_{NN}}$=193 GeV. The U+U data are consistent within uncertainties with the suppression pattern observed in Au+Au collisions.

References

[1] L. Adamczyk et al. J/ψ production at low p_T in Au+Au and Cu+Cu collisions at $\sqrt{s_{NN}}$ = 200 GeV at STAR. *Phys.Rev.*, C90:024906, 2014.

[2] L. Adamczyk et al. J/ψ production at high transverse momenta in p+p and Au+Au collisions at $\sqrt{s_{NN}}$ = 200 GeV. *Phys.Lett.*, B722:55–62, 2013.

[3] A. Adare et al. J/ψ Production vs Centrality, Transverse Momentum, and Rapidity in Au+Au Collisions at $\sqrt{s_{NN}}$ = 200 GeV. *Phys.Rev.Lett.*, 98:232301, 2007.

[4] Yun-peng Liu, Zhen Qu, Nu Xu, and Peng-fei Zhuang. J/psi Transverse Momentum Distribution in High Energy Nuclear Collisions at RHIC. *Phys.Lett.*, B678:72–76, 2009.

[5] Xingbo Zhao and Ralf Rapp. Charmonium in Medium: From Correlators to Experiment. *Phys.Rev.*, C82:064905, 2010.

[6] R. E. Nelson, R. Vogt, and A. D. Frawley. Narrowing the uncertainty on the total charm cross section and its effect on the j/ψ cross section. *Phys. Rev. C*, 87:014908, 2013.

[7] A. Adare et al. Transverse-Momentum Dependence of the J/ψ Nuclear Modification in d+Au Collisions at $\sqrt{s_{NN}}$ = 200 GeV. *Phys.Rev.*, C87(3):034904, 2013.

Elliptic Flow of Thermal Photons in Chemically Non-Equilibrated QCD Medium

Akihiko Monnai[1]

[1]RIKEN BNL Research Center, Brookhaven National Laboratory, Upton, NY 11973, USA

DOI: http://dx.doi.org/10.3204/DESY-PROC-2014-04/87

Heavy-ion experiments have recently revealed that azimuthal momentum anisotropy – elliptic flow – of direct photons from a QCD medium is a few times larger than hydrodynamic predictions. I present a possible explanation for the enhancement based on late quark chemical equilibration. The color glass theory indicates that the medium is initially gluon-rich. Thermal photons are then mainly produced after quarks are produced, at which point large flow anisotropy is developed. The numerical estimations indicate that slow chemical equilibration visibly enhances the elliptic flow of thermal photons.

1 Introduction

The quark-gluon plasma (QGP) is a deconfined phase of quantum chromodynamics (QCD). After its experimental realization at BNL Relativistic Heavy Ion Collider (RHIC) [1] and CERN Large Hadron Collider (LHC) [2], there have been extensive studies on its properties. Large azimuthal momentum anisotropy, heavy quark diffusion and jet quenching observed in the experiments indicate that the quarks and gluons are strongly-coupled. The bulk medium follows the description of a relativistic fluid with small viscosity [3]. On the contrary, photons and leptons are weakly coupled to the medium as they are not sensitive to the strong interaction. The transparency makes them unique probes to investigate the hot medium. Heavy particles, such as weak bosons, are mostly created at the time of collision while photons and dileptons can be produced thermally, which implies the existence of collectivity in those observables.

In this study, I focus on thermal photons. The photons created in the hard process are called prompt photons and those emitted softly from the medium are called thermal photons. One of the most useful observables for the quantification of the collectivity is elliptic flow v_2, which is defined in Fourier expansion of particle spectra with respect to the azimuthal angle

$$\frac{dN}{d\phi} = \frac{N}{2\pi}[1 + 2v_1 \cos(\phi - \Psi_1) + 2v_2 \cos(\phi - \Psi_2) + 2v_3 \cos(\phi - \Psi_3) + ...], \tag{1}$$

where ϕ is the angle in momentum space and Ψ_n are the respective reaction planes. The quantity is sensitive to the magnitude of medium interaction as they are non-vanishing only when non-central geometry and/or fluctuation in the collision is converted into momentum anisotropy. Hadronic v_2 and v_3 are found large, which is considered as an evidence for the aforementioned strongly-coupled QGP. Surprisingly, on the other hand, direct photon v_2 is found large at RHIC [4] and LHC [5]. It is a few times larger than hydrodynamic predictions and almost comparable to pion v_2, even though the quantity should reflect the small flow anisotropy in early stages of the time-evolution. This phenomenon is now recognized as “photon v_2 puzzle”. Recent experimental data also indicate the existence of large direct photon v_3 comparable to the pionic counterpart, which implies that the enhancement is at least partially due to the properties of the medium itself.

2 Chemically non-equilibrated fluid

A heavy-ion system before the collision is described as the color glass condensate, a state of saturated gluons [6]. The system locally equilibrates in a short time ~ 1 fm/c after the collision and form the quark-gluon plasma, which behaves as a fluid until it reaches freeze-out. An important observation is that thermalization and chemical equilibration do not necessarily occur simultaneously [7]. When the system is chemically non-equilibrated at the onset of hydrodynamic evolution, thermal photon emission is suppressed because of the scarcity of quarks. This can lead to enhancement of photon v_n as the contribution of later stages where the flow anisotropy is already large becomes effectively large [8].

The inviscid hydrodynamic equations of motion of a chemically non-equilibrated system are energy-momentum conservation and rate equations for the energy momentum tensor and the number currents in the QGP phase:

$$\partial_\mu T_q^{\mu\nu} + \partial_\mu T_g^{\mu\nu} = 0, \tag{2}$$

$$\partial_\mu N_q^\mu = 2r_b n_g - 2r_b \frac{n_g^{\mathrm{eq}}}{(n_q^{\mathrm{eq}})^2} n_q^2, \tag{3}$$

$$\partial_\mu N_g^\mu = (r_a - r_b) n_g - r_a \frac{1}{n_g^{\mathrm{eq}}} n_g^2 + r_b \frac{n_g^{\mathrm{eq}}}{(n_q^{\mathrm{eq}})^2} n_q^2 + r_c n_q - r_c \frac{1}{n_g^{\mathrm{eq}}} n_q n_g, \tag{4}$$

where r_a, r_b and r_c are reaction rates for (a) gluon splitting, (b) the quark pair production and (c) gluon emission from a quark, respectively. The subscript *eq* denotes that the variable is in chemical equilibrium. Local thermalization of the quark and the gluon components is assumed and the total energy density and the total pressure are defined as $e = e_q + e_g$ and $P = P_q + P_g$. n_q and n_g are the number densities for quarks and gluons, respectively. Late quark chemical equilibration corresponds to $r_b < r_a, r_c$ because the pair creation is the process which changes the quark number density. Here the matter-antimatter degrees of freedom is included in N_q^μ. It is note-worthy that the inverse of the reaction rate gives the chemical relaxation time τ_i. Since the parton picture is no longer applicable in the hadronic phase, the system is simply assumed to be in chemical equilibrium below the crossover temperature.

The hydrodynamic medium is characterized by the equation of state and the chemical reaction rates. The former is given by a hyperbolic interpolation of the parton gas of u, d, g and the resonance gas of hadrons with mass up to 2.5 GeV as $s = c(T) s_{\mathrm{par}} + [1 - c(T)] s_{\mathrm{had}}$ where the interpolation function is $c(T) = \{1 + \tanh[(T - T_c)/\Delta T]\}/2$. The connecting temperature $T_c = 0.17$ GeV and the crossover width $\Delta T = 0.017$ GeV are chosen. This preserves the consistency with the parton gas model used to estimate the equilibrium parton densities n_q^{eq} and n_g^{eq}. The latter is parametrized as $r_i = c_i T$ $(i = a, b, c)$ where c_i is the dimensionless parameter. The initial conditions for the energy density is based on an analytical Glauber model [9]. The numerical estimation is performed in the (2+1)-dimensional boost invariant geometry. Thermal photon emission rate is based on the hyperbolic interpolation of the rates in the hadronic [10] and the QGP phases [11]. Note that the parameters are chosen for demonstration of the chemical equilibration effects and precision analyses will be discussed elsewhere.

3 Numerical results

Elliptic flow of thermal photons is shown in Fig. 1 along with the time-evolution of the quark number density for different quark chemical equilibration parameters. $c_b = 0.2, 0.5$ and 2.0 roughly corresponds to $\tau_{\mathrm{chem}} = 1/c_b T \sim 5.0, 2.0$ and 0.5 fm/c when the average medium temperature is $T \sim 0.2$ GeV. Au-Au collisions at $\sqrt{s_{NN}}$ =200 GeV are considered. The impact parameter is set to $b = 7$ fm at the thermalization time $\tau_{\mathrm{th}} = 0.4$ fm/c. One can see that late quark chemical equilibration leads to enhancement of thermal photon v_2. It is note-worthy that the typical chemical equilibration time suggested in a pre-equilibrium model [7] is 2 fm/c.

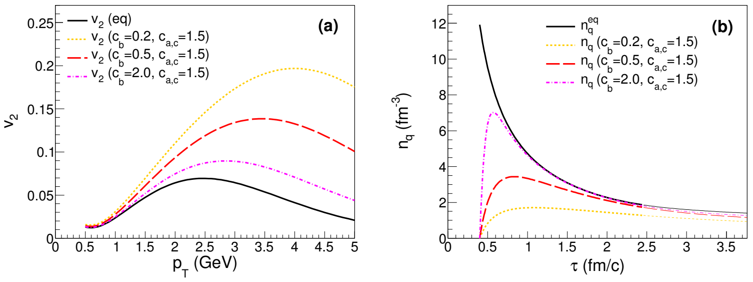

Figure 1: (a) Elliptic flow of thermal photons and (b) time-evolution of the quark number density for different quark chemical equilibration rates. Thin lines for the number density indicate that the medium temperature is near the crossover $T < T_c + \Delta T$.

Figure 2 shows the dependence of thermal photon v_2 and that of the time-evolution of the gluon number density on gluon-involved equilibration parameters for a fixed c_b. The elliptic flow is slightly reduced for late gluon equilibration because gluons are initially overpopulated and larger number of gluons in the early stage leads to earlier production of quarks with small anisotropy. Quantitatively, it can be seen that the quark equilibration process plays bigger role in the thermal photon v_2 modification than the gluon one.

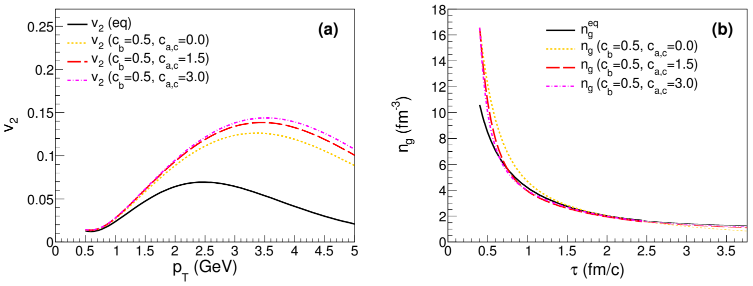

Figure 2: (a) Elliptic flow of thermal photons and (b) time-evolution of the gluon number density for different gluon chemical equilibration rates. Thin lines for the number density indicate that the medium temperature is near the crossover $T < T_c + \Delta T$.

Transverse-momentum spectra of thermal photons show slight reduction for the late chemical equilibration cases due to the suppression in the photon emission. The magnitude is found to be not significant for the current parameter settings, but the introduction of more sophisticated photon emission rate and the dynamical equation of state would be important for quantitative discussion as the spectra and v_2 would both be sensitive to the input [12].

4 Conclusion and outlook

Thermal photon elliptic flow from a chemically non-equilibrated QGP fluid is estimated by the newly-developed hydrodynamic model coupled to the rate equations for the parton number densities. This is motivated by the fact that a high-energy heavy-ion system is initially gluon-rich because the colliding nuclei are described as the color glass condensate. The numerical analyses indicate that thermal photon v_2 is visibly enhanced by late quark chemical equilibration, contributing positively to the resolution of the "photon v_2 puzzle". The fact that the difference in thermalization and chemical equilibration times affects phenomenology implies that the interplay of pre- and post-equilibrium physics is important, which is in good analogy to the fact that thermal and chemical freeze-out have to be treated separately at the end of a hydrodynamic estimation for hadronic spectra. Future prospects include introduction of more quantitative photon emission rate, initial conditions, equation of state and transport processes as well as estimation of the contribution of prompt photons, which are naively believed to have almost vanishing anisotropy, for the comparison to the experimental data of direct photons. It would also be important to investigate the effects of other mechanisms, *e.g.*, Ref. [13] for the comprehensive understanding of photon physics in heavy-ion collisions.

Acknowledgments

The work is inspired by fruitful discussion with B. Müller. The author would like to thank for valuable comments by Y. Akiba and L. McLerran on the paper. The work of A.M. is supported by RIKEN Special Postdoctoral Researcher program.

References

[1] K. Adcox *et al.* [PHENIX Collaboration], Nucl. Phys. **A757**, 184 (2005); J. Adams *et al.* [STAR Collaboration], Nucl. Phys. **A757**, 102 (2005); B. B. Back *et al.* [PHOBOS Collaboration], Nucl. Phys. **A757**, 28 (2005); I. Arsene *et al.* [BRAHMS Collaboration], Nucl. Phys. **A757**, 1 (2005).

[2] K. Aamodt *et al.* [The ALICE Collaboration], Phys. Rev. Lett. **105**, 252302 (2010).

[3] B. Schenke, S. Jeon and C. Gale, Phys. Rev. Lett. **106**, 042301 (2011).

[4] A. Adare *et al.* [PHENIX Collaboration], Phys. Rev. Lett. **109**, 122302 (2012).

[5] D. Lohner [ALICE Collaboration], J. Phys. Conf. Ser. **446**, 012028 (2013).

[6] L. D. McLerran and R. Venugopalan, Phys. Rev. **D49**, 2233 (1994); **D49**, 3352 (1994).

[7] A. Monnai and B. Müller, arXiv:1403.7310 [hep-ph].

[8] A. Monnai, Phys. Rev. C **90**, 021901 (2014).

[9] P. F. Kolb, J. Sollfrank and U. W. Heinz, Phys. Rev. **C62**, 054909 (2000).

[10] C. T. Traxler and M. H. Thoma, Phys. Rev. **C53**, 1348 (1996).

[11] S. Turbide, R. Rapp and C. Gale, Phys. Rev. **C69**, 014903 (2004); F. Arleo, P. Aurenche, F. W. Bopp, I. Dadic, G. David, H. Delagrange, D. G. d'Enterria and K. J. Eskola *et al.*, hep-ph/0311131.

[12] F. Gelis, H. Niemi, P. V. Ruuskanen and S. S. Rasanen, J. Phys. **G30**, S1031 (2004).

[13] A. Monnai, arXiv:1408.1410 [nucl-th].

Results on Heavy-Flavour Production in pp, p–Pb and Pb–Pb Collisions with ALICE at the LHC

Grazia Luparello[1] for the ALICE Collaboration

[1]Università di Trieste and INFN - Trieste, via A. Valerio 2, Trieste, Italy

DOI: http://dx.doi.org/10.3204/DESY-PROC-2014-04/92

The ALICE Collaboration has measured heavy-flavour production through the reconstruction of hadronic decays of D mesons at mid-rapidity and via semi-electronic (at mid-rapidity) and semi-muonic (at forward rapidity) decays of charm and beauty hadrons in pp, p–Pb and Pb–Pb collisions. A summary of the most recent results from p–Pb collisions at $\sqrt{s_{NN}} = 5.02$ TeV and Pb–Pb collisions at $\sqrt{s_{NN}} = 2.76$ TeV is presented in this paper.

1 Introduction

Heavy quarks are effective probes of the Quark Gluon Plasma (QGP) formed in high-energy nucleus-nucleus collisions, since they are produced on a short time scale with respect to that of the QGP. They traverse the strongly interacting medium and lose energy through radiative [1] and collisional [2] processes. Theoretical calculations predict a dependence of the energy loss on the colour charge and on the mass of the parton traversing the medium, resulting in a hierarchy in the energy loss with beauty quarks losing less energy than charm quarks, and charm quarks losing less energy than light quarks and gluons [3, 4]. The energy loss is experimentally investigated via the nuclear modification factor R_{AA}, defined as the ratio of the yield in nucleus-nucleus collisions to that observed in pp collisions scaled by the number of binary nucleon-nucleon collisions. In the absence of medium effects, R_{AA} is expected to be unity for heavy flavours, since the production yields are proportional to the number of binary nucleon-nucleon collisions. The expected hierarchy in the energy loss described above can be verified comparing the R_{AA} of different particle species, namely $R_{\mathrm{AA}}(\mathrm{B}) > R_{\mathrm{AA}}(\mathrm{D}) > R_{\mathrm{AA}}(light)$. For this comparison it should be considered that the R_{AA} of the different hadronic species are also affected by the different production kinematics and fragmentation function of gluons, light and heavy quarks. The R_{AA} can be modified also due to initial-state effects, since the nuclear environment affects the quark and gluon distributions as described either by calculations based on phenomenological modifications of the Parton Distribution Functions (PDF) [5] or by the Colour Glass Condensate (CGC) effective theory [6]. Partons can also lose energy in the initial stages of the collision via initial-state radiation [7], or they can experience transverse momentum broadening due to multiple soft collisions prior to the hard scattering [8]. Initial-state effects are addressed by studying p–Pb collisions. Finally, in nucleus-nucleus collisions the charmed hadron azimuthal anisotropy, quantified via the second order coefficient of the Fourier decomposition of the particle momentum azimuthal distribution (v_2), tests whether also charm quarks participate in the collective expansion dynamics and possibly thermalize in the QGP.

2 Open heavy-flavour measurements in ALICE

The excellent performance of the ALICE detector [9] allows open heavy-flavour measurements in several decay channels and in a wide rapidity range. At mid-rapidity ($|y| < 0.5$) D mesons are reconstructed via their hadronic decay channels: $\mathrm{D}^0 \to \mathrm{K}^-\pi^+$, $\mathrm{D}^+ \to \mathrm{K}^-\pi^+\pi^+$, $\mathrm{D}^{*+} \to \mathrm{D}^0\pi^+ \to \mathrm{K}^-\pi^+\pi^-$, $\mathrm{D}_\mathrm{s}^+ \to \phi\pi^+ \to \mathrm{K}^-\mathrm{K}^+\pi^+$ and their charge conjugates. D-meson selection is based on the reconstruction of decay vertices displaced by a few hundred μm from the interaction vertex, exploiting the high track-position resolution close to the interaction vertex provided by the Inner Tracking System (ITS). The large combinatorial background is reduced by selections applied on the decay topology and by the identification of charged kaons and pions in the Time Projection Chamber (TPC) and Time-Of-Flight (TOF) detector. Electrons are identified at mid-rapidity through their specific energy loss in the TPC gas combined with the information from the TOF and from the electromagnetic calorimeter (EMCal). At forward rapidity, open heavy-flavour production is studied in the semi-muonic decay channel. Muons are reconstructed in the five tracking stations of the Muon Spectrometer ($-4 < \eta < -2.5$). The reconstructed tracks are matched with tracklets measured in the trigger stations to reject punch-through hadrons.

3 Results

Figure 1 shows the nuclear modification factor (R_pPb) measured in p–Pb collisions at $\sqrt{s_\mathrm{NN}}$=5.02 TeV as a function of p_T for heavy-flavour decay electrons (left) and muons (right). The measurement of D-meson R_pPb is reported in [10]. The results are compatible with unity within uncertainties without any significant dependence on the rapidity interval investigated. The measurements confirm that initial-state effects due to the presence of cold-nuclear matter are small in the measured p_T range. Theoretical predictions based on pQCD calculations including the EPS09 [5] nuclear modification of the PDF can describe the measurements. The D-meson R_pPb is also compatible with calculations based on the CGC [6] and with a model including cold-nuclear-matter energy loss, nuclear shadowing and k_T-broadening [11].

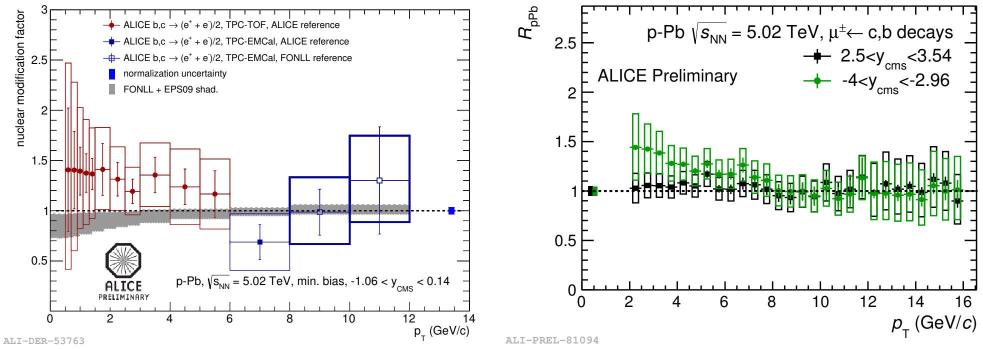

Figure 1: R_pPb of heavy-flavour decay electrons at mid-rapidity and heavy-flavour decay muons at forward (p-going direction) and backward (Pb-going direction) rapidities in minimum-bias p–Pb collisions, as a function of p_T.

Open heavy-flavour production is also studied in p–Pb collisions as a function of the event activity. The ratio $Q^{\mathrm{mult}}_{\mathrm{pPb}}(p_{\mathrm{T}}) = \frac{\mathrm{d}N^{\mathrm{mult}}_{\mathrm{pPb}}/\mathrm{d}p_{\mathrm{T}}}{<N^{\mathrm{mult}}_{\mathrm{coll}}>\mathrm{d}N_{\mathrm{pp}}/\mathrm{d}p_{\mathrm{T}}}$ is used to study the possible multiplicity-dependent modification of the p_T-differential yields in p–Pb collisions with respect to the binary-scaled yields measured in pp collisions. Events are divided in classes based on the energy measured in the Zero Degree Calorimeters located in the Pb-going direction (ZNA). The average number of nucleon-nucleon collisions for the considered ZNA energy event class, $< N^{\mathrm{mult}}_{\mathrm{coll}} >$, is calculated with the hybrid approach described in [12]. Figure 2 demonstrates that the $Q^{\mathrm{mult}}_{\mathrm{pPb}}$ of prompt D mesons for events with high and low multiplicities is compatible with unity within uncertainties, thus no multiplicity-dependent modification of D-meson production in p–Pb collisions relative to the binary-scaled pp production is observed.

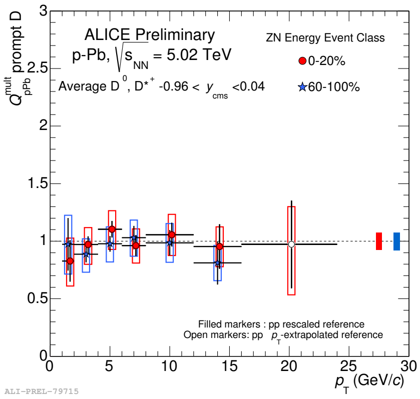

Figure 2: Prompt D-meson $Q^{\mathrm{mult}}_{\mathrm{pPb}}$ in the 0-20% and 60-100% ZNA energy classes.

In Pb–Pb collisions, the open heavy-flavour R_{AA} measured with ALICE in the different channels [13] shows a strong reduction of the yields at large trasverse momenta ($p_{\mathrm{T}} > 5$ GeV/c) in the most central collisions relative to a binary-scaled pp reference. This suppression is interpreted as due to charm quark in-medium energy loss. The expected mass ordering of the energy loss is also investigated: Fig. 3 (left) shows the D-meson R_{AA} as a function of centrality, represented as the average number of nucleons participating in the interaction, compared to the one of J/ψ from beauty-hadron decays measured by CMS [14]. The D-meson p_{T} range was chosen in order to obtain a significant overlap with the p_{T} distribution of B mesons decaying to J/ψ with $6.5 < p_{\mathrm{T}} < 30$ GeV/c, thus allowing a consistent comparison. A similar trend as a function of centrality is observed, but the D-meson R_{AA} is systematically lower than the one of J/ψ from B decays. This is consistent with the expectation of a smaller in-medium energy loss for beauty than for charm quarks. A comparison with the R_{AA} of charged hadrons and pions is also done (not shown): a similar suppression is observed, although the uncertainties do not allow yet to draw a conclusion on the colour-charge dependence of the in-medium energy loss. Figure 3 (right) shows the v_2 of heavy-flavour decay electrons and muons in the centrality interval 20-40%. The two results are compatible within uncertainties. For $2 < p_{\mathrm{T}} < 3$ GeV/c a positive v_2 is observed ($> 3\sigma$ effect). The D-meson v_2 measured in the 30-50% centrality class is larger than zero with a 5.7σ significance in the interval $2 < p_{\mathrm{T}} < 6$ GeV/c and comparable in magnitude to the one of charged hadrons [15] (not shown). These results indicate that heavy quarks participate in the collective motion of the system. At high p_{T}, v_2 results could give insight into the path-length dependence of the in-medium energy loss, but the present statistics

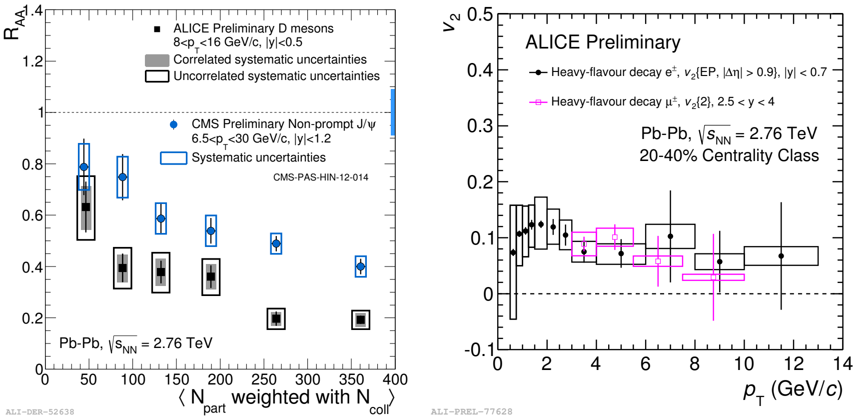

Figure 3: Left: $R_{\rm AA}$ of prompt D mesons and of non-prompt J/ψ measured by CMS [14] as a function of centrality, expressed in terms of the number of nucleons participating in the interaction. Right: Heavy-flavour decay electron and muon v_2.

does not allow to conclude on this.

In summary, in p–Pb collisions the open heavy-flavour $R_{\rm pPb}$ is consistent with unity indicating that initial-state effects are small. In Pb–Pb collisions a large suppression of open heavy-flavour yields is observed at intermediate and high $p_{\rm T}$. Since initial-state effects are small, these results can be interpreted as a final-state effect due to the interaction of the charm quarks with the hot and dense medium. The v_2 measured in Pb–Pb semi-central collisions is larger than zero at low $p_{\rm T}$, suggesting that heavy quarks participate in the collective motion of the system.

References

[1] M. Gyulassy and M. Plumer, Phy. Lett. **B243**, 432 (1990); R. Baier, Y. L. Dokshitzer, A. H. Mueller, S. Peigne and D. Schiff, Nucl. Phys. **B484**, 265 (1997).

[2] M. H. Thoma and M. Gyulassy, Nucl. Phys. **B351**, 491 (1991); E. Braaten and M. H. Thoma, Phys. Rev. **D44**, 1298; (1991); Phys. Rev. **D44**, 2625 (1991).

[3] Y. L. Dokshitzer, D. E. Kharzeev, Phys. Lett. **B519**, 199-206 (2001).

[4] N. Armesto, C. A. Salgado, U. A. Wiedemann, Phys. Rev. **D69** 114003 (2004).

[5] K. Eskola, H. Paukkunen, C. Salgado, JHEP **04** 065 (2009).

[6] H. Fujii and K. Watanabe, arXiv:1308.1258.

[7] I. Vitev, Phys. Rev. **C 75** 064906 (2007).

[8] M. Lev and B. Petersson, Z. Phys. **C21** 155 (1983); X. N. Wang, Phys. Rev. **C61** 064910 (2000).

[9] B. B. Abelev *et al.* [ALICE Collaboration], arXiv:1402.4476 [nucl-ex].

[10] B. Aberlev *et al.* [ALICE Collaboration], arXiv:1405.3452 [nucl-ex].

[11] R. Sharma, I. Vitev and B. W. Zhang, Phys. Rev. **C 80** 054902 (2009).

[12] A. Toia, arXiv:1410.0481 [nucl-ex].

[13] B. Abelev *et al.* [ALICE Collaboration], PRL 109 112301 (2012); JHEP **9** 112 (2012).

[14] CMS Collaboration, CMS-PAS-HIN-12-014 (2013).

[15] B. Abelev *et al.* [ALICE Collaboration], PRL 111 102301 (2013); Phys. Rev. **C90** 034904 (2014).

Search for Muonic Atoms at RHIC

Kefeng Xin[1] for the STAR Collaboration

[1]Rice University, 6100 Main St MS-315, Houston, Texas, USA

DOI: http://dx.doi.org/10.3204/DESY-PROC-2014-04/39

We present the search results for muonic atoms on $\sqrt{s_{NN}} = 200$ GeV Au+Au collisions collected by the STAR experiment at RHIC. With the muon identification at low momentum, the invariant mass spectra were reconstructed. Clear signals are observed at the expected atom masses. Two particle correlations show that the production of the daughter particles happens at the same space-time point, presenting the signature of atom ionization. The fraction of primordial muons is extracted from π-μ correlations.

1 Introduction

Muonic atoms are like ordinary atoms except that the electrons are replaced with muons. These atoms have been studied in many fundamental physics experiments, such as precision measurements of proton size [1] and nuclear quadrupole moments [2]. Muonic atoms with pions in the core have been produced from intense K_l beam at Brookhaven National Lab [3] and Fermilab [4]. However hydrogen-like muonic atoms with more exotic particles in the core (kaons or antiproton) have never been observed. Heavy-ion experiments, with large amount of thermal muons and hadrons produced, make an ideal environment for the production of such exotic atoms. This provides us a great opportunity to make these discoveries.

Muons that are involved in the atom production make the study particularly interesting in heavy-ion experiments, because thermal leptons are considered to be ideal penetrating probes of hot QCD matter as their production rates rapidly increase with the temperature of the medium. However, one difficulty of measuring the thermal leptons is that they are mixed with a large amount of leptons from weak hadronic decays, which carry little information of the hot and dense matter. Muonic atoms are only produced by particles right after freeze-out, i.e. hadrons and thermal muons or muons from resonance decays like $\rho \to \mu^+\mu^-$, not by the muons from the weak hadronic decays, which are produced at a relatively late stage. Thus the idea of measuring the distributions of muonic atoms in heavy-ion collisions has been suggested by several theorists, Melvin Schwartz, Gordon Baym, Gerald Friedman, [5], Joseph Kapusta, Agnes Mocsy, [6] etc.

2 Analysis and Results

The dataset used in this analysis is from Au+Au collisions at $\sqrt{s_{NN}} = 200$ GeV collected by the STAR detector in year 2010. Central triggered events are selected to maximize the particle multiplicities. A total of 231 million events passed the event level selections. Particles are identified from the time-of-flight detector and the time projection chamber. The muon momentum is limited to 0.15-0.25 GeV/c to ensure the purity of the sample. The corresponding momenta for kaons and protons/antiprotons are 0.7-1.17 GeV/c and 1.33-2.22 GeV/c respectively.

The invariant mass reconstruction is done with the combinatorial method. The combinatorial signal is constructed by pairing a hadron and a muon with opposite electric charges (unlike-sign method) from the same event. The background is constructed in two ways: a mixed-event method, in which a hadron and a muon with opposite electric charges from two different events are paired; and a like-sign method, in which a hadron and a muon with the same electric charge from a same event are paired.

Note that the Coulomb effect becomes stronger when the two charged particles are close in phase space. In the unlike-sign method, two particles carry opposite charges, which produce attractive Coulomb force and thus enhance the mass distributions, especially at the low mass region. In contrast, in the like-sign method, the repulsive Coulomb force from the same charge suppresses the mass distributions at the low mass region. In the mixed-event method, there is no Coulomb effect for hadron-muon pairs. Therefore, the mixed-event backgrounds are used for acceptance correction of like-sign backgrounds:

$$LS_{+-}(corrected) = \sqrt{LS_{++}LS_{--}}\frac{ME_{+-}}{\sqrt{ME_{++}ME_{--}}}, \tag{1}$$

where LS and ME stands for like-sign and mixed-event respectively, and the index stands for the charges for hadrons and leptons. Details of this correction are discussed in [7] [8].

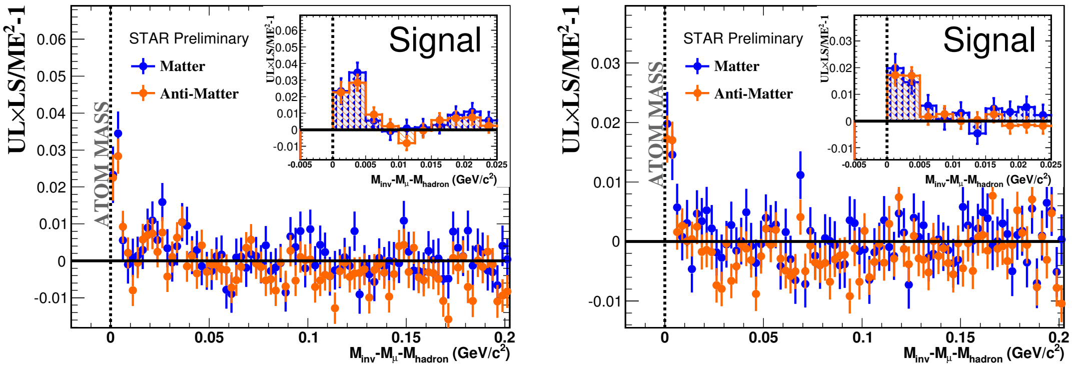

(a) p-μ^- and $\bar{p}$-μ^+ pairs.

(b) K^--μ^+ and K^+-μ^- pairs.

Figure 1: The pair invariant mass distributions of $UL \times LS/ME^2 - 1$ show peaks at the atom masses.

We adopted the following observable to cancel the trivial Coulomb effect and preserve the signal:

$$UL \times LS/ME^2 - 1 \tag{2}$$

where $UL \times LS$ stands for unlike-sign × like-sign, to cancel the Coulomb effect, and ME stands for mixed-event for normalization. After the rejection of the Coulomb force, we observe the sharp peaks at the expected zero net mass in Fig. 1. The error bars show the statistical uncertainties. The signal is robust in both K-μ and p-μ systems and their antimatter systems.

Femtoscopic correlations between two particles have also been used as a probe of muonic atoms. The correlation as a function of k^*, which is the magnitude of the momentum of either particle in the pair rest frame, shows how the interactions of the two particles change with respect to their distance in phase space. STAR has thoroughly studied the K-π system [9], in which only Coulomb interation dominates. For non-identified particles, a leading particle can be selected, and two cases can be distinguished by $C_+(k^*)$ and $C_-(k^*)$, which stand for the leading particle travels faster and slower, respectively. Then the double ratio $C_+(k^*)/C_-(k^*)$ can be calculated to show the difference of the two cases. This method was successfully used in previous measurements to probe the space-time asymmetry of the emission of two particles [9].

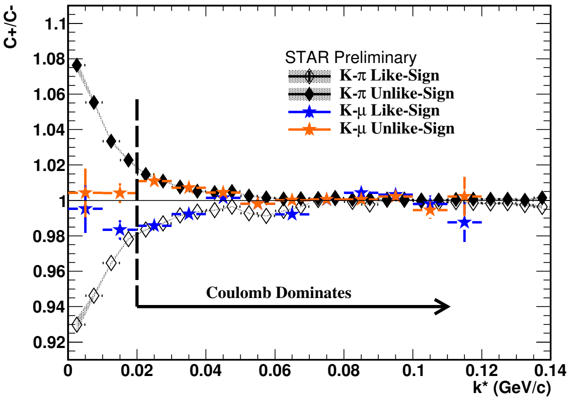

Figure 2: The double ratio of the K-π and K-μ systems show significant difference at low k*. The convergence to unity of K-μ suggests the ionization at the beam pipe after the production of muonic atoms.

The measurement of K-π system is performed from the dataset and kinetic region similar as K-μ system which we used for muonic atom signal extraction. The origin of the non-unity in double ratio comes from the Coulomb interactions between the kaons and pions, which are later on enhanced in $C_+(k^*)$ and suppressed in $C_-(k^*)$ because of the space-time emission asymmetries of kaons and pions. The double ratio of $K-\mu$ system, overlaid on top of K-π system, can be separated in two regions as shown in Fig. 2. On the right of the dashed line, where only Coulomb interactions are expected in both systems, the double ratios of the two systems are consistent. This is consistent with the existence of the Coulomb force, which is a necessary condition to form muonic atoms. On the left of the dashed line, where the muonic atoms are expected to appear, when getting to very low k^*, instead of divergence, the double ratios of $K-\mu$ system show convergence to unity. The unity double ratio provides a signature of muonic atoms disassociation at the detector beam pipe, where the hadrons and the muons are separated from the bound state at the same space-time point.

The π-μ correlations are also studied. A large amount of muons from weak decays can pass the track selections, and mix with the primordial muons. Thus these π-μ interactions inherit the interactions from π-π interactions, which have two major sources, the electrostatic Coulomb interactions and quantum interference from identical pions [10]. The later factor generates a strong enhancement on the correlation functions. We denote the three correlation functions as the follows:

- A for correlations between pions and muons from simulated weak decays from real pions.
- B for correlations between pions and inclusive muons, which is measured from data.
- C' for correlations between pions and primordial muons.

The three functions satisfy the linear relationship: $B = \alpha \times C' + \beta \times A$, where α stands for the fraction of primordial muons from inclusive muons produced from the collisions. C' is then estimated by π-π correlations, because of the fact that pion mass and muon mass are fairly close. To avoid quantum statistics enhancement, the correlation function from Coulomb between like-sign pairs is estimated from reversed unlike-sign pairs C. The relation then becomes: $B = \alpha \times 1/C + \beta \times A$. The minimum χ^2 fitting is performed in Fig. 3. If two particles have similar trajectories and orientation, implying that they are close in momenta space, the detector will not be able to have enough spacial resolution to distinguish them and will merge the two tracks. The fitting range is selected between 0.02-0.2 GeV/c, discarding the very low k^* where the missing track problem is significant. The fitting results show that the fraction of primordial muons is 22.0±0.4%.

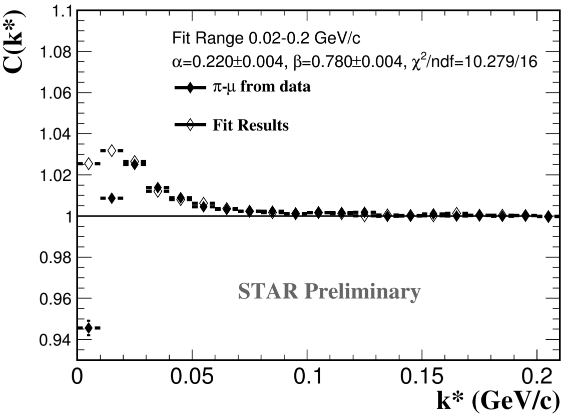

Figure 3: Measured π-μ correlation function, fitted by π-π correlation function and simulated π-μ_{prim}.

3 Conclusions

Au+Au collisions at $\sqrt{s_{NN}} = 200$ GeV collected by the STAR experiment are used in this measurement to search for muonic atoms. The invariant mass distributions show clear signals at the expected mass position for K^+-μ^-, K^--μ^+, p-μ^-, and antiproton-μ^+. The signal is robust after long-range Coulomb effect is rejected. The double ratio of K-μ system indicates the kaons and muons that are very close in phase space are emitted at the same space and time, which is consistent with muonic atom ionization. The fraction of primordial muons is extracted from the correlation method.

References

[1] Aldo Antognin, *et al.*, Science **339** 417 (2013).
[2] Y. Tanaka and B. M. Steffen, Phys. Rev. Lett. **51** 18 (1983).
[3] R. Coombes, *et al.*, Phys. Rev. Lett. **37** 5 (1976).
[4] S. H. Aronson, *et al.*, Phys. Rev. Lett. **48** 16 (1982).
[5] G. Baym, G. Freidman, R. J. Hughes, and B. Jack, Phys. Rev. **D48** 9 (1993).
[6] J. Kapusta and A. Mocsy, Phys. Rev. C **59** 5 (1999).
[7] A. Adare, *et al.*, Phys. Rev. C **81** 5 (2010).
[8] L. Adamczyk, *et al.*, Phys. Rev. C **86** 5 (2012).
[9] J. Adams, *et al.*, Phys. Rev. Lett. **91** 26 (2003).
[10] J. Adams, *et al.*, Phys. Rev. C **71** 044906 (2005).

Relativistic heavy ion physics at JINR: status of the BM@N and MPD experiments

Alexander Zinchenko for the MPD and BM@N Collaborations

JINR, 141980 Dubna, Moscow region, Russia

DOI: http://dx.doi.org/10.3204/DESY-PROC-2014-04/177

The future accelerator facility NICA (JINR, Dubna) will supply ion species ranging from polarized proton to heavy ions with design luminosity of up to 10^{27} cm^{-2}c^{-1} for Au nuclei in the region of the collider energy up to $\sqrt{s_{NN}} = 11$ GeV. It will complement the existing accelerator Nuclotron, which is being currently upgraded in order to be able to accelerate Au nuclei up to $E_{kin} = 4.65$A GeV ($\sqrt{s_{NN}} = 3.5$ GeV). These machines will host two heavy ion experiments: BM@N (Baryonic Matter at Nuclotron) and MPD (MultiPurpose Detector), which are described in this paper.

1 NICA complex

The Nuclotron-based Ion Collider fAcility (NICA) [1], shown in Fig. 1, is a new accelerator complex being constructed at JINR, Dubna, Russia. NICA's aim is to provide collisions of heavy ions over a wide range of atomic masses, from Au+Au collisions at $\sqrt{s} = 4 - 11$A GeV (for Au^{79+}) and an average luminosity of L = 10^{27} cm^{-2}s^{-1} to proton-proton collisions with $\sqrt{s_{pp}} = 20$ GeV and L = 10^{32} cm^{-2}s^{-1}.

Study of heavy ion collisions at the collider with the MultiPurpose Detector (MPD) will be complemented by spin physics research with polarized beams of protons and deuterons with the Spin Physics Detector (SPD) as well as a fixed-target program at center of mass energy from 1 to 4 GeV at the BM@N (Baryonic Matter at Nuclotron) detector.

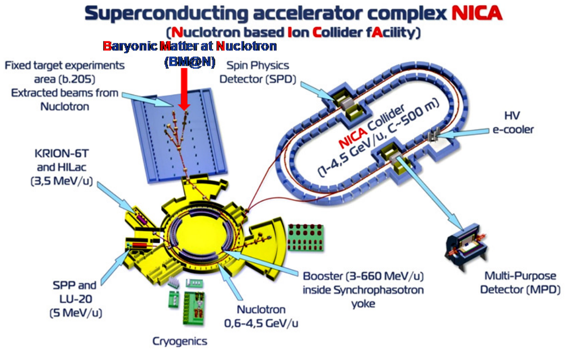

Figure 1: NICA complex.

2 MPD experiment

The main goal of the NICA/MPD program [2] is a comprehensive experimental investigation of the properties and dynamics of the hot and dense nuclear matter in a poorly explored region of the QCD phase diagram, with a main emphasis on such QCD subjects as properties of deconfinement phase transition, critical phenomena and chiral symmetry restoration.

The NICA/MPD experimental program includes simultaneous measurements of observables that are presumably sensitive to high nuclear density effects and phase transitions. In the first stage of the project are considered - multiplicity and spectral characteristics of the identified hadrons including strange particles, multi-strange baryons and antibaryons; event-by-event fluctuations in multiplicity, charges and transverse momentum; collective flows (directed, elliptic and higher ones) for observed hadrons. In the second stage the electromagnetic probes (photons and dileptons) will be measured.

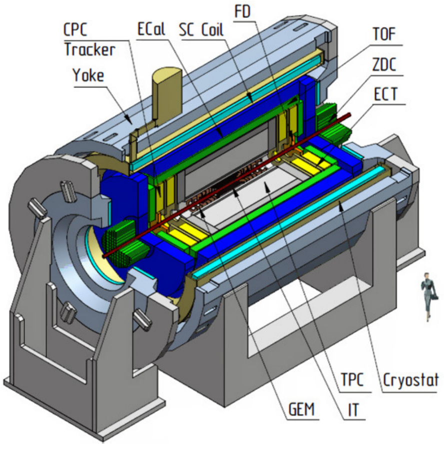

Figure 2: MPD detector.

The detector for exploring phase diagram of strongly interacting matter in a high track multiplicity environment has to cover a large phase space, be functional at high interaction rates and comprise high efficiency and excellent particle identification capabilities. The MPD detector [3, 4], shown in Fig. 2, matches all these requirements. It consists of a barrel part and two end caps. The barrel part is a set of various subdetectors. The main tracker is the time projection chamber (TPC) supplemented by the inner tracker (IT). IT and TPC have to provide precise tracking, momentum determination and vertex reconstruction. The time of flight (TOF) system must be able to identify charged hadrons and nuclear clusters in a broad pseudorapidity range. The electromagnetic calorimeter (ECAL) should identify electrons, photons and measure their energy with high precision. The zero degree calorimeter (ZDC) should provide event centrality and event plane determination, and also measurement of the energy deposited by spectators. There are also a straw-tube tracker (ECT) and a fast forward detector (FFD).

The magnet of MPD is a solenoid with a thin superconducting NbTi winding and a flux return iron yoke. The magnet should provide a homogeneous magnetic field of 0.5 T. The field inhomogeneity in the tracker area of the detector is about 0.1%.

The MPD time projection chamber (TPC) is the main tracking detector that has to provide charged particles momentum measurement with sufficient resolution (about 2% at $p_t = 300$ MeV/c), two track separation (with a resolution <1 cm), vertex determination and dE/dx measurement (dE/dx resolution better than 8%) at pseudorapidities $|\eta| < 2.0$ and $p_t > 100$ MeV/c. TPC readout system is based on Multi-Wire Proportional Chambers (MWPC) with cathode readout pads.

The identification of charged hadrons (PID) at intermediate momentum ($0.1 - 3$ GeV/c) is achieved by the time-of-flight (TOF) measurements which are complemented by the energy loss (dE/dx) information from the TPC and IT detector systems. TOF system should provide a large phase space coverage $|\eta| < 3.0$, high combined geometrical and detection efficiency (better than 80%), identification of pions and kaons with $0.1 < p_t < 2$ GeV/c and (anti)protons with $0.3 < p_t < 3$ GeV/c. The choice for the TOF system is multigap Resistive Plate Counters (mRPC) which have good time resolution of $\sigma < 70$ ps. The barrel covers the pseudorapidity region $|\eta| < 1.5$ with the average efficiency above 90%. The end cap system covers the pseudorapidity region $1.5 < |\eta| < 3.0$.

Currently, the MPD physics program is under careful evaluation through the extensive feasibility studies. As they show, the MPD detector will provide good conditions for the strangeness measurements in heavy ion collisions, both in the hyperon [6] and hypernuclei sectors (Fig. 3 left panel).

Electromagnetic probes (electron-positron pairs) will also be accessible (Fig. 3 right panel) [7] for studies, e.g., of the low-mass dilepton enhancement in heavy ion collisions.

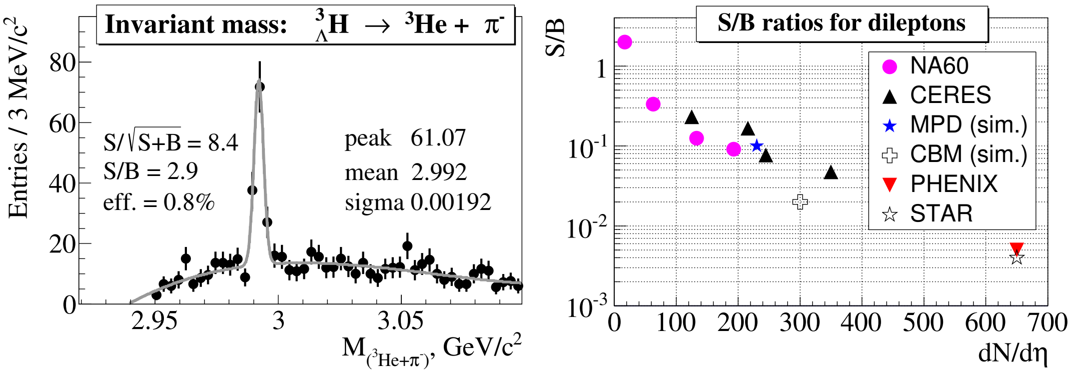

Figure 3: Some results from MPD feasibility studies: left - reconstructed invariant mass of ^{3}He and π^-; right - signal-to-background ratios obtained in different experiments for low-invariant mass region of lepton pairs versus charged particle density.

3 BM@N experiment

A successful operation of the NICA complex will require the existing machine Nuclotron to be upgraded in order to accelerate Au nuclei. After that, the improved Nuclotron beams will also be used to run a fixed target experiment BM@N [5]. The detector will allow to study A+A collisions by measuring a variety of observables.

Particle yields, ratios, transverse momentum spectra, rapidity and angular distributions, as well as fluctuations and correlations of hadrons will be studied as a function of the collision energy and centrality. A sketch of the proposed experimental set-up is shown in Fig. 4. It combines high precision track measurements with time-of-flight information for particle identification and total energy measurements for event characterization. The charged track multiplicity will be measured with the set of GEM (Gas Electron Multipliers) detectors located downstream of the target inside the analyzing magnet of 0.8 T

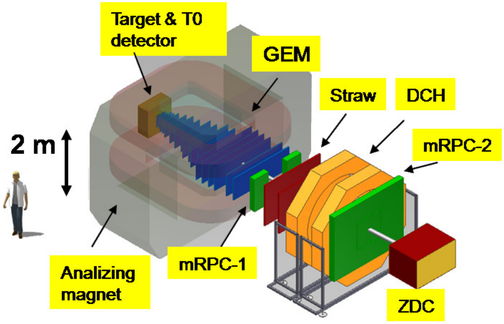

Figure 4: BM@N detector.

and drift chambers (Straw, DCH) situated outside the magnetic field. Design parameters of the time-of-flight detectors based on multigap Resistive Plate Chambers (mRPC-1,-2) with a strip read-out allow efficient discrimination between particle species with momentum up to a few GeV/c. The Zero Degree Calorimeter (ZDC) is designed for the collision centrality analysis by measuring the energy of forward going particles. The Recoil detector, partially covering the backward hemisphere (-1< η <1.2) near the target, is planned for the independent analysis of the collision centrality by the measurement of the energy of the target fragments.

The BM@N project is being realized by a Collaboration of more than 100 physicists and engineers from 12 countries. According to the project realization plan, the first elements of the BM@N detector will be installed at the Nuclotron beam line in early 2015 to perform test beam measurement. The physics data taking is planned to start in 2016. At present, an active R&D program and beam line development works are complemented with intensive Monte Carlo simulation studies for optimization of the detector design. Figure 5 illustrates the quality of hyperon reconstruction in the BM@N detector with the GEM tracker. The obtained results indicate that even in high multiplicity central Au+Au collisions the proposed set-up has very good reconstruction capability for strange hyperons.

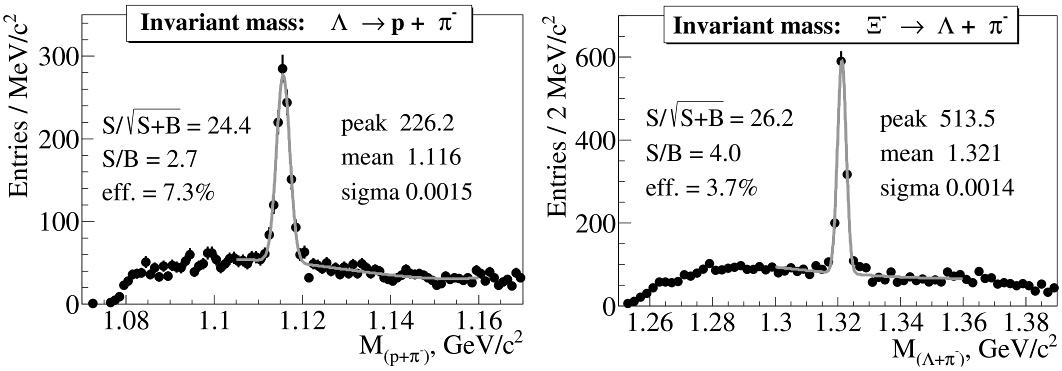

Figure 5: Some results from BM@N feasibility studies: reconstructed Λ (left) and Ξ^- (right) hyperon invariant mass peaks.

References

[1] http://nica.jinr.ru

[2] NICA White Paper, https://indico.cern.ch/event/275003/contribution/1/material/paper/0.pdf.

[3] K. U. Abraamyan et al., Nucl. Instrum. Meth. **A628**, 99 (2011)

[4] http://nica.jinr.ru/files/CDR_MPD/MPD_CDR_en.pdf.

[5] http://nica.jinr.ru/files/BM@N/BMN_CDR.pdf

[6] V. Vasendina, A. Zinchenko, these Proceedings.

[7] V. Vasendina et al., Phys. Part. Nucl. Lett. **10**, 769 (2013).

LHCb results in proton-nucleus collisions at the LHC

Katharina Müller

Winterthurerstr. 190, CH-8057 Zurich, Switzerland

DOI: http://dx.doi.org/10.3204/DESY-PROC-2014-04/251

The forward acceptance of the LHCb detector allows it to probe proton-ion collision in a unique kinematic range, complementary to the other LHC experiments. The production of J/Ψ and Υ-mesons decaying into two muons is studied at the LHCb experiment in proton-lead collisions at a proton-nucleon centre-of-mass energy $\sqrt{s_{NN}} = 5$ TeV. The analysis is based on a data sample corresponding to an integrated luminosity of 1.6 nb^{-1}. The nuclear modification factor and the forward-backward production ratio are determined for J/Ψ and Υ(1S) mesons. Clear suppression of prompt J/Ψ production is observed with respect to the production in *pp* collisions at large rapidity, while the suppression of J/Ψ from *b*-hadron decays is less pronounced. The nuclear modification factor for Υ(1S) mesons in the forward region is found to be similar to those for J/Ψ from *b*-hadron decays. Furthermore a first observation of Z bosons in proton-lead collisions is reported.

1 Introduction

In ultra-relativistic heavy-ion collisions, the production of heavy quarkonia or electroweak bosons are expected to be suppressed with respect to proton-proton collisions, if a quark-gluon plasma, QGP, is created [1]. The suppression of heavy quarkonia and Z boson production with respect to *pp* collisions can also take place in proton-nucleus (pA) collisions, where a quark-gluon plasma is not expected to be created and only cold nuclear matter effects, such as nuclear absorption, parton shadowing and parton energy loss in initial and final states occur [2, 3, 4]. The study of pA collisions therefore provides important input to disentangle the QGP effects from cold nuclear effects, probe nuclear parton distribution functions which are poorly constrained, and provide a reference sample for nucleus-nucleus collisions.

In early 2013, the LHCb detector [5] collected two data samples corresponding to 1.6 nb^{-1} of proton-lead collisions at a centre-of-mass energy per proton-nucleon pair of $\sqrt{s_{NN}} = 5$ TeV. The two data samples correspond to two different beam configurations, with the proton (lead) beam into the direction of LHCb, referred to as forward (backward). Owing to the asymmetric beam configuration the LHCb acceptance corresponds to $1.5 < y < 4.0$ ($-5.0 < y < -2.5$) for the forward (backward) configuration. Results on J/Ψ [6], Υ [7] and Z [8] production are reported below.

2 J/Ψ and Υ production

J/Ψ [6] and Υ [7] mesons are reconstructed in the di-muon final states with the transverse momentum, p_T, of the di-muon system restricted to $p_T < 14$ GeV/c ($p_T < 15$ GeV/c) for J/Ψ (Υ). The excellent vertexing capability of LHCb allows a separation of prompt J/Ψ mesons and J/Ψ mesons from b-hadron decays (J/Ψ from b). The number of prompt J/Ψ and J/Ψ from b candidates are determined by a combined fit to the di-muon invariant mass and pseudo-proper time distributions. The pseudo-proper time is defined as $t_z = (z_{J/\Psi} - z_{PV}) \times M_{J/\Psi}/p_z$, where $z_{J/\Psi}$ is the z position of the J/Ψ decay vertex, z_{PV} that of the primary vertex, p_z the z component of the measured J/Ψ momentum, and $M_{J/\Psi}$ the mass of the J/Ψ.

Figure 1 shows the projections of the combined fit in two rapidity (y) bins in the forward and the backward region. The number of candidates for J/Ψ from b is about a factor of 10 smaller than for prompt J/Ψ.

The invariant di-muon mass distribution for the Υ candidates of the two samples are shown in Fig. 2. Higher combinatorial background in the backward region is observed for J/Ψ and Υ production due to the larger multiplicity in lead-proton collisions. Measurements for J/Ψ production are performed in three bins of rapidity; the low statistics of the Υ sample do not allow a differential measurement.

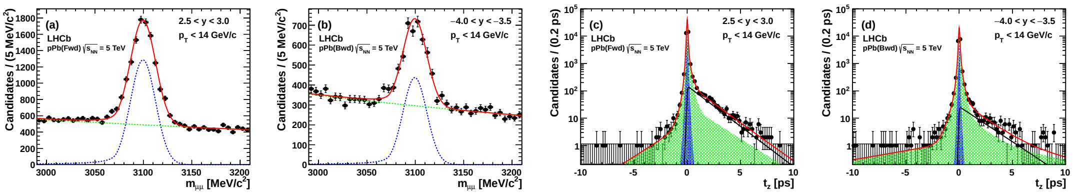

Figure 1: Projections of the combined fit: di-muon invariant mass (left two plots) and pseudo-proper time (right two plots) in the forward and backward region [6].

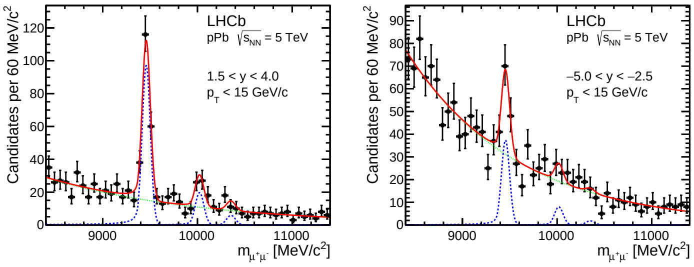

Figure 2: Di-muon invariant mass distribution for Υ candidates in the forward (left) and backward (right) region [7].

3 Cold nuclear effects

Nuclear effects are usually characterised by the nuclear modification factor R_{pA} and the forward-backward production ratio R_{FB},

$$R_{pA} = \frac{d\sigma_{pA}/dy}{A d\sigma_{pp}/dy}, \qquad R_{FB} = \frac{d\sigma_{pA(y>0)}/dy}{d\sigma_{pA(y<0)}/dy}, \tag{1}$$

which depend on the production cross-section of a given particle in pA collisions and for R_{pA} also on the cross-section in pp collisions at the same centre-of-mass energy as well as the atomic number A. The advantage of measuring the R_{FB} is that it does not rely on the knowledge of the production cross-section in pp collisions and that experimental systematic uncertainties and theoretical scale uncertainties cancel partially.

To determine the nuclear modification factor R_{pA}, the reference cross-sections in pp collisions at $\sqrt{s_{NN}} = 5$ TeV are needed [9, 10]. These are obtained by a power-law fit to the previous LHCb measurements of J/Ψ and Υ production at 2.76 TeV, 7 TeV and 8 TeV. Figure 3 shows the nuclear modification factors (left two plots) and the forward-backward production ratios (right two plots), for prompt J/Ψ mesons and J/Ψ from b as functions of rapidity [6], compared to different theoretical predictions [2, 11, 3, 4]. A clear suppression of about 40% at large rapidity is observed for prompt J/Ψ production. The measurements agree with most predictions. The data show a modest suppression of J/Ψ from b production in the forward region, with respect to that in pp collisions. This is the first indication of the suppression of b hadron production in proton-lead collisions. The nuclear modification factor and forward-backward production ratio for J/Ψ from b reflect that cold nuclear matter effects on b hadrons are less pronounced than for J/Ψ.

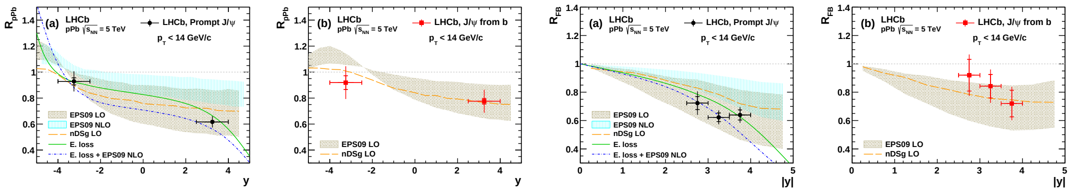

Figure 3: Forward-backward production ratios (R_{FB}, left two plots) and nuclear modification factor (R_{pA}, right two plots) for prompt J/Ψ and J/Ψ from b as functions of rapidity [6] together with theoretical predictions from (yellow dashed line and brown band) [2, 11], (blue band) [3], and (green solid and blue dash-dotted lines) [4].

Figure 4 shows R_{pA} and R_{FB} for $\Upsilon(1\text{S})$ [7] together with the LHCb results of prompt J/Ψ and J/Ψ from b with theoretical predictions. The data are consistent with a suppression in the forward region and a possible enhancement in the backward region. In the forward region, the suppression of $\Upsilon(1S)$ mesons is smaller than that of prompt J/Ψ mesons and similar to J/Ψ from b, indicating that the cold nuclear matter effects on $\Upsilon(1\text{S})$ mesons and J/Ψ from b are similar. Data and theoretical predictions which include coherent energy loss and nuclear shadowing as parametrised with EPOS09 [4] agree within the large experimental uncertainties.

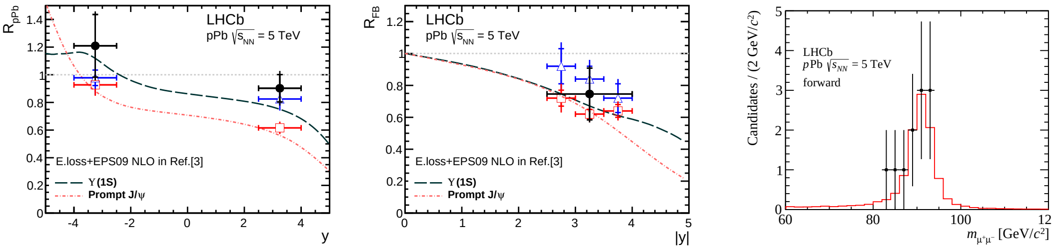

Figure 4: R_{FB} and R_{pA} for Υ, prompt J/Ψ and J/Ψ from b as functions of rapidity [7] (left two plots) with theoretical predictions including energy loss and nuclear shadowing [4]. Di-muon invariant mass for the Z candidates in the forward sample (right plot) [8].

4 Inclusive Z boson production in proton-lead collisions

The Z candidates are reconstructed in the di-muon final state [8]. Background contributions from muon mis-identification and the decay of heavy flavour mesons are determined from data. A total of 15 candidates are selected with a purity of above 99%, corresponding to a significance of $10.4\sigma(6.8\sigma)$ for the Z signal in the forward (backward) direction. Figure 4 (right plot) shows the di-muon invariant mass of the Z candidates in the forward direction. The inclusive Z boson production cross-section is measured to be $\sigma(Z \to \mu\mu) = 13.5^{+5.4}_{-4.0} \pm 1.2$ nb in the forward and $\sigma(Z \to \mu\mu) = 10.7^{+8.4}_{-5.1} \pm 1.0$ nb in the backward configuration, where the first uncertainty is statistical and the second systematic. The large experimental uncertainties do not allow definite conclusions on the presence of nuclear effects.

References

[1] T. Matsui and H. Satz. J/ψ Suppression by Quark-Gluon Plasma Formation. *Phys.Lett.*, B178:416, 1986.

[2] E.G. Ferreiro, F. Fleuret, J.P. Lansberg, and A. Rakotozafindrabe. Impact of the Nuclear Modification of the Gluon Densities on J/ψ production in pPb collisions at $\sqrt{s_{NN}} = 5$ TeV. *Phys.Rev.*, C88(4):047901, 2013.

[3] J.L. Albacete, N. Armesto, R. Baier, G.G. Barnafoldi, J. Barrette, et al. Predictions for $p + Pb$ Collisions at $\sqrt{s_{NN}} = 5$ TeV. *Int.J.Mod.Phys.*, E22:1330007, 2013.

[4] Francois Arleo and Stephane Peigne. Heavy-quarkonium suppression in p-A collisions from parton energy loss in cold QCD matter. *JHEP*, 1303:122, 2013.

[5] Jr. Alves, A. Augusto et al. The LHCb Detector at the LHC. *JINST*, 3:S08005, 2008.

[6] R Aaij et al. Study of J/ψ production and cold nuclear matter effects in pPb collisions at $\sqrt{s_{NN}} = 5$ TeV. *JHEP*, 1402:072, 2014.

[7] Roel Aaij et al. Study of Υ production and cold nuclear matter effects in pPb collisions at $\sqrt{s_{NN}} = 5$ TeV. *JHEP*, 1407:094, 2014.

[8] R. Aaij et al. Observation of Z production in proton-lead collisions at LHCb. *JHEP*, 1409:030, 2014.

[9] ALICE and LHCb Collaborations. Reference pp cross-sections for J/ψ studies in proton-lead collisions at $\sqrt{s_{NN}} = 5.02$ TeV and comparisons between ALICE and LHCb results. 2013.

[10] The LHCb Collaboration. Reference pp cross-sections for $\Upsilon(1S)$ studies in proton-lead collisions at $\sqrt{s_{NN}} = 5.02$ TeV and comparisons between ALICE and LHCb results. 2014.

[11] Z. Conesa del Valle, E.G. Ferreiro, F. Fleuret, J.P. Lansberg, and A. Rakotozafindrabe. Open-beauty production in pPb collisions at $\sqrt{s_{NN}}$=5 TeV: effect of the gluon nuclear densities. *Nucl.Phys.*, A926:236–241, 2014.

On Parton Number Fluctuations

Stéphane Munier

Centre de physique théorique, École polytechnique, CNRS, Palaiseau, France

DOI: http://dx.doi.org/10.3204/DESY-PROC-2014-04/163

Parton evolution with the rapidity essentially is a branching diffusion process. We describe the fluctuations of the density of partons which affect the properties of QCD scattering amplitudes at moderately high energies. We arrive at different functional forms of the latter in the case of dipole-nucleus and dipole-dipole scattering.

1 Quantum chromodynamics at high density

Quantum chromodynamics in the high-energy/high-density regime is a very rich field from a theoretical viewpoint since it involves genuinely nonlinear physics, and nontrivial fluctuations. The latter are deemed *a goldmine for modern physics* [1]. From a phenomenological viewpoint, there is a wealth of data from different experiments which await interpretation. (For a review, we refer the reader to the recent textbook by Kovchegov and Levin [2]).

Electron-proton (or better, nucleus) scattering is maybe the best experiment to probe QCD in this regime, as was done at HERA, an $e^{\pm}p$ facility. The electron interacts with the proton through a quark-antiquark pair, which appears as a quantum fluctuation of a (virtual) photon of the Weizsäcker-Williams field of the electron. The probability amplitudes for these fluctuations follow from a simple QED calculation. The $q\bar{q}$ pair is a color dipole, and hence electron-hadron scattering may be related to dipole-hadron scattering. If one looks at events in which the $q\bar{q}$ pair has a small-enough size (as compared to the typical size of a hadron), as is possible by selecting longitudinally-polarized highly-virtual photons, then perturbative QCD may be used as a starting point to compute some properties of the dipole-hadron scattering amplitudes.

As for the interaction of protons and/or nuclei as is currently performed at the LHC, the observables need to be carefully chosen if one wants to be able to predict cross sections from first principles – at least in the present state of the art of the theory. Indeed, one needs a hard momentum scale to justify the use of perturbation theory, and the latter must be found in the final state in the form of e.g. the transverse momentum of a jet. It turns out that an observable such as $p_\perp$-broadening in proton-nucleus collisions, namely the transverse momentum distribution of single jets, may also be related to the dipole-nucleus amplitude.

We will first review the formulation of the rapidity evolution of the dipole-nucleus scattering amplitude in QCD in the high-energy limit. The latter is given by the Balitsky-Kovchegov (BK) equation. We will relate the known shape of its solution to gluon-number fluctuations in the quantum evolution of the dipole. We will then be able to predict the form of geometric scaling for dipole-dipole scattering, which turns out to be different from the solution to the BK equation.

2 Dipole-nucleus scattering

Let us start with the scattering of a dipole off a nucleus at relatively low energy. The forward elastic amplitude T is a function of the dipole size r_0, which is given by the McLerran-Venugopalan model:

$$T(r_0) = 1 - e^{-\frac{r_0^2 Q_A^2}{4}}. \tag{1}$$

This formula resums multiple exchanges of pairs of gluons between the bare dipole and the nucleus (see Fig. 1a). Q_A is the saturation momentum of the nucleus. Equation (1) essentially means that a dipole of size larger than $\sim 1/Q_A$ is absorbed ($T \sim 1$), while the nucleus is transparent to dipoles of size smaller than $\sim 1/Q_A$. For our purpose, we may approximate $T(r_0)$ by the step function $\Theta(\ln r_0^2 Q_A^2/4)$.

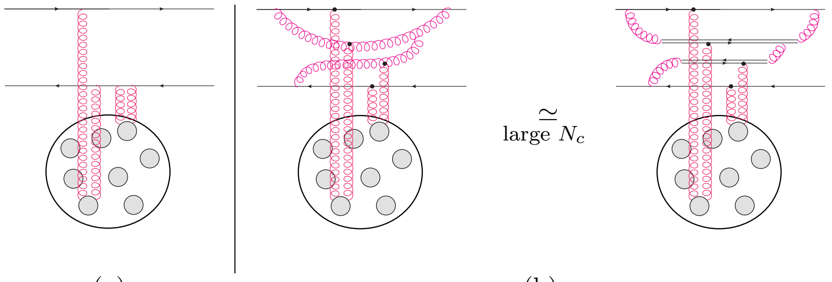

(a) (b)

Figure 1: Particular graphs contributing to the dipole-nucleus scattering amplitude at low (a) and high (b) energy in the restframe of the nucleus.

Going to higher energies $\sqrt{s}$ by increasing the rapidity of the dipole, the scattering process gets dominated by high-occupancy quantum fluctuations of the initial dipole (see Fig. 1b). The rapidity ($y \equiv \ln s$) dependence of the amplitude is given by the Balitsky-Kovchegov (BK) equation

$$\partial_y T(r_0, y) = \bar{\alpha} \int \frac{d^2 r_1}{2\pi} \frac{r_0^2}{r_1^2 (r_0 - r_1)^2} \left[T(r_1, y) + T(r_0 - r_1, y) - T(r_0, y) - T(r_1, y) T(r_0 - r_1, y)\right] \tag{2}$$

($\bar{\alpha} \equiv \frac{\alpha_s N_c}{\pi}$), whose large-$y$ solutions are traveling waves, namely fronts which translate (almost) unchanged in shape towards negative values of the $\ln r_0^2$ variable as the rapidity increases. The linear part of this equation (the first three terms in the r.h.s.) form the BFKL equation, whose kernel possesses as eigenfunctions the power functions $|r_0|^{2\gamma}$, the corresponding eigenvalues being $\bar{\alpha}\chi(\gamma)$, where $\chi(\gamma) \equiv 2\psi(1) - \psi(\gamma) - \psi(1-\gamma)$. Introducing the particular eigenvalue $\chi(\gamma_0)$, where γ_0 is such that $\chi'(\gamma_0) = \chi(\gamma_0)/\gamma_0$, the shape of T as a function of the dipole size r_0 in the region $T \ll 1$ and the y-dependence of the saturation scale read

$$T(r_0, y) \underset{r_0 \ll 1/Q_s(y)}{\sim} \ln \frac{1}{r_0^2 Q_s^2(y)} e^{\gamma_0 \ln(r_0^2 Q_s^2(y))} \quad \text{and} \quad Q_s^2(y)/Q_A^2 \simeq e^{\bar{\alpha}\chi'(\gamma_0) y}. \tag{3}$$

The BK equation (2) can be established in the framework of the dipole model (see e.g. [2]), where gluons are replaced by zero-size $q\bar{q}$ pairs. In this model, the Fock state of the incoming dipole which is "seen" by the nucleus at the time of the interaction is built from successive independent splittings of dipoles. At a given rapidity y, the latter Fock state can be thought of as a collection of n dipoles, generated by a splitting process which belongs to a class of processes generically called *branching diffusion*.

The main point we wanted to make at this conference and in Ref. [3] was that T has an elegant and useful probabilistic interpretation in the dipole picture: *It represents the probability that the largest dipole present in the Fock state of the incoming $q\bar{q}$ pair at the time of the interaction has a size which is larger than the inverse nuclear saturation momentum,* $1/Q_A$. Indeed, according to the McLerran-Venugopalan model, a given dipole interacts with the nucleus only if its size is larger than $1/Q_A$, hence it is necessary and sufficient that at least one of the dipoles in the Fock state be larger than $1/Q_A$ for the scattering to take place. Thus solving the BK equation amounts to understanding the statistics of the extremal particles in a branching random walk (BRW). Our first task is to recover the shape of the amplitude (3), previously obtained through a analysis of the BK equation, from the latter statistics.

We observe that the extremal particle in a BRW has fluctuations which can originate only from two places: From the first stages of the rapidity evolution, when the overall number of dipoles is small and thus subject to large statistical fluctuations (we shall call this type of stochasticity "front fluctuations"), and from the tip of the distribution, where by definition, particle numbers keep small. Elsewhere, the evolution is essentially deterministic since it acts on a large number of objects. The effect of the front fluctuations is to shift the particle distribution by Δ. We conjecture[1] that the distribution of Δ is $\propto e^{-\gamma_0 \Delta}$. The effect of the tip fluctuations is instead to send randomly particles ahead of the front by δ. We conjecture the same exponential law $\propto e^{-\gamma_0 \delta}$.

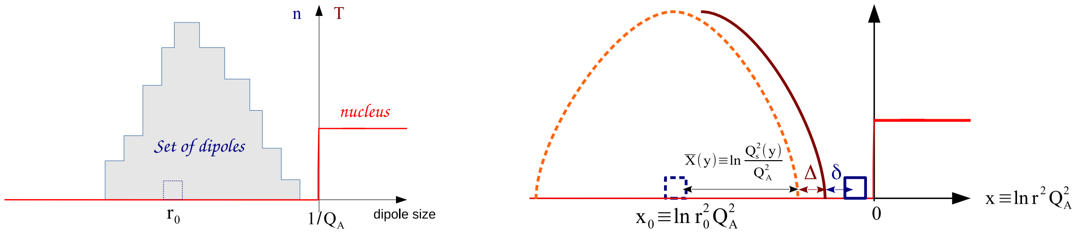

(a) (b)

Figure 2: (a) Sketch of the dipole distribution (as seen at a given impact parameter) in a particular realization of the evolution to the rapidity y of an initial dipole of size r_0. (b) Model for the evolution of a given realization, with the "front" and "tip" fluctuations described in the text.

We introduce our notations in Fig. 2. According to the previous discussion, in a particular event, the scattering occurs if $x_0 + \bar{X}(y) + \Delta + \delta \geq 0$. Hence the amplitude T simply is the average of this condition over Δ and δ:

$$T \propto \int_0^{+\infty} d\delta\, e^{-\gamma_0 \delta} \int_0^{+\infty} d\Delta\, e^{-\gamma_0 \Delta} \Theta(x_0 + \bar{X}(y) + \Delta + \delta) \propto (-x_0 - \bar{X}(y)) e^{\gamma_0 (x_0 + \bar{X}(y))}. \quad (4)$$

---

[1] Arguments in favor of this conjecture were presented in Ref. [4].

Switching back to the QCD variables, we recover the expression of T given in Eq. (3). We conclude that *the shape of the dipole-nucleus scattering amplitude as a function of the dipole size is directly related to the event-by-event fluctuations of the size of the largest dipole*, which in turn stem from the fluctuations of the numbers of gluons produced in the QCD evolution.

3 Dipole-dipole scattering

While the dipole-nucleus amplitude probes the statistics of the largest dipole in the quantum evolution, the physics of dipole-dipole scattering is a bit different: Indeed, since the elementary amplitude (for dipoles of respective sizes r_0 and R_0) at zero rapidity is essentially $T(r_0, R_0) \sim \alpha_s^2 \delta(\ln r_0^2/R_0^2)$, it is the very shape of the dipole number distribution that is actually probed (Fig. 3). So in order to compute the shape of the amplitude, we need on one hand the probability distribution of the front fluctuations used before, and on the other hand the shape of the dipole number density from the deterministic evolution. We also need to implement *saturation* in the evolution (see Fig. 3c) to comply with the unitarity constraint $T \leq 1$. All in all, we obtain

$$T(r_0, y) \underset{r_0 \ll 1/Q_s(y)}{\sim} \ln^2 \frac{1}{r_0^2 Q_s^2(y)} e^{\gamma_0 \ln(r_0^2 Q_s^2(y))} \quad \text{where} \quad Q_s^2(y) R_0^2 \simeq e^{\bar{\alpha}\chi'(\gamma_0) y}. \tag{5}$$

Interestingly enough, it differs from the dipole-nucleus case; compare Eq. (3) to Eq. (5). This is the main prediction of the way of looking at QCD evolution we have promoted at this conference and in Ref. [3].

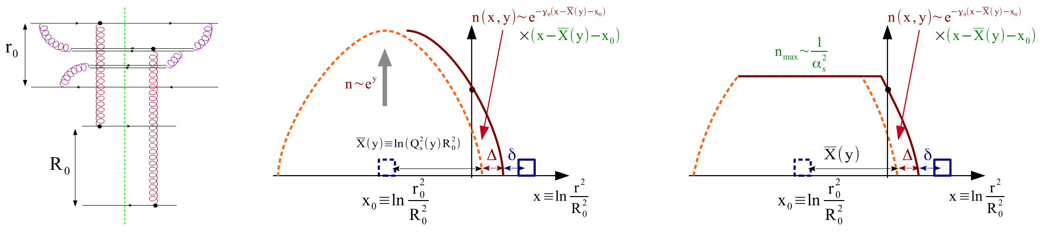

(a) (b) (c)

Figure 3: (a) Graph contributing to dipole-dipole scattering at high energies. (b) Sketch of the evolution of the dipole number density, model including fluctuations. (c) The same, but with saturation.

We refer the reader to [3] for the details, references, and more results, in particular on the finite-y corrections to the saturation scale in both the dipole-dipole and dipole-nucleus cases.

References

[1] E. Scapparone, plenary talk at this conference.

[2] Y.V. Kovchegov and E. Levin. *Quantum Chromodynamics at High Energy.* Cambridge Monographs on Particle Physics, Nuclear Physics and Cosmology. Cambridge University Press, 2012.

[3] A. H. Mueller and S. Munier, Phys. Lett. B **737** (2014) 303.

[4] A. H. Mueller and S. Munier, "Phenomenological picture of fluctuations in branching random walks," arXiv:1404.5500 [cond-mat.dis-nn] to appear in Phys. Rev. E (2014).

Proton-lead measurements using the ATLAS detector

Martin Spousta for the ATLAS Collaboration
Charles University in Prague

DOI: http://dx.doi.org/10.3204/DESY-PROC-2014-04/275

Measurements of soft and hard particle production in proton-lead collisions at the LHC have provided surprising results. Measurements of jets and high-p_T hadrons have shown an unexpected enhancement in the production of high-p_T charged particles and a similarly unexpected variation of the jet yield with proton-lead collision centrality. Studies of correlations in the production of soft particles have provided results that suggest strong collective behavior similar to that observed in lead-lead collisions. We give a brief report on the latest proton-lead measurements done by ATLAS.

1 Introduction

Proton-nucleus collisions at high energies provide an opportunity to study the effect of an extended nuclear target on the dynamics of soft and hard scattering processes and subsequent particle production. This involves extraction of nuclear parton distribution functions as well as disentangling the potential interplay between the soft and hard processes. In this short report we summarize the recent measurements done by ATLAS [1, 2, 3, 4, 5, 6, 7] that may improve our understanding of the physics of proton-nucleus collisions.

The analyses summarized here use the data from proton-lead (p+Pb) collisions measured by the ATLAS experiment. The LHC provided p+Pb collisions in two runs. During the first run in September 2012 and the second run in early 2013 ATLAS has recorded integrated luminosity of approximately 1 $\mu\mathrm{b}^{-1}$ and 29 nb^{-1}, respectively. The LHC was configured with a 4 TeV proton beam and a 1.57 TeV per-nucleon Pb beam that together produced collisions with a nucleon-nucleon centre-of-mass energy of $\sqrt{s_\mathrm{NN}} = 5.02$ TeV. The higher energy of the proton beam results in a net rapidity shift of the nucleon-nucleon centre-of-mass frame relative to the ATLAS rest frame. This rapidity shift is 0.47 towards the proton beam direction.

Some of the measurements are evaluated for several intervals in collision centrality characterized by the total transverse energy measured from the section of ATLAS forward calorimeter (FCal) spanning the pseudorapidity interval $3.2 < \eta < 4.9$, $\sum E_\mathrm{T}^\mathrm{Pb}$. Centrality intervals were defined in terms of percentiles of $\sum E_\mathrm{T}^\mathrm{Pb}$ determined using standard techniques [8]. The Glauber model [9] and its Glauber-Gribov extension [10] were used to estimate $\langle N_\mathrm{part} \rangle$ or the average value of the nuclear thickness function, $\langle T_\mathrm{Pb} \rangle$, for each centrality interval. The Glauber-Gribov model takes into account event-to-event fluctuations in the nucleon-nucleon cross-section, σ_NN. Two sets of Glauber-Gribov $\langle N_\mathrm{part} \rangle$ results were obtained for two different values of the parameter, Ω, that determines the width of the assumed Gaussian fluctuations in σ_NN.

2 Charged particle multiplicities and p_T spectra

Historically, the basic experimental observables quantifying the particle production are the charged particle multiplicity and pseudorapidity distributions. Previous measurements at RHIC have shown that the rapidity integrated particle multiplicity in d+Au collisions scales with number of inelastically interacting, or "participating", nucleons, N_part. This scaling behaviour has been interpreted as a result of coherent multiple soft interactions of the projectile nucleon in the target nucleus, the so called wounded-nucleon model. The characteristic centrality dependence of charged hadron pseudorapidity distributions showing a strong increase in the yields of nucleus-going direction that was previously observed can be explained by the phenomenology of soft hadron production or in parton saturation models.

Similar features as those seen previously are observed in the charged particle multiplicities measured by ATLAS [2]. In the most peripheral collisions (centrality interval 60-90%), $\mathrm{d}N_\mathrm{ch}/\mathrm{d}\eta$ has what appears to be a double-peak structure, similar to that seen in proton-proton (pp) collisions [11]. In more central collisions, the shape of $\mathrm{d}N_\mathrm{ch}/\mathrm{d}\eta$ becomes progressively more asymmetric, with more particles produced in the Pb-going direction than in the proton-going direction. The increase in the particle production in central relative to the most peripheral collisions is roughly linear in pseudorapidity. The N_part scaling of multiplicities exhibits a strong sensitivity to the Glauber modeling: while the standard Glauber modeling leads to a strong increase in the multiplicity per participant pair with increasing N_part, the Glauber-Gribov approach leads to a much milder centrality dependence.

The expected particle production rate in p+Pb collisions is determined by the product of the inelastic nucleon-nucleon cross-section, σ_NN, and the nuclear thickness function, $\langle T_\mathrm{Pb}\rangle$, which is averaged over a distribution of proton impact parameters incident on the nuclear target. The "nuclear modification factor" R_pPb can be therefore written as

$$R_\mathrm{pPb}(p_\mathrm{T}, y^\star) = \frac{1}{\langle T_\mathrm{Pb}\rangle}\frac{1/N_\mathrm{evt}\ \mathrm{d}^2N_\mathrm{pPb}/\mathrm{d}y^\star \mathrm{d}p_\mathrm{T}}{\mathrm{d}^2\sigma_\mathrm{pp}/\mathrm{d}y\,\mathrm{d}p_\mathrm{T}}, \quad (1)$$

where nucleon-nucleon cross-section is approximated by pp cross-section, σ_pp, neglecting isospin effects. In the absence of nuclear effects at high-p_T, the R_pPb will be unity. The nuclear modification factor was extracted in two measurements, see Refs.[3, 4]. The reference pp cross-section was determined using the interpolation of cross-sections measured at the centre-of-mass energy of 2.76 and 7 TeV. The nuclear modification factors increase with momentum in the region $0.1 < p_\mathrm{T} < 2$ GeV, then they reach a maximum and decrease up to $p_\mathrm{T} \approx 8$ GeV and stay constant within the experimental uncertainties until p_T of ≈ 20 GeV. The magnitude of the peak strongly depends both on rapidity and centrality. It increases from the proton-going to Pb-going direction and from peripheral to central collisions. The constant region is less sensitive to the different centrality and rapidity intervals. The absolute magnitude of the R_pPb and its centrality behaviour strongly depend on the choice of the geometric model.

The nuclear modification factor of charged particles show signs of increasing in the region of $p_\mathrm{T} \gtrsim 30$ GeV. This trend does not have a strong rapidity dependence but is more pronounced in peripheral events. This result seems to show the same unexpected trend as was observed by the CMS Collaboration [12].

3 Jets and Z bosons

The nuclear modification factor R_{pPb} was measured also for jets [5] using as a reference the inclusive jet cross-section in $\sqrt{s} = 2.76$ TeV pp collisions x_T-interpolated to 5.02 TeV using previous ATLAS measurements of jet production at 2.76 and 7 TeV. Results were also reported for the central-to-peripheral ratio R_{CP}, made with respect to the 60-90% centrality bin. The centrality-inclusive R_{pPb} results for 0-90% collisions indicated only a modest enhancement over the geometric expectation. This is generally consistent with predictions from the modification of the parton distribution functions in the nucleus.

The results of the R_{CP} measurement indicate a strong, centrality-dependent reduction in the yield of jets in central collisions relative to that in peripheral collisions. The reduction becomes more pronounced with jet p_{T} and at more forward (p-going) rapidities. These two results are reconciled by the centrality-dependent R_{pPb} results, which show a suppression in central collisions and enhancement in peripheral collisions which is systematic in p_{T} and y^*. The R_{CP} and R_{pPb} data at forward rapidities were replotted as a function of $p_{\mathrm{T}} \cosh(y^*)$, the approximate total jet energy. When plotted this way, the results from different rapidity bins fall into roughly a single trend. This suggests that the mechanism responsible for the observed effects may depend only on the total jet energy or, more generally, on the underlying parton-parton kinematics such as the fractional longitudinal momentum of the parton originating in the proton x_p. If the relationship between the centrality intervals and proton-lead collision impact parameter determined within the geometric models is correct, these results imply large, impact parameter-dependent changes in the number of partons available for hard scattering. However, they may also be the result of a correlation between the kinematics of the scattering and the soft interactions resulting in particle production at backward (Pb-going) rapidities.

The influence of nuclear environment on the production of high-p_{T} particles was further tested by measuring the production of Z bosons [6]. The Z bosons were reconstructed via the di-electron and di-muon decay channels. Results from the two channels are consistent and combined to obtain a total cross-section of 144.1 ± 10.8 nb within the fiducial acceptance region. The total measured cross-section is compared to a baseline pQCD model in which nuclear binding and motion effects are neglected. The p_{T} dependence of the cross-section is in a good agreement with baseline pQCD, however the rapidity dependence shows significant asymmetry compared to the baseline pQCD. A relative excess in the Z boson differential cross-section is seen in the backward (Pb-going) part of the rapidity distribution. This asymmetry is more pronounced in central events and is apparently absent in peripheral events which are roughly symmetric about the centre of mass. Whether the relative asymmetry in central events compared to peripheral events is interpreted as an excess at backward rapidity or a deficit at forward rapidity depends on the choice of Glauber model centrality implementation. This centrality ordering is similar to that observed by ATLAS in high-p_{T} forward jets in p+Pb. The Z boson yield is expected to scale with number of binary collisions, $N_{\mathrm{coll}} = N_{\mathrm{part}} - 1$, however deviations from this scaling are observed, similarly as in the case of the charged particle yields. The charged particle yields are expected to scale with N_{part} and so the ratio $(\mathrm{d}N_Z/\mathrm{d}\eta)/(\mathrm{d}N_{\mathrm{ch}}/\mathrm{d}y)$ was fitted by a function of the form $a \cdot (N_{\mathrm{part}} - 1)/N_{\mathrm{part}}$ which describes the data well. The agreement in the geometric scaling trends between these two very different observables suggests that both are reflecting the consequences of the initial state conditions of the nucleus.

4 Ridge and flow

One striking observation in high-energy nucleus-nucleus collisions is the large anisotropy of particle production in the azimuthal angle ϕ. This anisotropy is often studied via a two-particle correlation of particle pairs in relative pseudorapidity ($\Delta\eta$) and azimuthal angle ($\Delta\phi$). The anisotropy manifests itself as a strong excess of pairs at $\Delta\phi \sim 0$ and π, and the magnitude of the excess is relatively constant out to large $|\Delta\eta|$. The azimuthal structure of this "ridge-like" correlation is commonly characterized by its Fourier harmonics, $\mathrm{d}N_{pairs}/\mathrm{d}\Delta\phi \sim 1+\sum_n 2v_n^2 \cos n\Delta\phi$. The v_n values are commonly interpreted as the collective hydrodynamic response of the created matter to the collision geometry and its density fluctuations in the initial state. For a small collision system, such as *pp* or p+A collisions, it was assumed that the transverse size of the produced system is too small for the hydrodynamic flow description to be applicable. Thus, it came as a surprise that ridge-like structures were also observed in two-particle correlations in high-multiplicity *pp* and p+Pb collisions.

Recent measurement done by ATLAS [7] explores the detailed properties of the ridge-like correlations and the flow via the two particle correlation (2PC) method. The two-particle correlations and v_n coefficients are obtained as a function of p_{T} for pairs with $2 < |\Delta\eta| < 5$ in different intervals of event activity, defined by either N_{ch}, the number of reconstructed tracks, or total transverse energy measured in FCal on the Pb-fragmentation side, $\sum E_{\mathrm{T}}^{\mathrm{Pb}}$. Significant long-range correlations (extending to $|\Delta\eta| = 5$) are observed for pairs at the near-side ($|\Delta\phi| < \pi/3$). A similar long-range correlation is also observed on the away-side ($|\Delta\phi| > 2\pi/3$), after subtracting the recoil contribution estimated using the 2PC in low activity events. The v_n, $(n = 2, 3, 4, 5)$ values increase with p_{T} to $3-4$ GeV and then decrease for higher p_{T}, but remain positive in the measured p_{T} range. The $v_1(p_{\mathrm{T}})$ function is observed to change sign at $p_{\mathrm{T}} \approx 1.5-2.0$ GeV and to increase to about 0.1 at $p_{\mathrm{T}} > 4$ GeV. The magnitudes of v_n increase with both N_{ch} and $\sum E_{\mathrm{T}}^{\mathrm{Pb}}$. The extracted $v_2(p_{\mathrm{T}})$, $v_3(p_{\mathrm{T}})$, and $v_4(p_{\mathrm{T}})$ are compared to the v_n coefficients in p+Pb collisions at $\sqrt{s_{\mathrm{NN}}} = 2.76$ TeV with similar N_{ch}. After applying a scale factor of $K = 1.25$ that accounts for the difference of mean p_{T} in the two collision systems, the shape of the $v_n(p_{\mathrm{T}}/K)$ distribution in Pb+Pb collisions is found to be similar to the shape of $v_n(p_{\mathrm{T}})$ distribution in p+Pb collisions. This suggests that the long-range ridge correlations in high-multiplicity p+Pb collisions and peripheral Pb+Pb collisions are driven by similar dynamics.

Acknowledgments

This work was supported by Charles University in Prague, projects INGOII LG13009, PRVOUK P45, and UNCE 204020/2012.

References

[1] ATLAS Collaboration. *JINST*, 3:S08003, 2008.

[2] ATLAS Collaboration. ATLAS-CONF-2013-096. https://cds.cern.ch/record/1599773.

[3] ATLAS Collaboration. ATLAS-CONF-2013-107. https://cds.cern.ch/record/1624333.

[4] ATLAS Collaboration. ATLAS-CONF-2014-029. http://cds.cern.ch/record/1704978.

[5] ATLAS Collaboration. ATLAS-CONF-2014-024. http://cds.cern.ch/record/1702986.

[6] ATLAS Collaboration. ATLAS-CONF-2014-020. http://cds.cern.ch/record/1702971.

[7] ATLAS Collaboration. arXiv:1409.1792.

[8] ATLAS Collaboration. *Phys.Lett.*, B710:363–382, 2012.

[9] M. Miller, K. Reygers, S. Sanders, and P. Steinberg. *Ann. Rev. Nucl. Part. Sci.*, 57:205–243, 2007.

[10] V. Guzey and M. Strikman. *Phys. Lett.*, B633:245–252, 2006.

[11] ATLAS Collaboration. *Phys. Lett.*, B688:21–42, 2010.

[12] CMS Collaboration. CMS-PAS-HIN-12-017. http://cds.cern.ch/record/1625865.

Soft Probes of the Quark-Gluon Plasma in ATLAS

Krzysztof W. Wozniak[1] on behalf of the ATLAS Collaboration

[1]Institute of Nuclear Physics, PAS, ul. Radzikowskiego 152, 31-342 Krakow, Poland

DOI: http://dx.doi.org/10.3204/DESY-PROC-2014-04/230

Measurements of low-p_{T} (< 5 GeV) particles in Pb+Pb collisions at the LHC provide valuable insight in the production and evolution of the quark-gluon plasma. In particular, measurements of the elliptic and higher order flow harmonics imprinted on the azimuthal angle distributions of low-p_T particles directly probe the strongly-coupled dynamics of the quark gluon plasma and test hydrodynamic model descriptions of its evolution. The large acceptance ATLAS detector makes it possible to measure flow event-by-event and to determine the correlations between different event planes and different flow harmonics.

In collisions of lead nuclei from two beams accelerated in the Large Hadron Collider (LHC) to the energy in the centre-of-mass of $\sqrt{s_{\mathrm{NN}}} = 2.76$ TeV a very high energy density is achieved in a relatively large volume. This leads to creation of a dense, strongly interacting matter - the Quark-Gluon Plasma (QGP). Such matter undergoes first an expansion and then a hadronization leading to particles observed in detectors. While the properties of most energetic partons (observed as jets) are affected mostly by the initial conditions of QGP, the production of particles with lower momenta is also sensitive to the later evolution of QGP. Detailed studies of various correlations between low-p_{T} particles were performed by the ATLAS experiment. In these analyses information from several parts of the ATLAS detector [1] was used. In the Inner Detector covering over 5 pseudorapidity units ($|\eta| < 2.5$) tracks of charged particles are reconstructed. The calorimeters register energy of hadrons, electrons and photons in the $|\eta| < 4.9$ range. The signal registered in the $3.1 < |\eta| < 4.9$ range (i.e. from Forward Calorimeters) is used as a measure of the centrality of Pb+Pb collisions.

In heavy-ion collisions, with an exception of the most central ones, the area of the overlap of nuclei has an elongated shape. The asymmetry of the QGP volume leads in hydrodynamical models to different pressure gradients and then to the azimuthal asymmetry of particle emission (flow). The asymmetry is studied using the Fourier expansion:

$$\frac{\mathrm{d}N_{\mathrm{ch}}}{\mathrm{d}\phi} \sim 1 + 2\sum_{n=1}^{\infty} v_n(p_{\mathrm{T}}, \eta)\cos(n(\phi - \Phi_n)),$$

where azimuthal angles ϕ and Φ_n of the charged particles and the reaction planes, respectively, are used.

The second Fourier harmonic, v_2, called elliptic flow, represents the magnitude of correlations connected with the elongated shape of the overlap of the nuclei. In the LHC experiments it is usually measured using particles with $p_{\mathrm{T}} > p_{\mathrm{T,min}}$, with $p_{\mathrm{T,min}} = 0.3 - 0.5$ GeV, with a model dependent extrapolation to $p_{\mathrm{T}} \approx 0$. No extrapolation is needed in ATLAS if *tracklets*, defined as two hits registered in the innermost pixel detector, compatible with the primary vertex position, are used to reconstruct particles with p_{T} down to 0.07 GeV. In Fig. 1 the dependence of the

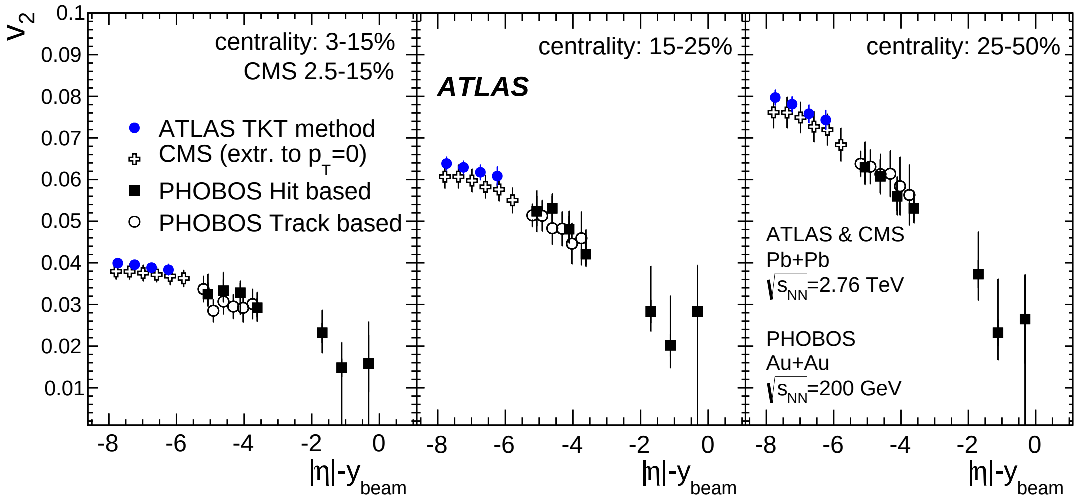

Figure 1: Integrated elliptic flow, v_2, presented as a function of $|\eta| - y_{beam}$ for three centrality intervals obtained by the ATLAS [2] and CMS [3] experiments for Pb+Pb collisions at $\sqrt{s_{\rm NN}} =$ 2.76 TeV and by the PHOBOS experiment [4] for Au+Au collisions at $\sqrt{s_{\rm NN}} = 200$ GeV.

integrated elliptic flow, v_2, on pseudorapidity, shifted by the rapidity of the beam, $y_{\rm beam}$, is presented. This shift corresponds to the Lorentz transformation of rapidity to the rest frame of one of the colliding nuclei. After such transformation the PHOBOS experiment observed an extended longitudinal scaling of v_2 at energies $\sqrt{s_{\rm NN}} = 19.6 - 200$ GeV [4]. The data points from ATLAS follow the trend seen by PHOBOS, unfortunately, the acceptance of the ATLAS detector is too small, to obtain any overlap with PHOBOS,

Flow harmonics can be also measured without determination of the event plane angle, Φ_n, using two-particle or many-particle correlations. If flow is the only source of the two-particle correlations, flow harmonics can be calculated as $v_n\{2\} = \sqrt{\langle \cos(n(\phi_a - \phi_b))\rangle}$. For $2k$-particle correlations ($k > 1$) especially useful are *cumulants*, which measure genuine $2k$-particle correlations. A comparison of flow harmonics obtained by ATLAS using the event plane method, $v_n\{\mathrm{EP}\}$, two-particle correlations, $v_n\{2\}$, four-particle cumulants, $v_n\{4\}$, and mean values of $p(v_n)$ distributions from event-by-event measurements, $v_n\{\mathrm{EbyE}\}$ is shown in Fig. 2 [5]. For all measured harmonics we observe $v_n\{2\} > v_n\{\mathrm{EP}\} > v_n\{\mathrm{EbyE}\} > v_n\{4\}$ relation. $v_n\{2\}$ are the largest beacuse of the non-flow contributions from short range correlations (for example resonance decays), suppressed in all other methods. The differences between $v_n\{\mathrm{EP}\}$, $v_n\{\mathrm{EbyE}\}$ and $v_n\{4\}$ are mainly due to flow fluctuations affecting each of them in a different way. In addition to four-particle cumulants, also six- and eight-particle cumulants are used by ATLAS to measure $v_2\{6\}$ and $v_2\{8\}$, respectively. They are very similar to $v_2\{4\}$, which means that already by using the four-particle cumulants non-flow contributions are efficiently suppressed [5].

Another comparison of the data and models of heavy-ion collisions is possible in a study of correlations between two or more event plane angles, Φ_n, measured in different η intervals for different harmonics [6]. The correlators are defined as $\langle \cos(c_1\Phi_1 + 2c_2\Phi_2 + ... + lc_l\Phi_l)\rangle$ with the constants c_n fulfilling the constraint $c_1 + 2c_2 + ... + lc_l = 0$. In Fig. 3 eight correlators with two event planes measured by ATLAS are presented [6]. Usually the correlations are positive, especially for $4(\Phi_2 - \Phi_4)$, $6(\Phi_2 - \Phi_6)$ and $6(\Phi_3 - \Phi_6)$, but for one of three plane correlations, $2\Phi_2 - \Phi_3 + 4\Phi_4$, it is negative [6]. The values and centrality dependence of correlators from the data and predicted by Glauber model are distinctly different. However, a good qualitative agreement with the data is seen for predictions from the AMPT model [7], which starting from the same initial state as the Glauber model in addition simulates final-state dynamics.

The correlations between magnitudes of flow harmonics measured by ATLAS [8] are presented in Figs. 4 and 5. The data points were obtained in narrow bins of flow vector, q_2 (defined in Ref. [8]), and centrality. The flow vector characterises the asymmetry of the particle production and is directly related to the shape of the initial volume of the QGP, while the centrality reflects its size mostly. For v_2 measured in different p_{T} intervals, linear correlations within fixed centrality are observed (Fig. 4) and only the slope of the linear fit changes with centrality. This suggests presence of viscous effects which are controlled by the overall system size and not its shape. Negative, approximately linear correlations between v_3 and v_2 are observed (Fig. 5 left), similar to anti-correlations between corresponding eccentricities calculated from the positions of participating nucleons. However, the correlations between v_4 and v_2 (Fig. 5 right) are non-linear and thus are not completely eccentricity driven [8].

Detailed studies of several aspects of flow phenomena in ATLAS provide a better understanding of the QGP initial state and evolution. In the flow harmonics calculated from multi-particle cumulants non-flow contributions are suppressed. Effects of final-state dynamics have large impact on correlations between event plane angles. The analysis of correlations between elliptic flow and other flow harmonics reveals viscous effects, anti-correlation of v_3 versus v_2 and non-linear terms in v_4 and v_5 dependence on v_2.

Acknowledgments:

This work was supported in part by the National Science Center grant DEC-2011/03/B/ST/02631 and by PL-Grid Infrastructure.

References

[1] ATLAS Collaboration, JINST 3, S08003 (2008).

[2] ATLAS Collaboration, arXiv:1405.3936v2 [hep-ex] (2014), accepted by Eur. Phys. J. C.

[3] CMS Collaboration, Phys. Rev. C 87, 014902 (2013).

[4] PHOBOS Collaboration, B.B. Back et al., Nucl. Phys. A757, 28 (2005).

[5] ATLAS Collaboration, arXiv:1408.4342 [hep-ex] (2014).

[6] ATLAS Collaboration, Phys. Rev. C80, 024905 (2014).

[7] Z.-W. Lin, C. M. Ko, B.-A. Li, B. Zhang, and S. Pal, Phys. Rev. C 72, 064901 (2005).

[8] ATLAS Collaboration, ATLAS-CONF-2014-022, http://cdsweb.cern.ch/record/1702980 (2014).

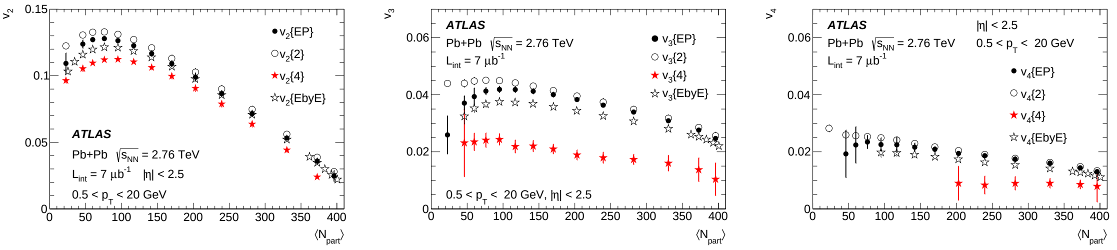

Figure 2: N_{part} dependence of flow harmonics: v_2 (left), v_3 (middle) and v_4 (right) obtained using several different methods [5].

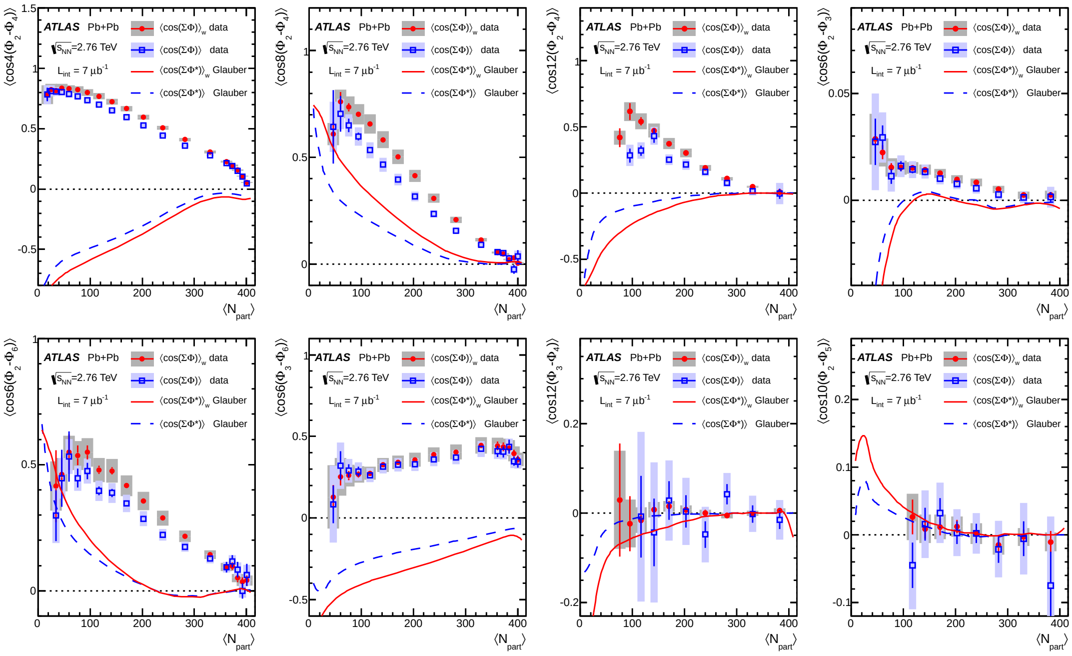

Figure 3: Centrality dependence of two-plane correlators (points) compared with correlations among participant-plane angles expected from the Glauber model (lines) [6].

Figure 4: The correlation between values of v_2 measured in 3-4 GeV p_T range and in 0.5-2 GeV p_T range for several centrality and q_2 intervals, overlaid with the centrality dependence without q_2 selection (grey band) [8]. Linear fits to the data points in each centrality are shown as straight lines.

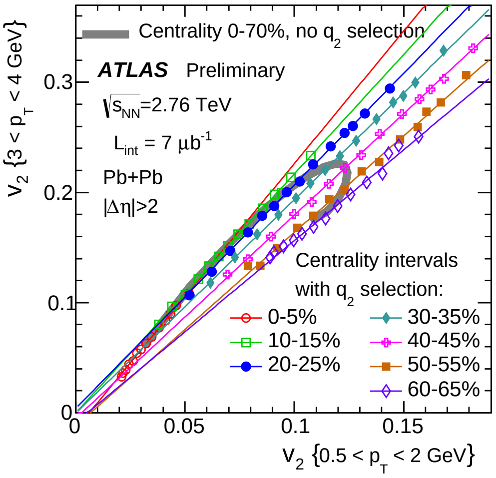

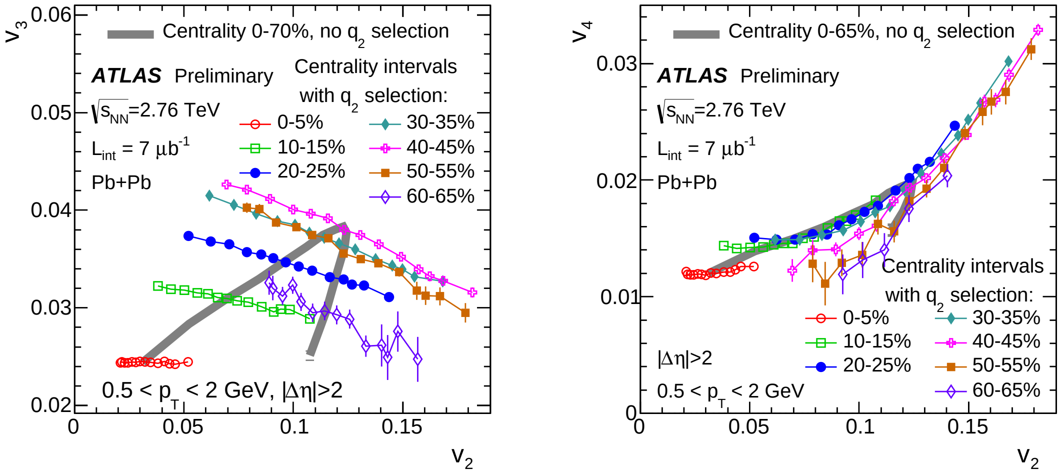

Figure 5: The correlation (left) between v_3 and v_2 and (right) between v_3 and v_2, all measured in 0.5-2 GeV p_T range [8]. Several different centrality selections (denoted by different symbols and colours) and q_2 intervals are used and overlaid with the centrality dependence without q_2 selection (grey band).

Measuring the gluon distribution in nuclei at an Electron-Ion Collider

Matthew A. C. Lamont

Brookhaven National Lab, Upton, NY, 11973, USA

DOI: http://dx.doi.org/10.3204/DESY-PROC-2014-04/44

Despite the successes of the HERA accelerator, where much information was gained on the structure of the nucleon, data on the structure of the nucleus at moderate-to-small x remains elusive, as only fixed-target high-x data currently exist. The small-x region, however, is of great interest. The nucleon structure in this region is dominated by gluons which show a rapid rise with decreasing x. At low-x, this growth must be tamed and the gluon distribution will be saturated. However, only tantalising hints of this have been observed so far. Therefore, the construction of an Electron-Ion Collider (EIC), colliding polarised electrons with polarised protons and also a wide variety of nuclei, will allow an exploration of the region of small-x in great detail, answering questions on both the spatial and momentum distributions of gluons and sea quarks in nuclei. In particular, the saturation region is more accessible in nuclei due to the amplification of the saturation scale with nuclear size ($Q_S \propto \mathrm{A}^{1/3}$). In this paper I present the current status of measuring the gluon distribution in nuclei in e+A collisions at an EIC.

1 Introduction

As the HERA measurements of structure functions showed, at small x, the gluon and sea-quark distributions dominate the structure of the nucleon [1]. In fact, if the structure functions continued to grow untamed with decreasing x, through a process of hard gluons splitting into softer gluons, then the cross-section would become larger than the black-disk limit. Therefore, this growth must be tamed at small x, when soft gluons can recombine into harder gluons. Saturation is achieved when these two processes match each other. This saturation phenomena is expected to be universal, appearing in both nucleons and nuclei. However, its effect is amplified in nuclei, where the saturation scale is expected to grow with nuclear size ($Q_S \propto \mathrm{A}^{1/3}$). Therefore, saturation effects should be visible at higher values of x than in nucleons. A review of saturation physics can be found in the literature [2]. A knowledge of this regime is of vital importance to understanding the underlying physics which governs the initial conditions of heavy-ion collisions at both RHIC and in particular, the LHC, where particle production is dominated by gluons from this unknown region. To that end, eRHIC is a machine that is being designed at Brookhaven National Lab that utilizes the current \$2B hadron facility of RHIC and would provide e+A collisions at high energy and high luminosity [3]. eRHIC would also provide polarized electrons and protons for the study of the spin structure of nucleons.

In this paper, I will not discuss the spin capabilities of an electron-ion collider, but rather focus on measurements that can be made in e+A collisions which will provide further insight into the structure of nuclei. For a detailed review of both the spin capabilities and a more in-depth coverage of the e+A physics than is allowed in this manuscript, please refer to the EIC White Paper [4].

2 Structure Functions

One of the first measurements that will be made in nuclear DIS collisions is of the cross-section as a function of (x,Q^2). Although this is one of the easiest measurements to make, it contains a lot of important information. This cross-section can be written in terms of structure functions:

$$\sigma_r(x,Q^2) = F_2^A(x,Q^2) - \frac{y^2}{Y^+}F_L^A(x,Q^2) \qquad (1)$$

The two structure functions of importance are F_2 and F_L, which reflect the quark and gluon momentum distributions respectively. In order to measure F_L directly, it is necessary to have high-statistics datasets over a number of energies. This was not possible at HERA and hence the gluon distribution in nucleons was inferred from the scaling violation of the F_2 distribution [1].

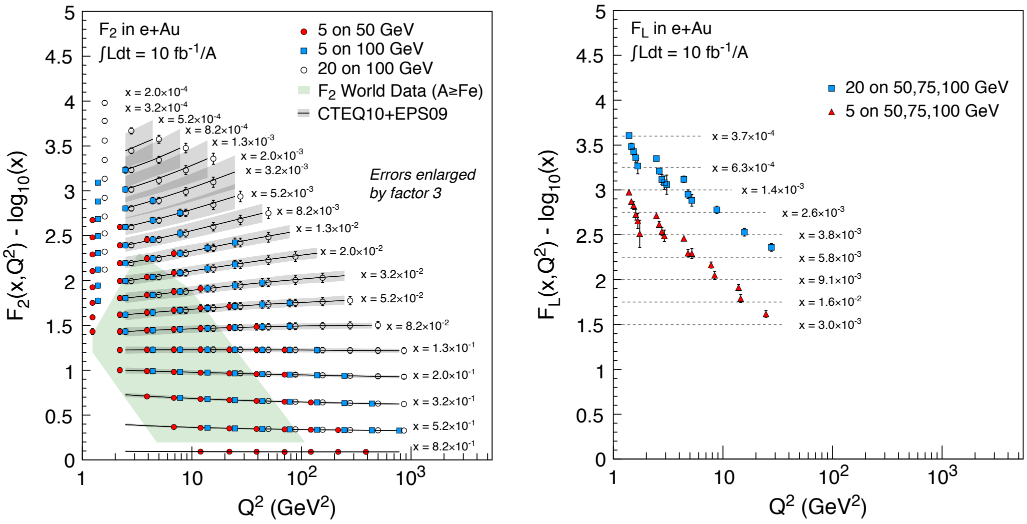

Figure 1: The F_2 (left) and F_L (right) distributions at eRHIC for e+Au collisions. The uncertainties on the pseudo-data are overwhelmingly systematic and represent an integrated luminosity of 10 fb^{-1}/A.

The left side of Figure 1 shows the (x, Q^2) coverage of the F_2 distribution according to the pseudo-data generated for three different eRHIC energies. These pseudo-data were generated using PYTHIA with EPS09 NLO PDFs and represent 10 fb^{-1}/A of data, corresponding to approximately 6 months running time. The highest energy (20x100 GeV beams) extend the phase-space to the lowest (x, Q^2) region while the lowest energy (5x50 GeV beams) extends this measurement to high-x. Also shown on the plot are the EPS09 predictions and their associated uncertainties, together with existing data from fixed target e+A collisions. At small-x, these uncertainties are very large and the data from eRHIC will have a significant impact on the EPS09 uncertainties. For clarity, both the errors coming from EPS09 and the pseudo-data have been enlarged by a factor of 3.

The right side of Figure 1 shows the corresponding F_L measurement. The F_L data were extracted using a Rosenbluth Separation analysis technique where, for each (x, Q^2) bin, a minimum of 3 data points were fit and were required to have a separation of at least 0.1 units of y^+. This technique, however, leads to large uncertainties and these are represented in the plot. Although these are significant, this will be a first measurement of F_L in nuclei.

3 Diffraction in $e + A$ collisions

One of the interesting results to come out of HERA was that a large fraction of events (10-15%) were diffractive. That is, in a significant fraction of collisions at very high energies, the nucleon stayed intact. Whilst this, in and of itself, is a large fraction of events, it is predicted that in nuclei, where saturation effects may be observed at eRHIC, this number could be a factor of 2 or 3 higher.

One of the most promising methods for observing saturation in diffractive collisions, other than the cross-section, is that of vector meson production. Figure 2 shows the cross-section for vector meson production in both coherent and incoherent diffractive collisions, as a function of the Mandelstam variable t, where the uncertainties correspond to an integrated luminosity of 10 fb^{-1}/A. Note that the Q^2 range is above the photo-production threshold. This is shown for both the J/ψ and the ϕ vector mesons. Both of these distributions were generated using the SARTRE MC event generator which has recently been developed for diffractive physics in e+A collisions [5].

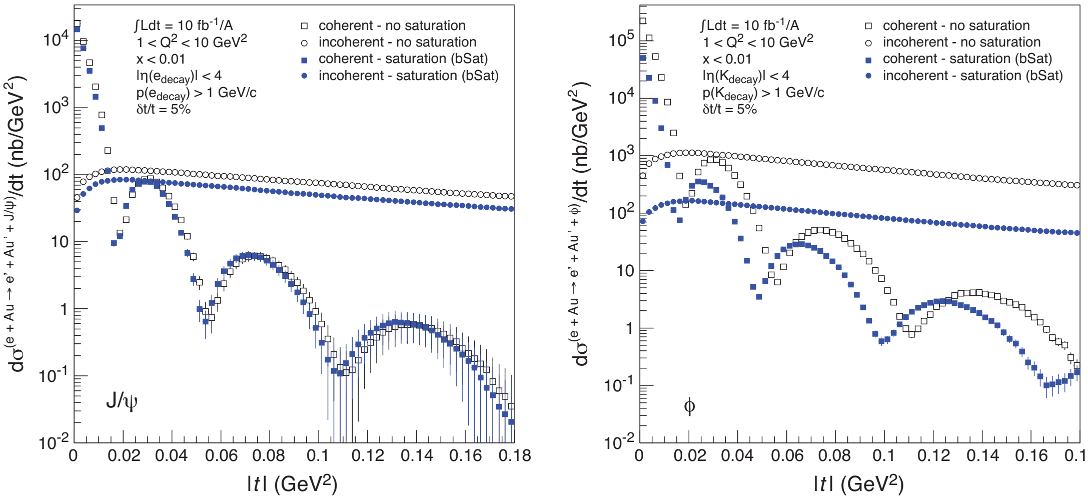

Figure 2: The coherent and incoherent diffractive distributions for the J/ψ (left) and the ϕ (right) vector mesons for an integrated luminosity of 10 fb^{-1}/A, respectively. All distributions were calculated using the SARTRE event generator.

This shows that in the case of the J/ψ, then there is very little difference between the distributions for the saturated and unsaturated case. However, for the ϕ, there is a very significant difference. This comes about because of the size of the wave-functions, where the ϕ wave function is much larger than that of the J/ψ and hence it is more sensitive to saturation effects. In fact, one can take these distributions and perform a Fourier Transform to obtain the input source distribution. Figure 3 shows examples of this for the saturated and unsaturated case for both the J/ψ and the ϕ mesons, which plots both the input Woods-Saxon distribution and the Fourier Transform of the coherent diffractive distribution. As can be seen in the figure, there is little difference between the cases for the J/ψ whereas there is a large difference in the two scenarios for the ϕ meson.

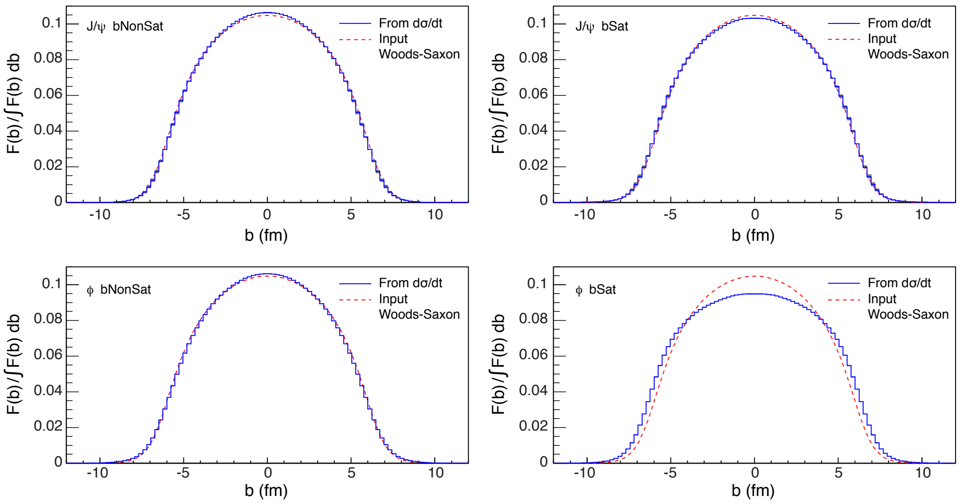

Figure 3: The Fourier Transform of the coherent diffraction distribution in the case of a saturated and unsaturated wave function for the J/ψ (top) and the ϕ (bottom) vector mesons presented in Figure 2. Also shown in each case are the input Woods-Saxon distributions.

Without an Electron-Ion Collider, these measurements cannot be made. Therefore, it is imperative that if we are to more fully understand the par tonic structure of the nucleus, an electron-ion collider is built.

References

[1] S. Aid *et al.*, (H1 Collaboration) Phys. Lett. **B354** (1995) 494-505.
[2] J. Jalilian-Marian and Y. V. Kovchegov, Prog. Part. Nucl. Phys. **56**, 104 (2006).
[3] E.-C. Aschenauer *et al.*, ArXiv:1409.1633.
[4] A. Accardi *et al.*, ArXiv:1212.1701.
[5] T. Toll and T. Ullrich, Phys. Rev. **C 87**, 024913 (2013).

Transverse Momentum Distributions of Charged Particles and Identified Hadrons in p–Pb Collisions at the LHC

Jacek Otwinowski [1] for the ALICE Collaboration

[1] IFJ PAN, Radzikowskiego 152, 31-342 Krakow, Poland

DOI: http://dx.doi.org/10.3204/DESY-PROC-2014-04/142

The transverse momentum distributions (p_{T}) of charged particles and identified hadrons in p–Pb collisions at $\sqrt{s_{\mathrm{NN}}} = 5.02$ TeV have been measured by ALICE at the LHC. Charged-particle tracks are reconstructed at mid-rapidity over a large momentum range $0.15 < p_{\mathrm{T}} < 50$ GeV/c. Light-flavour hadrons and resonances are identified in the various momentum regions, ranging from 0.15 GeV/c to 15 GeV/c, using specific energy loss ($\mathrm{d}E/\mathrm{d}x$), time-of-flight, topological particle-identification and invariant-mass reconstruction techniques. p_{T} spectra are measured for different charged particle multiplicity intervals. Results from p–Pb collisions are compared with pp and Pb–Pb results, and with theoretical models.

1 Introduction

Production of light-flavor hadrons in high energy p–Pb collisions at the LHC is used to study the cold nuclear matter effects (Cronin effect [1], shadowing and gluon saturation [2]), which might influence particle production. It is also possible to search for collective phenomena or indication of the final state effects, which might modify the measured hadron spectra. Here, the question is whether the p–Pb can be considered as a reference system for measurements in Pb–Pb collisions, where the quark-gluon plasma (QGP) [3] is expected to be produced.

In these proceedings, we present results on primary charged particles (98% hadrons) and identified light-flavor hadrons ($\pi^{\pm}$, $\mathrm{K}^{\pm}$, $\mathrm{K}^{0}_{\mathrm{s}}$, p, $\bar{\mathrm{p}}$, Λ, $\bar{\Lambda}$, Ξ^{-}, $\bar{\Xi}^{+}$) obtained by ALICE. Primary charged particles are defined in ALICE as all charged particles produced in the collision and their decay products, except for particles from weak decays of strange hadrons.

In order to quantify nuclear effects, the particle production in p–Pb collisions is compared to pp with use of nuclear modification factor,

$$R_{\mathrm{pPb}}(p_{\mathrm{T}}) = \frac{\mathrm{d}^2 N^{\mathrm{pPb}}_{\mathrm{ch}}/\mathrm{d}\eta \mathrm{d}p_{\mathrm{T}}}{\langle T_{\mathrm{pPb}}\rangle \mathrm{d}^2\sigma^{\mathrm{pp}}_{ch}/\mathrm{d}\eta \mathrm{d}p_{\mathrm{T}}}, \tag{1}$$

where $N^{\mathrm{pPb}}_{\mathrm{ch}}$ is the particle multiplicity in minimum-bias p–Pb collisions, $\sigma^{\mathrm{pp}}_{\mathrm{ch}}$ is the pp cross section, and $\langle T_{\mathrm{pPb}}\rangle = 0.0983 \pm 0.0035$ mb^{-1} is the average nuclear overlap function calculated for minimum bias p–Pb collisions [4] based on Glauber Monte Carlo simulations [5]. The pp reference spectra are constructed [6] using pp measurements at $\sqrt{s} = 2.76$ and 7 TeV at the LHC.

2 ALICE experiment

ALICE [7] is the dedicated heavy-ion experiment at the LHC. The particle tracks are reconstructed using the hit information from the six silicon layers of the Inner Tracking System (ITS) and up to 159 space points from the Time Projection Chamber (TPC). The relative p_{T} resolution obtained with the ITS and TPC combined tracking amounts to $\sigma_{p_{\mathrm{T}}}/p_{\mathrm{T}} = 1$–$5\%$ for $p_{\mathrm{T}} = 0.1$–20 GeV/c. ALICE has excellent particle identification (PID) capabilities in the broad transverse momentum range $p_{\mathrm{T}} = 0.1$–20 GeV/c, which is unique at the LHC. Charged hadrons with $p_{\mathrm{T}} = 0.1$–5 GeV/c are identified using the energy loss ($\mathrm{d}E/\mathrm{d}x$) from the ITS and TPC detectors, the time-of-flight measurement with TOF detector, and Cherenkov light from the high momentum particle identification detector (HMPID). Above $p_{\mathrm{T}} = 5$ GeV/c, they are identified based on the $\mathrm{d}E/\mathrm{d}x$ in the relativistic rise range of the Bethe-Bloch curve in the TPC. Strange hadrons which decay into charged particles ($\mathrm{K}^0_{\mathrm{s}} \to \pi\pi$, $\Lambda \to \pi p$ and $\Xi \to \pi\Lambda$) are identified via their decay topology and invariant mass analysis. In addition, the PID information for their decay products is used to improve signal to background ratio. More details about tracking and particle identification can be found in [8].

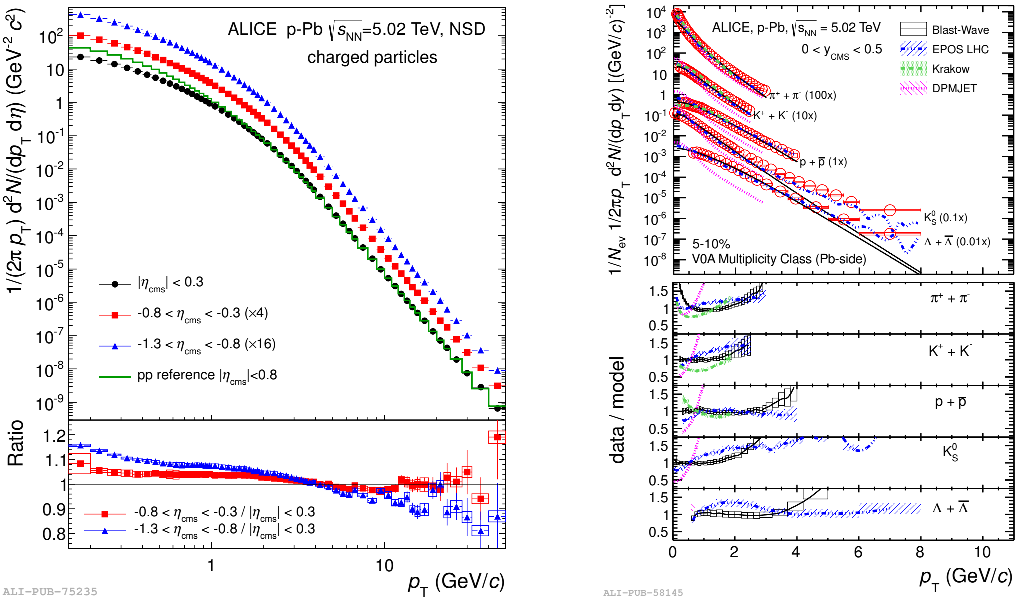

Figure 1: Left: p_{T} spectra measured in p–Pb collisions in three pseudorapidity ranges [4]. The pp reference spectrum is also shown [6]. Right: p_{T} spectra of identified hadrons measured in high multiplicity p–Pb collisions [9] compared to hydrodynamic models (see text for details).

3 Results

Figure 1 (left) shows the p_{T} spectra measured for charged particles in p–Pb collisions in three pseudorapidity ranges [4]. The constructed pp reference [6] at central rapidity is also shown. In the bottom panel, the ratios of the p_{T} spectra measured in two forward pseudorapidity regions with respect to central-pseudorapidity production are shown, indicating that the spectral shape is changing (spectra become softer) with increasing psedorapidity. The effect is particularly visible for p_{T} spectra measured in the most forward pseudorapidity interval, $-1.3 < \eta_{\mathrm{cms}} < -0.8$.

Figure 1 (right) shows the p_{T} spectra of identified hadrons measured in high multiplicity p–Pb collisions [9] in comparison to hydrodynamic (Blast-Wave [10], Kraków [11], EPOS LHC [12]) and QCD-inspired (DPMJET [13]) models. The hydrodynamic models describe data reasonably well for $p_{\mathrm{T}} < 2$ GeV/c while DPMJET fails in describing data for all p_{T}. This might indicate that collective phenomena (e.g. flow etc.) are present in high multiplicity p–Pb collisions.

Figure 2 shows p/π and $\Lambda/\mathrm{K}^0_{\mathrm{s}}$ ratios measured in low and high multiplicity p–Pb collisions [9] in comparison to measurements in peripheral and central Pb–Pb collisions [14]. Similar to Pb–Pb, the baryon-to-meson ratio increases with event multiplicity, however, the increase is smaller compared to Pb–Pb.

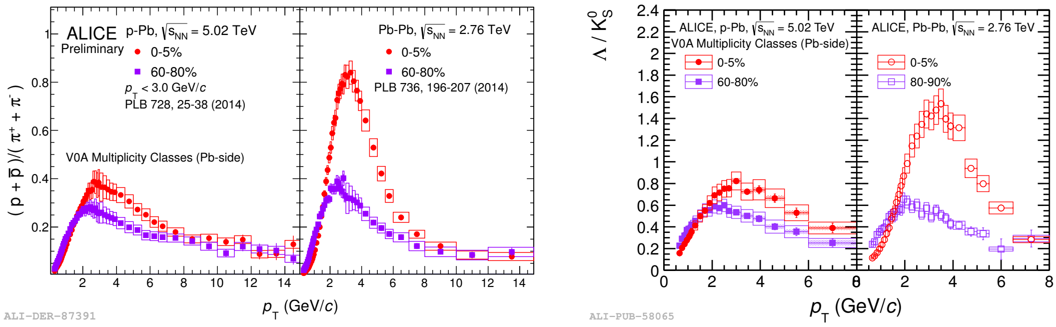

Figure 2: p/π (left) and $\Lambda/\mathrm{K}^0_{\mathrm{s}}$ (right) ratios measured in low (60-80%) and high (0-5%) multiplicity p–Pb collisions [9] in comparison to measurements in peripheral (60-80%) and central (0-5%) Pb–Pb collisions [14].

Figure 3 (left) shows the nuclear modification factor R_{pPb} measured in minimum bias p–Pb collisions [4] in comparison to nuclear modification factors measured in central Pb–Pb collisions ([4] and references therein). The results, showing a strong suppression in central Pb–Pb collisions and almost no suppression in p–Pb, indicate that the effect observed in Pb–Pb collisions is related to interaction with the matter in the final state. Figure 3 (right) shows R_{pPb} for identified hadrons measured in minimum bias p–Pb collisions. At low $p_{\mathrm{T}} < 2$ GeV/c, similar depletion is observed for all particle species. At intermediate $2 < p_{\mathrm{T}} < 7$ GeV/c, enhanced production of protons and Ξ is observed with the characteristic mass dependence, which might be related to collective phenomena (e.g. flow etc.). At high $p_{\mathrm{T}} > 7$ GeV/c, no modification of hadron production is observed, $R_{\mathrm{pPb}} \approx 1$.

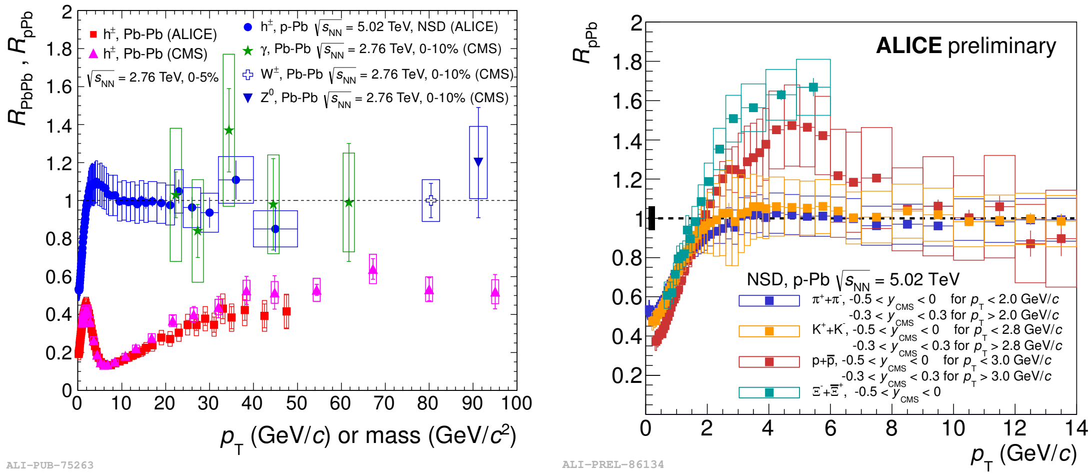

Figure 3: Left: Nuclear modification factors measured as a function of p_{T} in minimum-bias p–Pb collisions [4] and central Pb–Pb collisions ([4] and references therein). Right: R_{pPb} for identified hadrons measured in minimum-bias p–Pb collisions.

In summary, p_{T} spectra measured for light-flavor hadrons in minimum-bias p–Pb collisions, when compared to the reference pp spectrum, show a depletion at low p_{T} (similar for all hadron species), mass dependent enhancement at intermediate p_{T}, and no modification at high p_{T}. The study of the p_{T} spectra measured as a function of multiplicity in p–Pb collisions suggests that collective-like phenomena might develop in high multiplicity p–Pb events.

References

[1] J.W. Cronin *et al.*, Phys. Rev. **D11** 3105 (1975).
[2] C. Salgado *et al.*, J. Phys. **G39** 015010 (2012).
[3] B. Muller, J. Schukraft, and B. Wyslouch, Annu. Rev. Nucl. Part. Sci. **62** 361 (2012).
[4] ALICE Collaboration, Eur. Phys. J. **C74** 3054 (2014).
[5] M. Miller *et al.*, Annu. Rev. Nucl. Part. Sci. **57** 205 (2007).
[6] ALICE Collaboration, Eur. Phys. J. **C73** 2662 (2013).
[7] ALICE Collaboration, JINST **3** S08002 (2008).
[8] ALICE Collaboration, Int. J. Mod. Phys. **A29** 1430044 (2014).
[9] ALICE Collaboration, Phys. Lett. **B728** 25 (2014).
[10] P. Huovinen *et al.*, Phys. Lett. **B503** 58 (2001).
[11] P. Bozek, Phys. Rev. **C85** 014911 (2012).
[12] T. Pierog *et al.*, hep-ph/1306.0121 (2013).
[13] S. Roesler, R. Engel, and J. Ranft, hep-ph/0012252 (2000).
[14] ALICE Collaboration, Phys. Lett. **B736** 196 (2014).

Light (Hyper)Nuclei production at the LHC with ALICE

Ramona Lea[1] for the ALICE Collaboration

[1]Dipartimento di Fisica dell'Universita and Sezione INFN, Trieste, Italy

DOI: http://dx.doi.org/10.3204/DESY-PROC-2014-04/77

The excellent particle identification and momentum measurement capabilities of the ALICE detector allows for the identification of dueterons and ^{3}He and and their corresponding anti-nuclei. This is achieved via the measurement of their specific energy loss in the Time Projection Chamber and the velocity measurement by the Time Of Flight detector. Moreover, thanks to the Inner Tracking System capability to separate primary from secondary vertices, it is possible to identify (anti-)hypertritons exploiting their mesonic weak decay ($^3_\Lambda\mathrm{H} \rightarrow {}^3\mathrm{He} + \pi^-$). Results on the production yields of light nuclei and anti-nuclei in Pb–Pb and p–Pb are presented, together with the measurement of hypertriton production rates in Pb–Pb and upper limits for the production of lighter exotica candidates. The experimental results are compared with the predictions of both thermal (statistical) and coalescence models.

1 Introduction

High energy heavy-ion collisions offer the opportunity to measure light anti-nuclei and search for hypermatter. In fact, although the measurement is challenging as the production probability decreases with increasing mass, the data collected at the LHC allows for the measurement of such particles. Thanks to its unique performance for particle identification, the ALICE detector [1, 2] allows for the identification and the measurements of (anti-)nuclei (deuterons and ^{3}He and their corresponding anti-nuclei) and (anti-)hypertriton and gives the opportunity to search for predicted particles such as the H-Dibaryon and the Λn bound state. Usually two different approaches are used to describe the production yield of these particles: they can be formed at the kinetic freeze-out via the coalescence of nucleons (hyperons) close in phase-space, or their can born in thermal equilibrium [3, 4, 5]. In the thermal models the chemical freeze-out temperature T_{chem} is the key parameter at LHC energies: the production yields depend exponentially on this temperature and on the mass of the particle m ($\mathrm{d}N/\mathrm{d}y \sim \exp(-m/T_{\mathrm{chem}})$).

For the present analysis, the data of Pb–Pb collisions at $\sqrt{s_{\mathrm{NN}}} = 2.76$ TeV recorded in two periods during the years 2010 and 2011 and the data of p–Pb collisions at $\sqrt{s_{\mathrm{NN}}} = 5.02$ TeV recorded at the beginning of 2013 were used.

2 (Anti-)Nuclei

Nuclei and anti-nuclei are identified over a wide range of momentum using the combined information of the specific energy loss (dE/dx) measurement in the Time Projection Chamber (TPC) [6], the velocity measured by the Time Of Flight detector (TOF) [7] and the measurement of the Cherenkov radiation angle measured with the High Momentum Particle Identification Detector (HMPID) [7]. The measured energy loss signal in the TPC of a track is required to be within a 3σ region around the expected value for a given mass hypothesis: with this method it possible to provide a pure sample of ^{3}He in the (2-8) GeV/c transverse momentum interval, while it is limited to 1.4 GeV/c for deuterons. In order to extend deuteron identification, the measured time-of-flight and Cherenkov radiation allows for deuteron identification up to 8 GeV/c. The measured raw spectra were corrected for efficiency and acceptance. Figure 1 shows the deuteron transverse momentum p_{T} spectra in different centrality (multiplicity) classes in Pb–Pb (left panel) and p–Pb (right panel) collisions. In both colliding systems, a hardening of the spectrum with increasing centrality is observed as expected in a hydrodynamic description of the fireball as a radially expanding source. In order to extrapolate the yield in the regions where it is not measured, the spectra were fitted with a Blast-Wave function [8].

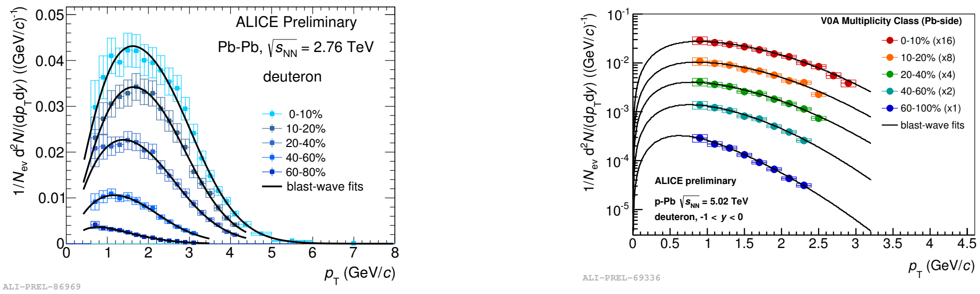

Figure 1: Transverse momentum spectra in different centrality (multiplicity) classes for deuterons in Pb–Pb (left) and in p–Pb (right) collisions at LHC energies.

Figure 2 shows the coalescence parameter $\mathrm{B}_2 = E_{\mathrm{deuteron}} \frac{d^3N_{\mathrm{deuteron}}}{dp^3_{\mathrm{deuteron}}} / \left(E_{\mathrm{proton}} \frac{d^3N_{\mathrm{proton}}}{dp^3_{\mathrm{proton}}}\right)^2$, for Pb–Pb (left) and p–Pb (right) collisions. In a simple coalescence model the B_2 parameter is independent of p_{T}: this is observed in peripheral Pb–Pb and p–Pb. More sophisticated models show that B_2 scales like the HBT radii [9]: the decrease with centrality in Pb–Pb can be explained as an increase in the source volume and the increasing with p_{T} in central Pb–Pb reflects the $\mathrm{k_T}$-dependence of the homogeneity volume in HBT.

3 (Anti-)Hypertriton

The hypertriton ${}^{3}_{\Lambda}\mathrm{H}$ is the lightest known hypernucleus and is formed by a proton, a neutron and a Λ. Its mass is 2.991 ± 0.002 GeV/c^2 and it has a lifetime comparable with the free Λ one (few hundreds of picoseconds) [10]. The (${}^{3}_{\Lambda}\overline{\mathrm{H}}$) ${}^{3}_{\Lambda}\mathrm{H}$ production yield was measured in Pb–Pb by exploiting its weak mesonic decay (${}^{3}_{\Lambda}\mathrm{H} \rightarrow {}^{3}\mathrm{He} + \pi^-$) ((${}^{3}_{\Lambda}\overline{\mathrm{H}} \rightarrow {}^{3}\overline{\mathrm{He}} + \pi^+$)), via the topological identification of secondary vertices and the analysis of the invariant mass distributions of the

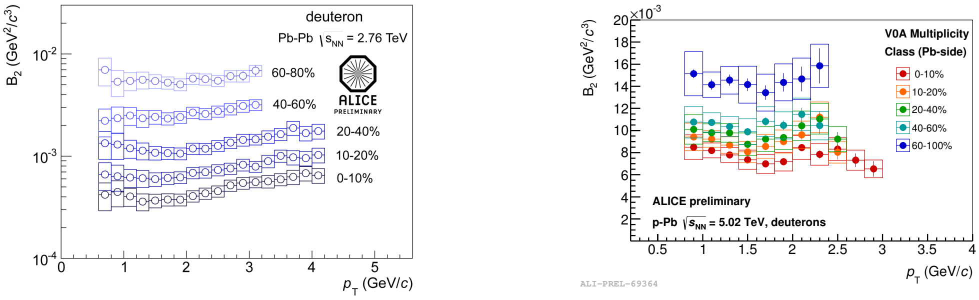

Figure 2: Coalescence parameter B_2 as a function of p_T for deuterons in in Pb–Pb (left) and p–Pb (right) collisions.

decay daughters. The measured ${}^{3}_{\Lambda}\mathrm{H}$ production yield $\mathrm{d}N/\mathrm{d}y$ is compared to different models as a function of the branching ratio ($B.R.$) in Figure 3 (left panel). At the theoretical value ($B.R. = 25$ %) [11], the model which describes better the obtained value is the equilibrium thermal model [3] with a temperature T_{chem} =156 MeV. This temperature is the one which best describes all the particle yields measured at LHC.

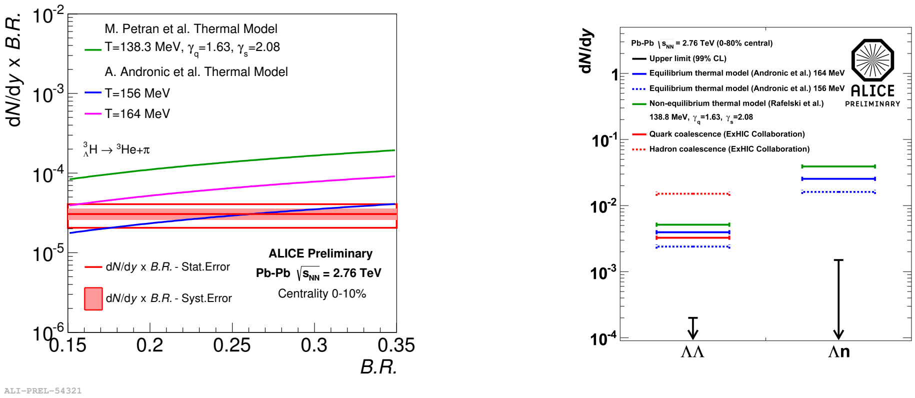

Figure 3: Left: $\mathrm{d}N/\mathrm{d}y$ comparison to different models for the hypertriton measurement. Right: upper limits for H-Dibaryon and Λn $\mathrm{d}N/\mathrm{d}y$ compared with several theoretical models.

4 Exotic Bound State

The H-Dibaryon is a hypothetical *uuddss* bound state (ΛΛ) first predicted by Jaffe in a bag model calculation [12]. Recent lattice calculations [13, 14, 15, 16] suggest that H-Dibaryon should be a bound state, with a binding energy of around 1 MeV/c^2. The same binding energy is also favored from the observed double-Λ hypernuclei, which gives the current constraints on the ΛΛ interaction (for a recent review see [17] and the references therein). In this analysis the decay of the H-Dibaryon into $\Lambda p \pi$ was investigated. In the measured invariant mass distribution no evidence of a signal for the H-Dibaryon was found [18], and an upper limit of dN/dy $2{\times}10^{-4}$ (99 %CL) was obtained. The HypHI collaboration at GSI found evidence for a possible Λn bound state with a mass of 2.054 GeV/c^2, decaying into a deuteron and a pion [19]. The invariant mass distribution of deuterons and pions from displaced vertices, where a possible Λn bound state is expected to be visible, was studied but no signal was observed [18]. This led to an upper limit of dN/dy $1.5{\times}10^3$ (99 %CL). The extracted limits are a factor of 10 lower than the thermal model predictions used to estimate the expected signal while this successfully describes the measured yields of deuterons, ^{3}He and $^3_\Lambda$H nuclei. Figure3 (right) shows the upper limits on the dN/dy of H-Dibaryon and Λn and are compared with several theoretical models.

5 Summary and Conclusions

The p_T spectra of deuteron and ^{3}He (not shown here) were measured in p–Pb and Pb–Pb collisions: a hardening of the spectra with increasing centrality is observed in both the colliding systems. The coalescence parameter B_2 was also determined; it was found to be independent from p_T in p–Pb and peripheral Pb–Pb collisions, while it increases with p_T in central Pb–Pb collisions. A decrease with centrality is also observed in Pb–Pb collisions. The production yield of deuterons, ^{3}He and $^3_\Lambda$H nuclei is in agreement with the current best thermal fit from equilibrium thermal model with a $T_\mathrm{chem} = 156$ MeV. On the other hand, the upper limits for exotica (H-Dibaryon and Λn) are lower than the thermal model expectation by at least an order of magnitude, therefore the existence of such states with the assumed decay branching fraction, mass and lifetime is questionable.

Acknowledgments

The author acknowledges financial support from Consorzio per la Fisica, Trieste.

References

[1] K. Aamodt *et al.* (ALICE collaboration), J. Phys. G: Nucl. Part. Phys. **32** 1295 (2006)

[2] K. Aamodt *et al.* (ALICE collaboration), JINST **3** S08002 (2008)

[3] A. Andronic *et al.*, Phys. Lett. **B697** 203 (2011)

[4] J. Cleymans *et al.*, Phys. Rev. **C84** 054916 (2011)

[5] M. Petráň *et al.*, CERN-PH-TH/2012-262, arXiv:1303.2098v2 [hep-ph] (2013)

[6] J. Alme *et al.*, Nucl. Instrum. Meth. **A622** 316-367 (2010)

[7] B. I. Abelev *et al.*, (ALICE Collaboration), arXiv:1402.4476 [nucl-ex]

[8] E. Schnedermann, J. Sollfrank and U. Heinz, Phys. Rev. C **48**, (1993) 2462

[9] R. Scheibl, U. Heinz, Phys. Rev. **C59** 1585 (1999)

[10] B. I. Abelev *et al.* (STAR Collaboration) 2010 *Science* **328** 58

[11] W. Gloeckle *et al.*, Nucl. Phys. **A639** 297 (1998)

[12] R. Jaffe, Phys. Rev. Lett. **38** 195 and erratum ibid 1977 **38** 617 (1977)

[13] S. R. Beane *et al.* (NPLQCD Collaboration), Phys. Rev. Lett. **106** 162001 (2011)

[14] T. Inoue *et al.* (HAL QCD Collaboration), Phys. Rev. Lett. **106** 162002 (2011)

[15] P. E. Shanahan, A. W. Thomas, R. D. Young, Phys. Rev. Lett. **107** 092004 (2011)

[16] J. Heidenbauer, U. G. Meiner, Phys. Lett. **B706** 100 (2011)

[17] E. Botta, T Bressani, G. Garbarino, Eur. Phys. J. **A48** 41 (2012)

[18] B. Dönigus (for the ALICE Collaboration), Nucl. Phys. **A904905** (0) 547c (2013)

[19] C. Rappold *et al.* (HypHI collaboration), Phys. Rev. **C88**, 041001(R) (2013)

The QCD critical end point driven by an external magnetic field in asymmetric quark matter

Pedro Costa[1], *Márcio Ferreira*[1], *Constança Providência*[1], *Hubert Hansen*[2], *Débora P. Menezes*[2]

[1]Centro de Física Computacional, Department of Physics, University of Coimbra, P-3004-516 Coimbra, Portugal

[2]IPNL, Université de Lyon/Université Lyon 1, CNRS/IN2P3, 4 rue E.Fermi, F-69622 Villeurbanne Cedex, France

[2]Departamento de Física, CFM, Universidade Federal de Santa Catarina, Florianópolis, SC, CP 476, CEP 88.040-900, Brazil

DOI: http://dx.doi.org/10.3204/DESY-PROC-2014-04/75

The effect of the isospin/charge asymmetry and an external magnetic field in the location of the critical end point (CEP) in the QCD phase diagram is investigated. By using the 2+1 flavor Nambu–Jona-Lasinio model with Polyakov loop (PNJL), it is shown that the isospin asymmetry shifts the CEP to larger baryonic chemical potentials and smaller temperatures, and in the presence of a large enough isospin asymmetry the CEP disappears. Nevertheless, a sufficiently high external magnetic field can drive the system into a first order phase transition again.

The QCD phase diagram under extreme conditions of density, temperature and magnetic field is the subject of intense studies [1]. Understanding the effect of an external magnetic field on the structure of the QCD phase diagram is very important: these extremely strong magnetic fields are expected to affect the measurements in heavy ion collisions (HIC) at very high energies, to influence the behavior of the first stages of the Universe and are also relevant to the physics of compact astrophysical objects like magnetars.

On the other hand, the effect of the isospin/charge asymmetry in the QCD phase diagram is also very interesting due to its role on the location of the critical end point (CEP): it was shown that for a sufficiently asymmetric system the CEP is not present [2, 3].

In the present work we describe quark matter subject to strong magnetic fields within the 2+1 PNJL model. The PNJL Lagrangian with explicit chiral symmetry breaking where the quarks couple to a (spatially constant) temporal background gauge field, represented in terms of the Polyakov loop and in the presence of an external magnetic field is given by [4]:

$$\begin{aligned}\mathcal{L} &= \bar{q}\left[i\gamma_\mu D^\mu - \hat{m}_f\right]q \;+\; G\sum_{a=0}^{8}\left[(\bar{q}\lambda_a q)^2 + (\bar{q}i\gamma_5\lambda_a q)^2\right] \\ &-K\left\{\det\left[\bar{q}(1+\gamma_5)q\right] + \det\left[\bar{q}(1-\gamma_5)q\right]\right\} + \mathcal{U}\left(\Phi,\bar{\Phi};T\right) - \frac{1}{4}F_{\mu\nu}F^{\mu\nu}, \qquad (1)\end{aligned}$$

where the quark sector is described by the SU(3) version of the Nambu–Jona-Lasinio model which includes the scalar-pseudoscalar (chiral invariant) and the t'Hooft six fermion interactions that breaks the axial $U_A(1)$ symmetry. The $q = (u, d, s)^T$ represents a quark field with three flavors, $\hat{m}_f = \mathrm{diag}_f(m_u^0, m_d^0, m_s^0)$ is the corresponding (current) mass matrix, $\lambda_0 = \sqrt{2/3}I$ where I is the unit matrix in the three flavor space, and $0 < \lambda_a \leq 8$ denote the Gell-Mann matrices. The coupling between the magnetic field B and quarks, and between the effective gluon field and quarks is implemented *via* the covariant derivative $D^\mu = \partial^\mu - iq_f A^\mu_{EM} - iA^\mu$ where q_f represents the quark electric charge ($q_d = q_s = -q_u/2 = -e/3$), A^{EM}_μ and $F_{\mu\nu} = \partial_\mu A^{EM}_\nu - \partial_\nu A^{EM}_\mu$ are used to account for the external magnetic field and $A^\mu(x) = g_{strong} \mathcal{A}^\mu_a(x) \frac{\lambda_a}{2}$ where $\mathcal{A}^\mu_a$ is the SU$_c(3)$ gauge field. We consider a static and constant magnetic field in the z direction, $A^{EM}_\mu = \delta_{\mu 2} x_1 B$. In the Polyakov gauge and at finite temperature the spatial components of the gluon field are neglected: $A^\mu = \delta^\mu_0 A^0 = -i\delta^\mu_4 A^4$. The trace of the Polyakov line defined by $\Phi = \frac{1}{N_c} \langle\langle \mathcal{P} \exp i \int_0^\beta d\tau\, A_4(\vec{x}, \tau)\ \rangle\rangle_\beta$ is the Polyakov loop which is the *exact* order parameter of the $\mathbb{Z}_3$ symmetric/broken phase transition in pure gauge.

To describe the pure gauge sector an effective potential $\mathcal{U}\left(\Phi, \bar{\Phi}; T\right)$ is chosen in order to reproduce the results obtained in lattice calculations [5]:

$$\frac{\mathcal{U}\left(\Phi, \bar{\Phi}; T\right)}{T^4} = -\frac{a\left(T\right)}{2} \bar{\Phi}\Phi + b(T) \mathrm{ln} \left[1 - 6\bar{\Phi}\Phi + 4(\bar{\Phi}^3 + \Phi^3) - 3(\bar{\Phi}\Phi)^2\right], \tag{2}$$

where $a\left(T\right) = a_0 + a_1 \left(\frac{T_0}{T}\right) + a_2 \left(\frac{T_0}{T}\right)^2$, $b(T) = b_3 \left(\frac{T_0}{T}\right)^3$. The standard choice of the parameters for the effective potential $\mathcal{U}$ is $a_0 = 3.51$, $a_1 = -2.47$, $a_2 = 15.2$, and $b_3 = -1.75$. T_0 is the critical temperature for the deconfinement phase transition within a pure gauge approach: it was fixed to a constant $T_0 = 270$ MeV, according to lattice findings. The parameters of the model are $\Lambda = 602.3\,\mathrm{MeV}$, $m^0_u = m^0_d = 5.5\,\mathrm{MeV}$, $m^0_s = 140.7\,\mathrm{MeV}$, $G\Lambda^2 = 1.385$ and $K\Lambda^5 = 12.36$.

The thermodynamical potential for the three flavor quark sector, Ω, in the mean field approximation is written as

$$\Omega(T,\, B,\, \mu_f) = 2G \sum_{f=u,\, d,\, s} \left\langle \bar{q}_f q_f \right\rangle^2 - 4K \left\langle \bar{q}_u q_u \right\rangle \left\langle \bar{q}_d q_d \right\rangle \left\langle \bar{q}_s q_s \right\rangle + \left(\Omega^{vac}_f + \Omega^{mag}_f + \Omega^{med}_f\right), \tag{3}$$

where the vacuum Ω^{vac}_f, the magnetic Ω^{mag}_f, the medium contributions Ω^{med}_f and the quark condensates $\left\langle \bar{q}_f q_f \right\rangle$ have been evaluated with great detail in [6, 7]. The mean field equations are obtained by minimizing the thermodynamical potential (3) with respect to the order parameters $\left\langle \bar{q}_f q_f \right\rangle$, Φ and $\bar{\Phi}$.

We start the discussion of our results by the location of the CEP when no external magnetic field is present.

It has been shown that the location of the CEP depends on the isospin [8]: as an example, in $\beta-$equilibrium matter the CEP occurs at larger baryonic chemical potentials and smaller temperatures [8]. Indeed, we are interested in d-quark rich matter as it occurs in neutron stars and in HIC: isospin asymmetry in neutron matter has $\mu_d \sim 1.2\mu_u$, and presently the attained isospin asymmetry in HIC corresponds to $\mu_u < \mu_d < 1.1\mu_u$. In the present work the effect of isospin on the CEP is studied: we increase systematically μ_d with respect to μ_u taking the s-quark chemical potential equal to zero ($\mu_s = 0$ leads to all CEP's occur at $\rho_s = 0$).

The results for the CEP in the previous conditions are presented in Fig. 1. For reference we also show the red full point that corresponds to the CEP with $\mu_u = \mu_d = \mu_s$. When the isospin asymmetry is increased the CEP moves to smaller temperatures and larger baryonic chemical potentials.

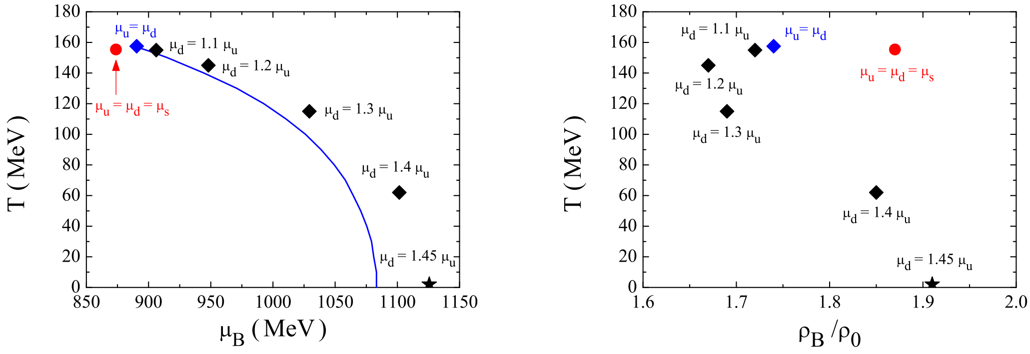

Figure 1: The influence of the isospin in the location of the CEP within the PNJL model: the full line is the first order phase transition line for zero isospin matter ($\mu_u = \mu_d$, $\mu_s = 0$). The chemical potential for the strange quark is always taken equal to zero, except the for the red point ($\mu_u = \mu_d = \mu_s$) which is given for reference. When $\mu_d > 1.45\mu_u$ the CEP doesn't exist anymore.

When the asymmetry is large enough, $\mu_d = 1.45\mu_u$, the CEP disappears (this CEP is represented in Fig. 1 by a star at $T = 0$). This scenario leads to $|\mu_u - \mu_d| = |\mu_I| = |\mu_Q| = 130$ MeV, below the pion mass and, accordingly, no pion condensation occurs under these conditions.

The CEP for (T, ρ_B) plane is shown in the right panel of Fig. 1. When $\mu_u < \mu_d < 1.2\mu_u$ the baryonic density of the CEP decreases with asymmetry but for $\mu_d \gtrsim 1.2\mu_u$ the opposite occurs and at the threshold ($\mu_d = 1.45\mu_u$) $\rho_B \sim 1.91\rho_0$.

Now, we investigate how a static external magnetic field will influence the localization of the CEPs previously calculated. The results are plotted in Fig. 2. In the left panel of Fig. 2 the red dots correspond to symmetric matter ($\mu_u = \mu_d = \mu_s$) and reproduce qualitatively the results previously obtained within the NJL model [9] being the trend qualitatively similar: the increasing of the intensity of the magnetic field leads to an increase of the CEP's temperature and to a decrease of the CEP's baryonic chemical potential until the critical value $eB \sim 0.4$ GeV^2; for stronger magnetic fields, both T and μ_B increase. In the right panel of Fig. 2 the CEP is given in a T vs. ρ_B plane. The results show that when eB increases from 0 to 1 GeV^2 the baryonic density at the CEP increases from $2\rho_0$ to $14\rho_0$.

Taking the isospin symmetric matter scenario $\mu_u = \mu_d$ and $\mu_s = 0$, the effect of the magnetic field on the CEP is very similar to the previous one (see blue diamonds in Fig. 2): the CEP's temperature is only slightly larger and the CEP's baryonic density is slightly smaller.

Also interesting is the case that occurs for the very asymmetric matter scenario: a first order phase transition driven by the magnetic field takes place if $\mu_d \gtrsim 1.45\mu_u$. Taking the threshold value $\mu_d = 1.45\mu_u$ it is seen that for eB <0.1 GeV^2 two CEPs may appear. Indeed, for sufficiently small values of eB the T^{CEP} is small and the Landau level effects are visible.

A magnetic field affects in a different way u and d quarks due to their different electric charge. A consequence is the possible appearance of two or more CEPs for a given magnetic field intensity. Two critical end points occur at different values of T and μ_B for the same magnetic field intensity for fields $0.03 \lesssim eB \lesssim 0.07$ GeV^2. Above 0.07 GeV^2 only one CEP remains. For stronger fields we get $T^{CEP} > 100$ MeV: Landau level effects are completely

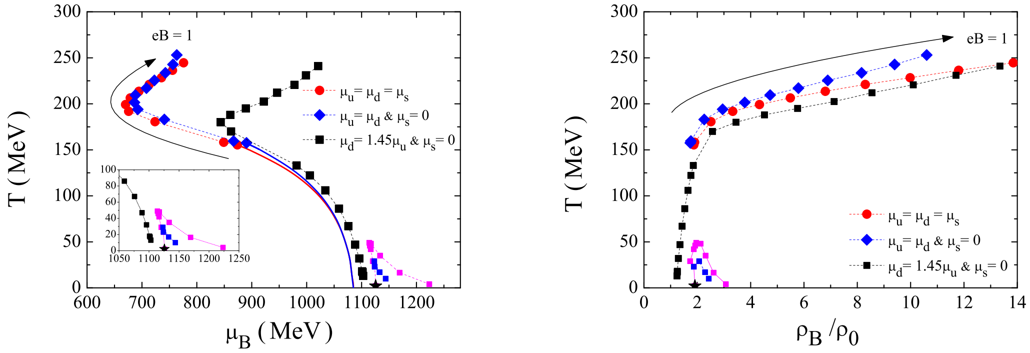

Figure 2: Effect of an external magnetic field on the location of the CEP: T^{CEP} vs μ_B^{CEP} (left panel) and T^{CEP} vs ρ_B^{CEP} (right panel). The full lines correspond to the first order transitions at $eB = 0$. Three scenarios are shown: $\mu_u = \mu_d = \mu_s$ (red dots), $\mu_u = \mu_d$; $\mu_s = 0$ (blue diamonds) and $\mu_d = 1.45\mu_u$, $\mu_s = 0$ (black squares) corresponding to the threshold isospin asymmetry above which no CEP occurs. In the last scenario for strong enough magnetic fields and low temperatures two or more CEP exist at different temperatures for a given magnetic field intensity (pink and blue squares).

washed out at these temperatures.

Acknowledgments

This work was supported by C.F.C., by Project No. CERN/FP/123620/2011 developed under the initiative QREN financed by the UE/FEDER through the program COMPETE "Programa Operacional Factores de Competitividade" by Grant No. SFRH/BD/51717/2011, by CNPq/Brazil and by FAPESC/Brazil.

References

[1] M. Ferreira, P. Costa and C. Providência, Phys. Rev. D **89**, 036006 (2014); D. P. Menezes, M. B. Pinto, L. B. Castro, P. Costa and C. Providência, Phys. Rev. C **89**, 055207 (2014); M. Ferreira, P. Costa, O. Loureno, T. Frederico and C. Providência, Phys. Rev. D **89**, 116011 (2014); M. Ferreira, P. Costa and C. Providência, Phys. Rev. D **90**, 016012 (2014).

[2] H. Ueda, T. Z. Nakano, A. Ohnishi, M. Ruggieri, and K. Sumiyoshi, Phys. Rev. D **88**, 074006 (2013).

[3] H. Abuki, Phys. Rev. D **87**, 094006 (2013).

[4] K. Fukushima, Phys. Lett. **B591**, 277 (2004); C. Ratti, M. A. Thaler, and W. Weise, Phys. Rev. D **73**, 014019 (2006).

[5] S. Roessner, C. Ratti and W. Weise, Phys. Rev. D **75**, 034007 (2007).

[6] D.P. Menezes, M.B. Pinto, S.S. Avancini, A. P. Martínez, and C. Providência, Phys. Rev. C **79**, 035807 (2009); D.P. Menezes, M.B. Pinto, S.S. Avancini and C. Providência, Phys. Rev. C **80**, 065805 (2009).

[7] S.S. Avancini, D.P. Menezes and C. Providência, Phys. Rev. C **83**, 065805 (2011).

[8] P. Costa, M. Ferreira, H. Hansen, D. P. Menezes and C. Providência, Phys. Rev. D **89**, 056013 (2014).

[9] Sidney S. Avancini, Débora P. Menezes, Marcus B. Pinto, and Constança Providência, Phys. Rev. D **85**, 091901 (2012).

Anisotropic flow from hard partons in ultra-relativistic nuclear collisions

Boris Tomášik[1,2], *Martin Schulc*[2]

[1]Univerzita Mateja Bela, Tajovského 40, 97401 Banská Bystrica, Slovakia
[2]Czech Technical University in Prague, FNSPE, Břehová 7, 11519 Prague 1, Czech Republic

DOI: http://dx.doi.org/10.3204/DESY-PROC-2014-04/96

Anisotropies of hadronic distribution in nuclear collisions are used for determination of properties of the nuclear matter. At the LHC it is important to account for the contribution to the flow due to momentum transferred from hard partons to the quark-gluon plasma.

In ultrarelativistic nuclear collisions, hadron momentum distributions are azimuthally anisotropic and parametrised with the help of Fourier expansion with amplitudes of individual modes usually denoted as v_n's. If spectra are summed over a large number of events, symmetry constraints dictate all odd amplitudes to vanish. In individual events, however, these constraints are not realised, because the event shapes fluctuate.

In general, the mechanism behind the modification of hadronic spectra is the blue-shift. Transverse expansion of the fireball enhances production of hadrons with higher p_t. If the normalisation and the slope of p_t spectrum depend on azimuthal angle, this indicates different transverse expansion velocity in different directions. Expansion is caused by pressure gradients in the initial state. We thus have a link between the initial state of the fireball and the observed hadronic spectra. (In fact, here we propose a mechanism which can break this link.)

The link is described by relativistic hydrodynamics. The scheme is based on fundamental conservation laws complemented by the equation of state. In non-ideal hydrodynamics it also involves transport coefficients, e.g. shear and bulk viscosity. The goal is to tune them so that hydrodynamic modelling yields results in accord with the observations.

Unfortunately, there are some problems. The initial conditions are unknown. They are set by energy depositions in early partonic interactions. Various models predict energy and momentum density profiles with different levels of spikiness. One can get the same result on flow anisotropies with different initial conditions if one re-tunes the transport coefficients [1]. This hinders the determination of viscosities from comparisons to data. The extracted values would depend on the assumptions that are made about *unknown* initial conditions.

This problem might be settled with the help of flow anisotropy fluctuations [2]. Simulations indicate that the values of v_n's in individual events follow to large extent the corresponding spatial anisotropies of the initial state [3, 4]. The departure from this proportionality has also been studied [4, 5]. The mechanism proposed in the present paper would break this proportionality since it produces flow anisotropy *during* the hydrodynamic evolution *without* the need for any anisotropy in the initial state.

We point out [6] that in nuclear collisions at LHC energies there is more than one dijet pair per event. (We might have to lower the threshold for what we count as hard parton; here we use $p_t > 3$ GeV/c.) They deposit most—if not all—of their energy and momentum into the plasma and are fully quenched. Since momentum must be conserved, the wakes behind the partons must stream and carry it. Such streams would generate anisotropy of collective expansion in every individual event. This leads to elliptic anisotropy even after a summation over large number of events. Indeed, isotropically produced jets generate elliptic anisotropy. The important detail is the possibility that the induced streams can interact and merge.

Suppose that two dijet pairs are produced in a non-central collision. The elliptic flow due to spatial deformation is directed parallel to the reaction plane. If both pairs are aligned with this plane, then all streams contribute to positive v_2, see Fig. 1 (left). On the other hand, if the jets are oriented under large angle with respect to the reaction plane, then the two streams directed inwards can meet, merge into one, and continue in a direction given by the sum of their two momenta. They do not contribute to the collective flow in their original direction. The chance of merger is higher in the latter case than in the former one since there the jets pass each other within a narrower path. Perpendicularly to the reaction plane the fireball is wider so the streams parallel to the reaction plane can well proceed without bothering each other. In addition to this mechanism, Fig. 1 (right) also suggests that contribution to triangular flow is created by the merger of two streams.

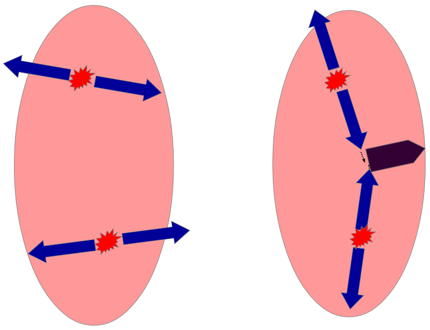

Figure 1: Transverse cross-section through the fireball with two dijet pairs produced. Reaction plane is horizontal. Left: two dijets both emitted in the direction of the reaction plane both contribute positively to the elliptic flow, which is dominant in the same direction. Right: if hard partons are produced off the reaction plane, some of their streams can come together and merge.

This picture is supported by our simulations. We developed 3+1D ideal hydrodynamic simulation code [7, 8] using the SHASTA scheme to handle shocks. We include force term J^μ

$$\partial_\mu T^{\mu\nu} = J^\nu \qquad (1)$$

which represents the dragging of the fluid by hard partons [9]

$$J^\nu = -\sum_i \frac{1}{(2\,\pi\,\sigma_i^2)^{\frac{3}{2}}} \exp\left(-\frac{(\vec{x}-\vec{x}_{\mathrm{jet},i})^2}{2\,\sigma_i^2} \right) \left(\frac{dE_i}{dt}, \frac{d\vec{P}_i}{dt} \right) \qquad (2)$$

where the sum goes through all hard partons in the system and the width σ_i was set to 0.3.

We first checked that indeed the streams are induced behind the partons and that they flow even after the partons are fully quenched (as was also observed in [9]). In a simulation with static medium we could see that the streams merge when they meet. Then, until their energy is spread over a larger volume, they continue flowing in common direction [7].

The mechanism has been included into more realistic simulation of nuclear collisions. In these studies it was not our aim to reach the complete description of data. We rather wanted to gain realistic estimate of the influence of our mechanism on the observed anisotropies. Therefore, we started our simulations always with smooth initial conditions calculated within the optical Glauber model. Any fluctuation on top of non-zero event-averaged flow harmonics is then

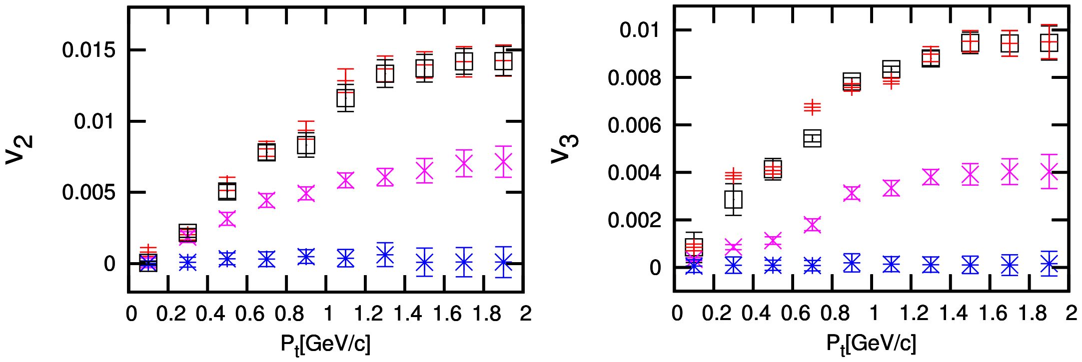

Figure 2: Anisotropy coefficients from central collisions. Two simulations with hard partons with different energy loss. One simulation with only energy and no momentum deposition (hot spots). One simulation with smooth initial conditions.

clearly a consequence of hard partons inducing flow anisotropies. We start our simulation with uniform profile in longitudinal rapidity stretched over 10 units and cut by half-Gaussian tails at both ends. This feature represents the approximate boost-invariance at highest LHC energies. Note that the use of 3+1D hydrodynamic model, which makes our simulation distinct from those reported in [10, 11], is important because the hard partons injected into plasma break the boost invariance and thus the possibility to reduce the dimensionality of the hydrodynamic model.

At the beginning of each event simulation we generate the positions and directions of the hard parton pairs. Their number fluctuates according to Poissonian and their p_T's follow from [6]

$$E\frac{d\sigma_{NN}}{d^3p} = \frac{1}{2\pi}\,\frac{1}{p_T}\,\frac{d\sigma_{NN}}{dp_T\,dy} = \frac{B}{(1+p_T/p_0)^n} \tag{3}$$

with $B = 14.7$ mb/GeV^2, $p_0 = 6$ GeV and $n = 9.5$. Momenta in a pair are back-to-back. The initial positions are generated from the distribution of the binary collisions calculated within optical Glauber model.

In an expanding fireball we assume that the energy loss of a parton scales with the entropy density as $dE/dx = dE/dx|_0\,(s/s_0)$ where $s_0 = 78.2/\mathrm{fm}^3$ (corresponds to energy density 20 GeV/fm^3). Hydrodynamic description of the collision is finished at the freeze-out hypersurface specified by temperature 150 MeV. Generation of final state hadrons is done with the help of THERMINATOR2 [12] Monte Carlo model.

In Fig. 2 we show the v_n's calculated in central collisions. To study the effect of momentum deposition we simulated 100 evolutions for every setting and generated 5 THERMINATOR2 events for each of them. For the momentum loss we made simulations with $dE/dx|_0$ set to 4 GeV/fm and 7 GeV/fm and they lead to the same momentum anisotropies. Their magnitude indicates that the effect is important and should be included in realistic simulations. Finally, we also simulated events where we put in hot spots with the same energy on top of the smooth initial conditions instead of hard partons. They deposit only energy and no momentum, and the generated flow anisotropies are about half of those initiated by hard partons.

Simulations of non-central collisions clearly show that the contribution enhances the observed anisotropies. In Fig. 3 we see about 50% addition to v_2 as compared to the case with smooth initial conditions. Triangular anisotropy is absent in the initial conditions and thus any v_3 is exclusively due to hard partons.

The presented results clearly demonstrate the necessity to include this mechanism into realistic hydrodynamic simulations which aim at extracting the properties of quark matter. For the alignment of the studied effect with the geometry of the fireball it is crucial to include more than one dijet pair into the simulation, unlike done in [13]. The interplay of many generated streams appears important.

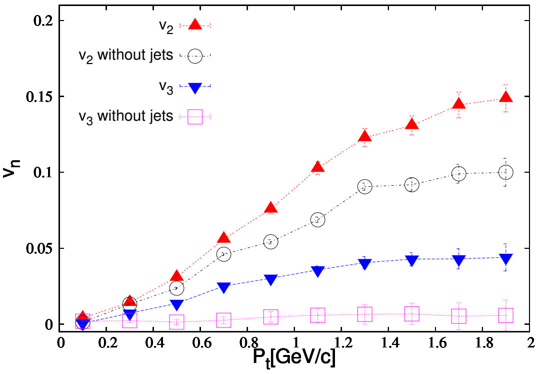

Figure 3: Coefficients v_2 and v_3 from 30–40% centrality events. Results of simulations with hard partons are compared with results from smooth initial conditions.

Acknowledgments

This work was supported in parts by APVV-0050-11, VEGA 1/0457/12 (Slovakia) and MŠMT grant LG13031 (Czech Republic).

References

[1] M. Luzum and P. Romatschke, Phys. Rev. C **78** (2008) 034915 [Erratum-ibid. C **79** (2009) 039903]

[2] U. Heinz, J. Phys. Conf. Ser. **455** (2013) 012044

[3] C. Gale, *et al.*,Phys. Rev. Lett. **110** (2013) 012302

[4] H. Niemi, G. S. Denicol, H. Holopainen and P. Huovinen, Phys. Rev. C **87** (2013) 5, 054901

[5] S. Floerchinger and U. A. Wiedemann, Phys. Rev. C **89** (2014) 034914

[6] B. Tomášik and P. Lévai, J. Phys. G **38** (2011) 095101

[7] M. Schulc and B. Tomášik, J. Phys. G **40** (2013) 125104

[8] M. Schulc and B. Tomášik, Phys. Rev. C **90** (2014) 064910

[9] B. Betz, *et al.*,Phys. Rev. C **79** (2009) 034902

[10] R. P. G. Andrade, J. Noronha and G. S. Denicol, Phys. Rev. C **90** (2014) 024914

[11] S. Floerchinger and K. C. Zapp, Eur. Phys. J. C **74** (2014) 3189

[12] M. Chojnacki, A. Kisiel, W. Florkowski and W. Broniowski, Comput. Phys. Commun. **183** (2012) 746

[13] Y. Tachibana and T. Hirano, Phys. Rev. C **90** (2014) 021902

Chapter 4

Hadrons in medium - hyperons and mesons in nuclear matter

Hyperon-nucleon interaction in chiral effective field theory

Johann Haidenbauer

Institute for Advanced Simulation, Forschungszentrum Jülich GmbH, D-52425 Jülich, Germany

DOI: http://dx.doi.org/10.3204/DESY-PROC-2014-04/134

Results of a study of the hyperon-nucleon system within chiral effective field theory are reported. The investigation is based on the scheme proposed by Weinberg which has been applied rather successfully to the nucleon-nucleon interaction in the past. Results for the ΛN and ΣN interactions in free space and nuclear matter, obtained up to next-to-leading order, are presented and discussed.

1 Introduction

Chiral effective field theory (EFT) as proposed in the pioneering works of Weinberg [1] is a powerful tool for the derivation of baryonic forces. In this scheme there is an underlying power counting which allows to improve calculations systematically by going to higher orders in a perturbative expansion. In addition, it is possible to derive two- and corresponding three-body forces as well as external current operators in a consistent way.

Recently, a hyperon-nucleon (YN) interaction has been derived up to next-to-leading order (NLO) in chiral EFT by the Jülich-Bonn-Munich group [2]. At that order there are contributions from one- and two-pseudoscalar-meson exchange diagrams and from four-baryon contact terms without and with two derivatives. SU(3) flavor symmetry is imposed for constructing the YN interaction in order to reduce the number of free parameters, in particular the number of low-energy constants (LECs) associated with the arising contact terms. In the actual calculation the SU(3) symmetry is broken, however, by the mass differences between the involved mesons (π, K, η) and between the baryons (N, Λ, Σ).

An excellent description of available ΛN and ΣN scattering data could be achieved at NLO. Corresponding results are reported in Sect. 3. In addition the in-medium properties of the EFT YN interaction have been investigated. Specifically, binding energies of the Λ and Σ hyperons in nuclear matter have been calculated, based on a conventional first-order Brueckner calculation, and these are also presented.

2 The YN interaction in chiral EFT

The derivation of the chiral baryon-baryon potentials for the strangeness sector at leading order (LO) using the Weinberg power counting is outlined in Refs. [3, 4]. Details for the NLO case can be found in Ref. [2], see also [5]. The LO potential consists of four-baryon contact terms without derivatives and of one-pseudoscalar-meson exchanges while at NLO contact terms with two derivatives arise, together with contributions from (irreducible) two-pseudoscalar-meson exchanges. The contributions from pseudoscalar-meson exchanges (π, η, K) are completely fixed by the assumed SU(3) flavor symmetry. On the other hand, the strength parameters associated with the contact terms, the LECs, need to be determined in a fit to data. How this is done is described in detail in Ref. [2]. Note that we impose also SU(3) symmetry for those contact terms which reduces the number of independent LECs that can contribute.

The reaction amplitudes are obtained from the solution of a coupled-channels Lippmann-Schwinger (LS) equation for the interaction potentials:

$$\begin{aligned} T^{\rho''\rho',J}_{\nu''\nu'}(p'',p';\sqrt{s}) &= V^{\rho''\rho',J}_{\nu''\nu'}(p'',p') + \\ & \sum_{\rho,\nu}\int_0^\infty \frac{dpp^2}{(2\pi)^3}\, V^{\rho''\rho,J}_{\nu''\nu}(p'',p)\frac{2\mu_\nu}{q_\nu^2-p^2+i\eta}T^{\rho\rho',J}_{\nu\nu',J}(p,p';\sqrt{s})\ . \end{aligned}$$

The label ν indicates the particle channels and the label ρ the partial wave. μ_ν is the pertinent reduced mass. The on-shell momentum in the intermediate state, q_ν, is defined by $\sqrt{s} = \sqrt{m^2_{B_{1,\nu}} + q_\nu^2} + \sqrt{m^2_{B_{2,\nu}} + q_\nu^2}$. Relativistic kinematics is used for relating the laboratory energy $T_{\rm lab}$ of the hyperons to the c.m. momentum.

We solve the LS equation in the particle basis, in order to incorporate the correct physical thresholds. Depending on the total charge, up to three baryon-baryon channels can couple. The Coulomb interaction is taken into account appropriately via the Vincent-Phatak method [6]. The potentials in the LS equation are cut off with a regulator function, $f_R(\Lambda) = \exp\left[-\left(p'^4+p^4\right)/\Lambda^4\right]$, in order to remove high-energy components [7]. We consider cutoff values in the range $\Lambda = 500 - 650\,\mathrm{MeV}$, similar to what was used for chiral NN potentials [7].

3 Results for ΛN and ΣN in free space and nuclear matter

Our results for ΛN and ΣN scattering are presented in Fig. 1. The bands (black/red for NLO and grey/green bands for LO) represent the variation of the cross sections based on chiral EFT within the considered cutoff region, i.e. 550-700 MeV in the LO case [3] and 500-650 MeV at NLO. For comparison also results for the Jülich '04 [8] meson-exchange model are shown (dashed line).

Obviously, the available ΛN and ΣN scattering data are very well described by our NLO EFT interaction. In particular, and as expected, the energy dependence exhibited by the data is visibly better reproduced within our NLO calculation than at LO. This concerns in especially the $\Sigma^+ p$ channel. But also for Λp the NLO results are now well in line with the data even up to the ΣN threshold. Furthermore, one can see that the dependence on the cutoff mass is strongly reduced in the NLO case. Additional results, for differential cross sections and for phase shifts, can be found in Ref. [2].

Besides an excellent description of the YN data the chiral EFT interaction yields a satisfactory value for the hypertriton binding energy, see Ref. [2]. Calculations for the four-body hypernuclei ${}^4_\Lambda$H and ${}^4_\Lambda$He based on the EFT interactions can be found in Ref. [9].

Recently, we have also investigated the properties of our YN interactions in nuclear matter [10]. Specifically, we performed a conventional first-order Brueckner calculation based on the standard choice of the single-particle (s.p.) potentials. Table 3 summarizes preliminary results for the Λ and Σ potential depths, $U_\Lambda(p_\Lambda = 0)$ and $U_\Sigma(p_\Sigma = 0)$, evaluated at the saturation point of nuclear matter, i.e. for $k_F = 1.35$ fm^{-1}. Corresponding results obtained for the Jülich

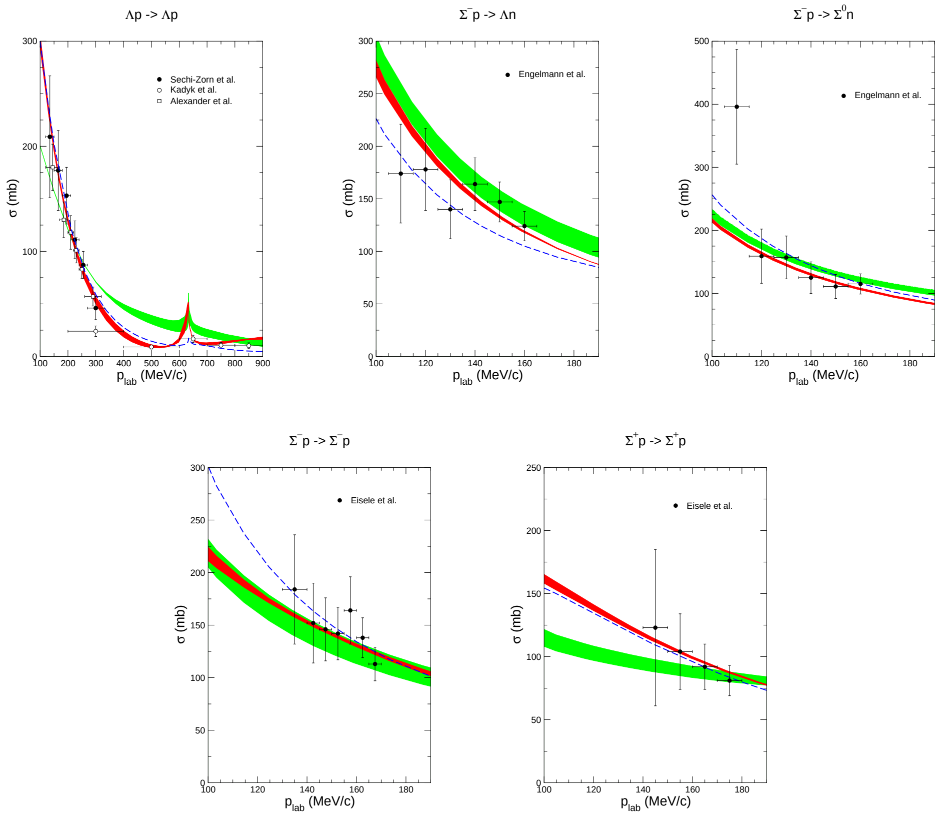

Figure 1: Total cross sections for ΛN, and ΣN scattering as a function of p_{lab}. The grey/green band shows the chiral EFT results to LO for variations of the cut-off in the range $\Lambda = 550$–700 MeV, while the black/red band are results to NLO for $\Lambda = 500$–650 MeV. The dashed curve is the result of the Jülich '04 [8] meson-exchange potential.

meson-exchange potentials from 2004 [8] and 1994 [11] are also included. In case of the EFT results we show the variation with the cutoff. These are comparable for U_Λ at LO and NLO, but noticeably reduced for U_Σ at NLO. The predictions for $U_\Lambda(0)$ are well in line with the 'empirical' value for the Λ binding energy in nuclear matter of about -27 to -30 MeV, deduced from the binding energies of finite Λ hypernuclei [12].

As already emphasized in Ref. [2] the interaction in the ${}^3S_1$ partial wave of the $\Sigma^+ p$ channel is repulsive, for the LO potential but also for the NLO interaction. As a consequence the predicted Σ s.p. potential is likewise repulsive, see Table 3. Such a repulsion is in accordance with evidence from the analysis of level shifts and widths of Σ^- atoms and from recently measured (π^-, K^+) inclusive spectra related to Σ^--formation in heavy nuclei [13, 14].

Table 1: Results for the s.p. potentials $U_\Lambda(0)$ and $U_\Sigma(0)$ (in MeV) based on our EFT interactions and the Jülich meson-exchange interactions.

	EFT LO	EFT NLO	Jülich '04 [8]	Jülich '94 [11]
Λ [MeV]	$550 \cdots 700$	$500 \cdots 650$		
$U_\Lambda(0)$	$-38.0 \cdots -34.4$	$-29.3 \cdots -22.9$	-51.2	-29.8
$U_\Sigma(0)$	$28.0 \cdots 11.1$	$17.4 \cdots 12.1$	-22.2	-71.45

4 Summary

Chiral effective field theory, successfully applied in Ref. [7] to the NN interaction, also works well for the baryon-baryon interactions in the strangeness sector [2, 15, 16]. In particular, the results for the YN interaction presented here, obtained to next-to-leading order in the Weinberg counting, are very encouraging. First there is a visible improvement in the quantitative reproduction of the available data on ΛN and ΣN scattering and, secondly, the dependence on the regularization scheme is strongly reduced as compared to the LO result. Indeed the description of the YN system achieved at NLO is now on the same level of quality as the one by the most advanced meson-exchange YN interactions.

Acknowledgements

I would like to thank N. Kaiser, U.-G. Meißner, A. Nogga, S. Petschauer, and W. Weise for collaborating on the topics covered by my talk. Work supported in part by DFG and NSFC (CRC 110).

References

[1] S. Weinberg, Phys. Lett. B **251** (1990) 288.
[2] J. Haidenbauer, S. Petschauer, N. Kaiser, U.-G. Meißner, A. Nogga, W. Weise, Nucl. Phys. A **915** 24 (2013).
[3] H. Polinder, J. Haidenbauer, U.-G. Meißner, Nucl. Phys. A **779** 244 (2006).
[4] J. Haidenbauer, U.-G. Meißner, A. Nogga, H. Polinder, Lect. Notes Phys. **724** 113 (2007).
[5] S. Petschauer, N. Kaiser, Nucl. Phys. A **916** 1 (2013).
[6] C.M. Vincent, S.C. Phatak, Phys. Rev. C **10** 391 (1974).
[7] E. Epelbaum, W. Glöckle, U.-G. Meißner, Nucl. Phys. A **747** 362 (2005).
[8] J. Haidenbauer, U.-G. Meißner, Phys. Rev. C **72** 044005 (2005).
[9] A. Nogga, Few Body Syst. **55**, 757 (2014).
[10] J. Haidenbauer, U.-G. Meißner, Nucl. Phys. A **936** 29 (2015).
[11] A. Reuber, K. Holinde, J. Speth, Nucl. Phys. A **570** 543 (1994).
[12] D.J. Millener, C.B. Dover, A. Gal, Phys. Rev. C **38** 2700 (1988).
[13] M. Kohno, Y. Fujiwara, Y. Watanabe, K. Ogata and M. Kawai, Phys. Rev. C **74** 064613 (2006).
[14] J. Dabrowski and J. Rozynek, Phys. Rev. C **78** 037601 (2008).
[15] H. Polinder, J. Haidenbauer, U.-G. Meißner, Phys. Lett. B **653** 29 (2007).
[16] J. Haidenbauer, U.-G. Meißner, Phys. Lett. B **684** 275 (2010).

Strangeness in the Universe? Advances and perspectives in the low-energy kaon-nucleon/nuclei interaction studies at the DAΦNE collider

C. Curceanu[1], *M. Bazzi*[1], *G. Beer*[2], *C. Berucci*[1,3], *D. Bosnar*[4], *A.M. Bragadireanu*[1,5], *M. Cargnelli*[3], *A. d'Uffizi*[1], *L. Fabietti*[6], *C. Fiorini*[7,8], *F. Ghio*[9], *C. Guaraldo*[1], *R.S. Hayano*[10], *M.Iliescu*[1], *T. Ishiwatari*[3], *M. Iwasaki*[11], *P. Levi Sandri*[1], *J. Marton*[3], *S. Okada*[11], *D. Pietreanu*[1,5], *K. Piscicchia*[1], *M. Poli Lener*[1], *T. Ponta*[5], *R. Quaglia*[7,8], *A. Romero Vidal*[12], *E. Sbardella*[1], *F Schembari*[7,8], *A. Scordo*[1], *H. Shi*[3], *D.L. Sirghi*[1,5], *F. Sirghi*[1,5], *H. Tatsuno*[11], *I. Tucakovic*[1], *O. Vazquez Doce*[6], *E. Widmann*[3], *J. Zmeskal*[3]

[1]INFN, Laboratori Nazionali di Frascati, Via Enrico Fermi 40, I-00044, Frascati (Roma), Italy
[2]Department of Physics and Astronomy, University of Victoria, Victoria, BC, Canada
[3]Stefan-Meyer-Institut für subatomare Physik, Vienna, Austria
[4]University of Zagreb, Zagreb, Croatia
[5]Horia Hulubei National Institute of Physics and Nuclear Engineering, Magurele, Romania
[6]Excellence Cluster Universe, Technische Universität München, Garching, Germany
[7]Politecnico di Milano, Dipartimento di Elettronica, Informazione e Bioingegneria, Milano, Italy
[8]INFN Sezione di Milano, Milano, Italy
[9]INFN Sezione di Roma I and Istituto Superiore di Sanità, Roma, Italy
[10]The University of Tokyo, Tokyo, Japan
[11]RIKEN, The Institute of Physics and Chemestry Research, Saitama, Japan
[12]University of Santiago de Compostela, Santiago de Compostela, Spain

DOI: http://dx.doi.org/10.3204/DESY-PROC-2014-04/21

The DAΦNE electron-positron collider at the Laboratori Nazionali di Frascati of INFN, Italy, has made available a unique quality low-energy negatively charged "kaons beam", which is used to study the kaon-nucleon/nuclei interactions at low energies, by the SIDDHARTA and AMADEUS collaborations. SIDDHARTA has already performed unprecedented precision measurements of kaonic atoms, and is being presently upgraded, as SIDDHARTA-2, to approach new frontiers. The AMADEUS experiment plans to perform in the coming years precision kaon-nuclei interactions at low-energies measurements, to study the possible formation of kaonic nuclei and of the $\Lambda(1405)$ and many other processes involving strangeness. These studies have implications going from particle and nuclear physics to astrophysics, helping to understand the role of strangeness in the Universe.

1 Low energy kaon-nucleon/nuclei studies at DAΦNE

The recently upgraded DAΦNE [1, 2] electron-positron collider at the Frascati National Laboratory of INFN produces the ϕ-resonance, which decays with a probability of about 50% in $K^+ K^-$, providing an excellent quality low-energy kaon "beam". This beam is intensively used for the study of the low-energy kaon-nucleon/nuclei interactions, a field still lacking experimental data. By making use of this beam, in 2009 the SIDDHARTA (SIlicon Drift Detector for Hadronic Atom Research by Timing Application) experiment performed a precision measurement of the strong interaction induced energy shift and width of the 1s level, via the measurement of the X-ray transitions of kaonic hydrogen, and high precision measurements of the kaonic helium3 and 4 X-ray transitions to the 2p level. The first exploratory measurement of kaonic deuterium was performed too. SIDDHARTA-2, a major upgrade of SIDDHARTA, presently under preparation, will measure the kaonic deuterium transitions to the 1s level. The final goal is to extract, for the first time, the isospin-dependent antikaon-nucleon scattering lengths, fundamental quantities to understand the chiral symmetry breaking mechanism. The AMADEUS (Antikaon Matter at DAΦNE: an Experiment with Unraveling Spectroscopy) experiment will perform the first complete study of the low-energy kaon-nuclei interactions by using a series of cryogenic gaseous targets, as d, ^{3}He, ^{4}He , 4He, and solid targets.

Among the aims of AMADEUS there are: the measurement of the $\Lambda(1405)$ decaying to Σ π in all possible charge combinations, and to give a definite answer to the debated question of the existence of the kaonic nuclei. If such states exist we will measure their properties (binding energies, width and decay channels). Presently, as a first step towards AMADEUS realization, we are analyzing the 2004-2005 KLOE data.

2 The SIDDHARTA and SIDDHARTA-2 experiments

In the SIDDHARTA experiment the monochromatic low-energy charged kaons produced at the DAΦNE collider are degraded in energy and stopped in a cryogenic gaseous target, where kaonic atoms are efficiently produced. An important element of the apparatus is the charged kaon trigger, which is based on the coincidence of the signals from two plastic scintillation counters mounted top and bottom of the e^+ e^- interaction point. The trigger system takes advantage of the back-to-back topology of the produced low-energy kaons: $\Phi \rightarrow K^+ K^-$ and its use drastically increases the signal-to-background ratio, because most of the background is generated by non interacting e^+ and e^- beam particles, uncorrelated in time with the collisions.

The kaons which are stopped inside the target produce highly excited kaonic atoms which deexcite to the fundamental level, emitting X rays. These X rays were detected by 144 Silicon Drift X-ray Detectors (SDDs) mounted around the target. A detailed description of the experimental setup is given in Ref. [3]. The setup was installed above the electron-positron interaction point at the DAΦNE collider in 2009. The following measurements were performed:

- kaonic hydrogen X-ray transitions to the 1s level, the most precise measurement ever [3];
- kaonic helium4 transitions to the 2p level, the first measurement using a gaseous target [3, 4];
- kaonic helium3 transitions to the 2p level, the first measurement ever [5, 6];
- kaonic deuterium X-ray transitions to the 1s level - as an exploratory measurement [7].

The 1s-state strong-interaction shift ϵ and width Γ of kaonic hydrogen were determined to be: $\epsilon = -283 \pm 36(\text{stat}) \pm 6(\text{syst})$ eV and $\Gamma = 541 \pm 89(\text{stat}) \pm 22(\text{syst})$ eV.

These are the most precise results ever compared to the previous measurements [8, 9]. The values of ϵ and Γ are consistent with the theoretical predictions [10]. The SIDDHARTA results allow the most precise evaluation of the K^-p scattering length, which yields strong constraints on the theoretical description of the low-energy antikaon-nucleon interactions [11, 12, 13]. For a more complete study of the isospin dependent antikaon-nucleon interaction, the measurement of the shift and width of kaonic-deuterium 1s state is mandatory. Presently, a major upgrade of the apparatus, SIDDHARTA-2, is undergoing. The upgrade is going to improve the signal/background ratio by a factor about 20 in order to perform the measurement of kaonic deuterium X-ray transitions to the 1s level and of other types of kaonic atoms transitions [14]

3 The AMADEUS experiment

The low-energy ($p \leq 100$ MeV/c) kaon-nuclei interaction studies represent the main aim of the AMADEUS experiment [15, 16]. These type of measurements require detecting all charged and neutral particles coming from the K^- interactions with various targets with an almost 4π acceptance. The AMADEUS collaboration plans to implement the existent KLOE detector [17, 18] in the free internal region between the beam pipe and the Drift Chamber inner wall (having a diameter of 50 cm) with a dedicated setup. The dedicated setup includes: the target, which can be either solid or a gaseous cryogenic one, a tracker system (TPC-GEM) and a trigger (scintillating fibers read by SiPM detectors). The negatively charged kaons may stop inside the target or interact at low energies, initiating a series of processes. Among these, a key-role is played by the generation of $\Lambda(1405)$ which can decay into $\Sigma^0\ \pi^0$, $\Sigma^+\ \pi^-$ or $\Sigma^-\pi^+$ We plan to study all these three channels in the same data sample. We plan as well to verify the possible existence of "kaonic nuclear cluster" by studying the Λp and Λd channels. Many other kaon-nuclei processes will be investigated, either for the first time, or in order to obtain more accurate results than those actually reported in literature. In the summer of 2012 a half cylinder carbon target was built and installed inside the Drift Chamber of KLOE as a first step towards the AMADEUS realization. The target thickness was optimized to have a maximum of stopped kaons (about 24% of generated) without degrading too much the energy of resulting charged particles inside the target material. The experiment run from October to the end of 2012. The analysis of these data is ongoing; it will provide new insights in the low-energy interactions of charged kaons in the nuclear matter.

4 Conclusions

The DAΦNE collider delivers an excellent quality low-energy charged kaons beam. Such a beam was intensively used by the SIDDHARTA collaboration to perform unique quality measurements of kaonic atoms (kaonic hydrogen and kaonic helium). SIDDHARTA-2 will perform the kaonic deuterium and other types of kaonic atoms transitions measurements in the near future. The kaonic-nuclei interactions at low-energies are being investigated by the AMADEUS collaboration to search for the possible formation and decay of "kaonic nuclear cluster" and of yet un-measured kaon-nuclei low-energy processes. SIDDHARTA, SIDDHARTA(-2) and AMADEUS are and will continue to provide unique quality results, which will help to understand the role of strangeness in the Universe.

Acknowledgments

We thank C.Capoccia, G.Corradi, B.Dulach and D.Tagnani from LNF-INFN and H.Schneider, L.Stohwasser and D.Stückler from Stefan-Meyer-Institut for their fundamental contribution in designing and building the SIDDHARTA setup. We thank the DAΦNE staff for the great working conditions and permanent support. Part of this work was supported by Hadron Physics I3 FP6 European Community program, Contract No.RII3 CT-2004-506078; the European Community-Research Infrastructure Integrating Activity Study of Strongly Interacting Matter (Hadron Physics 2, Grant Agreement No.227431 and HadronPhysics 3, Contract No.283286 under the Seventh Framework Programme of EU); Austrian Federal Ministry of Science and Research BMBWK 650962/0001 VI/2/2009; Romanian National Authority for Scientific Research,Contract No.2-CeX 06-11-11/2006; the Grant in-Aid for Specially Promoted Research (20002003), MEXT, Japan; the Austrian Science Fund (FWF):[P20651-N20]; the DFG Excellence Cluster Universe of the Technische Universität München and the Croatian Science Foundation under Project No. 1680

References

[1] C. Milardi *et al.*, Int. J. Mod. Phys.**A24**, 360 (2009).

[2] M. Zobov *et al.*, Phys. Rev. Lett **104**, 174801 (2010).

[3] M. Bazzi *et al.*, Phys. Lett.**B704**, 113 (2011).

[4] M. Bazzi *et al.*, Phys. Lett. **B681**, 310 (2009).

[5] M. Bazzi *et al.*, Phys. Lett. **B714**, 40 (2012).

[6] M. Bazzi *et al.*, Phys. Lett. **B697**, 199 (2011).

[7] M. Bazzi *et al.*, Nucl. Phys.**A907**, 69 (2013).

[8] M. Iwasaki *et al.*, Phys. Rev. Lett. **78**, 3067 (1997); T.M. Ito *et al.*, Phys. Rev. **C58**, 2366 (1998).

[9] G. Beer *et al.*, DEAR Collaboration, Phys. Rev. Lett. **94**, 21230 (2005).

[10] B. Borasoy, R. Nißler, W.Weise, Phys. Rev. Lett.**94**, 213401 (2005); B. Borasoy, U.-G. Meißner, R. Nißler, Phys. Rev.**C74**, 055201 (2006).

[11] A. Cieply, E. Friedman, A. Gal, D. Gazda, J. Mares, Phys. Lett. **B702**, 402 (2011).

[12] Y. Ikeda, T. Hyodo, W. Weise, Phys. Lett. **B706**, 63 (2011).

[13] Y. Ikeda, T. Hyodo, W. Weise, Nucl. Phys. **A881**, 98 (2012).

[14] The SIDDHARTA-2 Collaboration, SIDDHARTA-2 Proposal, https://www.lnf.infn.it/committee/private/documenti/SIDDHARTA2-proposal FINAL.pdf

[15] The AMADEUS Collaboration, Letter of Intent - Study of deeply bound kaonic nuclear states at DAΦNE2, http://www.lnf.infn.it/esperimenti/siddharta/LOI AMADEUS March2006.pdf

[16] The AMADEUS Collaboration, AMADEUS Phase-1: Physics, setup and Roll-in Proposal, LNF- 07-24(IR), 2007. (http://www.lnf.infn.it/sis/preprint/pdf/getfile.php?filename=LNF-07 24(IR).pdf)

[17] M. Napolitano, Nucl. Phys. Proc. Supp. **61B**, 589 (1998); KLOE and KLOE2 Collaboration, Nucl. Phys Proc. Suppl. **B249**, 225 (2012).

[18] The AMADEUS Collaboration, Nucl. Phys. **A804**, 286 (2008).

Cascade production in antikaon reactions with protons and nuclei

V.K. Magas[1,2], *A. Feijoo*[1], *A. Ramos*[1,2]
[1]Dept. d'Estructura i Constituents de la Matèria, Universitat de Barcelona,
Martí Franquès 1, E08028 Barcelona, Spain
[2]Institut de Ciències del Cosmos, Universitat de Barcelona,
Martí Franquès 1, E08028 Barcelona, Spain

DOI: http://dx.doi.org/10.3204/DESY-PROC-2014-04/170

We study the meson-baryon interaction in S-wave in the strangeness S=-1 sector using a chiral SU(3) Lagrangian extended to next-to-leading order (NLO). Our model has 7 new parameters, coming from NLO terms in the chiral Lagrangian, which are fitted to the large set of experimental data available for different two-body channels. We pay particular attention to the $K^- p \to K\Xi$ reactions, where the effect of the NLO terms in the Lagrangian is very important. In order to improve our model in these particular channels, we take into account phenomenologically the effects of the high spin hyperonic resonances, namely $\Sigma(2030)\ \left(\frac{7}{2}^+\right)$ and $\Sigma(2250)\ \left(\frac{5}{2}^-\right)$. Finally, the developed model is applied to simulate the Ξ production in nuclei.

1 Introduction

Chiral perturbation theory (χPT) is a powerful effective theory [1] that respects the chiral symmetry of the QCD Lagrangian and describes successfully the low energy hadron phenomenology. Unitary extensions of the theory ($U\chi PT$) permit to describe hadron dynamics in the vicinity of resonances, as in the case of the $\Lambda(1405)$ baryon located only 27 MeV below the $\bar{K}N$ threshold. In the last years interest in this problem is renewed due to the availability of more precise data coming from the measurement of the energy shift and width of the 1s state in kaonic hydrogen by the SIDDHARTA collaboration [2], which has permitted to better constrain the parameters of the meson-baryon Lagrangian at next-to-leading order (NLO) [3, 4, 5, 6].

In this work we attempt a study of the meson-baryon interaction in the $S = -1$ sector, paying a especial attention to the Ξ hyperon production reactions $K^- p \to K^+ \Xi^-\,, K^0 \Xi^0$, not employed in the NLO fits of earlier works, in spite of being especially sensitive to the NLO terms of the Lagrangian since the lowest-order tree level term does not contribute. A complete approach to Ξ production reactions must also implement the effect of high-spin resonances [7, 8, 9], which we also incorporate in our fit. Finally, we explore the Ξ hyperon production reaction on several nuclei.

2 Meson-baryon amplitudes from the chiral Lagrangian at NLO

The meson-baryon interaction up to NLO can be derived from the chiral Lagrangian [1] and reads $V_{ij}^{\rm NLO} = V_{ij}^{(1)} + V_{ij}^{(2)}$ with:

$$V_{ij}^{(1)} = -\frac{C_{ij}(2\sqrt{s}-M_i-M_j)}{4f^2}\sqrt{\frac{M_i+E_i}{2M_i}}\sqrt{\frac{M_j+E_j}{2M_j}}\,, V_{ij}^{(2)} = \frac{D_{ij}-2(k_\mu k'^\mu)L_{ij}}{f^2}\sqrt{\frac{M_i+E_i}{2M_i}}\sqrt{\frac{M_j+E_j}{2M_j}}\,, \tag{1}$$

where the indices i, j run over the allowed coupled channels, which in the present $S = -1$ study are K^-p, $\bar{K}^0n$, $\pi^0\Lambda$, $\pi^0\Sigma^0$, $\pi^+\Sigma^-$, $\pi^-\Sigma^+$, $\eta\Lambda$, $\eta\Sigma^0$, $K^+\Xi^-$ and $K^0\Xi^0$, C_{ij} is a matrix of numerical coefficients, f is the pion decay constant, and D_{ij} and L_{ij} are coefficient matrices that depend on the NLO parameters: b_0, b_D, b_F, d_1, d_2, d_3, d_4. The unitarized amplitude is determined from the solution of a Bethe-Salpeter equation $T_{ij} = V_{ij} + V_{il}G_lT_{lj}$, where the loop function G_l is properly regularized using dimensional regularization and depends on a subtraction constant a_l at a given energy scale which we take here to be $\mu = 1$ GeV (see [3, 4, 5, 6, 10] for more details). Therefore, at the lowest order, the unitarized amplitudes depend on 7 parameters: the decay constant f of the Weinberg-Tomozawa term, which is taken as a free parameter to partly simulate higher-order terms, plus the loop subtraction constants which, applying isospin symmetry arguments, reduce to 6. At next-to-leading order, there are 7 additional parameters to be fitted.

We present our results in the following, very brief, way: Fig. 1 shows the $K^-p \to K^0\Xi^0$ cross section obtained from our fits; Table 1 shows the corresponding threshold branching ratios.

Let us concentrate on the left subplot of Fig. 1. The first fit we perform is a *classical* WT fit to the cross section of different channels, excluding Ξ production channels, and to the threshold branching ratios. Obviously, the results for the $K^-p \to K^0\Xi^0$ reactions are rather bad, see *WT (no Ξ channels)* dotted line. When we force our WT model to fit also the Ξ production data - *WT* dashed line - some strength is built for the $K^-p \to K^0\Xi^0$ cross section, although the agreement is far from perfect. Now if we and into the game NLO terms of the chiral Lagrangian the progress is obvious - *NLO* line. Also we would like to comment that including NLO terms we improve the agreement in all the channels although for the $K^0\Xi^0$ and $K^+\Xi^-$ ones the changes are most drastic.

3 Inclusion of high spin resonances

The shape of the $\bar{K}N \to K\Xi$ cross sections reflects that terms of the type $\bar{K}N \to Y \to K\Xi$, where Y stands for some hyperon resonance, may also come into play. From the eight three- and four-star candidates listed in the PDG, the $7/2^+$ $\Sigma(2030)$ and the $5/2^-$(estimated) $\Sigma(2250)$ seem more appropriate, according to the phenomenological model of [8] and our previous fit [6] . As in [11, 7], we follow the Rarita-Schwinger scheme to describe the resonance fields and build up their contribution to the amplitude, which depends on four new parameters for each resonance: its mass M_R, width Γ_R, product of couplings to the initial and final states, $g_{R\bar{K}N}g_{RK\Xi}$, and a cut-off Λ_R which suppresses high-momentum contributions. The final amplitude for initial $i = K^-p, \bar{K}^0n$ and final $j = K^+\Xi^-, K^0\Xi^0$ channels reads $T_{ij} = \sqrt{4M_pM_\Xi}T_{ij} + T_{ij}^{5/2^-} + T_{ij}^{7/2^-}$.

The cross sections for the $K^-p \to K^0\Xi^0$ reaction, obtained from different fits that considers the effect of these two hyperon resonances, are shown on the right subplot of Fig. 1. The dotted

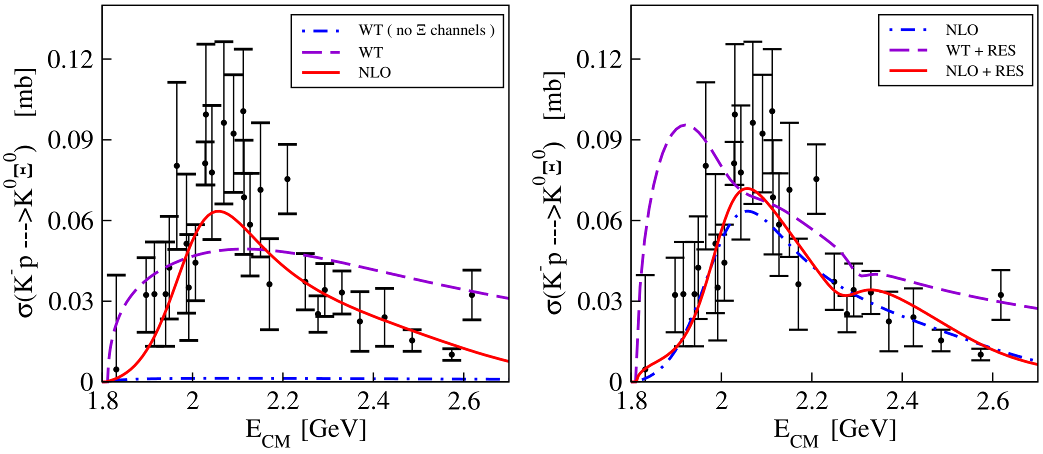

Figure 1: **Left subplot:** $K^-p \to K^0\Xi^0$ cross section as a function of the center-of-mass energy for the NLO different fits, see text for more details. **Right subplot:** $K^-p \to K^+\Xi^-$ cross section as a function of the center-of-mass energy for different fits, in particular including the contribution from high spin resonances. For both sub-figures the experimental data are taken from [12, 13, 14, 15, 16, 17, 18].

NLO line (the Ξ production data are now included in all fits) repeats the best fit without resonance contribution, i.e. it is the same as in Fig. 1A and should be used for more clear comparison. We have tried to fit the data adding the resonance terms to the WT model - *WT+Res* dashed line. Such a test clearly shows the absolute necessity of the NLO term to reproduce data on Ξ production. The full line *NLO+Res* corresponds to our best fit, where we take into account the simultaneous effect of the NLO Lagrangian and two hyperon resonances.

We note that our fit reproduces very satisfactorily all other elastic and inelastic cross sections in the $S = -1$ channel. The inclusion of resonances affect these other channels indirectly through their fine tuning effect on the parameters of the chiral Lagrangian at NLO. An example of the quality of the fit is shown in Table 1, where the threshold branching ratios between several channels are shown for different fitting schemes.

Table 1: Threshold branching ratios for different fitting schemes:

Model	γ	R_n	R_c
WT (no Ξ)	2.34	0.185	0.665
WT	2.30	0.185	0.665
NLO	2.31	0.186	0.660
WT+Res	2.48	0.202	0.667
NLO+Res	2.50	0.188	0.664
Exp. data	2.36 ±0.04	0.189 ±0.015	0.664 ±0.011

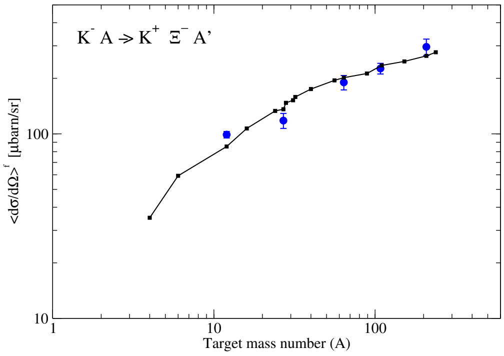

Figure 2: Cross section for Ξ hyperon production in (K^-, K^+) reaction on various nuclei [19].

4 Ξ production in nuclei

Finally, we perform an exploratory study on Ξ hyperon production in nuclei as a precursor reaction to form double-Λ hypernuclei. We employ a local density approach to describe the different nuclear targets. The propagation of antikaons before they reach the interaction point and that of the produced kaons as they leave the nucleus is taken within an eikonal approximation, which we consider to be a fair choice given the high momentum value of the incoming K^- ($p_{K^-} = 1.65$ GeV/c) and emitted K^+ ($0.95 < p_{K^+} < 1.30$ GeV/c; $1.7^\circ < \Theta_{K^+,Lab} < 13.6^\circ$). Our results for the calculated Ξ production cross section on several nuclei are shown by the square symbols joined by the solid line in Fig. 2. We obtain a good agreement with data [19], a fact that stimulates us to continue our investigations focussing on the production of bound Ξ states, much in line to what other theoretical works have attempted before [20, 21, 22].

Acknowledgement

This work is supported by the European Community-Research Infrastructure Integrating Activity *Study of Strongly Interacting Matter* (HadronPhysics3, Grant Agreement 283286) under the Seventh Framework Programme, by the contract FIS2011-24154 from MICINN (Spain), and by the Generalitat de Catalunya contract 2014SGR-401.

References

[1] J. Gasser and H. Leutwyler, Nucl. Phys. **B250** 465 (1985).

[2] M. Bazzi, G. Beer, L. Bombelli, A. M. Bragadireanu, M. Cargnelli, G. Corradi, C. Curceanu (Petrascu) and A. d'Uffizi *et al.*, Phys. Lett. **B704** 113 (2011).

[3] Y. Ikeda, T. Hyodo, W. Wiese, Nucl. Phys. **A881** 98 (2012).

[4] Zhi-Hui Guo, J. A. Oller, Phys. Rev. **C87** 035202 (2013).

[5] M. Mai and U. -G. Meissner, Nucl. Phys. **A900** 51 (2013).

[6] V. K. Magas, A. Feijoo and A. Ramos, AIP Conf. Proc. **1606** 208 (2014); arXiv:1311.5025 [hep-ph]; A. Feijoo, V.K. Magas, A. Ramos, Proceedings of the 13th International Workshop on Meson Production, Properties and Interaction, Krakow, Poland (2014).

[7] K. Shing Man, Y. Oh and K. Nakayama,, Phys. Rev. **C83** 055201 (2011).

[8] D. A. Sharov, V. L. Korotkikh, D. E. Lanskoy, Eur. Phys. J. **A47** 109 (2011).

[9] B. Jackson, Y. Oh, H. Haberzettl and K. Nakayama, Phys. Rev. **C89** 025206 (2014).

[10] B. Borasoy, R. Nissler, W. Wiese, Eur. Phys. J. **A25** 79 (2005).

[11] K. Nakayama, Y. Oh and H. Habertzettl, Phys. Rev. **C74** 035205 (2006).

[12] G. Burgun *et al.*, Nucl. Phys. **B8** 447 (1968)

[13] J. R. Carlson *et al.*, Phys. Rev. **D7** 2533 (1973).

[14] P. M. Dauber *et al.*, Phys. Rev. **179** 1262 (1969).

[15] M. Haque *et al.*, Phys. Rev. **152** 1148 (1966).

[16] G. W. London *et al.*, Phys. Rev. **143** 1034 (1966).

[17] T. G. Trippe, P. E. Schlein, Phys. Rev. **158** 1334 (1967).

[18] W. P. Trower *et al.*, Phys. Rev. **170** 1207 (1968).

[19] T. Iijima *et al.*, Nucl. Phys. **A546** 588 (1992).

[20] C. B. Dover and A. Gal, Annals Phys. **146** 309 (1983).

[21] C. B. Dover, D. J. Millener and A. Gal, Nucl. Phys. **A572** 85 (1994).

[22] T. Harada, Y. Hirabayashi and A. Umeya, Phys. Lett. **B690** 363 (2010).

Energy and density dependence of the $\bar{K}N$ and ηN amplitudes near threshold

Aleš Cieplý[1], *Jaroslav Smejkal*[2]

[1]Nuclear Physics Institute, 250 68 Řež, Czech Republic
[2]Institute of Experimental and Applied Physics, Czech Technical University in Prague,
Horská 3a/22, 128 00 Praha 2, Czech Republic

DOI: http://dx.doi.org/10.3204/DESY-PROC-2014-04/102

Chirally motivated model is used to describe meson-baryon interactions at low energies. After fixing free parameters to available experimental data on reactions in the free space the model is extrapolated to subthreshold energies and to nonzero nuclear densities. The impact of nuclear matter on the elastic $\bar{K}N$ and ηN amplitudes is discussed.

1 Introduction

The modern approach to low-energy meson baryon interactions is based on chiral dynamics that implements the QCD symmetries in a nonperturbative region infested by presence of baryon resonances. There, the standard perturbation theory fails but the higher order contributions can be (at least in their major part) accounted for by using coupled channels and resummation techniques based on Lippmann-Schwinger or Bethe-Salpeter equation.

In our contribution we demonstrate the effects of nuclear medium on the $\bar{K}N$ and ηN amplitudes. We employ effective separable potentials that match the meson-baryon amplitudes up to NLO order in the chiral perturbative expansion. These potentials are then inserted into Lippmann-Schwinger equation to get the amplitudes which are then used to calculate the measurable quantities, typically cross sections or branching ratios of specific processes. The separable potentials are particularly useful for in-medium applications where the off-shell form factors provide a natural extension to account for two-body inelasticities related to many particle dynamics. This feature represents an advantage over more popular on-shell approaches based on dispersion relation for the inverse of the scattering T-matrix or on the so called N/D method.

2 The model

In the present work we consider low energy s-wave interactions of the basic 0^- meson octet (π, K, $\bar{K}$, η) with the $1/2^+$ octet of baryons (N, Λ, Σ, Ξ). The separable potential model adopted by us was invented by Kaiser, Siegel and Weise [1] who related the kernel of the Lippmann-Schwinger equation to the scattering amplitude constructed from an effective chiral Lagrangian.

The potential matrix reads as

$$V_{ij}(k,k';\sqrt{s}) = g_i(k^2)\, v_{ij}(\sqrt{s})\, g_j(k'^2) \tag{1}$$

$$v_{ij}(\sqrt{s}) = -\frac{C_{ij}(\sqrt{s})}{4\pi f_i f_j}\sqrt{\frac{M_i M_j}{s}} \tag{2}$$

where the indexes i, j run over the space of involved meson-baryon coupled channels and the off-shell form factors are taken in the Yamaguchi form, $g_j(k) = 1/[1+(k/\alpha_j)^2]$, with the inverse ranges α_j introduced as free parameters of the model. The central inter-channel couplings C_{ij} are energy dependent and determined by the chiral SU(3) symmetry, k (k') denotes the CMS meson momenta in the initial (final) state, $\sqrt{s}$ is the total CMS energy and M_j stand for baryon masses. f_j represents a meson decay constant and we allow for its different physical values f_π, f_K and f_η depending on the meson in a specific j-th channel. The transition amplitudes obtained as simple algebraical solutions of the Lippmann-Schwinger equation are also separable,

$$F_{ij}(k,k';\sqrt{s}) = g_i(k^2)\, f_{ij}(\sqrt{s})\, g_j(k'^2) \tag{3}$$

$$f_{ij}(\sqrt{s}) = \left[(1 - v\cdot G(\sqrt{s}))^{-1}\cdot v\right]_{ij} \tag{4}$$

where the Green function $G(\sqrt{s})$ is diagonal in the channel space and becomes density dependent in nuclear medium. In general, the intermediate state Green function can be written as

$$G_n(\sqrt{s},\rho) = -4\pi \int_{\Omega_n(\rho)} \frac{d^3p}{(2\pi)^3}\frac{g_n^2(p^2)}{k_n^2 - p^2 - \Pi_n(\sqrt{s},p;\rho) + \mathrm{i}0} \tag{5}$$

Here the impact of nuclear medium is twofold. Foremostly, for channels involving nucleons the Pauli exclusion principle restricts the integration space to a domain Ω_n of allowed nucleon momenta. In addition, the in-medium hadron selfenergies shift the pole of the propagator by a sum of meson and baryon selfenergies represented by the $\Pi_n(\sqrt{s},p;\rho)$ in Eq. (5). In a free space, when the integration goes over the whole momentum space and $\Pi_n(\sqrt{s},p;\rho) = 0$, the integral has an analytical form while in nuclear matter the integration has to be performed numerically. Normally, one also constructs the meson selfenergies from the in-medium meson-baryon amplitudes, so a selfconsistent treatment is required (see Ref. [2] for details).

The model was successfully applied to describe the available low energy experimental data for K^-p reactions including the recent precise measurement of the kaonic hydrogen characteristics by the SIDDHARTA collaboration. Later on, the same methodology was used to describe the data on πN scattering and $\pi p \longrightarrow \eta n$ reaction. We refer the reader to our previous publications [3] and [4] for the details of the fitting procedure, the quality of the fits, and for all other relevant information including references to the experimental data. In general, the quality of the fits in the $\bar{K}N$ sector is quite good when only the TW term is accounted for while the inclusion of higher order NLO contributions is mandatory to achieve realistic description of the experimental data in the $\pi N - \eta N$ sector.

3 $\bar{K}N$ and ηN amplitudes

In Figure 1 we demonstrate the impact of nuclear medium on the elastic K^-p amplitude as obtained with the NLO30 model from Ref. [3]. The energy dependence of the amplitude in vacuum (shown by the dotted lines) is clearly affected by the presence of the $\Lambda(1405)$ resonance with a peak of the imaginary part $\Im F_{K^-p}$ located around 1400 MeV. We note in passing that the NLO30 model generates poles of the amplitude at energies $z_{\bar{K}N}$ = (1418 – i44) MeV and $z_{\pi\Sigma}$ = (1355 – i86) MeV, so the peak and poles positions are not trivially related. The Pauli blocking shifts the $\Lambda(1405)$ structure above the $\bar{K}N$ threshold and the resonance is partially dissolved in nuclear matter. However, the incorporation of hadron selfenergies has an opposing effect moving the structure back below the threshold and leading to a rapid increase of attraction in the real part of the amplitude for energies about 30 MeV below the $\bar{K}N$ threshold. Since the K^-n amplitude is much smaller in magnitude and its energy dependence is not so profound, the overall effect on K^- propagation in nuclear matter is as follows. While antikaon feels a moderate attraction at energies around and above the threshold much larger attraction is anticipated at subthreshold energies. This result is in line with phenomenological analysis of kaonic atoms, though even more attraction is required by the data, apparently due to $\bar{K}NN$ absorption [5].

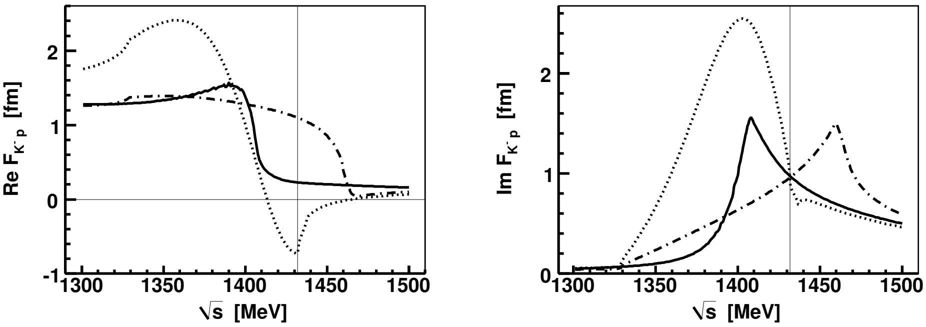

Figure 1: Energy dependence of the real (left panel) and imaginary (right panel) parts of the K^-p amplitude generated with the NLO30 model of Ref. [3]. The dotted lines show the free-space amplitude, the dot-dashed lines demostrate the effect of Pauli blocking and the dashed lines show the combined effect of Pauli blocking and hadron selfenergies. The $\bar{K}N$ threshold is marked by the thin vertical line.

While the subthreshold energy dependence of the $\bar{K}N$ amplitude is strongly affected by nuclear medium, the effect on the ηN amplitude is much less profound at least at subthreshold energies. This can be seen in Fig. 2 where the impacts of Pauli blocking and hadron selfenergies are visualized. The peak structure observed in the figure can be assigned to the $N^*(1535)$ resonance generated dynamically by the model. It is shifted to higher energies due to Pauli blocking and made more pronounced. The implementation of hadron selfenergies spreads the resonance structure over a large interval of energies and it practically dissolves in the nuclear matter. The main difference with respect to the $\bar{K}N$ case may be related to a different origin of the dynamically generated resonances. While the $\Lambda(1405)$ results from a quasi-bound $\bar{K}N$ molecular state the $N^*(1535)$ originates from a virtual $K\Xi$ state that is shifted to much lower energies by inter-channel dynamics. In effect, the in-medium dynamics of the $N^*(1535)$ resonance is not so strongly correlated with the ηN system as it is in the $\bar{K}N$ sector. Still, the ηN scattering length is reduced from $a_{\eta N}$ = (0.65 + i0.15) fm in a free space to about $a_{\eta N}$ = (0.35 + i0.13) fm in nuclear matter. This results into a sizeable reduction of η-nuclear attraction at the ηN threshold. However, the effect is much smaller at energies about 20-30

MeV below the threshold that are relevant for a possible existence of η-nuclear bound states.

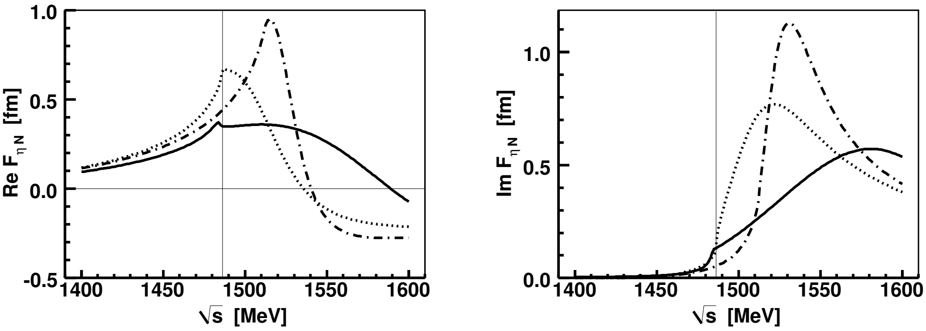

Figure 2: Energy dependence of the real (left panel) and imaginary (right panel) parts of the ηN amplitude obtained with the NLO30$_\eta$ model from Ref. [4]. The dotted lines show the free-space amplitude, the dot-dashed lines demostrate the effect of Pauli blocking and the dashed lines show the combined effect of Pauli blocking and hadron selfenergies. The ηN threshold is marked by the thin vertical line.

4 Summary

We have looked at an impact of nuclear medium on the energy dependence of the $\bar{K}N$ and ηN amplitudes. The most striking feature of the in-medium $\bar{K}N$ amplitude is represented by a sharp increase of the $\bar{K}N$ attraction at energies about $30-40$ MeV below the threshold. As it was shown in Refs. [2], [5] an anticipated energy shift from threshold to subthreshold $\bar{K}N$ energies provides a link between the shallow $\bar{K}$-nuclear optical potentials obtained microscopically from threshold $\bar{K}N$ interactions and the phenomenological deep ones deduced from kaonic atoms data. On the contrary, the ηN attraction is reduced in nuclear matter, both by the Pauli blocking and by the hadron selfenergies. Nevertheless, the subthreshold energy region is affected only moderately and it was shown in [6] that the in-medium ηN attraction appears sufficient to bind the η mesons in nuclei.

Acknowledgments

The work of A. C. was supported by the Grant Agency of Czech Republic, Grant No. P203/12/2126.

References

[1] N. Kaiser, P. B. Siegel, W. Weise, Nucl. Phys. **A594** 325 (1995).
[2] A. Cieplý, E. Friedman, A. Gal, D. Gazda, J. Mareš, Phys. Rev. **C84** 045206 (2011).
[3] A. Cieplý, J. Smejkal, Nucl. Phys. **A881** 115 (2012).
[4] A. Cieplý, J. Smejkal, Nucl. Phys. **A919** 46 (2013).
[5] E. Friedman, A. Gal, Nucl. Phys. **A881** 150 (2012).
[6] A. Cieplý, E. Friedman, A. Gal, J. Mareš, Nucl. Phys. **A925** 126 (2014).

Search for a $\pi\Lambda N - \pi\Sigma N$ dibaryon in p+p@3.5 GeV

J.C. Berger-Chen[1,2], *L. Fabbietti*[1,2] for the HADES Collaboration

[1]Physik Department E12, Technische Universität München, 85748 Garching, Germany
[2]Excellence Cluster 'Origin and Structure of the Universe', 85748 Garching, Germany

DOI: http://dx.doi.org/10.3204/DESY-PROC-2014-04/101

This work is dedicated to the search for a $\pi\Lambda N - \pi\Sigma N$ resonance $\mathcal{Y}$ with the quantum numbers $(Y, I, J^P) = (1, \frac{3}{2}, 2^+)$. The double charged $\Sigma(1385)N - \Delta(1232)Y$ quasibound state was looked for in the reaction $pp \to \mathcal{Y}^{++}K^0$ with its unique decay into Σ^+ and proton measured with the HADES setup at a kinetic beam energy of 3.5 GeV. The analysis including background determination and a description of the data with a K^0_S Monte Carlo cocktail are presented.

1 Introduction

Recently, a relativistic three-body Fadeev formalism suitable for two-body p-wave interactions was applied to calculate the $\pi\Lambda N - \pi\Sigma N$ coupled channel system with $I = \frac{3}{2}$ and $J^P = 2^+$ [1]. Dominant p-wave interactions in the πN and $\pi\Lambda - \pi\Sigma$ channels were found with a large contribution of the $\Delta(1232)$ and $\Sigma(1385)$ resonances. A rather robust $\pi\Lambda N$ resonance located around 10-20 MeV/c^2 below the $\pi\Sigma N$ threshold was obtained, which can be viewed as an s-wave dibaryon $\mathcal{Y}$ with $(Y, I, J^P) = (1, \frac{3}{2}, 2^+)$ equivalent to an $\Sigma(1385)N - \Delta(1232)Y$ quasibound state bound by over 50 MeV. The double charged state can be uniquely measured in p+p collisions at energies above the $\Sigma(1385)$ production threshold ($pp \to \mathcal{Y}^{++}K^0 \to \Sigma^+ pK^0$), whereas the $\mathcal{Y}^+$ formed together with a K^+ ($\mathcal{Y}^+ \to \Sigma^+ n/\Sigma^0 p$) may not be distinguishable from the decay of a $\bar{K}NN$ quasibound state ($K^- pp \to \Sigma^+ n/\Sigma^0 p$). Thus, the HADES p+p data measured at 3.5 GeV, which is well above $\Sigma(1385)$ production threshold [2], are perfectly suited to search for the $\mathcal{Y}^{++}$ dibaryon in its unique decay. Thereby, knowledge gained by a previous analysis [3] on exclusive K^0 production channels in the same data set were incorporated meaning that the determined cross sections and angular anisotropies were included in this work. The main result of that analysis was the finding of predominant contributions by K^0 channels associated with resonances ($\Delta(1232)$ and $\Sigma(1385)$) thus confirming earlier observations made in the study of resonance contributions ($\Lambda(1405)$, $\Sigma(1385)^0$, $\Lambda(1520)$, $\Delta(1232)$, N^*, K^{*0}) to the $\Sigma^\pm\pi^\pm pK^+$ final states [4].

2 The HADES experiment

The **H**igh-**A**cceptance **Di**-**E**lectron **S**pectrometer (HADES) [5] is a versatile detector system located at GSI Helmholtzzentrum (Darmstadt, Germany) and is provided by the SIS18 with heavy ion beams of 1-2 AGeV or proton beams up to 3.5 GeV impinging on a fixed target. The

HADES setup has an azimuthal coverage of 85% and an acceptance in polar angles from 18° to 85°. The momentum resolution was determined to be $\Delta p/p \approx 3\%$.

The most important detector components used in the presented analysis are first of all the Multi-Wire Drift Chambers (MDCs), where two layers are mounted in front of the superconducting magnet with a toroidal field and two layers behind it to help in track finding, momentum reconstruction and particle identification via the specific energy loss information. Furthermore, a Time-Of-Flight wall at the end of the setup allows for online multiplicity triggering to enhance inelastic events in the recorded data sample.

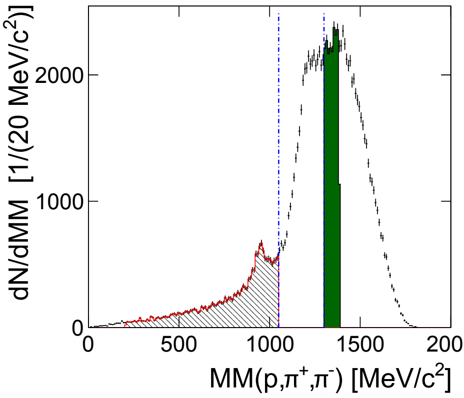

Figure 1: Missing mass spectrum with respect to the proton, π^+ and π^-. The red-hatched and green-filled areas indicate the mass regions used for the low mass (LM) and the high mass (HM) sideband sample. The blue dash-dotted lines show the cut on the Σ^+ mass.

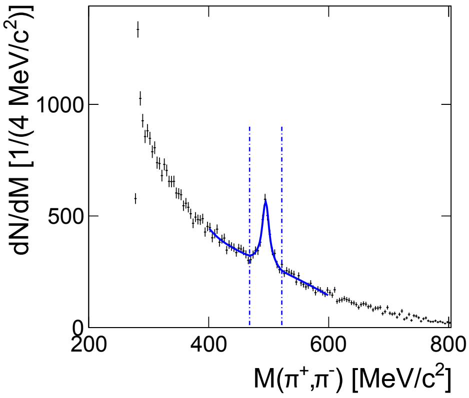

Figure 2: $\pi^+\pi^-$-invariant mass spectrum including secondary vertex cuts [3] and fitted with the sum of two Gaussians, a Landau and a polynomial. The blue dash-dotted lines indicate the 3σ-cut region on the K^0_S mass.

3 The analysis and preliminary results

As mentioned above the $\pi\Lambda N - \pi\Sigma N$ resonance, which can be denoted as $\mathcal{Y}$, can be uniquely measured through the reaction $pp \rightarrow \mathcal{Y}^{++}K^0 \rightarrow \Sigma^+ p K^0$. Since the long-lived K^0_L cannot be detected by the HADES setup, this analysis concentrates on the short-lived K^0_S and its charged decay into π^+ and π^- ($BR \approx 69.20\%$). A four particle selection was implemented to enhance the above reaction by choosing events with a proton, π^+, π^+ and a π^-. The proton is thereby assumed to be produced directly, whereas one of the π^+ should originate from the decay of the Σ^+. This way, only the decay of the Σ^+ into a neutron and a π^+ ($BR \approx 48.31\%$) was considered neglecting the branching into proton and π^0 ($BR \approx 51.57\%$), since the heavier baryon is more likely to be boosted into the forward region, where HADES has no acceptance.

3.1 Background determination

The background determination in the four particle data sample is a crucial step in this analysis and consists mainly of combinatorial background generated by non-strange reactions. Contri-

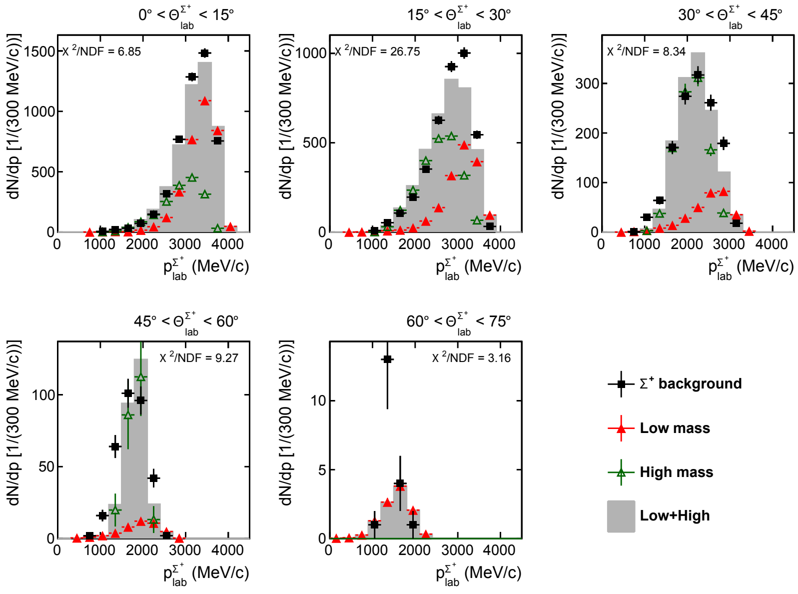

Figure 3: Momentum distribution of the Σ^+ background in five bins of $\Theta^{\Sigma^+}_{lab}$ with the cuts: MM(p,π^+,π^-) = 1050-1300 MeV/c^2 and 810 MeV/c^2 > MM(p,π^+,π^+,π^-) > 1045 MeV/c^2. Overlayed are the spectra for the LM and HM sideband samples with their sum in gray.

butions from other K^0_S production channels can be modeled in a first attempt by an incoherent Monte Carlo cocktail, which individual cross sections were obtained in a separate analysis of the same data set [3]. To emulate the background, a so-called sideband analysis was performed on the missing mass distribution to the proton, π^+ and π^- (Fig. 1). Only a rough cut on the primary vertex was applied here to reject off-target events. Furthermore, no additional mass cut, e.g. on the K^0_S, was applied to keep enough statistics for the sideband analysis. A data sample was defined in this spectrum, which contains data with missing masses lower (LM) and higher (HM) than the Σ^+ (1050 MeV/c^2 > MM(p,π^+,π^-) > 1300 MeV/c^2) and thus include only background. They are indicated as red-hatched and green-filled areas in the plot and are chosen such to have about the same integral. This background sample needs to reproduce the kinematics, which remains in the Σ^+ mass region. Therefore, the momentum distributions of the sideband samples LM and HM were fitted in five individual Θ_{lab} bins to describe the momentum distribution of a Σ^+ background sample, which was obtained through a cut on the missing mass spectrum to the four particles proton, π^+, π^+ and π^- (810 MeV/c^2 > MM(p,π^+,π^+,π^-) > 1045 MeV/c^2). From the exclusive analysis discussed in [3] it is known that the reaction $pp \rightarrow \Sigma^+ p K^0_S$ does not contribute in these mass regimes. Figure 3 shows the mentioned momentum distributions of Σ^+ candidates and quotes the achieved χ^2/NDF for each Θ_{lab} bin, which mostly stays below 10 except for $\Theta_{lab} = 15° - 30°$ with $\chi^2/NDF = 26.75$. The conclusion is, that the sideband sample does not fully describe the Σ^+ background and further work is necessary here. However, the description is good enough to use the so determined relative contributions of the LM and HM samples to the full background model for a first try to search for a signal of the $\mathcal{Y}^{++}$ dibaryon, which should be located around 10-20 MeV/c^2 below the $\pi\Sigma N$ threshold (2267 MeV/c^2) [1].

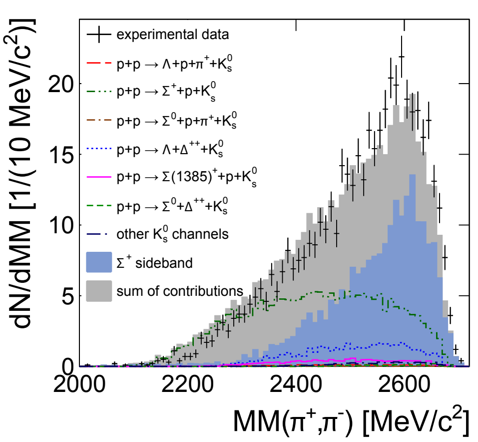

Figure 4: Missing mass spectrum with respect to the π^+ and π^- with a cut on the K^0_S and the Σ^+ mass. The contributions of the K^0_S reactions are according to the findings of [3].

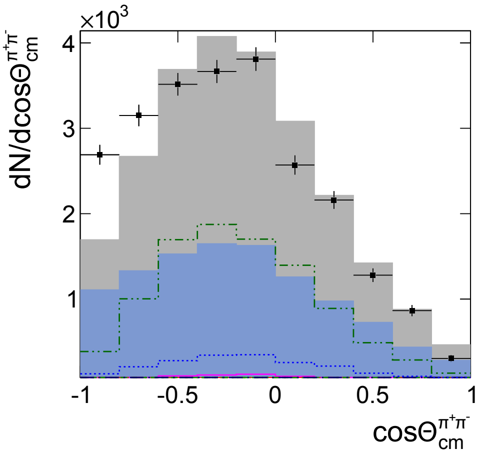

Figure 5: Angular distribution of the $\pi^+\pi^-$-system in the center-of-mass with a cut on the K^0_S and on the Σ^+ mass. The color code is the same as written in the label of Figure 4.

3.2 Preliminary results

In Figure 4 the MM(π^+,π^-) distribution is depicted, which contains a cut on the Σ^+ mass (1050 MeV/c^2 < MM(p,π^+,π^-) < 1300 MeV/c^2) and a 3σ-cut on the K^0_S mass determined in the $\pi^+\pi^-$-invariant mass distribution (Fig. 2) by a fit with a sum of two Gaussians for the signal and a Landau plus a polynomial function for the background. However, no enhancement is seen in the interesting region below the $\pi\Sigma N$ threshold. The missing mass spectrum is rather well described by the incoherent K^0_S cocktail determined in [3] and the background model, from which the relative contribution was obtained by a simultaneous fit to this missing mass spectrum and the $\pi^+\pi^-$-angular distribution $cos\Theta^{\pi^+\pi^-}_{cm}$ (Fig. 5) with fixed cross sections and angular anisotropies for the K^0_S reactions. Although the χ^2/NDF extracted from the simultaneous fit to the two spectra of 5.07 is rather good, some disagreement between model and data is observed at $cos\Theta^{\pi^+\pi^-}_{cm} < -0.5$, which can be due to the imperfect background model.

4 Summary and outlook

The $\pi\Lambda N - \pi\Sigma N$ resonance $\mathcal{Y}$ with $(Y, I, J^P) = (1,\frac{3}{2},2^+)$ was searched for in the reaction $pp \to \mathcal{Y}^{++}K^0 \to \Sigma^+ pK^0 \to n\pi^+ pK^0$. Thereby, a sideband analysis was performed to model the Σ^+ background in the distribution MM(p, π^+, π^-). A satisfactory description was achieved to use this background model in the further study of the missing mass spectrum MM(π^+, π^-) with help of the K^0_S reaction cocktail determined in [3]. No obvious enhancement is seen in the MM(π^+, π^-) below the $\pi\Sigma N$ threshold, in fact the data is described rather well by the model. However, no interference effects were taken into account, which can be only studied with help of a Partial Wave Analysis (PWA) similar as for the search of the K^-pp quasibound state in the same data set [6].

Acknowledgements

The authors gratefully acknowledge the support of the TUM Graduate School's Faculty Graduate Center Physics at Technische Universität München, Germany, PTDC/FIS/113339/2009 LIP Coimbra, NCN grant 2013/10/M/ST2/00042 SIP JUC Cracow, Helmholtz Alliance HA216/EMMI GSI Darmstadt, VH-NG-823, Helmholtz Alliance HA216/EMMI TU Darmstadt, 283286, 05P12CRGHE HZDR Dresden, Helmholtz Alliance HA216/EMMI, HIC for FAIR (LOEWE), GSI F&E Goethe-University, Frankfurt VH-NG-330, BMBF 06MT7180 TU München, Garching BMBF:05P12RGGHM JLU Giessen, Giessen UCY/3411-23100, University Cyprus CNRS/IN2P3, IPN Orsay, Orsay MSMT LG 12007, AS CR M100481202, GACR 13-06759S NPI AS CR, Rez, EU Contract No. HP3-283286.

References

[1] H. Garcilazo and A. Gal. Relativistic three-body calculations of a Y=1, I=3/2, JP=2+ $\pi\Lambda N$ – $\pi\Sigma N$ dibaryon. *Nucl. Phys.*, A897:167–178, 2013.

[2] G. Agakishiev et al. Baryonic resonances close to the $\bar{K}$-N threshold: The Case of $\Sigma(1385)^+$ in pp collisions. *Phys. Rev.*, C85:035203, 2012.

[3] G. Agakishiev et al. Associate K^0 production in p+p collisions at 3.5 GeV: The role of $\Delta(1232)^{++}$. *Phys. Rev.*, C90:015202, 2014.

[4] G. Agakishiev et al. Production of $\Sigma^{\pm}\pi^{\pm}pK^+$ in p+p reactions at 3.5 GeV beam energy. *Nucl. Phys.*, A881:178–186, 2012.

[5] G. Agakishiev et al. The High-Acceptance Dielectron Spectrometer HADES. *Eur. Phys. J.*, A41:243–277, 2009.

[6] E. Epple. Experimental news from a theoretical state: The 'ppK^-'. *PoS*, BORMIO2014:049, 2014.

η' mesic nucleus spectroscopy with (p, d) reaction at GSI

Yoshiki K. Tanaka[1], *Yassid Ayyad*[2], *Jose Benlliure*[3], *Kai-Thomas Brinkmann*[4], *Stefan Friedrich*[4], *Hiroyuki Fujioka*[5], *Hans Geissel*[4,6], *Jnaneswari Gellanki*[7], *Chenlei Guo*[8], *Eric Gutz*[4], *Emma Haettner*[6], *Muhsin N. Harakeh*[7], *Ryugo S. Hayano*[1], *Yuko Higashi*[9], *Satoru Hirenzaki*[9], *Christine Hornung*[4], *Yoichi Igarashi*[10], *Natsumi Ikeno*[11,12], *Kenta Itahashi*[13], *Masahiko Iwasaki*[13], *Daisuke Jido*[14], *Nasser Kalantar-Nayestanaki*[7], *Rituparna Kanungo*[15], *Ronja Knoebel*[4,6], *Nikolaus Kurz*[6], *Volker Metag*[4], *Ivan Mukha*[6], *Tomofumi Nagae*[5], *Hideko Nagahiro*[9], *Mariana Nanova*[4], *Takahiro Nishi*[1], *Hooi Jin Ong*[2], *Stephane Pietri*[6], *Andrej Prochazka*[6], *Christophe Rappold*[6], *Moritz P. Reiter*[6], *Jose Luis Rodríguez Sánchez*[3], *Christoph Scheidenberger*[4,6], *Haik Simon*[6], *Branislav Sitar*[16], *Peter Strmen*[16], *Bao-hua Sun*[8], *Ken Suzuki*[17], *Imrich Szarka*[16], *Maya Takechi*[18], *Isao Tanihata*[2,8], *Satoru Terashima*[8], *Yuni N. Watanabe*[1], *Helmut Weick*[6], *Eberhard Widmann*[17], *John S. Winfield*[6], *Xiaodong Xu*[6], *Hiroki Yamakami*[5], *Jianwei Zhao*[8]

[1]The University of Tokyo, 7-3-1 Hongo, Bunkyo, 113-0033 Tokyo, Japan
[2]RCNP, Osaka University, 10-1 Mihogaoka, Ibaraki, 567-0047 Osaka, Japan
[3]Universidade de Santiago de Compostela, 15782 Santiago de Compostela, Spain
[4]Universität Giessen, Heinrich-Buff-Ring 16, 35392 Giessen, Germany
[5]Kyoto University, Kitashirakawa-Oiwakecho, Sakyo-ku, 606-8502 Kyoto, Japan
[6]GSI, Planckstrasse 1, 64291 Darmstadt, Germany
[7]KVI-CART, University of Groningen, Zernikelaan 25, 9747 AA Groningen, the Netherlands
[8]Beihang University, Xueyuan Road 37, Haidian District, 100191 Beijing, China
[9]Nara Women's University, Kita-Uoya Nishi-Machi, 630-8506 Nara, Japan
[10]KEK, 1-1 Oho, Tsukuba, 305-0801 Ibaraki, Japan
[11]Tohoku University, 6-3 Aoba, Aramaki, Aoba, Sendai, 980-8578 Miyagi, Japan
[12]YITP, Kyoto University, Kitashirakawa-Oiwakecho, Sakyo-ku, 606-8502 Kyoto, Japan
[13]Nishina Center, RIKEN, 2-1 Hirosawa, Wako, 351-0198 Saitama, Japan
[14]Tokyo Metropolitan University, 1-1 Minami-Osawa, Hachioji, 192-0397 Tokyo, Japan
[15]Saint Mary's University, 923 Robie Street, Halifax, Nova Scotia B3H 3C3, Canada
[16]Comenius University Bratislava, Mlynská dolina, 842 48 Bratislava, Slovakia
[17]Stefan-Meyer-Institut für subatomare Physik, Boltzmangasse 3, 1090 Vienna, Austria
[18]Niigata University, 8050 Ikarashi 2-no-cho, Nishi-ku, 950-2181 Niigata, Japan

DOI: http://dx.doi.org/10.3204/DESY-PROC-2014-04/106

We have performed a spectroscopic experiment using the $^{12}\mathrm{C}(p, d)$ reaction at 2.5 GeV incident energy to search for η' mesic nuclei for the first time. A missing-mass spectrum of the reaction was obtained around the η' emission threshold using the fragment separator FRS at GSI. An overview of the experiment including the status of the analysis is given.

1 Introduction

One feature of the η' meson is its large mass compared with other pseudoscalar mesons. This is theoretically understood as a consequence of the $U_A(1)$ anomaly, which contributes to the η' mass only with spontaneous and/or explicit breaking of chiral symmetry in the low-energy region of QCD [1, 2]. In the nuclear medium, in which chiral symmetry is partially restored, the mass of the η' meson can be reduced. Such a mass reduction induces an attraction between an η' and a nucleus, and η' meson-nucleus bound states (η' mesic nuclei) may exist [3, 4, 5].

So far, there are some theoretical and experimental studies for the η' meson in the nuclear medium. For example, in Nambu–Jona-Lasinio model calculations, around 150 MeV mass reduction is predicted at normal nuclear density [3, 6]. Experimentally, the CBELSA/TAPS collaboration claimed an attractive potential of about -37 MeV and an absorption width of $15-25$ MeV at nuclear matter density for an average η' momentum of 1050 MeV/c [7]. This small width implies that the decay width of η' mesic nuclei can be small as well.

In order to search for η' mesic nuclei and study in-medium properties of the η' meson, we performed an inclusive measurement of the $^{12}\mathrm{C}(p,d)$ reaction for the first time in August 2014 [8]. A proton beam with kinetic energy of 2.5 GeV was used potentially to produce η' mesic states in $^{11}\mathrm{C}$ nuclei, and the missing-mass for the reaction was measured by analyzing the momentum of the ejectile deuteron. In such an inclusive measurement, the signal-to-noise ratio is expected to be very small due to other background processes such as multi-pion production ($p+N \to d+\pi$'s). Thus a measurement with good statistics is required. Our simulation shows that observation of peak structures in an inclusive spectrum is feasible with the experimental conditions prevailing at the Fragment Separator (FRS) of GSI [9], if the mass reduction of the η' meson at normal nuclear density is as large as 150 MeV and the in-medium width is around 20 MeV [8].

2 Experiment

2.1 Experimental setup

Figure 1 shows the detector setup in the initial experiment carried out at the FRS. A 2.5 GeV proton beam with an intensity of the order of 10^{10} per a 4-second spill accelerated in SIS-18 synchrotron impinged onto a 4 g/cm^2 thick carbon target, and the ejectile deuterons were momentum-analyzed by the FRS used as a spectrometer. The tracks of the deuterons were measured by two sets of multi-wire drift chambers (MWDC's) at a dispersive focal plane (S4) with the dispersion of 3.6 cm/% to derive their momenta. The overall missing-mass resolution is expected to be about $\sigma \sim 1.6$ MeV/c^2, which is dominated by the straggling of the energy loss in the target. This is much smaller than the expected decay width of η' mesic nuclei and is sufficient for the measurement.

With this setup, a large amount of protons produced by the (p,p') inelastic scattering reach the S4 focal plane as a background. Thus, particle identification is necessary based on the velocity difference between the signal deuterons ($\beta_d \sim 0.83$) and the background protons ($\beta_p \sim 0.95$). Plastic scintillators (SC2H, SC2V, SC41, and SC42) were installed at the S2 and S4 areas for time-of-flight (TOF) measurements. Moreover, high-refractive-index aerogel Čerenkov detectors (HIRAC and mini-HIRAC) with silica aerogel radiators of a refractive index of $1.17-1.18$ [10] and a total-reflection Čerenkov detector (TORCH) with an Acrylite radiator were placed for further rejection of the background protons.

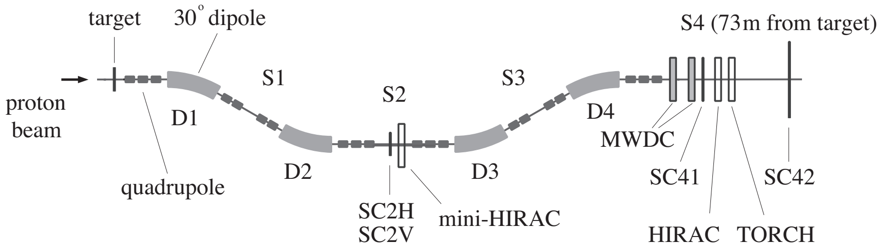

Figure 1: A schematic view of the experimental setup at the FRS. See the text for details.

2.2 Particle identification

A measured TOF spectrum between S2 and S4 with an unbiased trigger is shown in Figure 2. The smaller peak on the right side corresponds to the signal deuterons, and the higher peak on the left side is the background protons. The TOF difference between these two peaks is about 20 ns, which is consistent with our calculation. The ratio of the deuterons to the protons was about 1 to 200, and the total particle rate at the S4 focal plane was about 8×10^5/spill.

In the production measurements, we used a hardware trigger based on the S2-S4 TOF to reject the background protons and reduce the acquisition rate to the order of 10^3/s. Figure 3 shows the S2-S4 TOF and the TOF between the two scintillators at S4 (SC41-SC42) under this trigger condition. The proton peak seen in Figure 2 is rejected without influencing the signal deuterons. In Figure 3, accidental multi-proton events are still visible, whose amount is about the same as that of the signal deuterons. These can be rejected in the offline analysis by the TOF between the two S4 scintillators as shown in Figure 3, a waveform analysis of the S2 scintillator signals, and an analysis of the three Čerenkov detectors.

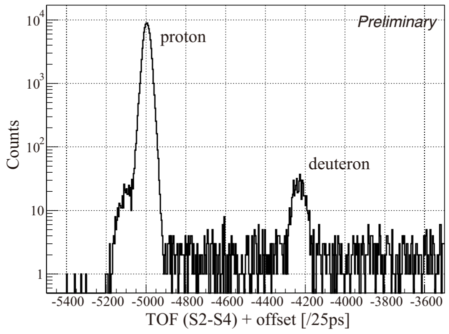

Figure 2: A measured TOF histogram between S2 and S4 by SC2H and SC41 with an unbiased trigger.

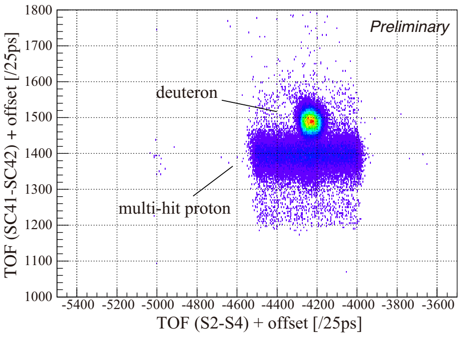

Figure 3: Measured TOF between S2 and S4 by SC2H and SC41 and TOF between two scintillators (SC41-SC42) at S4 with the TOF(S2-S4) trigger.

2.3 Momentum calibration

The momentum calibration was carried out by measuring the $d(p, d)p$ backward elastic scattering using a 1.6 GeV proton beam and a CD_2 target. In this reaction, monochromatic deuterons with the momentum of 2.8 GeV/c are emitted, which is at the middle of the momentum range in the production measurement. By measuring these deuterons at the S4 focal plane, the proper functionality of the whole system was confirmed and the ion-optical properties of the spectrometer were obtained.

2.4 Summary of measurements

We measured the $^{12}\mathrm{C}(p, d)$ reaction with a 2.5 GeV proton beam for about 5 days. The excitation energy from roughly -90 MeV to $+40$ MeV from the η' emission threshold was investigated by measurements with several scaling factors for the FRS magnetic fields from 0.98 to 1.02. High statistical significance was achieved by measuring about $(5\text{–}10)\times 10^6$ deuterons for each setting.

As a reference, the $d(p, d)$ reaction was also measured in the same momentum range of the deuterons using a 2.5 GeV proton beam and a CD_2 target. In this measurement, peak structures related to η' mesic states are not expected. Thus, it provides information for understanding the background processes in this inclusive measurement.

3 Summary and future prospects

We have performed an inclusive measurement of the $^{12}\mathrm{C}(p, d)$ reaction with a 2.5 GeV proton beam to search for η' mesic nuclei for the first time. A missing-mass spectrum of the $^{12}\mathrm{C}(p, d)$ reaction was measured around the η' emission threshold with the expected spectral resolution of $\sigma \sim 1.6$ MeV/c^2. The analysis of the spectrum is now in progress.

For FAIR, we are planning a semi-exclusive measurement of the (p, dp) reaction as well as an inclusive measurement of the (p, d) reaction with better statistics. The R&D is on-going.

Acknowledgements

The experiment was performed in the framework of the Super-FRS collaboration for FAIR. This work is partly supported by a Grant-in-Aid for JSPS Fellows (No. 258155).

References

[1] D. Jido, H. Nagahiro, and S. Hirenzaki, Phys. Rev. C **85** 032201(R) (2012).
[2] S. H. Lee and T. Hatsuda, Phys. Rev. D **54** 1871 (1996).
[3] H. Nagahiro, M. Takizawa, and S. Hirenzaki, Phys. Rev. C **74** 045203 (2006).
[4] H. Nagahiro and S. Hirenzaki, Phys. Rev. Lett. **94** 232503 (2005).
[5] H. Nagahiro *et al.*, Phys. Rev. C **87** 045201 (2013).
[6] P. Costa, M. C. Ruivo, and Yu. L. Kalinovsky, Phys. Lett. B **560** 171 (2003).
[7] M. Nanova *et al.*, Phys. Lett. B **727** 417 (2013); M. Nanova *et al.*, *ibid.* **710** 600 (2012).
[8] K. Itahashi *et al.*, Prog. Theor. Phys. **128** 601 (2012).
[9] H. Geissel *et al.*, Nucl. Instr. Meth. B **70** 286 (1992).
[10] M. Tabata *et al.*, Nucl. Instr. Meth. A **623** 339 (2010).

Dilepton Production in Transport-based Approaches

Janus Weil[1], *Stephan Endres*[1], *Hendrik van Hees*[1], *Marcus Bleicher*[1], *Ulrich Mosel*[2]

[1]Frankfurt Institute for Advanced Studies , Ruth-Moufang-Str. 1, 60438 Frankfurt, Germany
[2]Institut für Theoretische Physik, JLU Giessen, Heinrich-Buff-Ring 16, 35392 Giessen, Germany

DOI: http://dx.doi.org/10.3204/DESY-PROC-2014-04/173

We investigate dilepton production in transport-based approaches and show that the baryon couplings of the ρ meson represent the most important ingredient for understanding the measured dilepton spectra. At low energies (of a few GeV), the baryon resonances naturally play a larger role and affect already the vacuum spectra via Dalitz-like contributions, which can be captured well in an on-shell-transport scheme. At higher energies, the baryons mostly affect the in-medium self energy of the ρ, which is harder to tackle in transport models and requires advanced techniques.

1 Introduction

Lepton pairs are known to be an ideal probe for studying phenomena at high densities and temperatures. They are created at all stages of a heavy-ion collision, but unlike hadrons they can escape the hot and dense zone almost undisturbed (since they only interact electromagnetically) and thus can carry genuine in-medium information out to the detector. Dileptons are particularly well-suited to study the in-medium properties of vector mesons, since the latter can directly convert into a virtual photon, and thus a lepton pair [1, 2]. One of the groundbreaking experiments in this field was NA60 at the CERN SPS, which revealed that the ρ spectral function is strongly broadened in the medium. Calculations by Rapp et al. have shown that this collisional broadening is mostly driven by baryonic effects, i.e., the coupling of the ρ meson to baryon resonances (N^*, Δ^*) [3]. In the low-energy regime, the data taken by the DLS detector have puzzled theorists for years and have recently been confirmed and extended by new measurements by the HADES collaboration [4, 5, 6, 7, 8, 9]. At such low energies, it is expected that not only the in-medium properties are determined by baryonic effects, but that already the production mechanism of vector mesons is dominated by the coupling to baryons (even in vacuum).

2 The model: hadronic transport + VMD

Already our previous investigations [10] based on the GiBUU transport model [11] have shown that the baryonic N^* and Δ^* resonances can give important contributions to dilepton spectra at SIS energies, both from pp and AA collisions, via Dalitz-like contributions. This finding was based on the assumption that these resonances decay into a lepton pair exclusively via an intermediate ρ meson (i.e. strict vector-meson dominance). In the transport simulation, the Dalitz decays $R \to e^+e^-N$ are treated as a two-step process, where the first part is an $R \to \rho N$

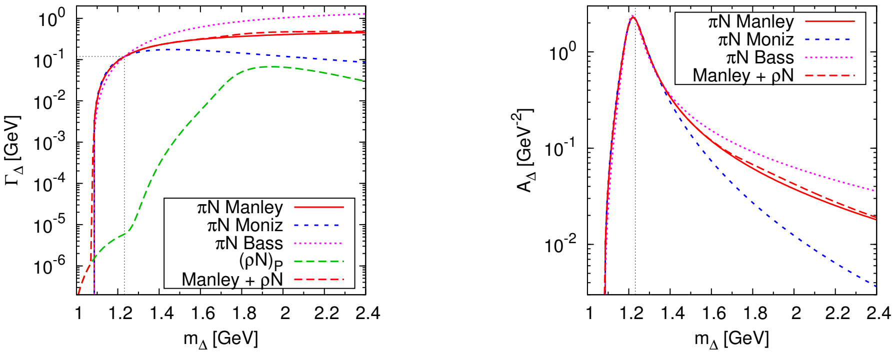

Figure 1: Partial widths for the πN and ρN decay channels (left) and spectral function (right) of the Δ resonance as a function of the off-shell mass.

decay, followed by a subsequent conversion of the ρ into a lepton pair ($\rho \to e^+e^-$). The branching ratios for the $R \to \rho N$ decay are taken from the partial-wave analysis by Manley et al. [12], while the decay width for the second part is calculated under the strict-VMD assumption as $\Gamma_{ee}(m) = \Gamma_0 \cdot (M/m)^3$. For the present study we extend the VMD assumption also to the $\Delta(1232)$ state, whose dilepton contribution has been subject to much controversy recently. Since the Δ is too light to decay into an on-shell ρ meson, it is difficult to determine its coupling to the ρ experimentally, and consequently Manley and other analyses do not find any sign of a $\Delta \to \rho N$ decay. Nevertheless the Δ has a photonic decay mode, which means that also a dilepton Dalitz decay channel must exist. The latter has been claimed to be particularly significant for dilepton spectra at SIS energies [13]. However, this argument was based on the continuation of the photon decay into the time-like region neglecting the involved electromagnetic transition form factor [14]. Unfortunately this form factor is essentially unknown in the time-like region from the experimental point of view. However, it is clear that it can significantly alter the dilepton yield from the Δ (easily by an order of magnitude) [15]. In order to deal with this situation, we choose to apply the assumption of strict VMD not only to the N^* and Δ^* resonances, but also to the Δ itself, assuming a p-wave (i.e. $L = 1$) decay into ρN. Together with the other resonance channels, this results in a consistent model with clear assumptions, which can be tested against experiment. One free parameter that is left to fix in this approach is the on-shell branching ratio of $\Delta \to \rho N$. We use a value of $5 \cdot 10^{-5}$, in order to produce dilepton yields which are roughly equivalent to the radiative decay for small Δ masses and compatible with the HADES data at low energies. Fig. 1 shows the partial decay width into ρN, which is extremely small at the Δ pole mass, but grows significantly when going to larger masses. But even in the very high-mass tail, the additional decay mode has only little influence on the overall width and spectral function of the Δ (even less than the different parametrizations of the πN width).

3 Dilepton spectra from p+p collisions

Fig. 2 shows a comparison of our simulation results for p+p collisions (inside the detector acceptance) to the dilepton mass spectra measured by the HADES collaboration at three different beam energies. Since the mesonic decay channels have not changed with respect to earlier works [10], we concentrate here on the discussion of the baryonic contributions. The Δ is shown in two approaches, a QED-like radiative decay [14] (neglecting the occurring form factor), and a VMD decay $\Delta \to \rho N \to e^+e^-N$. While both give rather similar results at low energies (where the form-factor effects are still small), the differences get larger at higher energies. There the VMD curve develops a clear peak at the ρ mass and a bump around $m_\Delta - m_N \approx 300$ MeV (from the on-shell Δs), while the QED curve is flat and structureless (due to the absence of a form factor). However, both models agree on the fact that the Δ contribution becomes sub-dominant at higher energies and is exceeded by other contributions (in particular the higher resonances N^* and Δ^* become more significant). Thus the data can not distinguish between both models.

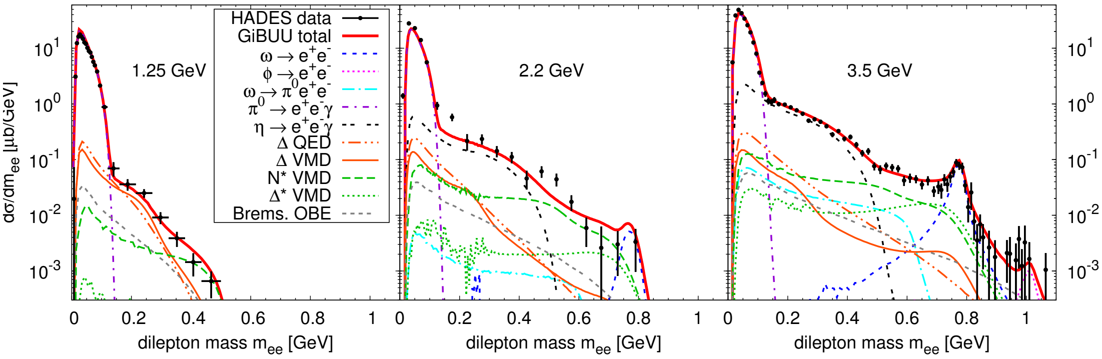

Figure 2: Dilepton mass spectra for pp collisions, in comparison to the data from [4, 5, 6].

4 Dilepton spectra from A+A collisions

Fig. 3 shows our results of dilepton spectra from nucleus-nucleus collisions compared to the HADES data. The light CC system has been measured at two different energies (1 and 2 AGeV) and the heavier ArKCl at the intermediate energy of 1.76 AGeV. The best agreement with data is achieved in the CC system at 2 AGeV, where the spectrum above the pion mass is dominated by the η Dalitz and the baryonic VMD channels. In the 1 AGeV reaction, we see some underestimation at intermediate masses around 300 MeV, despite the inclusion of OBE Bremsstrahlung according to Shyam et al. [16]. Since there are many channels contributing with similar strength here, it is hard to tell where the underestimation originates from. In the medium-size ArKCl system, we see a similar underestimation at intermediate masses and a slight excess in the vector-meson pole region. One may be surprised that a pure (on-shell) transport approach without explicit inclusion of in-medium spectral functions achieves such a good agreement here, but that just shows the importance of Dalitz-like contributions of the baryons, which are captured well by our transport treatment.

5 Conclusions

We have shown that the HADES dilepton data from pp and AA collisions can be described rather well with a combination of a resonance-model-based transport approach with a strict-VMD coupling of the baryons to the em. sector, where a mix of different baryonic resonances contributes to the total dilepton yield. We can not reproduce the dominant contribution of

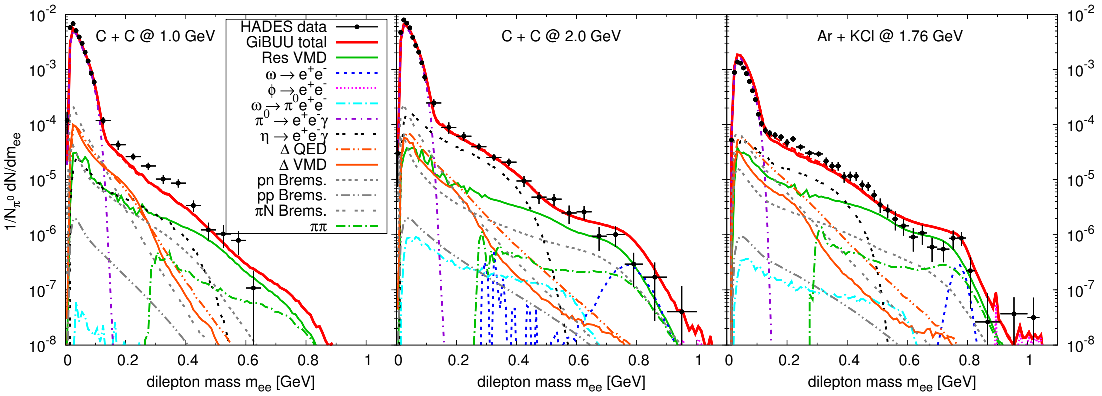

Figure 3: Dilepton mass spectra for AA collisions, in comparison to the data from [7, 8, 9].

the Δ(1232), which was claimed in other models [13]. In order to improve the description of heavy systems and to make the connection to higher energies, a proper dynamic treatment of in-medium spectral functions is required, which may be provided by the so-called "coarse-graining" approach, which is subject of ongoing investigations [17].

Acknowledgments

This work was supported by the Hessian Initiative for Excellence (LOEWE) through the Helmholtz International Center for FAIR and by the Federal Ministry of Education and Research (BMBF). J.W. acknowledges funding of a Helmholtz Young Investigator Group VH-NG-822 from the Helmholtz Association and GSI.

References

[1] S. Leupold, V. Metag, U. Mosel, Int. J. Mod. Phys. E 19, 147 (2010)
[2] R. Rapp, J. Wambach, H. van Hees, Landolt-Börnstein I/23, 4 (2010)
[3] H. van Hees, R. Rapp, Phys. Rev. Lett. 97, 102301 (2006)
[4] G. Agakishiev et al. (HADES Collaboration), Phys. Lett. B 690, 118 (2010)
[5] G. Agakishiev et al. (HADES Collaboration), Eur. Phys. J. A 48, 64 (2012)
[6] G. Agakishiev et al. (HADES Collaboration), Phys. Rev. C 85, 054005 (2012)
[7] G. Agakichiev et al. (HADES Collaboration), Phys. Rev. Lett. 98, 052302 (2007)
[8] G. Agakishiev et al. (HADES Collaboration), Phys. Lett. B 663, 43 (2008)
[9] G. Agakishiev et al. (HADES Collaboration), Phys. Rev. C 84, 014902 (2011)
[10] J. Weil, H. van Hees, U. Mosel, Eur. Phys. J. A 48, 111 (2012)
[11] O. Buss, T. Gaitanos, K. Gallmeister, H. van Hees, M. Kaskulov et al., Phys. Rep. 512, 1 (2012)
[12] D. Manley, E. Saleski, Phys. Rev. D 45, 4002 (1992)
[13] E. Bratkovskaya, J. Aichelin, M. Thomere, S. Vogel, M. Bleicher, Phys. Rev. C 87(6), 064907 (2013)
[14] M.I. Krivoruchenko, A. Faessler, Phys. Rev. D 65, 017502 (2002)
[15] G. Ramalho, M. Pena, Phys. Rev. D 85, 113014 (2012)
[16] R. Shyam, U. Mosel, Phys. Rev. C 82, 062201 (2010)
[17] S. Endres, H. van Hees, J. Weil, M. Bleicher, J. Phys. Conf. Ser. 503, 012039 (2014)

Chapter 5

Neutrinos and related astrophysical implications

Non-relativistic Majorana neutrinos in a thermal bath and leptogenesis

Simone Biondini

Technische Universität München, James-Franck-Str. 1, 85747 Garching, Germany

DOI: http://dx.doi.org/10.3204/DESY-PROC-2014-04/13

Neutrino oscillations, the evidence of dark matter and the baryon asymmetry in the universe can not be explained by the standard model of particle physics. Majorana fermions enter in many scenarios of physics beyond the standard model. For example, in the simplest leptogenesis framework, heavy Majorana neutrinos are at the origin of the baryon asymmetry. In the strong wash-out regime non-relativistic Majorana neutrinos produce the lepton asymmetry that is partially reprocessed into a baryon asymmetry. Moreover, all the interactions occur in a thermal medium, namely the universe in its early stage. We discuss an effective field theory approach to study the dynamics of non-relativistic Majorana particles in a thermal bath made of standard model particles. In particular, the decay width of Majorana neutrinos and the CP asymmetries are key ingredients for most leptogenesis models. We address the derivation of such quantities at finite temperature. We provide a formalism to calculate the thermal corrections to the CP asymmetry in the case of a hierarchical mass spectrum for heavy Majorana neutrinos.

1 Motivation and introduction

The standard model (SM) of particle physics can explain almost all the available experimental data and observations. However, few remarkable evidences, such as the dark matter and the baryon asymmetry in the universe, demand for new physics. Let us focus on the existing imbalance between matter and anti-matter in the universe that may be expressed in terms of the baryon to photon ratio [1]

$$\eta \equiv \frac{n_B - n_{\bar{B}}}{n_\gamma} = (6.21 \pm 0.16) \times 10^{-10} \,. \tag{1}$$

It is not possible to reproduce such a value within the SM, being its CP violating source too small [2]. Many models for the dynamical generation of the baryon asymmetry have been proposed. Among those leptogenesis [3] is both theoretically and phenomenologically interesting since one can make some connections with the low-energy neutrino physics [4]. In the leptogenesis framework a lepton asymmetry is generated by the CP violating decays of heavy Majorana neutrinos into leptons and anti-leptons in different amounts. These heavy states can in principle explain the smallness of the SM neutrinos via the see-saw mechanism. The net lepton asymmetry is then partially reprocessed into a baryon asymmetry through the so called sphalerons transitions.

In the simplest realization of leptogenesis, the lepton asymmetry is generated by the decay of the lightest heavy Majorana neutrino. The heavier ones decouple earlier from the entire dynamics. One may characterize the properties of the heavy neutrinos in the thermal bath by exploiting the definition of the *decay parameter* [4], that reads

$$K = \frac{\Gamma(T=0)}{H(T=M_1)} = \frac{\frac{M_1|F_1|^2}{8\pi}}{\sqrt{g_*}1.66\frac{M_1^2}{M_{\rm Pl}}} = \frac{\frac{|F_1|^2v^2}{M_1}}{8\pi\sqrt{g_*}1.66\frac{v^2}{M_{\rm Pl}}} = \frac{\tilde{m_1}}{m_*} \,. \tag{2}$$

The $\Gamma(T=0) \equiv \Gamma_0$ is the in-vacuum total decay width of the heavy Majorana neutrino and $H(T=M_1)$ the Hubble rate evaluated at a temperature of the order of the heavy neutrino mass, M_1. As shown in (2), the decay parameter can be also written in terms of low-energy neutrino quantities where F_1 is the Yukawa coupling between the heavy Majorana neutrino and SM Higgs and lepton doublet, g_* is the effective number of relativistic particles at $T \sim M_1$, $M_{\rm Pl}$ is the Planck scale, v^2 is the electroweak vacuum expectation value and $m_* \simeq 1.1$ eV. According to the neutrino oscillation experiments, one can choose the scale for $\tilde{m_1}$ to be $\mathcal{O}(10)$ eV (according to solar neutrino mass difference). This estimation provides an important information: the lightest heavy neutrinos remain coupled with the SM bath even after the temperature of the cooling system has dropped below the scale M_1. Therefore, the final lepton asymmetry is generated when the heavy neutrinos are non-relativistic. We refer to this scenario as strong wash-out regime [4]. In the next two sections, we show how the effective field theory (EFT) approach may help to address the dynamics of non-relativistic Majorana fermions in a thermal bath. Indeed we may explore the following hierarchy of scales $M_1 \gg T \gg M_W$, where the M_W represents the electroweak scale. The last inequality is well satisfied in the leptogenesis scenario under consideration.

2 Thermal width in the EFT framework

In this section we derive the heavy neutrino thermal width, already calculated in [5] and [6], by using an EFT approach. The thermal corrections to the width are induced by the SM particles in the thermal bath and the calculation in a fully relativistic thermal field theory framework requires the evaluation of two-loop diagrams at finite temperature. On the other hand, by exploiting the EFT, one can split the calculation into two steps: the first one-loop computation is required to match the full theory with the EFT. This can be done setting the temperature to zero, so it amounts at the calculation of typical in-vacuum matrix elements. The second one-loop computation is required to calculate the thermal corrections in the EFT. At the accuracy of the result presented here, only tadpole diagrams are involved.

The low-energy Lagrangian contains SM particles and non-relativistic excitations of Majorana neutrinos at typical energies and momenta smaller than M_1. For heavy neutrinos at rest, up to fluctuation much smaller than M_1, the EFT Lagrangian reads

$$\mathcal{L}_{\rm EFT} = N^\dagger \left(i\partial_0 - i\frac{\Gamma_0}{2} \right) N + \frac{\mathcal{L}^{(1)}}{M_1} + \frac{\mathcal{L}^{(2)}}{M_1^2} + \frac{\mathcal{L}^{(3)}}{M_1^3} + \mathcal{O}\left(\frac{1}{M_1^4} \right) \,, \tag{3}$$

where $\mathcal{L}^{(1)}$, $\mathcal{L}^{(2)}$ and $\mathcal{L}^{(3)}$ contain dimension five, six and seven operators respectively. To show the procedure, we consider the dimension five operator in $\mathcal{L}^{(1)}$. On symmetry grounds, only the operator $a\, N^\dagger N \phi^\dagger \phi$ contributes, where a is the corresponding matching coefficient.

The operator describes the interaction between heavy Majorana neutrinos and SM Higgs at low energies. In order to determine the coefficient a, we consider the heavy neutrino-Higgs scattering both in the fundamental theory and the low-energy, as shown in figure 1. A one-loop calculation at $T = 0$ is necessary to fix $a = -(3/8\pi)\lambda|F_1|^2$, where λ is the Higgs self-coupling.

Finally we compute the thermal correction to the neutrino width by considering the tadpole diagram in the EFT. It describes the thermal modification induced by thermal Higgs bosons. The leading order thermal width reads

$$\Gamma_\phi = 2\frac{\text{Im}\, a}{M_1}\langle\phi^\dagger(0)\phi(0)\rangle_T = -\frac{\lambda|F|^2 M_1}{8\pi}\left(\frac{T}{M_1}\right)^2 \tag{4}$$

where relativistic and thermal corrections factorize as a result of the EFT treatment.

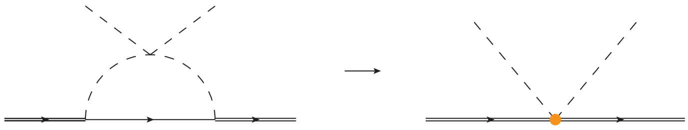

Figure 1: Matching of the dimension five operator. The one-loop process in the fundamental theory is matched onto the effective low-energy interaction. The solid double line stands for the heavy Majorana neutrino, dashed line for Higgs bosons and solid line for SM leptons.

3 CP violating parameter at finite temperature

In this section we want to show how to compute thermal corrections to the CP asymmetry at leading order in the SM couplings. The unflavoured CP asymmetry is defined as follows

$$\epsilon_1 = \sum_f \frac{\Gamma(N_1 \to \ell_f + X) - \Gamma(N_1 \to \bar{\ell}_f + X)}{\Gamma(N_1 \to \ell_f + X) + \Gamma(N_1 \to \bar{\ell}_f + X)} \tag{5}$$

and it arises from the interference between one-loop and tree level diagrams [3]. We focus only on the vertex diagram shown in figure 2 (left diagram). We consider the case of a hierarchically ordered heavy neutrino mass spectrum with two mass eigenstates, M_1 and M_2, such that $M_2 \gg M_1$. At least two neutrinos are needed as one can easily see from the combination of the Yukawa couplings appearing in the $T = 0$ expression for the unflavoured CP asymmetry

$$\epsilon_1 = \frac{\text{Im}\left[(F_1^* F_2)^2\right]}{16\pi|F_1|^2}\left(\frac{M_1}{M_2}\right) + \mathcal{O}\left(\frac{M_1}{M_2}\right)^3 , \tag{6}$$

where we have expanded the known result in [7] according to the hierarchy $M_2 \gg M_1$.

We calculate the leading order thermal correction to the quantity in (6) that arises from the effective low-energy interaction between non-relativistic Majorana neutrino and SM Higgs at energy scales of order $T \ll M_1$. This is done in complete analogy with the thermal width by considering the matching in figure 2. However, there is an important difference with respect to the previous case: we need to construct two subsequent effective theories. We have to integrate

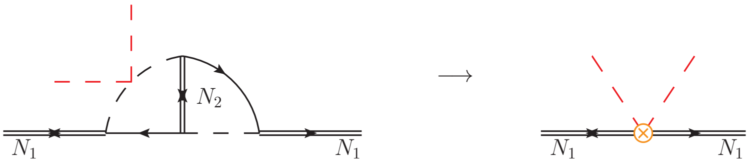

Figure 2: The matching of the fundamental process onto the effective low-energy interaction is shown. The red-dashed lines stand for thermal Higgs bosons from the plasma.

out the energy modes of order M_2 as a first step and integrate out the energy modes of order M_1 in a second stage. Therefore, one is finally left with the proper degrees of freedom: non-relativistic heavy neutrinos that decay and generate the CP asymmetry in a SM thermal bath. The final result is organized according to the power counting of the two effective theories: an expansion in M_1/M_2 and an expansion in T/M_1. It has the form

$$\epsilon_{1,T} \sim \epsilon_1 \, \lambda \left(\frac{T}{M_1} \right)^2 + \cdots \, , \tag{7}$$

where the dots stand for higher orders terms.

Acknowledgements

I would like to thank N. Brambilla, M. Escobedo and A. Vairo for the collaboration on the work presented here based on [8], [9], and the organizers of *PANIC 2014*.

References

[1] E. Komatsu *et al.* [WMAP Collaboration], Astrophys. J. Suppl. **180** (2009) 330 [arXiv:0803.0547 [astro-ph]].

[2] C. Jarlskog, Phys. Rev. Lett. **55** (1985) 1039.

[3] M. Fukugita and T. Yanagida, Phys. Lett. B **174** (1986) 45.

[4] W. Buchmuller, P. Di Bari and M. Plumacher, Annals Phys. **315** (2005) 305 [hep-ph/0401240].

[5] A. Salvio, P. Lodone and A. Strumia, JHEP **1108** (2011) 116 [arXiv:1106.2814 [hep-ph]].

[6] M. Laine and Y. Schröder, JHEP **1202** (2012) 068 [arXiv:1112.1205 [hep-ph]].

[7] L. Covi, E. Roulet and F. Vissani, Phys. Lett. B **384** (1996) 169 [hep-ph/9605319].

[8] S. Biondini, N. Brambilla, M. A. Escobedo and A. Vairo, JHEP **1312** (2013) 028 [arXiv:1307.7680, arXiv:1307.7680].

[9] S. Biondini, N. Brambilla, M. A. Escobedo and A. Vairo, "Thermal corrections to the CP asymmetry in leptogenesis for hierarchical neutrino masses"

The OPERA Experiment: Latest Results

Annika Hollnagel[1] on behalf of the OPERA Collaboration

[1]Hamburg University, Luruper Chaussee 149, D-22761 Hamburg, Germany

DOI: http://dx.doi.org/10.3204/DESY-PROC-2014-04/54

The long-baseline neutrino oscillation experiment OPERA has been designed for the direct observation of ν_τ appearance in the CNGS ν_μ beam. The OPERA detector is located at the LNGS underground laboratory, with a distance of 730 km from the neutrino source at CERN. It is a hybrid detector, combining the micrometric precision of emulsion cloud chambers with electronic detector elements for online readout.

While CNGS beam data taking lasted from 2008 to 2012, the neutrino oscillation analysis is still ongoing. Updated results with increased statistics are presented, including the recent observation of ν_τ appearance at $4.2\,\sigma$.

1 Introduction

During the last decades, neutrino oscillations have been studied by many experiments, and a standard picture of 3-flavour oscillations via the mixing of neutrino mass eigenstates has emerged. However, most experiments - such as the first observation of atmospheric neutrino oscillations by Super-Kamiokande [1] - work in disappearance mode. The observation of neutrino oscillations in appearance mode is required to firmly establish this 3-flavour framework.

Similar to DONuT [2] in its capability to identify τ leptons from ν_τ CC interactions on an event-by-event basis, the goal of OPERA[1] [3] is to provide the first direct observation of ν_τ appearance via $\nu_\mu \to \nu_\tau$ oscillations in a long-baseline beam of ν_μ. Although the detector is not optimised for other purposes, ν_e appearance in the sub-leading channel of $\nu_\mu \to \nu_e$ oscillations has also been studied.

2 The OPERA Experiment

2.1 Detector and neutrino beam

Due to the low cross sections involved, the detection of neutrino interactions in general requires a large target mass, while on the other hand, micrometric precision is needed for the observation of the short-lived τ leptons. The OPERA detector was designed as a hybrid apparatus to fulfill both requirements.

High-resolution ($\mathcal{O}$ (μm)) AgBr nuclear emulsions on plastic bases are interleaved with Pb plates to form *Emulsion Cloud Chamber* (ECC) modules called *bricks* - see Figure 1(a) for a schematic view and dimensions. At the downstream side of each brick, extra *Changeable Sheet* (CS) emulsion doublets act as an interface between ECC and *Electronic Detector* (ED)

---

[1] **OPERA: O**scillation **P**roject with **E**mulsion **T**r**a**cking **A**pparatus.

components [4]. Altogether, the detector comprises about 150 000 bricks, resulting in a total target mass of 1.25 kt.

The bricks are arranged in two *target* regions of 31 vertical walls, perpendicular to the neutrino beam direction. Each wall is followed by planes of horizontal and vertical *Target Tracker* (TT) scintillator strips, allowing the location of neutrino interactions within the target, i.e. the identification of the respective brick. Downstream of each target region, a magnetic *spectrometer* - made from iron core dipole magnets, *Resistive Plate Chamber* (RPC & XPC) detectors, and *Precision Tracker* (PT) drift tubes - is used for the identification of μ momentum and charge. Upstream of these two identical *Super Modules* (SM), a RPC *VETO* system is installed. Figure 1(b) shows a lateral view of the detector.

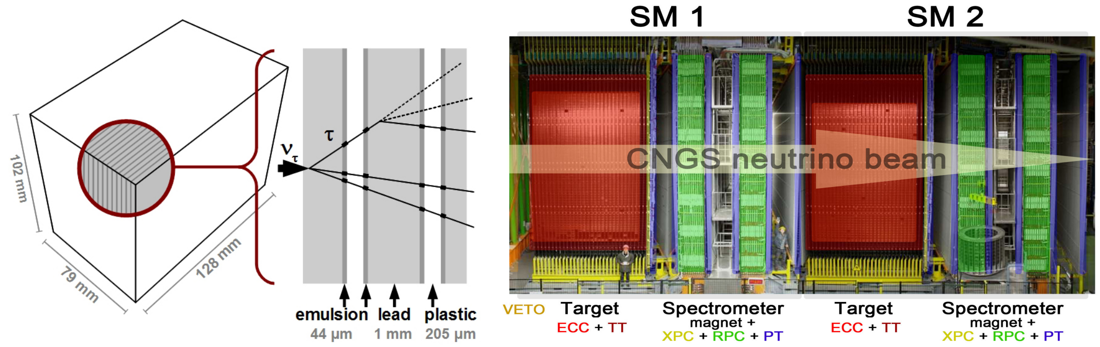

(a) ECC brick module.

(b) Lateral view (whole detector).

Figure 1: The OPERA detector.

The CNGS[2] ν_μ beam [5, 6] is a conventional neutrino beam, using 400 GeV-p from the CERN-SPS[3], a graphite target, and a magnetic horn focusing system. The resulting average ν_μ energy is ~ 17 GeV - well-above the threshold for τ lepton production in ν_τ CC interactions. While negligible for ν_τ, the contaminations with other flavours are 2.1 % for $\overline{\nu}_\mu$ and 1 % for $\nu_e + \overline{\nu}_e$, respectively. Between 2008 and 2012, a total of 17.97×10^{19} p.o.t. have been delivered.

With the detector location at the LNGS[4] underground laboratory, the baseline of the experiment is 730 km.

3 Neutrino oscillation results

3.1 $\nu_\mu \to \nu_\tau$ oscillations

The data sample used for the present results on $\nu_\mu \to \nu_\tau$ oscillations consists of 4685 fully analysed neutrino interactions with predefined selection criteria [7]: 0μ events and 1μ events with μ momentum of less than 15 GeV were searched for ν_τ appearance in the 1st and 2nd most probable bricks of 2008 + 2009 data, as well as in the 1st most probable bricks of 2010 + 2011 + 2012. In this sample, 4 ν_τ candidate events have been confirmed, their ECC reconstructions are shown in Figure 2.

---

[2] **CNGS: C**ERN **N**eutrinos to **G**ran **S**asso.

[3] **SPS: S**uper **P**roton **S**ynchrotron.

[4] **LNGS: L**aboratori **N**azionali del **G**ran **S**asso.

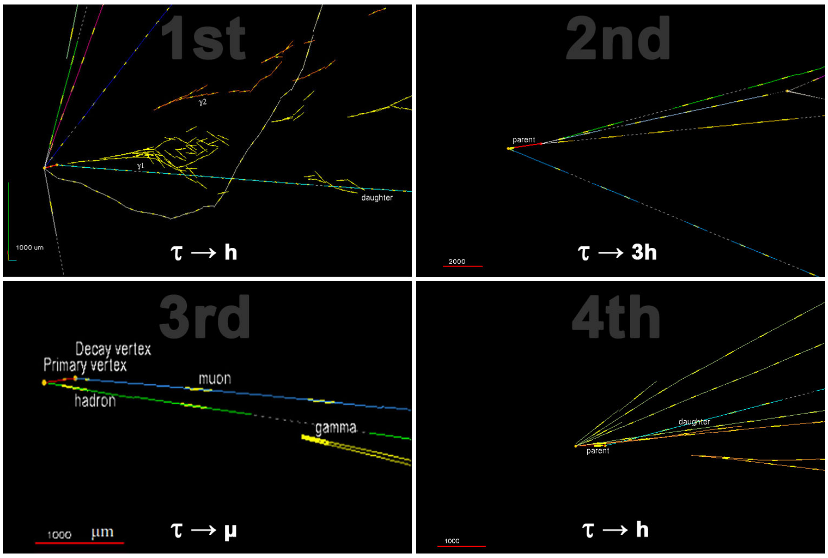

Figure 2: ECC reconstructions of the four confirmed ν_τ candidates.

With an expected signal of 2.11 ± 0.42 events[5] and a background of 0.233 ± 0.041, the 4 observed events correspond to a p-value of 1.24×10^{-5} (Fisher method) or 1.03×10^{-5} (likelihood analysis) for the no-oscillation hypothesis, both giving a significance of $4.2\,\sigma$ for the first observation of ν_τ appearance. A measurement of Δm^2_{23} has also been performed, resulting in intervals of $[1.8, 5.0] \times 10^{-3}\,\text{eV}^2$ (Feldman-Cousins) and $[1.9, 5.0] \times 10^{-3}\,\text{eV}^2$ (Bayes) at 90 % C.L., respectively.

Further details on the analysis procedure, the kinematics of the ν_τ candidate events, and the backgrounds can be found in [8, 9, 10].

3.2 $\nu_\mu \to \nu_e$ oscillations

With the possibility of electron identification, OPERA is also able to perform an appearance search in the sub-leading channel of $\nu_\mu \to \nu_e$ [11].

In the unbiased 2008+2009 data sample of 5255 located ν CC interactions (corresponding to 5.25×10^{19} p.o.t.), 19 ν_e candidate events have been found, while 19.8 ± 2.8 background events are expected from beam contamination and 1.4 events from standard 3-flavour oscillations (see Figure 3(a)). A cut on the reconstructed energy $E_{\nu,rec}$ of the ν_e candidates at $< 20\,\text{GeV}$ to increase the signal-to-noise ratio results in 4 remaining ν_e candidates, with an expected signal of 1 event and a background expectation of 4.6. The number of observed events is compatible with the no-oscillation hypothesis, allowing to derive an upper limit of $\sin^2(2\theta_{13}) < 0.44$ at 90 % C.L.[6]

For non-standard oscillations in the parameter space of large $\Delta m^2_{new} > 0.1\,\text{eV}^2$ suggested by the LSND and MiniBooNE experiments, new limits could be derived by introducing a cut of $E_{\nu,rec} < 30\,\text{GeV}$, reducing the number of observed ν_e candidate events to 6. With an expected

---

[5] Assumptions: $\Delta m^2_{23} = 2.32 \times 10^{-3}\,\text{eV}^2$, $\sin^2(2\theta_{23}) = 1$.

[6] Assumptions: $\sin^2(2\theta_{13}) = 0.098$, $\sin^2(2\theta_{23}) = 1$, $\Delta m^2_{23} = \Delta m^2_{31} = 2.32 \times 10^{-3}\,\text{eV}^2$, $\delta_{CP} = 0$.

background of 9.4 events (incl. 1.3 events from 3-flavour oscillations), the Bayesian upper limit on large $\sin^2(2\theta_{new})$ is 7.2×10^{-3}. Figure 3(b) shows the exclusion plot in the Δm^2_{new} vs. $\sin^2(2\theta_{new})$ plane.

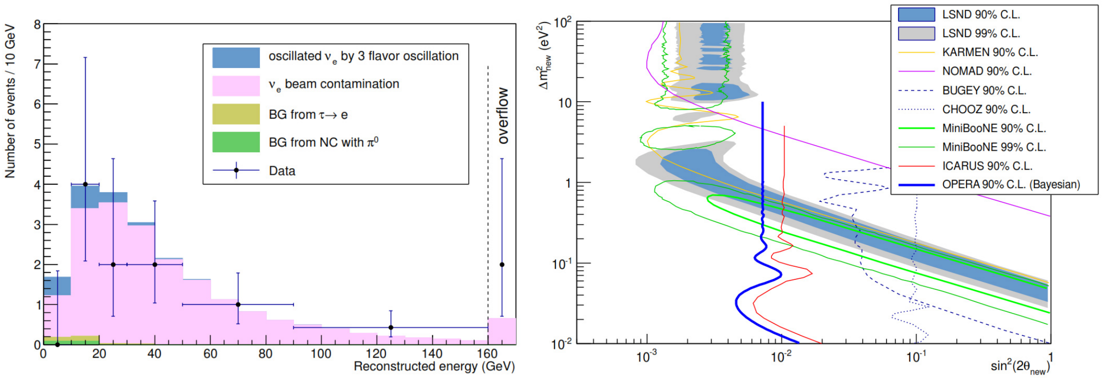

(a) Reconstructed energy of the ν_e candidates.

(b) Exclusion plot (non-standard scenario).

Figure 3: $\nu_\mu \to \nu_e$ oscillation analysis.

4 Conclusion

OPERA is a long-baseline neutrino oscillation experiment. Data taking in the CNGS beam lasted from 2008 to 2012, with a total exposure of 17.97×10^{19} p.o.t.

In the main analysis of $\nu_\mu \to \nu_\tau$ oscillations, 4 ν_τ interactions have been confirmed within the current data sample of 4685 fully analysed events. Using statistical methods, this result constitutes the first observation of ν_τ appearance in a ν_μ beam at $4.2\,\sigma$ significance.

In the sub-leading channel of $\nu_\mu \to \nu_e$ oscillations, new limits could be derived in the parameter space of non-standard neutrino oscillations.

References

[1] Y. Fukuda et al. [Super-Kamiokande Collaboration]. *Phys.Rev.Lett.*, 81:1562–1567, 1998.

[2] K. Kodama et al. [DONuT Collaboration]. *Phys.Rev.*, D78:052002, 2008.

[3] R. Acquafredda et al. [OPERA Collaboration]. *JINST*, 4:P04018, 2009.

[4] A. Anokhina et al. [OPERA Collaboration]. *JINST*, 3:P07005, 2008.

[5] G. Acquistapace et al. CERN-98-02, INFN-AE-98-05, CERN-YELLOW-98-02. 1998.

[6] R. Baldy et al. CERN-SL-99-034-DI, CERN-SL-99-34-DI, INFN-AE-99-05, INFN-AE-99-5. 1999.

[7] N. Agafonova et al. [OPERA Collaboration]. *PTEP*, 2014(10):101C01, 2014.

[8] N. Agafonova et al. [OPERA Collaboration]. *Phys.Lett.*, B691:138–145, 2010.

[9] N. Agafonova et al. [OPERA Collaboration]. *JHEP*, 1311:036, 2013.

[10] N. Agafonova et al. [OPERA Collaboration]. *Phys.Rev.*, D89(5):051102, 2014.

[11] N. Agafonova et al. [OPERA Collaboration]. *JHEP*, 1307:004, 2013.

Initial probe of δ_{CP} by T2K with combined electron neutrino appearance and muon neutrino disappearance.

H.M. O'Keeffe[1] on behalf of the T2K collaboration

[1]Physics Department, Lancaster University, Lancaster, UK, LA1 4YB

DOI: http://dx.doi.org/10.3204/DESY-PROC-2014-04/164

T2K is a long-baseline neutrino oscillation experiment in which a ν_μ beam is produced at the J-PARC facility and detected 295 km away by the Super-Kamiokande, water Cherenkov detector. Up to May 2013, T2K has accumulated 6.57×10^{20} protons on target, approximately 8% of the experimental goal. T2K has observed 120 ν_μ candidates, which show a clear disappearance oscillation pattern, and 28 ν_e candidates, with which ν_e appearance was established. The measurement of ν_e appearance is particularly important because it enables us to determine $\delta_{\rm CP}$ when θ_{23} and θ_{13} are known. Using values of θ_{23} determined by T2K disappearance measurements and θ_{13} measured by reactor $\bar{\nu}_e$ experiments, T2K has obtained the first constraint on $\delta_{\rm CP}$ from a ν_e appearance measurement.

1 The Tokai to Kamioka experiment

The Tokai to Kaimoka (T2K) experiment is a long-baseline neutrino oscillation experiment located in Japan. An intense, high purity ν_μ beam is produced (at J-PARC) by colliding a 30 GeV proton beam with a stationary graphite target, resulting in a beam of secondary hadrons. Three magnetic horns are used to select π^+, which decay to produce an almost pure beam of ν_μ (approximately 1% ν_e contamination). The neutrino beam is directed 2.5° away from the axis between the target and the far detector 295 km away. This off-axis technique produces a narrow band beam with a peak energy around 0.6 GeV. This corresponds to the energy of the first $\nu_\mu \rightarrow \nu_e$ oscillation maximum.

The near detector complex is located 280 m downstream from the neutrino production point and consists of an on-axis Interactive Neutrino GRID (INGRID) detector and an off-axis near detector (ND280). INGRID is used to monitor the beam intensity and direction. ND280 is used to measure the neutrino flux and interaction cross-sections, which reduces systematic uncertainties on the oscillation analyses. The off-axis detector consists of several sub-detectors inside a 0.2 T magnet, namely a π^0 detector, two active fine grain detectors, three gaseous argon time projection chambers, an electromagnetic calorimeter and a side muon range detector.

The far detector, located 295 km from the neutrino production point, is the Super-Kamiokande water Cherenkov detector. Super-Kamiokande is divided into an inner and outer detector. The inner detector has a 22.5 kton water fiducial volume that is surrounded by 11,129 photomultiplier tubes (PMTs). The inner detector and PMTs are surrounded by a 2 m wide outer detector. Neutrino interactions with water produce Cherenkov light which can be used to distinguish between electron and muon-like events. Good separation between ν_e and ν_μ candidates is achieved via a particle identification variable, with a probability of misidentifying a μ as an e of $< 1\%$.

T2K was optimised to perform a high precision measurement of the mixing parameters θ_{23} and Δm^2_{32} via ν_μ disappearance and to search for the mixing angle θ_{13} via ν_e appearance in the far detector. Recent work from the collaboration has provided the first hints that the parameter δ_{CP} may not be zero. Up to May 2013 T2K has collected 6.57×10^{20} protons on target.

2 Joint ν_μ and ν_e analysis

Charged current (CC) ν_μ interactions in the near detector are used to constrain the energy spectrum of the neutrino beam and neutrino interaction cross section parameters. Details of this analysis are given in [1]. CC interactions that pass the selection criteria are divided into three classes: CC-0π, which is dominated by CC quasi elastic scattering (CCQE) interactions; CC$-1\pi^+$, from CC resonant pion production; and finally CC-other which covers all remaining CC topologies that are selected. The three samples are fitted with a total of 25 beam parameters, 21 cross section parameters and 210 parameters that describe ND280 detector systematics. The fit to the ND280 data gives estimates for 22 beam flux parameters at the far detector (Super-Kamiokande), 5 common cross section parameters and their covariance. Inclusion of information from ND280 reduces the uncertainty on the expected number of electron-like events at the far detector from 27.2% to 8.8%.

At Super-Kamiokande, candidate events are selected if they are in time with the T2K neutrino beam, the energy of the Cherenkov ring is above 30 MeV, the ring occurs in the inner detector and there is low activity in the outer detector. A further cut is applied to ensure that the event vertex is at least 2 m from the wall of the inner tank and such events are"fully contained fiducial volume" (FCFV). Full details are given in [1]. Candidate ν_e interactions in the FCFV sample are identified by looking for events with a single electron-like Cherenkov ring with a reconstructed electron momentum above 100 MeV/c and reconstructed neutrino energy below 1250 MeV. The momentum cut is necessary to eliminate decay-electrons from stopping muons generated by CC interactions in the detector. Finally, additional contamination from π^0 events, which can mimic ν_e interactions is reduced by using a new reconstruction algorithm based upon the work in [2]. The application of this cut removes 69% of the π^0 background events relative to previous T2K ν_e appearance selections [3].

A binned extended maximum likelihood fit is used to determine the neutrino oscillation parameters. The likelihood comprises of four components: a normalization term ($\mathcal{L}_{norm}$), a spectral shape term ($\mathcal{L}_{shape}$), a systematics term ($\mathcal{L}_{syst}$) and a constraint term ($\mathcal{L}_{const}$) from other measurements. The likelihood is therefore:

$$\mathcal{L}(N_{obs}, \overrightarrow{x}, \overrightarrow{o}, \overrightarrow{f}) = \mathcal{L}_{norm}(N_{obs}; \overrightarrow{o}, \overrightarrow{f}) \times \mathcal{L}_{shape}(\overrightarrow{x}; \overrightarrow{o}, \overrightarrow{f}) \times \mathcal{L}_{syst}(\overrightarrow{f}) \times \mathcal{L}_{const}(\overrightarrow{o}),$$

where N_{obs} is the number of observed events, $\overrightarrow{x}$ is a set of kinematic variables, $\overrightarrow{o}$ represents the oscillation parameters and $\overrightarrow{f}$ describes the systematic uncertainties. Full details of the likelihood fit used in the T2K analysis is given in [1]. In the fit, values for several oscillation parameters are fixed as follows: $\sin^2\theta_{12} = 0.306, \Delta m^2_{21} = 7.6 \times 10^{-5}\text{eV}^2$ [4], $\sin^2\theta_{23} = 0.5, |\Delta m^2_{32}| = 2.4 \times 10^{-3}\text{eV}^2$ [5] and $\delta_{\text{CP}} = 0$. For the normal (inverted) hierarchy case, the best-fit value (68% confidence level) is $\sin^2 2\theta_{23} = 0.140^{+0.038}_{-0.032}(0.170^{+0.045}_{-0.037})$. In total, 28 candidate ν_e events were observed, which is significantly larger than the predicted background of 4.92 ± 0.55. Figure 1 shows the best fit reconstructed neutrino energy for the 28

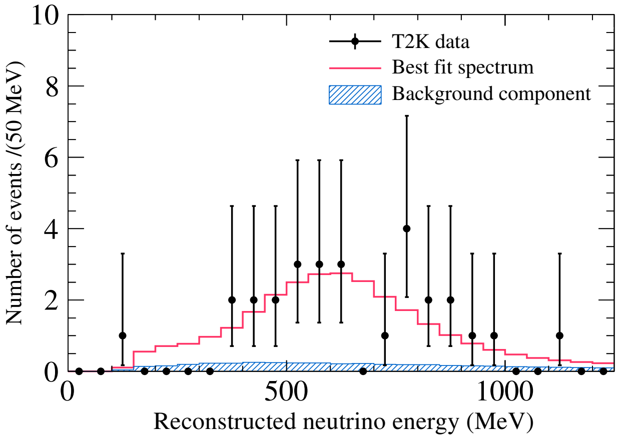

Figure 1: The $E_\nu^{\rm rec}$ distribution for ν_e candidates with the MC prediction at the best fit of $\sin^2\theta_{13} = 0.144$ (normal hierarchy).

observed ν_e events. The significance for a non-zero value of θ_{13} is calculated to be 7.3σ using the difference of log likelihood values between the best-fit value of θ_{13} and $\theta_{13} = 0$ and using a test statistic having fixed values of θ_{23} and $\delta_{\rm CP}$.

Using any value of the parameters θ_{23} and $\delta_{\rm CP}$ consistent with their present uncertainties returns a significance of greater than 7σ. The uncertainty associated with θ_{23} and Δm^2_{32} are taken into account via the $\mathcal{L}_{const}$ term in the fit and marginalising the likelihood over θ_{23} and Δm^2_{32}. Values of $\sin^2\theta_{23}$ and Δm^2_{32} are taken from the T2K ν_μ disappearance results [5]. Performing the fit for all values of $\delta_{\rm CP}$ results in the allowed contours shown in Figure 2

Constraints on the parameter $\delta_{\rm CP}$ can be obtained by combining the T2K results with the measured θ_{13} value from reactor anti-neutrino experiments. Details of the constraint are given in [1]. The combined T2K and reactor neutrino measurement indicates a preferred value of $-\pi/2$ for $\delta_{\rm CP}$. The Feldman-Cousins method is used to determine the 90% C.L. limits shown in Figure 3. The data excludes values of $\delta_{\rm CP}$ between 0.19π and 0.80π at 90% C.L. for the normal hierarchy. For the inverted hierarchy values between $-\pi$ and -0.97π and -0.04π and π are excluded at 90%C.L.

3 Conclusions

The T2K experiment has made the first observation of ν_e appearance in a ν_μ beam at a baseline of 295 km and peak beam energy of 0.6 GeV. A best fit value for $\sin^2 2\theta_{13} = 0.140^{+0.038}_{-0.032}$ ($0.170^{+0.045}_{-0.037}$) for the normal (inverted) neutrino mass hierarchy and assuming fixed values of $|\Delta m^2_{32}| = 2.4 \times 10^3$ eV^2, $\sin^2\theta_{23} = 0.5$ and $\delta_{\rm CP} = 0$. This best fit value has a significance of 7.3σ over the hypothesis of $\sin^2 2\theta_{13} = 0$. By combining the T2K result with the world average value of θ_{13} from reactor experiments, $\delta_{\rm CP}$ between 0.19π and 0.80π at 90% C.L. for the normal hierarchy. For the inverted hierarchy values between $-\pi$ and -0.97π and -0.04π and π are excluded at 90% C.L. The T2K experiment will continue to take data and investigate

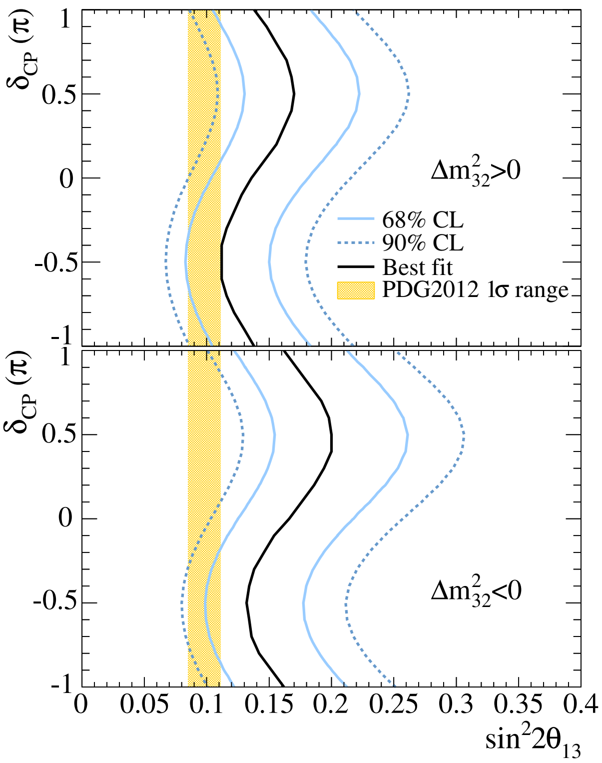

Figure 2: Allowed region of 68% (thin, solid, light blue) and 90% C.L. (dashed, blue) for $\sin^2 2\theta_{13}$ for each value of δ_{CP}. The thick (black) solid line is the best fit value for each value of δ_{CP}. Run1-4 data, marginalized over $\sin^2\theta_{23}$ and Δm^2_{32}. The values of $\sin^2\theta_{23}$ and Δm^2_{32} are varied in the fit with the constraint from [5]. The shaded region shows the average value of θ_{13} from the PDG 2012 [6].

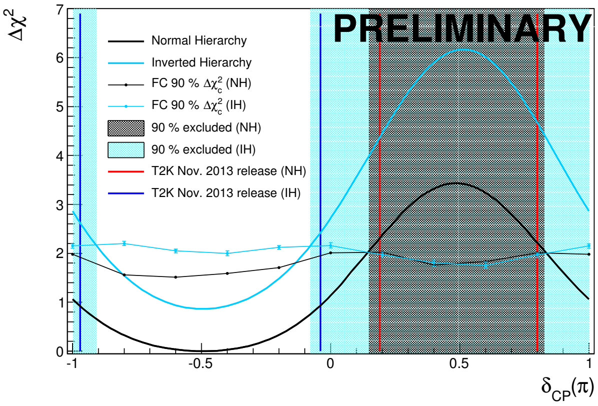

Figure 3: Profiled $\Delta\chi^2$ as a function of δ_{CP} for the combined reactor neutrino results and T2K joint three flavour frequentist analysis. The critical $\Delta\chi^2$ values and excluded regions obtained at the 90% C.L. for the normal and inverted hierarchies are overlaid.

CP violation in the lepton sector more precisely.

References

[1] K. Abe *et al.* (T2K Collaboration), Phys. Rev. Lett. **112**, 061802 (2014).

[2] R.B. Patterson *et al.*, Nucl.Instrum.Meth. **A608**, 206 (2009).

[3] K. Abe *et al.* (T2K Collaboration), Phys.Rev.Lett **107**, 041801 (2011).

[4] G.L. Fogli *et al.*, Phys.Rev. **D84**, 053007 (2011).

[5] K. Abe *et al.* (T2K Collaboration), arXiv:1308.0465 [hep-ex], (2013).

[6] J. Beringer *et al.* (Particle Data Group), Phys.Rev. **D86, 010001, (2012).**

Status of the Karlsruhe Tritium Neutrino Experiment KATRIN

Kathrin Valerius[1] for the KATRIN Collaboration

[1]Institut für Kernphysik, Karlsruher Institut für Technologie, Karlsruhe, Germany

DOI: http://dx.doi.org/10.3204/DESY-PROC-2014-04/80

Precision measurements of the kinematics of weak decays represent the only model independent approach to address the still unknown absolute scale of neutrino masses in a laboratory experiment. The KATRIN experiment, currently under construction at the Karlsruhe Institute of Technology, aims to improve the neutrino mass sensitivity obtained through precision spectroscopy of tritium β decay by an order of magnitude to 200 meV/c^2 (90% CL). In this contribution we present an overview of the status of the major components of the experimental set-up and report results from first commissioning measurements.

1 Introduction

Neutrino properties, and in particular the open question regarding the scale of neutrino rest masses, bear fundamental relevance to many current research topics in cosmology, theoretical particle physics, and astroparticle physics. Neutrino oscillation experiments, while providing us with a consistent neutrino mixing scheme and accurate measurements of two independent neutrino mass differences, cannot address the absolute mass scale.

Precision cosmology and the search for neutrinoless double beta decay can be used as sensitive probes of neutrino masses. However, these methods rely on multi-parameter cosmological models or on the assumption of neutrinos being of Majorana nature, respectively. By contrast, precision measurements of the kinematics of β decays (^{3}H, ^{187}Re) or electron capture processes (^{163}Ho) allow for a direct, i.e. model independent, neutrino mass search (see [1] for a recent review). The most mature technique relies on the spectroscopy of tritium β decay near its kinematic endpoint at 18.6 keV. Due to the phase space factor, the shape of the β-decay energy spectrum $\mathrm{d}N/\mathrm{d}E$ carries an imprint of the neutrino mass values m_i $(i = 1, 2, 3)$:

$$\frac{\mathrm{d}N}{\mathrm{d}E} \propto F(Z,E) \cdot p_\mathrm{e} \cdot (E + m_\mathrm{e}) \cdot (E_0 - E) \cdot \sum_{i=1}^{3} |U_\mathrm{ei}|^2 \sqrt{(E_0 - E)^2 - m_i^2} \cdot \Theta(E_0 - E - m_i). \quad (1)$$

Here, p_e and E are the electron momentum and energy, the Fermi function $F(Z,E)$ describes the Coulomb interaction of the outgoing electron with the daughter nucleus, and E_0 is the Q-value of the decay. Given the smallness of neutrino mass splittings, typical experimental resolution will not be sufficient to resolve the individual m_i. Hence, the observable is an effective squared "electron type" neutrino mass, $m_{\nu,\beta}^2 = \sum_{i=1}^{3} |U_\mathrm{ei}|^2 \, m_i^2$, where the U_{ei} denote elements of the PMNS mixing matrix.

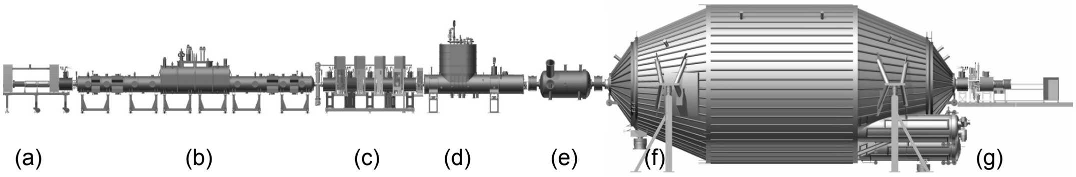

Figure 1: Overview of the KATRIN set-up: (a) calibration and monitoring system, (b) windowless gaseous tritium source, (c) differential and (d) cryogenic pumping sections, (e) pre-spectrometer, (f) main spectrometer, (g) detector system.

The present state of the art of tritium β-decay experiments is defined by electrostatic spectrometers using magnetic adiabatic collimation (MAC-E filters), a technique which allowed two experiments at Mainz and Troitsk to place upper limits on $m_{\nu,\beta}$ at about 2 eV/c^2 [2, 3]. Using the same basic principle, the upcoming KArlsruhe TRItium Neutrino experiment (KATRIN) will push the sensitivity on $m_{\nu,\beta}$ further by an order of magnitude. KATRIN is currently in its construction and commissioning phase at the Karlsruhe Institute of Technology. In the following we review the status of the major components and present results from the initial commissioning runs of the spectrometer and detector section.

2 The KATRIN Experiment

Main components An overview of the KATRIN set-up, spanning about 70 m in length, is presented in Fig. 1. The principal components can be grouped into the tritium-bearing Source and Transport Section (**a**–**d**) and the tritium-free Spectrometer and Detector Section (**e**–**g**).

Source and Transport Section. A high-luminosity windowless gaseous tritium source delivers 10^{11} β-decay electrons per second. The active volume consists of a 10 m long beam tube of 90 mm diameter. Molecular tritium gas is injected at the center and differentially pumped and recycled at both ends. The closed loops of the tritium processing system circulate about 40 g of T_2 per day. A complex cryostat system utilising a novel two-phase neon cooling concept will allow to maintain an extremely stable operating temperature inside the beam tube ($\Delta T <$ 30 mK at $T = 30$ K). Tests of the refrigeration system validated the concept, even surpassing the stringent stability requirement [4]. A comprehensive control and monitoring apparatus has been developed [5] to ensure the stability and to monitor minute fluctuations of the column density – a key parameter of the experiment which critically affects both the statistical accuracy of the measurement and the energy loss of the electrons traversing the source.

Electrons starting in the source are adiabatically guided through the pumping units and towards the spectrometer via a strong magnetic field produced by a chain of superconducting solenoids. The purpose of the successive differential (DPS) and cryogenic (CPS) pumping sections is to reduce the tritium flow rate by a combined factor of 10^{14}, thus preventing tritium from entering the spectrometer section. Manufacturing of both pumping sections is scheduled to be completed in 2015; the five superconducting solenoids of the DPS have already been delivered and are currently being tested on site. Likewise, the assembly of the source cryostat is under way and scheduled to be finished in mid-2015, when all components of the Source and Transport Section will be integrated and subject to a staged commissioning process.

Spectrometer and Detector Section. The KATRIN beam line features a pre-spectrometer to select the upper few 100 eV portion of the tritium β spectrum, and a large, high-resolution main spectrometer ($\Delta E = 0.93$ eV at $E \approx 18.6$ keV). With its length of 23 m, diameter of 10 m and volume of about 1240 m^3, the main spectrometer is one of the largest ultra-high vacuum recipients ever built. The spectrometer vessel has been on site at Karlsruhe since end of 2006. Since then, in a multi-year effort, an elaborate two-layer inner electrode made up of $\sim$ 22,000 wires has been installed inside the main spectrometer, which allows to apply a screening electric potential to shield against cosmics-induced background electrons. After completion of the wire electrode installation, the spectrometer was prepared for UHV conditions by performing a baking cycle at $T \approx 300°$C. The detector system [6], comprising a 148-pixel PIN diode, passive and active background shielding, calibration devices and two superconducting magnets, was installed and commissioned together with the data acquisition unit in 2011-12.

Neutrino mass sensitivity. The aim of improving the neutrino mass sensitivity by a factor 10 demands an improvement by a factor of 100 in the experimental observable $m^2_{\nu,\beta}$ (cf. Eq. 1). It also implies that a background level of 10^{-2} cps is required – similar to what has been achieved at previous, much smaller experiments. KATRIN is expected to reach its full sensitivity potential after 3 net years of measurement (corresponding to about 5 calendar years of running), at which point statistical and systematic uncertainties will contribute about equally to the total measurement uncertainty [7]. At its full sensitivity, KATRIN can discover a neutrino mass as small as 350 meV at 5σ significance, or place an upper limit at 200 meV (90% CL).

3 Results of the first commissioning phase

In summer 2013, an extensive campaign of commissioning runs was conducted, with two major objectives: (a) to test the transmission properties of the main spectrometer, and (b) to investigate the overall background rate and validate the background model based on simulations and on previous tests with the smaller pre-spectrometer. For this measurement programme, a high-definition calibration electron source (small energy spread, angular selectivity, fast-pulse operation; see [9] for a general concept) was attached to one end of the main spectrometer, and the detector system was connected at the opposite side.

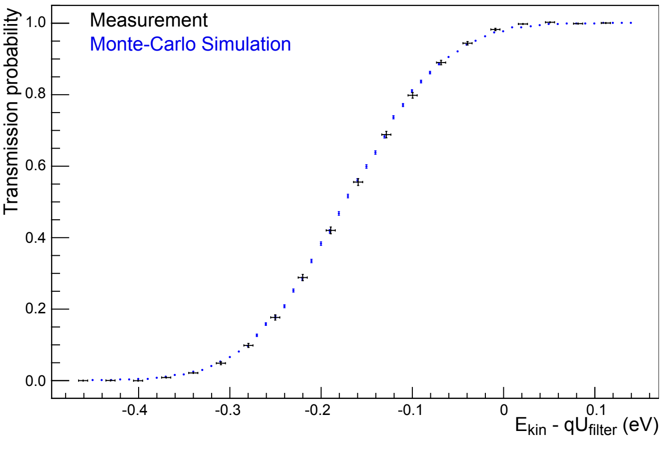

Figure 2: Transmission test of the KATRIN main spectrometer at filter potential $U_{\text{filter}} = 18.6$ kV [8].

These first commissioning measurements successfully validated the design concepts of the KATRIN Spectrometer and Detector section: Firstly, they demonstrated that the main spectrometer indeed acts as a precision MAC-E filter. Figure 2 shows that the shape of the high-pass transmission characteristics is well understood by Monte-Carlo simulations taking into account the small residual energy spread of the calibration electron source. Furthermore, the thorough simulation-optimised electromagnetic design of the main spectrometer paid off, as the spectrometer did not exhibit any signs of elevated background rates caused by Penning trap-type storage conditions. Such effects had plagued previous experiments and also the KATRIN pre-spectrometer in its initial configuration [10]. First investigations regarding background composition have been carried out; in compliance with the expectation from simulation models [11], a considerable portion was found to originate from stored electrons deposited by ^{219}Rn and ^{220}Rn decays in the spectrometer volume. Countermeasures have been implemented successfully [12] and will be tested further in the upcoming second round of commissioning runs, along with additional passive and active background suppression methods.

4 Summary

While components of the Source and Transport Section are still in the construction phase, commissioning of the already completed Spectrometer and Detector Section has commenced. Important concepts employed in the realisation of the experiment have been proven to be successful (e.g., vacuum and precision high-voltage systems, electromagnetic design of the spectrometers). As of fall 2014, a second commissioning campaign is ongoing to investigate details of the transmission characteristics and to test further background reduction mechanisms. Integration of the Source and Transport components into the beam-line are foreseen for 2015, and data-daking with the completed KATRIN set-up is expected to begin in 2016.

References

[1] G. Drexlin, V. Hannen, S. Mertens, and C. Weinheimer. Current direct neutrino mass experiments. *Advances in High Energy Physics*, 2013:293986, 2013.

[2] C. Kraus, B. Bornschein, L. Bornschein, J. Bonn, B. Flatt, A. Kovalik, B. Ostrick, E.W. Otten, J.P. Schall, T. Thümmler, and C. Weinheimer. Final results from phase II of the mainz neutrino mass search in tritium β decay. *The European Physical Journal C - Particles and Fields*, 40(4):447–468, 2005.

[3] V.N. Aseev, A.I. Belesev, A.I. Berlev, E.V. Geraskin, A.A. Golubev, N.A. Likhovid, V.M. Lobashev, A.A. Nozik, V.S. Pantuev, V.I. Parfenov, A.K. Skasyrskaya, F.V. Tkachov, and S.V. Zadorozhny. Upper limit on the electron antineutrino mass from the Troitsk experiment. *Physical Review D*, 84:112003, 2011.

[4] S. Grohmann, T. Bode, M. Hötzel, H. Schön, M. Süßer, and T. Wahl. The thermal behaviour of the tritium source in KATRIN. *Cryogenics*, 55-56(0):5–11, 2013.

[5] M. Babutzka, M. Bahr, J. Bonn, B. Bornschein, A. Dieter, G. Drexlin, K. Eitel, S. Fischer, F. Glück, S. Grohmann, M. Hötzel, T.M. James, W. Käfer, M. Leber, B. Monreal, F. Priester, M. Röllig, M. Schlösser, U. Schmitt, F. Sharipov, M. Steidl, M. Sturm, H.H. Telle, and N. Titov. Monitoring of the operating parameters of the KATRIN windowless gaseous tritium source. *New Journal of Physics*, 14(10):103046, 2012.

[6] J.F. Amsbaugh, J. Barrett, A. Beglarian, T. Bergmann, H. Bichsel, L.I. Bodine, J. Bonn, N.M. Boyd, T.H. Burritt, Z. Chaoui, S. Chilingaryan, T.J. Corona, P.J. Doe, J.A. Dunmore, S. Enomoto, J. Fischer, J.A. Formaggio, F.M. Fränkle, D. Furse, H. Gemmeke, F. Glück, F. Harms, G.C. Harper, J. Hartmann, M.A. Howe, A. Kaboth, J. Kelsey, M. Knauer, A. Kopmann, M.L. Leber, E.L. Martin, K.J. Middleman, A.W. Myers, N.S. Oblath, D.S. Parno, D.A. Peterson, L. Petzold, D.G. Phillips II, P. Renschler, R.G.H. Robertson, J. Schwarz, M. Steidl, D. Tcherniakhovski, T. Thümmler, T.D. Van Wechel, B.A. VanDevender, S. Vöcking, B.L. Wall, K. L. Wierman, J.F. Wilkerson, and S. Wüstling. Focal-plane detector system for the KATRIN experiment. *ArXiv e-prints*, April 2014.

[7] KATRIN collaboration. KATRIN design report. *FZKA scientific report*, 7090, 2005.

[8] S. Groh. PhD thesis, Karlsruhe Institute of Technology, in preparation.

[9] M. Beck, K. Bokeloh, H. Hein, S. Bauer, H. Baumeister, J. Bonn, H.-W. Ortjohann, B. Ostrick, S. Rosendahl, S. Streubel, K. Valerius, M. Zboril, and C. Weinheimer. An angular-selective electron source for the KATRIN experiment. *ArXiv e-prints*, November 2014.

[10] F.M. Fränkle, F. Glück, K. Valerius, K. Bokeloh, A. Beglarian, J. Bonn, L. Bornschein, G. Drexlin, F. Habermehl, M.L. Leber, A. Osipowicz, E.W. Otten, M. Steidl, T. Thümmler, C. Weinheimer, J.F. Wilkerson, J. Wolf, and S.V. Zadorozhny. Penning discharge in the KATRIN pre-spectrometer. *Journal of Instrumentation*, 9(7):P07028, 2014.

[11] S. Mertens, G. Drexlin, F.M. Fränkle, D. Furse, F. Glück, S. Görhardt, M. Hötzel, W. Käfer, B. Leiber, T. Thümmler, N. Wandkowsky, and J. Wolf. Background due to stored electrons following nuclear decays in the KATRIN spectrometers and its impact on the neutrino mass sensitivity. *Astroparticle Physics*, 41:52–62, 2013.

[12] S. Görhardt. *Background Reduction Methods and Vacuum Technology at the KATRIN Spectrometers*. PhD thesis, Karlsruhe Institute of Technology, 2014.

Neutrino Physics with the Precision IceCube Next Generation Upgrade (PINGU)

Tomasz Palczewski[1] for the IceCube/PINGU Collaboration

[1]Department of Physics and Astronomy, The University of Alabama, Tuscaloosa, AL, 35487

DOI: http://dx.doi.org/10.3204/DESY-PROC-2014-04/84

The IceCube Neutrino Observatory at the geographic South Pole is the largest neutrino telescope on Earth. IceCube and its low energy extension, DeepCore, were fully assembled at the end of 2010. DeepCore lowered the IceCube neutrino energy threshold to about 10 GeV, allowing access to a rich variety of atmospheric neutrino oscillation physics, and further improving sensitivity to indirect searches for WIMP dark matter and other phenomena. The recent measurements of a relatively large θ_{13} mixing angle and the first observations of atmospheric neutrino oscillations in the tens of GeV region in DeepCore open the possibility to determine the Neutrino Mass Hierarchy (NMH) in the proposed new in-fill array called Precision IceCube Next Generation Upgrade (PINGU). PINGU would lower the neutrino energy threshold and significantly increase the sensitivity to the NMH. For every year of the PINGU detector operation, on the order of one hundred thousand atmospheric neutrinos will be collected. These high statistics will allow PINGU to distinguish between the normal and inverted NMH at 3σ significance with an estimated 3.5 years of data.

1 Introduction

In the past 15 years, the neutrino oscillations have been studied in many different experiments, using neutrinos from man-made neutrino sources (beams, reactors), from the Sun, and from the atmosphere [1]. Neutrino oscillations occur because the neutrino flavor eigenstates are different than neutrino mass eigenstates. This phenomenon can be described in the standard three-flavor mixing scheme (3 x 3 ”PMNS” mixing matrix) [2]. Recently, the last unknown mixing angle θ_{13} was measured by reactor and accelerator experiments [3, 4, 5]. The moderately large value of $\theta_{13}(\simeq 9^\circ)$ opens a new epoch in the studies of CP violation and determination of the neutrino mass hierarchy [6]. The measurement of the NMH with PINGU relies on the fact that Earth has an average density close to that of MSW resonance for neutrinos in the few GeV energy range. Therefore, significant oscillation probability modifications will occur for atmospheric neutrinos passing through Earth. The character of those modifications strongly depends on the sign of the NMH. This effect can be studied in a detector with a neutrino energy threshold of a few GeV and a large fiducial volume to acquire sufficient statistics. In addition, flavor identification and directional reconstruction in the same energy regime is required. The NMH determination depends on oscillations of both the neutrinos and anti-neutrinos. The survival probability distribution for muon neutrinos and muon anti-neutrinos in Normal Hierarchy (NH) and Inverted Hierarchy (IH) are shown in Fig. 1.

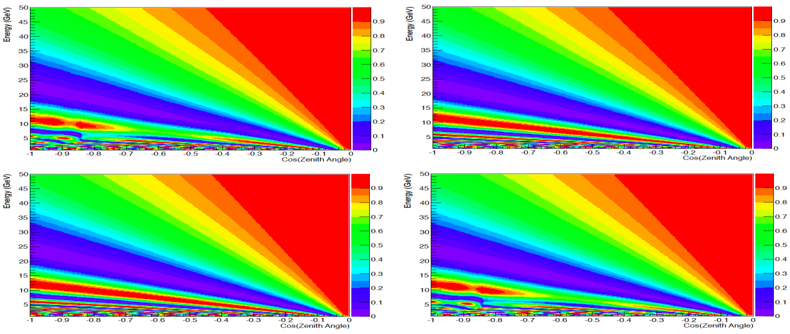

Figure 1: Survival probabilities for muon neutrinos passing through the Earth as a function of energy and zenith angle. A value of Cos(Zenith Angle) = -1 is a directly up going neutrino which is passing through the Earth's core. Muon neutrinos and NH (top left), muon neutrinos and IH (top right), muon anti-neutrinos and NH (bottom left), muon anti-neutrinos and IH (bottom right).

2 IceCube/DeepCore and proposed PINGU detector

IceCube consists of 86 cables ("strings"), each instrumented with 60 Digital Optical Modules (DOMs). The DOM consists of a 10 inch photomultiplier tube (PMT), calibration light sources and digitizing electronics. The DOMs are deployed at depths between 1450m and 2450m below the surface. The horizontal distance between most of the IceCube strings is 125 m and the vertical spacing between DOMs is 17 m. Eight strings near the center are more densely spaced with 42 - 72 m horizontal spacing and 7 m vertical spacing. Most DOMs on these eight strings contain PMTs with 35% higher quantum efficiency than standard IceCube DOMs. These eight densely instrumented strings in conjunction with the twelve IceCube strings surrounding them make up the DeepCore detector. IceCube also includes 81 surface stations, called IceTop. A sketch of IceCube and DeepCore strings, and IceTop stations is shown in Fig. 2. This configuration lowered the neutrino energy threshold to 10 GeV. The PINGU design follows closely that which was used for IceCube and DeepCore. PINGU will consist of 40 new strings with 20 m horizontal distance between strings and 5 m vertical distance between DOMs.

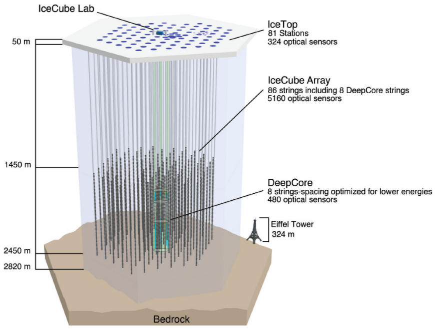

Figure 2: A sketch of IceCube and DeepCore strings, and IceTop stations.

3 Neutrino Mass Hierarchy with PINGU

The proposed PINGU detector, described in Sec. 2, has no ability to distinguish between neutrinos and anti-neutrinos. However, atmospheric neutrinos in a few GeV energy region have an interaction cross section with matter almost two times larger than anti-neutrinos. Furthermore, the atmospheric neutrino flux is larger than the atmospheric anti-neutrino flux. Therefore, a potentially measurable effect, connected with significant oscillation probability modifications (see Fig. 1), remains. The distinguishability metric defined as follows [7]:

$$S_{tot} = \sqrt{\frac{(N_{i,j}^{IH} - N_{i,j}^{NH})^2}{N_{i,j}^{IH}}}$$

where $N_{i,j}$ is the number of muon neutrino events in the i and jth bin in neutrino energy and cosine of zenith angle, can be used to quantify the observable difference between the NH and IH. The distinguishability metrics for one year of simulated PINGU data after applying the selection criteria and event reconstruction described in [8] are shown in Fig. 3.

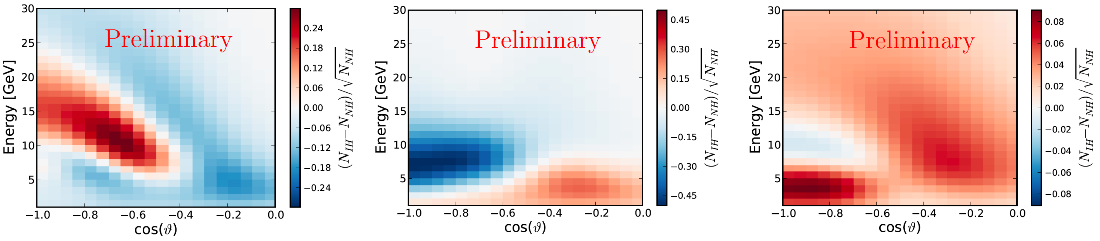

Figure 3: Distinguishability metrics for one year of simulated PINGU data: ν_μ CC (left), ν_e CC (middle), ν_τ CC events (right).

Three independent methods of determining the NMH significance in PINGU were developed: the log likelihood ratio method, the Asimov approach, and the Fisher information matrix method. Full details of these statistical methods are given in [8]. The first method is the most detailed, but it is too computationally intensive to incorporate the full range of systematics. Therefore, it was used mainly as a statistical error estimation benchmark to the other methods. The results from different methods were validated with each other and also agree well with external studies [9]. The main systematic error sources come from the energy calibration scale and physics-related uncertainties from limited knowledge of flux normalization and neutrino cross sections, and known precision of oscillation parameters. The systematic error studies connected with particle identification, cross section details, and ice model are not conducted. The significance of the neutrino mass hierarchy determination as a function of time, using the Fisher/Asimov approach including particle ID performance and a full complement of systematics (reconstruction errors are not included), under assumption of IH and θ_{23} in the first octant is shown in Fig. 4 (left). The influence of the change of the θ_{23} octant is shown in Fig 4(right).

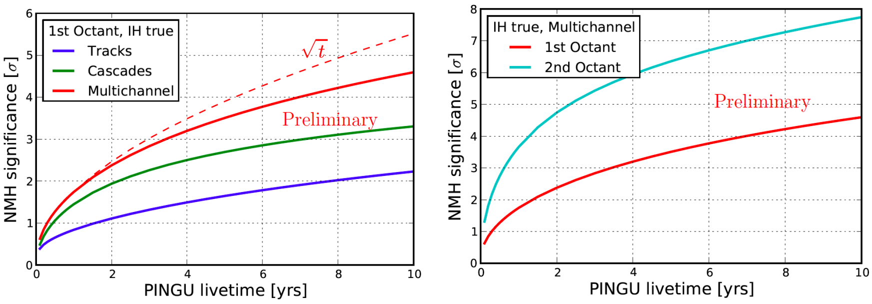

Figure 4: The significance of the neutrino mass hierarchy determination as a function of time for the IH and the first octant (left) and compared to the second octant (right) for multichannel case. The red dashed line (left) shows the expectation for a $\sqrt{t}$ dependence.

4 Conclusions

PINGU has the potential to answer one of the most important questions in the fundamental neutrino physics, namely what the sign of the Neutrino Mass Hierarchy is. We expect PINGU to be very competitive with the significance and timescale quoted for the other proposed experiments (INO, HyperK, LBNF/NOνA, JUNO) [10]. PINGU will be able to distinguish between the normal and inverted NMH at 3 σ level in 3.5 years. Beyond the measurement of the NMH, PINGU has a rich physics program. PINGU will have highly competitive sensitivity to ν_μ disappearance, θ_{23} octant and maximal mixing, and ν_τ appearance. Furthermore, PINGU will extend IceCube's and DeepCore's dark matter searches to WIMP masses below 20 GeV and improve sensitivity in the detection of low-energy supernova neutrinos.

Acknowledgments

The full IceCube/PINGU Collaboration author list and acknowledgments page can be found online here: https://icecube.wisc.edu/collaboration/authors/pingu

References

[1] J. Beringer *et al.* (PDG), PR **D86**, 010001 (2012).
[2] Z. Maki, M. Nakagawa and S. Sakata, Prog. Theor. Phys. **28**, 870, (1962).
[3] K. Abe *et al.*, Phys. Rev. Lett. **107**, 041801, (2011).
[4] F.P. An *et al.*, Phys. Rev. Lett. **108**, 171803 (2012).
[5] R.P. Litchfield, SLAC-eConf-C**120521**, (2012).
[6] H. Minakata, arXiv, 1209.1690, (2012).
[7] E. K. Akhmedov, S. Razzaque and A.Y. Smirnov, JHEP **1302**, 082 (2013).
[8] M.G. Aartsen *et al.*, arXiv, 1401.2046, (2014).
[9] W. Winter, Phys. Rev. **D88**, 013013, (2013).
[10] M. Blennow *et al.*, arXiv, 1311.1822, (2014).

Search for Sterile Neutrinos with the Borexino Detector

Mikko Meyer[1]

[1]Institut für Experimentalphysik, Universität Hamburg, Luruper Chaussee 149, D-22761 Hamburg, Germany

on behalf of the Borexino/SOX Collaboration:
M. Agostini, K. Altenmüller, S. Appel, G. Bellini, J. Benziger, N. Berton, D. Bick, G. Bonfini, D. Bravo, B. Caccianiga, L. Cadonati, F. Calaprice, A. Caminata, P. Cavalcante, A. Chavarria, A. Chepurnov, M. Cribier, D. D'Angelo, S. Davini, A. Derbin, L. di Noto, M. Durero, A. Empl, A. Etenko, S. Farinon, V. Fischer, K. Fomenko, D. Franco, F. Gabriele, J. Gaffiot, C. Galbiati, S. Gazzana, C. Ghiano, M. Giammarchi, M. Göger-Neff, A. Goretti, L. Grandi, M. Gromov, C. Hagner, Th. Houdy, E. Hungerford, Aldo Ianni, Andrea Ianni, N. Jonquères, M. Kaiser, V. Kobychev, D. Korablev, G. Korga, D. Kryn, T. Lachenmaier, T. Lasserre, M. Laubenstein, B. Lehnert, T. Lewke, J. Link, E. Litvinovich, F. Lombardi, P. Lombardi, L. Ludhova, G. Lukyanchenko, I. Machulin, S. Manecki, W. Maneschg, S. Marcocci, J. Maricic, Q. Meindl, G. Mention, E. Meroni, M. Meyer, L. Miramonti, M. Misiaszek, M. Montuschi, P. Mosteiro, V. Muratova, R. Musenich, B. Neumair, L. Oberauer, M. Obolensky, F. Ortica, K. Otis, M. Pallavicini, L. Papp, L. Perasso, A. Pocar, G. Ranucci, A. Razeto, A. Re, A. Romani, N. Rossi, R. Saldanha, C. Salvo, S. Schönert, L. Scola, H. Simgen, M. Skorokhvatov, O. Smirnov, A. Sotnikov, S. Sukhotin, Y. Suvorov, R. Tartaglia, G. Testera, C. Veyssière, D. Vignaud, M. Vivier, R. B. Vogelaar, F. von Feilitzsch, H. Wang, J. Winter, M. Wojcik, A. Wright, M. Wurm, O. Zaimidoroga, S. Zavatarelli, K. Zuber, G. Zuzel

DOI: http://dx.doi.org/10.3204/DESY-PROC-2014-04/7

Several observed anomalies in the neutrino sector could be explained by a fourth (sterile) neutrino with a squared mass difference in the order of $1\,\mathrm{e}V^2$ to the other three standard neutrinos. This hypothesis can be tested with an artificial MCi neutrino (^{51}Cr) or a kCi anti-neutrino (^{144}Ce$-^{144}$Pr) source deployed near or inside a large low background detector like Borexino. The SOX project (Short baseline neutrino Oscillation with BoreXino) aims for the detection of sterile neutrinos and will also allow to measure the neutrino magnetic moment, the electroweak mixing angle as well as the g_V and g_A coupling constants at low energy.

1 Introduction

The leptonic flavor mixing of neutrinos has been well established by a number of experiments. In the common picture, the three neutrino flavors $(\nu_e, \nu_\mu, \nu_\tau)$ are linear combinations of the three neutrino mass eigenstates (ν_1, ν_2, ν_3) separated by the two squared mass differences of $\Delta m^2_{21} = 8 \cdot 10^{-5}\,\mathrm{e}V^2$ and $\Delta m^2_{31} = 2.4 \cdot 10^{-3}\,\mathrm{e}V^2$.

However, a number of short baseline experiments have measured a neutrino deficit with respect to the expectations. These results are commonly defined as *neutrino anomalies.* From the historical point of view the LSND result has been the first result which was inconsistent with the standard scenario and pointed to the possibility of the existence of a fourth (sterile) neutrino (3+1 model). Recently, the re-calculation of the $\bar{\nu}_e$ flux from reactors together with the re-evaluation of the inverse beta decay cross section (due to the change of the neutron lifetime), resulted in an observed anti-neutrino deficit of about 7% for experiments within 100 m of the reactors. This discrepancy is known as the reactor anomaly and could be explained by a fourth (sterile) neutrino [1].

In the nineties, two solar neutrino experiments (GALLEX and SAGE) performed calibration campaigns with artificial neutrino sources (^{51}Cr and ^{37}Ar) to check their detector efficiencies. Both experiments observed independently a lower neutrino flux than expected and a recent global re-analysis confirmed the anomaly at 3σ [2].

One powerful method to probe the neutrino anomaly is to repeat similar source experiments with more intense ν_e and $\bar{\nu}_e$ sources at a large low background detector like Borexino [3, 4, 5]. Thanks to the good energy and vertex resolution, it might even be possible to observe the characteristic neutrino oscillation pattern within the detector, if the Δm^2 is in the favored range of $1\,\mathrm{e}V^2$ and the mixing angle is not to small.

2 The Borexino detector

Borexino is a 300 t liquid scintillator detector designed for the real-time detection of solar neutrinos at the LNGS in Italy [6]. The detection of the solar ν_e is performed by neutrino electron scattering (NC+CC) and via the inverse beta decay (IBD) for the $\bar{\nu}_e$ geo-neutrinos. Borexino has provided a precise spectroscopy of solar neutrinos [7], including recently the first direct detection of the primary pp neutrinos from the Sun [8].

The Borexino detector consists of a nylon vessel with an diameter of 9.5 m (target area) surrounded by the buffer and water tank as shielding. The scintillation light originating from neutrino interactions are detected by 2,214 PMTs mounted on the so-called *stainless steel sphere.*

The inner nylon vessel contains the liquid scintillator composed from PC (pseudocumene, 1,2,4-trimethylbenzene) and PPO (2,5-diphenyloxazole) as a wavelength shifter. As part of a R&D effort, Borexino has reached an unprecedented radio-purity. Currently, the ^{238}U and ^{232}Th concentration is as low as 10^{-19} g/g. Other backgrounds include ^{85}Kr, ^{210}Bi and most importantly ^{210}Po. The energy response throughout the detector volume was carefully measured and calibrated by radioactive sources. At 1 MeV the energy resolution was determined to 4.5% and the vertex resolution is about 15 cm at 0.7 MeV [5].

3 Search for sterile neutrinos with the Borexino detector

The search for possible light sterile neutrinos can be performed by using either monochromatic neutrino sources like ^{51}Cr or ^{37}Ar, or by using intense anti-neutrino sources (^{144}Ce, ^{106}Ru or ^{90}Sr) with a continuous β-spectrum. The size of the source used by an experiment should be as compact as possible to observe the characteristic (anti-)neutrino oscillation pattern. The Borexino experiment will use the ^{144}Ce anti-neutrino source and possibly the ^{51}Cr neutrino source.

3.1 Anti-neutrino emitters in Borexino

During the first phase of the SOX project an anti-neutrino source with a continuous β-spectrum will be placed underneath the Borexino detector (8.25 m from the detector center). The detection of the $\bar{\nu}_e$ is then performed via the inverse beta decay (IBD), $p+\bar{\nu}_e \to e^+ + n$. The signature is provided by the positron annihilation (prompt signal) followed by the neutron capture on hydrogen (delayed signal). This coincidence allows an efficient way to suppress background and is often referred to as the golden channel of neutrino physics. The anti-neutrino detection was successfully applied for the geo-neutrino analysis [9] and is also widely used by other experiments [10]. A suitable $\bar{\nu}_e$ source must have $Q_\beta > 1.806\,\mathrm{MeV}$ (above the IBD threshold) and a half life long enough to allow the production and transportation of the source to the detector [11]. The Borexino collaboration has decided to use ^{144}Ce$-^{144}$Pr, which features $Q_\beta\left(^{144}Pr\right)$ of 2.996 MeV. ^{144}Ce can be extracted from spent nuclear fuel followed by column chromatography. Due to the high IBD cross-section [12] the source activity can be in the order of 100 kCi.

3.2 Neutrino emitters in Borexino

As a further option the deployment of a neutrino source underneath the Borexino detector is under consideration. For that purpose the ^{51}Cr source used by the GALLEX experiment could be refurbished. ^{51}Cr is an electron capture source, $^{51}\mathrm{Cr} + e^- \to {}^{51}\mathrm{V} + \nu_e$, featuring four monochromatic neutrino lines. In 81.6% (8.5%) of the time it decays to the ground state of ^{51}V and emits a 747 keV (752 keV) ν_e, while in 9% (0.9%) of the time a 427 keV (432 keV) ν_e is emitted to the first excited state of ^{51}V followed by the emission of a 320 keV γ. The dominant ν_e line is very similar to the 0.862 MeV ν_e from the radioactive decay of ^{7}Be in the Sun. The ^{51}Cr source will be produced by neutron irradiation of ^{50}Cr at nuclear reactors. Natural chromium consists mainly of ^{52}Cr (83.9%) and ^{53}Cr (9.5%). Since ^{53}Cr has a relatively large thermal neutron cross section of 18.7 barn, enriched ^{50}Cr has has to be used in order to reach the desired activity of 5-10 MCi.

3.3 Sensitivity and expected results

The analysis of short baseline neutrino oscillation in Borexino can be performed in two ways. The standard disappearance procedure is a rate analysis. If neutrino oscillation occur, the expected number of events with respect to the non-oscillation scenario will be lower. This technique relies on a precise knowledge of the source activity and background estimation. The second technique is called oscillometry and is an almost unique feature of the Borexino experiment or of a similar large liquid scintillator detector [5]. The physics potential of the SOX concept is shown in Figure 1. During the first phase the cerium source and possibly the chromium source will be placed underneath the detector. This will allow testing the parameter region currently favored by global fits. Depending on the results, the cerium source might also be placed inside the water tank or in the center of the detector.

4 Conclusion

The Borexino detector is an ideal candidate to search for sterile neutrinos. During the first phase of the experimental setup, an anti-neutrino source will be placed in a tunnel underneath the large low background detector Borexino. The source will arrive at the end of 2015 at the

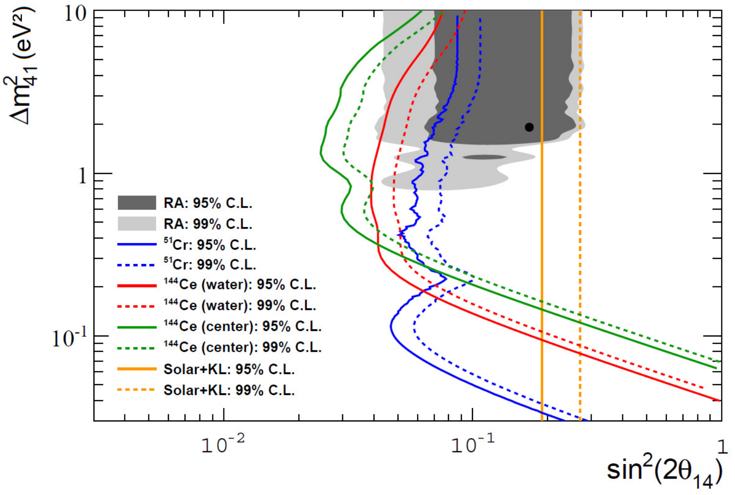

Figure 1: Sensitivity for the SOX project [3]. The cerium source sensitivity for the first phase (see text for details) is similar to the sensitivity of the shown chromium source.

Laboratori Nazionali del Gran Sasso. First results are expected in 2016. Additional physics of the SOX concept includes studies of the magnetic moment of the neutrino as well as the measurement of the Weinberg angle [3].

References

[1] G. Mention, M. Fechner, Th. Lasserre, Th.A. Mueller, D. Lhuillier, et al. The Reactor Antineutrino Anomaly. *Phys.Rev.*, D83:073006, 2011.

[2] C. Giunti, M. Laveder, Y.F. Li, Q.Y. Liu, and H.W. Long. Update of Short-Baseline Electron Neutrino and Antineutrino Disappearance. *Phys.Rev.*, D86:113014, 2012.

[3] G. Bellini et al. SOX: Short distance neutrino Oscillations with BoreXino. *JHEP*, 1308:038, 2013.

[4] B. Ricci N. Ferrari, G. Fiorentini. The Cr-51 neutrino source and Borexino: a desirable marriage. *Phys. Letters B*, 387:427–431, 1996.

[5] M. Pallavicini. The SOX project: a search for sterile neutrinos with BoreXino. *PoS*, Neutel2013:026, 2013.

[6] G. Alimonti et al. The Borexino detector at the Laboratori Nazionali del Gran Sasso. *Nucl.Instrum.Meth.*, A600:568–593, 2009.

[7] G. Bellini et al. Final results of Borexino Phase-I on low energy solar neutrino spectroscopy. *Phys.Rev.*, D89:112007, 2014.

[8] G. Bellini et al. Neutrinos from the primary proton-proton fusion process in the Sun. *Nature*, 512(7515):383–386, 2014.

[9] G. Bellini et al. Measurement of geo-neutrinos from 1353 days of Borexino. *Phys.Lett.*, B722:295–300, 2013.

[10] Y. Abe et al. First Measurement of θ_{13} from Delayed Neutron Capture on Hydrogen in the Double Chooz Experiment. *Phys.Lett.*, B723:66–70, 2013.

[11] Th. Lasserre. Testing the Reactor and Gallium Anomalies with Intense (Anti)Neutrino Emitters. *Nucl.Phys.Proc.Suppl.*, 235-236:214–219, 2013.

[12] P. Vogel and John F. Beacom. The angular distribution of the neutron inverse beta decay, $\bar{\nu}_e + \mathrm{p} \rightarrow \mathrm{e}^+ + \mathrm{n}$. *Phys. Rev.*, D60:053003, 1999.

The Hunt for neutrinoless double beta decay with the NEXT experiment

David Lorca[1] on behalf of the NEXT Collaboration

[1]Instituto de Fisica Corpuscular (IFIC), CSIC & Univ. de Valencia, E-46071 Valencia, Spain

DOI: http://dx.doi.org/10.3204/DESY-PROC-2014-04/65

The NEXT-100 detector will search for the neutrinoless double beta decay of ^{136}Xe using an electroluminescent high-pressure xenon gas TPC filled with 100 kg of enriched Xe. An observation of this hypothetical process would establish a Majorana nature for the neutrino and prove the violation of lepton number. A scaled-down prototype, NEXT-DEMO, has been built to demonstrate the feasibility of the technology. NEXT-DEMO includes an energy plane made of PMTs and a tracking plane made of SiPMs. X-ray energy depositions, produced by the de-excitation of xenon atoms after their interaction with gamma rays, have been used to characterize the detector response. With this method, the released energy by gammas coming from ^{22}Na source has been corrected, achieving an energy resolution of 5.691% FWHM and 1.62% FWHM at the 29.7 keV and 511 keV peaks respectively, which extrapolate to 0.62% FWHM and 0.73% FWHM at $Q_{\beta\beta}$ value of Xenon.

1 Introduction

Double beta decay ($\beta\beta$) is a very rare nuclear transition in which a nucleus with Z protons decays into a nucleus with Z+2 protons and same mass number A. It can only be observed in those isotopes where the β decay mode is forbidden due to the energy of the daughter nuclei being higher than the energy of the parent nuclei, or highly suppressed. Two decay modes are usually considered: the standard two-neutrino mode ($\beta\beta 2\nu$), which has been observed in several isotopes with typical half-lives in the range of $10^{18} - 10^{21}$ years [1], and the neutrinoless mode ($\beta\beta 0\nu$), which violates lepton-number conservation, and is therefore forbidden in the Standard Model of particle physics.

An observation of $\beta\beta 0\nu$ would prove that neutrinos are Majorana particles, that is, identical to their antiparticles [2], and would provide direct information on neutrino masses [1]. Besides, it would demonstrate that total lepton number is violated, a result that can be linked to the cosmic asymmetry between matter and antimatter through the process known as leptogenesis [3].

The half-life of $\beta\beta 0\nu$, if mediated by light, Majorana neutrino exchange, can be written as

$$(T_{1/2}^{0\nu})^{-1} = G^{0\nu} \left| M^{0\nu} \right|^2 m_{\beta\beta}^2 \tag{1}$$

where $G^{0\nu}$ is an exactly-calculable phase-space integral for the emission of two electrons; $\left| M^{0\nu} \right|$ is the nuclear matrix element of the transition, which has to be evaluated theoretically; and $m_{\beta\beta}$ is the effective Majorana mass of the electron neutrino:

$$m_{\beta\beta} = \left| \sum U_{ei}^2 m_i \right| \tag{2}$$

where m_i are the neutrino mass eigenstates and U_{ei} are elements of the neutrino mixing matrix.

The aim of all $\beta\beta0\nu$ experiments is to measure the decay rate of this disintegration. However, the measurement is limited by the experimental sensitivity of the detector employed, which can be expressed as

$$T_{1/2} \propto a \cdot \epsilon \cdot \sqrt{\frac{M \cdot t}{\Delta E \cdot B}} \tag{3}$$

where M is the isotope mass, ΔE is the energy resolution, B is the background rate, ϵ is the detection efficiency and a is a term which includes nuclear matrix elements [1].

Due to the presence of the two neutrino mode, together with background events which can fall in the energy Region of Interest (ROI) where the neutrinoless mode is expected, ΔE is a must to resolve the possible $\beta\beta0\nu$ events. In addition, an appropriate selection of detector components and surroundings should be done in such a way to reduce background rate as low as possible. Besides, current generation of $\beta\beta0\nu$ experiments have explored the region of neutrino masses corresponding to 160-250 meV (depending of n.m.e.) [4] by using from tens to a few hundred kilos of isotope mass. The non detection of a signal creates the necessity of increase the isotope mass in the new generation up to the ton scale to explore new areas.

2 The NEXT Concept

The NEXT experiment combines good energy resolution, a low background rate and the possibility to scale-up the detector to large masses of $\beta\beta$ isotope by using a high-pressure xenon gas (HPXe) electroluminescent (EL) time projection chamber (TPC) to search for $\beta\beta0\nu$ in ^{136}Xe.

Whit this technology, an energy resolution better than 1% FWHM can be achieved in NEXT at $Q_{\beta\beta}$ of Xe thanks to the small Fano Factor of gaseous xenon ($F_{HPXe} = 0.15 \pm 0.02$) [5], compared with other media such as liquid xenon (LXe) ($F_{LXe} \sim 20$), together with the low fluctuations introduced by an EL-based amplification. Besides, HPXe provides topological information of the events, allowing to discriminate between signal events (a twisted track of about 10 cm long, with two energy depositions at both ends) from background events (single electrons with only one blob at the end and most of the time accompanied by an X-ray [6]). Furthermore, ^{136}Xe constitutes 8.86% of all natural xenon, but the enrichment process is relatively simple and cheap compared to that of other $\beta\beta$ isotopes, thus making ^{136}Xe the most obvious candidate for a future multi-ton experiment.

The detection process in NEXT implies independent systems for tracking and calorimetry. Particles interacting in the HPXe transfer their energy to the medium ionizing and exciting its atoms. The excitation energy is manifested in the prompt emission of VUV ($\sim$ 178 nm) scintillation light. The ionization electrons drift toward the TPC anode thanks to the presence of a moderate electric field, entering in a region with an even more intense electric field. There, secondary VUV photons are generated isotropically by electroluminescence. Therefore both scintillation and ionization produce an optical signal, to be detected with a plane of PMTs (the energy plane) located behind a transparent cathode. The detection of the primary scintillation light constitutes the start-of-event, whereas the detection of EL light provides an energy measurement. Electroluminescent light provides tracking as well, since it is detected a few millimeters away from production at the anode plane, via an array of MPPCs (the tracking plane).

3 NEXT-DEMO: R&D and results

To demonstrate that the NEXT concept is feasible, a scaled prototype, NEXT-DEMO, was developed. NEXT-DEMO is a cylindrical pressure vessel made of stainless steel, able to withstand up to 20 bar of internal pressure. It is 60 cm long and 30 cm in diameter, and holds $\sim$ 1.5 kg of Xe at 10 bar. Three wire grids, the cathode, gate and anode, limit the two active regions of the TPC. The primary scintillation light is directly detected by a plane of 19 Hamamatsu R7378A PMTs behind the cathode grid. Electroluminescent light produced by ionization electrons, is once again detected in the energy plane but the forward going photons are also detected in an array of 256 tetraphenyl butadiene (TPB) coated Hamamatsu S10362-11-050P SiPMs. The tracking plane is used to reconstruct the position of energy deposits and, ultimately, the topology of an event as a whole.

In this prototype, the abundance of xenon K-shell X-ray emission during data taking with a ^{22}Na source has been identified as a multitool for the characterisation of the fundamental parameters of the gas as well as the equalisation of the response of the detector [7]. The advantage of using these events is that they are distributed all over the volume of the detector and the range of the $\sim$30 keV electrons produced is small, around 0.6 mm at 10 bar [8], releasing almost all their energy in a single point. Such depositions have been used to extract correction factors which describe the detector geometry effects. In addition, both loss of charge due to electron attachment with gas impurities and temporal fluctuations during the EL generation due to temperature and pressure oscillations have been corrected.

The mentioned corrections have been applied to the reconstructed energy released by gammas coming from a ^{22}Na (see [7]), where an energy resolution for the K$_\alpha$ peak (29.7 keV) and photopeak (511 keV) of (5.691 ± 0.003)% FWHM and (1.62 ± 0.01)% FWHM were extracted respectively. Independently extrapolating these two values to the ^{136}Xe $Q_{\beta\beta}$ assuming the dominance of photon shot noise Poisson statistics results in a predicted energy resolution at $Q_{\beta\beta}$ of 0.6256% FWHM and 0.7353% FWHM respectively.

4 NEXT-100

Following the previous ideas, the NEXT collaboration plans to build the NEXT-100 detector, described in [6], which will be formed by a HPXe TPC containing 100 kg of xenon, enriched at 90% in its ^{136}Xe isotope, at 15 bar. The pressure vessel is built with low activity stainless steel, and contains an inner copper shield, 12 cm thick and made of radio pure copper, to attenuate the radiation coming from the high-energy gammas emitted in the decays of ^{208}Tl and ^{214}Bi, present in the external detector. The energy measurement in NEXT-100 is provided by a total of 60 Hamamatsu R11410-10 photomultipliers (PMTs) covering 32.5% of the cathode area constitute the energy plane. This PMT model has been specially developed for radiopure, xenon-based detectors. The tracking function is provided by an array of around 7200 SiPMs, 1 cm pitch, located behind the EL region, and coated with TPB.

All materials present in the NEXT-100 detector have been chosen according to rigorous radiopurity requirements, which together with the detection technique employed by NEXT, produce an expected background rate of $5\cdot10^4$ counts/(kg·keV·year) [6]. After 5 years of data taking, a sensitivity of $5.9\cdot10^{25}$ years is predicted or, in terms of the effective neutrino Majorana mass $m_{\beta\beta}$, a value of around 100 meV, making NEXT one of the most competitive experiments in the field [9].

NEXT-100 is approved for operation in the Laboratorio Subterráneo de Canfranc (LSC), in Spain, where the installation of seismic platform, lead castle, gas system, emergency recovery system and vessel are already completed. Underground operations with non-enriched xenon will start in 2015 and the physics case with enriched xenon is planned for early 2016.

5 Conclusions

The search for $\beta\beta0\nu$ is one of the major current challenges in neutrino physics. Due to the high sensitivity provided by a HPXe TPC with EL amplification, NEXT-100 promises to be one of the leading experiments in the field, exploring the region of neutrino mass down to 100 meV. One of its prototypes, NEXT-DEMO, has demonstrated the main issues of such technology, helping in the design of the final detector. In addition, xenon K-shell X-ray depositions have been identified as a useful tool for the characterization of this type of detectors, providing the spatial calibration needed for close-to-optimal energy resolution.

Acknowledgments

This work was supported by the following agencies and institutions: the European Research Council under the Advanced Grant 339787-NEXT; the Ministerio de Economía y Competitividad of Spain under grants CONSOLIDER-Ingenio 2010 CSD2008-0037 (CUP), FPA2009-13697-C04 and FIS2012-37947-C04; the Director, Office of Science, Office of Basic Energy Sciences, of the US Department of Energy under contract no. DE-AC02-05CH11231; and the Portuguese FCT and FEDER through the program COMPETE, project PTDC/FIS/103860/2008.

References

[1] J. J. Gomez-Cadenas, J. Martin-Albo, M. Mezzetto, F. Monrabal and M. Sorel, "The Search for neutrinoless double beta decay," Riv. Nuovo Cim. **35**, 29 (2012) [arXiv:1109.5515 [hep-ex]].

[2] J. Schechter and J. W. F. Valle, "Neutrinoless Double beta Decay in SU(2) x U(1) Theories," Phys. Rev. D **25**, 2951 (1982).

[3] S. Davidson, E. Nardi and Y. Nir, "Leptogenesis," Phys. Rept. **466**, 105 (2008) [arXiv:0802.2962 [hep-ph]].

[4] A. Gando and others, "Limit on Neutrinoless $\beta\beta$ Decay of Xe-136 from the First Phase of KamLAND-Zen and Comparison with the Positive Claim in Ge-76," Phys.Rev.Lett., 110 (2013) [arXiv:1211.3863 [hep-ex]].

[5] David Nygren, "High-pressure xenon gas electroluminescent TPC for 0-ν $\beta\beta$-decay search," NIM A, 603, 337-348, (2009), [doi = "http://dx.doi.org/10.1016/j.nima.2009.01.222"].

[6] [NEXT Collaboration], "NEXT-100 Technical Design Report (TDR): Executive Summary," arXiv:1202.0721 [physics.ins-det].

[7] David Lorca and others, "Characterisation of NEXT-DEMO using xenon K_α X-rays," [arXiv:1407.3966 [hep-ex]].

[8] M. J. Berger and others, "Computer Programs for Calculating Stopping-Power and Range Tables for Electrons, Protons, and Helium Ions (version 1.2.3)," ESTAR, PSTAR and ASTAR (2005) ["http://physics.nist.gov/Star"].

[9] J. J. Gomez-Cadenas, J. Martin-Albo, M. Sorel, P. Ferrario, F. Monrabal, J. Munoz-Vidal, P. Novella and A. Poves, "Sense and sensitivity of double beta decay experiments," JCAP **1106**, 007 (2011), [arXiv:1010.5112 [hep-ex]].

The effect of Quantum Gravity on astrophysical Neutrino flavor observables.

Jonathan Miller[1], *Roman Pasechnik*[2]

[1]Departamento de Física Universidad Técnica Federico Santa María
Casilla 110-V, Valparaíso, Chile
[2]Theoretical High Energy Physics, Department of Astronomy and Theoretical Physics, Lund University, Sölvegatan 14A, SE 223-62 Lund, Sweden

DOI: http://dx.doi.org/10.3204/DESY-PROC-2014-04/180

At the quantum level, an interaction of a neutrino with a graviton may trigger the collapse of the neutrino flavor eigenstate to a neutrino mass eigenstate. We will present that such an essentially quantum gravity effect may have strong consequences for neutrino oscillation phenomena in astrophysics due to the relatively large scattering cross section of relativistic neutrinos off massive sources of gravitational fields (the case of gravitational Bethe-Heitler scattering). This results in a new technique for the indirect detection of gravitons by measuring the flavor composition of astrophysical neutrinos.

A theoretical extrapolation of fundamental Quantum Mechanics concepts to Einstein's gravity suffers from major difficulties with quantization of space-time, ultraviolet behavior and non-renormalizability of the resulting theory. Typically quantum gravity effects are disregarded as being irrelevant at energy scales smaller than the Planck scale, $M_{Pl} \sim 10^{19}$ GeV. Due to suppression, quantum gravity effects are referred to as unobservable [1, 2].

We propose a new approach for indirect experimental studies of (local) quantum gravity interactions based upon an effect on neutrino oscillation observables of a neutrino interaction with an energetic graviton. This may happen in large-angle energetic gravitational Bremsstrahlung off an astrophysical neutrino passing through an external classical gravitational potential. This gravitational Bethe-Heitler (GBH) process can be considered in the quasi-classical approxi-

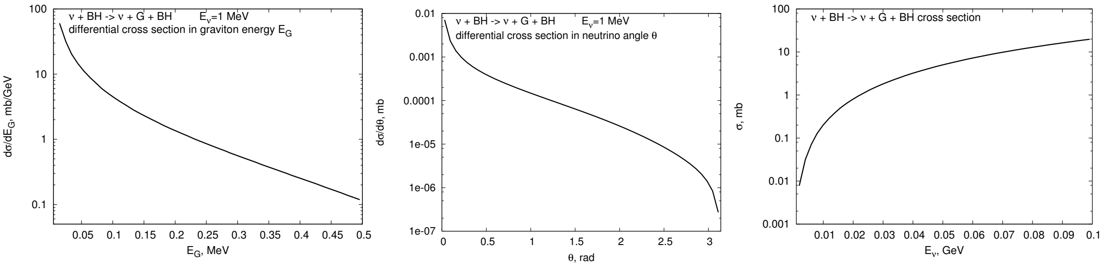

Figure 1: Differential cross section versus radiated graviton energy E_G (left), polar angle of the final-state neutrino θ_ν, and the integrated cross section as a function of incoming neutrino energy E_ν for GBH scattering of a neutrino off a massive object.

mation for large angle and/or large energy graviton emission (Born approximation). Such a process may happen with high probability, such as in the case of scattering off a massive source of gravitational field (star or a black hole). The neutrino interaction serves as a direct *quantum measurement* of the microscopic properties of the gravitational field at astrophysical scales.

Weakly-interacting neutrinos are an efficient carrier of information at astrophysical scales due to not being absorbed or scattered by interstellar mediums. This property of neutrinos enables us to utilize them for large-scale astrophysical *experiments*. In the identified experiment neutrinos *change* their quantum state due to a local quantum gravity process (in terms of local graviton coupling to a fundamental matter particle) and convey information about this process through the cosmological medium to Earth. Elementary particles in the mass basis are eigenstates of the Hamiltonian of quantum-gravitational interactions similar to how leptons and quarks are weak eigenstates in the flavor and CKM bases. The second important neutrino property that neutrino mass and flavor eigenstates are not the same.

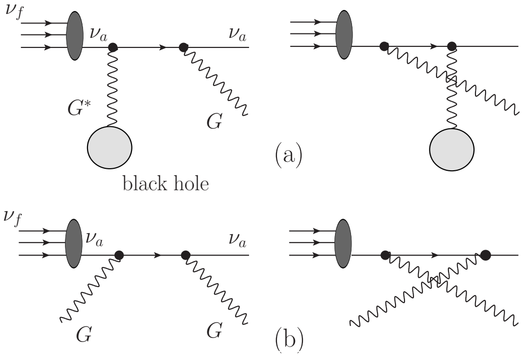

Figure 2: The quantum gravity processes which causes the decoherence of the neutrino flavor eigenstate ($f = e, \mu, \tau$) effectively converting it to a mass eigenstate ($a = 1, 2, 3$) – GBH scattering of neutrino off a massive object (a), and gravitational Compton scattering (b). The ellipse is a projection to a mass state and the circle is a classical source of gravitational field.

Consider a relativistic neutrino propagating in the gravitational potential of a static black hole. At the quantum level a graviton interacts only with a definite mass state (or gravitational mass eigenstate) $a = 1, 2$ or 3. Expressed equivalently definite mass eigenstates (propagating states) are conserved by the quantum gravity hamiltonian while superpositions, such as the flavor eigenstates, are not. Astrophysical neutrinos are initially produced in electroweak processes in a definitive flavor state, $f = e, \mu$ or τ, which are coherent superpositions of mass eigenstates. This neutrino is quantum mechanically observed by the energetic graviton as being in a definite mass state. This means that between the production in an astrophysical source and the detection in an Earth based detector, the neutrino exists in a definite mass state and has experienced *quantum decoherence*.

The neutrino is *converted* to mass state with a probability $P_{\nu_f \to \nu_a} = |\Psi_{\nu_f \to \nu_a}|^2$, given in terms of the corresponding wave function $\Psi_{\nu_f \to \nu_a}$ which projects out a flavor state ν_f onto a mass state ν_a and is typically expressed in terms of the corresponding PMNS mixing matrix element, $\Psi_{\nu_f \to \nu_a} = V_{af} e^{-i \frac{m_a^2}{2E_\nu} L}$.

We consider the case shown in Fig. 2(a), the graviton exchange is with negative momentum transfer squared $t = -q^2 < 0$ in the t-channel with the propagator stretched between the relativistic neutrino of mass m_ν and energy $E_\nu \gg m_\nu$ and a massive classical gravitational field source with mass $M \gg E_\nu$. The cross section has been calculated for the gravitational scattering of scalar particles with $M \gg m$ in [3]. We use their formula as a good approximation to estimate the neutrino-solar mass cross section numerically. In this case, as an order-of-magnitude estimate, the GBH cross section at the Born level behaves as

$$\sigma_{\mathrm{GBH}} \sim \frac{M^2 E_\nu^2}{M_{Pl}^6}\,, \quad M \gg E_\nu \gg m_\nu\,, \tag{1}$$

and thus may not be very small since the Planck scale suppression can be largely eliminated by having a mass M of a heavy classical source in numerator. In particular, for a solar mass object $M \sim 10^{57}$ GeV, we have $M^2/M_{Pl}^6 \sim 1$ GeV^{-4}, so there is no significant suppression of the cross section for relativistic neutrinos.

Note that the Bethe-Heitler calculation in QED to first order gives the correct cross section for photon Bremsshtrahlung for extended objects such as a nucleus as shown in Ref. [4]. Similarly, we expect that the GBH result for a point-like classical source should be roughly correct to first order for extended objects, like a star or dark matter distribution.

The traditional source of decoherence typically referred to in astrophysical neutrino oscillations studies can be called *propagation decoherence*. Here the neutrino mass states have separated or dispersed so that they no longer interfere at large distances from the production point. This source of decoherence depends on the energy resolution of the detection process, the energy of the neutrino, the masses of the neutrino mass states, and details of the production and detection processes. Beyond the characteristic length the propagating neutrino mass states no longer interfere during the interaction process [5].

Note that while the flux due to *quantum decoherence* is a flux of pure mass eigenstates, that in the propagation decoherence case the flux is not of pure mass eigenstates, but rather decoherent (spatially separated) mass eigenstates. No quantum measurement of the state of these neutrinos has taken place, and the neutrino still exists as a superposition of mass states. These two situations are the same when detected in the case where the flux does not pass through matter; in the case where the flux passes through matter, the effect due to matter is different for the two cases. In the *quantum decoherence* case, the neutrino flux experiences regeneration as fluxes of neutrinos in pure mass eigenstates. In the propagation decoherence case, the neutrino flux experiences regeneration as a superposition of mass eigenstates.

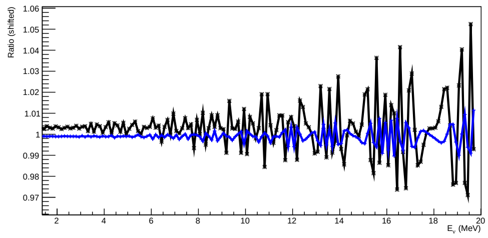

Figure 3: Ratio for neutrinos which have undergone propagation decoherence (blue) and neutrinos which have undergone graviton induced decoherence (black).

The theory of neutrino propagation, including neutrino propagation in medium and neutrino propagation where the neutrino experiences propagation decoherence, is well presented in [5] [6]. These papers give the essentials of neutrino propagation in matter and propagation decoherence, but no explicit formula is given for a neutrino which undergoes propagation decoherence and then experiences the Earth matter effect.

For simplicity consider just two regimes, the vacuum and the earth (with constant density) and two neutrino flavors. Due to the discontinuity at the earth's surface, the flavor amplitudes should be matched at the border between the two regimes. The flavor at the point before the density jump is used to determine the initial state [6].

The condition for the wave packet separation to be complete is given explicitly by [7]. They note that this is different than the effect due to averaging (Section 2.1) over the energy, despite the effect being computationally the same for vacuum[5]. We expect significant (> 1 km) wave packet separation for supernova more than 10 kpc distant.

The amplitude of the state at the boundary between regimes can be given by $A_{ee}^{dec} = \cos^2(\theta)\, e^{i\frac{3\pi}{4}} + \sin^2(\theta)\, e^{-i\frac{3\pi}{4}}$ and $A_{e\mu}^{dec} = \sin(\theta)\cos(\theta)\left(e^{-i\frac{3\pi}{4}} - e^{i\frac{3\pi}{4}}\right)$. These give the flavor amplitudes of a neutrino produced in a ν_e state which has travelled through vacuum and experienced wave packet separation when it reaches the Earth vacuum transition. An amplitude which depends on the phase between the wave packets would be incorrect for large wave packet separations. This amplitude is then projected to the new matter basis.

The ratio of neutrinos which have undergone *propagation decoherence* and at the same time propagated through a region of constant density to those which have only propagated through the vacuum is given by the following expression

$$\begin{aligned} R_p &= \Big(\cos(x_m)^2 (3+\cos(4\theta)) + (2+\cos(4\theta_m - 8\theta) + \cos(4\theta_m - 4\theta))\sin(x_m)^2 \\ &- 2\sin(2x_m)\sin(2\theta_m - 2\theta)\sin(2\theta)\Big)/(3+\cos(4\theta)). \end{aligned} \tag{2}$$

Analogically, the ratio of neutrinos which have undergone *quantum decoherence* in the presence of the matter effect (medium of constant density) to those which have propagated through the vacuum takes a different form

$$R_q = \frac{5+\cos(4\theta_m)+\cos(4\theta_m-4\theta)+\cos(4\theta)+4\cos(2x_m)\cos(2\theta)\sin(2\theta_m-2\theta)}{6+2\cos(4\theta)}. \tag{3}$$

A difference between the ratios R_p and R_q could be measurable and indicates the difference between *propagation decoherence* and *quantum decoherence* in the presence of the matter effect. Measurement of such a difference could serve as a clear example of graviton detection. In the presence of an additional jump in matter density the corresponding numerical results are presented in Fig.3, demonstrating that measurement of graviton induced decoherence is possible.

More details of this work can be found at [8] and this research was supported in part by the National Science Foundation under Grant No. NSF PHY11-25915 and by PROYECTO BASAL FB 0821 CCTVal and by Fondecyt (Grant No. 11130133).

References

[1] F. Dyson, *The World on a String*, review of *The Fabric of the Cosmos: Space, Time, and the Texture of Reality* by Brian Greene, New York Review of Books, Volume 51, Number 8, May 13, (2004);
F. Dyson, *Is a Graviton Detectable?*, Poincare Prize Lecture International Congress of Mathematical Physics Aalborg, Denmark, Aug. 6, 2012.

[2] T. Rothman and S. Boughn, Found. Phys. **36**, 1801 (2006).

[3] B. M. Barker, S. N. Gupta, J. Kaskas, Phys. Rev. 182 (1969) 1391-1396.

[4] H.K. Tseng, R.H. Pratt, Phys. Rev. A 19, 1525 (1979).

[5] M. Beuthe, Phys. Rept. **375**, 105 (2003) [hep-ph/0109119].

[6] M. Blennow and A. Y. Smirnov, Adv. High Energy Phys. **2013**, 972485 (2013) [arXiv:1306.2903].

[7] Y. Farzan and A. Y. Smirnov, Nucl. Phys. B **805**, 356 (2008) [arXiv:0803.0495].

[8] J. Miller and R. Pasechnik, [arxiv:1305.4430].

CANDLES – Search for Neutrino-less Double Beta Decay of ^{48}Ca –

S. Umehara[1], *T. Kishimoto*[1,2], *M. Nomachi*[1], *S. Ajimura*[1], *T. Iida*[1], *K. Nakajima*[1], *K. Ichimura*[1], *K. Matsuoka*[1], *T. Ishikawa*[1], *D. Tanaka*[1], *M. Tanaka*[1], *T. Maeda*[1], *S. Yoshida*[2], *K. Suzuki*[2], *H. Kakubata*[2], *W. Wang*[2], *V. T. T. Trang*[2], *W. M. Chan*[2], *M. Doihara*[2], *T. Ohata*[2], *K. Tetsuno*[2], *Y. Tamagawa*[3], *I. Ogawa*[3], *S. Tomita*[3], *G. Fujita*[3], *A. Kawamura*[3], *T. Harada*[3], *Y. Inukai*[3], *K. Sakamoto*[3], *M. Yoshizawa*[3], *K. Fushimi*[4], *R. Hazama*[5], *N. Nakatani*[5], *H. Ohsumi*[6], *K. Okada*[7]

[1]Research Center for Nuclear Physics, Osaka University, Ibaraki 567-0047, Japan
[2]Graduate School of Science, Osaka University, Toyonaka, Osaka 560-0043, Japan
[3]Graduate School of Engineering, University of Fukui, Fukui 910-8507, Japan
[4]Faculty of Integrated Arts and Science, The University of Tokushima, Tokushima 770-8502, Japan
[5]Faculty of Human Environment, Osaka Sangyo University, Osaka 574-8530, Japan
[6]Faculty of Culture and Education, Saga University, Saga 840-8502, Japan
[7]Department of Computer Science and Engineering, Kyoto Sangyo University, Kyoto 603-8555, Japan

DOI: http://dx.doi.org/10.3204/DESY-PROC-2014-04/97

CANDLES is the project to search for neutrino-less double beta decay of ^{48}Ca. Now we installed the CANDLES III system at the Kamioka underground laboratory. The CANDLES III system realizes the low background condition by a characteristic structure and data analyses for background rejection. Here we report performances of the CANDLES III system.

1 Double beta decay of ^{48}Ca

The neutrino-less double beta decay ($0\nu\beta\beta$) is acquiring great interest after the confirmation of neutrino oscillation which demonstrated nonzero neutrino mass. Measurement of $0\nu\beta\beta$ provides a test for the Majorana nature of neutrinos and gives an absolute scale of the effective neutrino mass. Many experiments have been carried out so far and many projects have been proposed.

Among double beta decay nuclei, ^{48}Ca has an advantage of the highest $Q_{\beta\beta}$-value (4.27 MeV). This large $Q_{\beta\beta}$-value gives a large phase-space factor to enhance the $0\nu\beta\beta$ rate and the least contribution from natural background radiations in the energy region of the $Q_{\beta\beta}$-value. Therefore good signal to background ratio is ensured in a $0\nu\beta\beta$ measurement. For the $0\nu\beta\beta$ measurement of ^{48}Ca, we proposed CANDLES(CAlcium fluoride for the study of Neutrinos and Dark matters by Low Energy Spectrometer) system[1].

2 CANDLES III at Kamioka observatory

We installed the detector system CANDLES III at the Kamioka underground laboratory (2700 m.w.e.). The CANDLES III system consists of 96 CaF_2(pure) scintillators with total mass of 305 kg and liquid scintillator with total volume of 2 m^3. The CaF_2(pure) scintillators, which are main detectors, are immersed in the liquid scintillator. The liquid scintillator acts as a $4\,\pi$ active shield to veto external backgrounds. Scintillation lights from the CaF_2(pure) and the liquid scintillator are viewed by 62 large photomultiplier tubes (13" × 48 and 20" × 14). The signal of the CaF_2(pure) scintillator has a decay time of 1 μsec although the liquid scintillator has a width of around a few tens nsec. Thus the signals from the CaF_2(pure) can be discriminated against the background signals on the liquid scintillator by observing pulse shapes.

3 Background in the $Q_{\beta\beta}$ region

As mentioned above, backgrounds can be strongly limited because of the highest $Q_{\beta\beta}$-value of ^{48}Ca. The remaining backgrounds are following processes:
(a) $^{212}\mathrm{Bi} \underset{\beta}{\longrightarrow} {}^{212}\mathrm{Po} \underset{\alpha}{\longrightarrow} {}^{208}\mathrm{Pb}$ (Th-chain)
(b) $^{208}\mathrm{Tl} \underset{\beta}{\longrightarrow} {}^{208}\mathrm{Pb}$(Th-chain)
(c) γ-ray from neutron capture
In this section we mention about study for the rejection of process (a) and (b).

^{212}Po nucleus in process (a) has short half-life 0.299 μsec. On the other hand, the CaF_2(pure) scintillator has long decay constant (~ 1 μsec). Thus radiations emitted by consecutive decays of ^{212}Bi and ^{212}Po are measured as one event in ADC gate (4 μsec) for the CaF_2(pure) scintillator. Energy deposited by the consecutive decays in the CaF_2(pure) scintillator is $E_{max} = 5.3$ MeV, because a quenching factor for α-ray is around 35%. Thus the process is serious backgrounds in a interesting energy window for the $0\nu\beta\beta$ measurement. In order to reject the events, we measured the pulse shape of the consecutive events by using the characteristic 500 MHz flash ADC. Details of the analyses are described in [2, 3]. As the result of the analyses, the background from process (a) will be reduced by the 3 orders of magnitude.

The other background candidate is process (b) of ^{208}Tl events. ^{208}Tl has large Q_β-value through it emits 2.6 MeV γ-ray. The probability which the high energy γ-rays are contained in a single CaF_2(pure) scintillator is small. However the $0\nu\beta\beta$ decay is extremely the rare process. Thus the background has to be seriously considered.

In order to reject the ^{208}Tl events, we applied a time correlation analysis. The ^{208}Tl events has a preceding α-decay with a half life of 3 minutes ($^{212}\mathrm{Bi} : E_\alpha = 6.1$ MeV). Thus we can reject the ^{208}Tl events by identifying the preceding α-ray. For identifying the α-ray, we need the good position resolution and the pulse shape discrimination between α- and γ-rays. Details of the analyses are shown in [4]. Based on techniques of the position reconstruction and the pulse shape discrimination, we applied the time correlation analysis for ^{208}Tl. The energy spectrum of the candidate events of the preceding α-rays is shown in figure 1-a). The peak at 1.7 MeV was likely due to the α-rays coming from the preceding ^{212}Bi decays. To confirm origin of the peak, we analyzed the distribution of time lag Δt between the preceding and the delayed events. The time lag Δt distribution of the preceding events with energy of 1.6 - 1.8 MeV is shown in figure 1-b). In order to obtain the half-life, we fitted the time spectrum with two exponential function. The half-life derived from the Δt distribution was 187 ± 56 sec. The half-life nearly agreed with one of ^{208}Tl(183 sec). Thus it was concluded that the peak at 1.7 MeV was due to

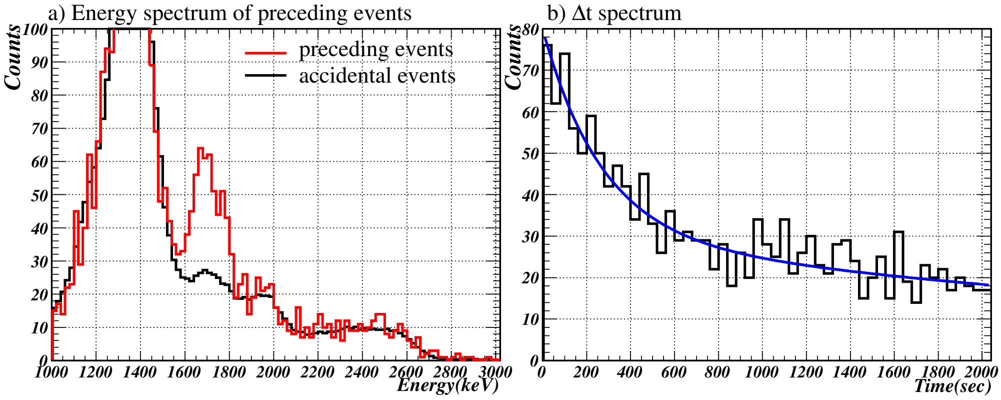

Figure 1: a) The energy spectra of the preceding events of ^{208}Tl. Red (black) line corresponds to the preceding (accidental) events. The peak at 1.7 MeV was due to ^{212}Bi decay (E_α = 6.1 MeV). b) Δt distribution between the preceding and delayed events. By fitting with two exponential function, we obtained the half-life of 187 ± 56 sec.

^{212}Bi α-rays and we found that ^{208}Tl can be rejected by the time correlation analysis.

As mentioned above, it is important to detect the preceding ^{212}Bi. Thus installation of a fast read-out DAQ system leads the good rejection efficiency for ^{208}Tl, because of least detecting loss in dead time. In early 2013 we installed a new DAQ system, of which read-out speed was improved 2.4 times as high as the previous one[5]. The dead time was decreased from 21% to 2%. As the result the event rate of the selected ^{212}Bi events was improved from 8.9±0.9 events/day to 12.7±0.7 events/day. This means that the rejection efficiency of ^{208}Tl was improved by 30%.

4 Analysis

In order to check the background rejection, we performed a pilot run. The criteria to select candidate events for $0\nu\beta\beta$ are given as follows.
(1) CaF_2(pure) scintillators fire.
(2) No liquid scintillator fires.
(3) The events are not process (a) events.
(4) The events are not candidate of the ^{208}Tl events of process (b).
As mentioned in section 2, criteria (1) and (2) are applied by using the pulse shapes difference between the CaF_2(pure) and liquid scintillators. Criteria (3) and (4) are described in section 3.

A selection of the candidate events was made for 4987 kg·days of data from Jun. to Sep. 2013. The energy spectrum using the 26 CaF_2(pure) scintillators, which are the high purity scintillators, is shown in figure 2. As the result, we observed 6 events in the $0\nu\beta\beta$ window of 4.17 - 4.48 MeV.

Here we estimated background rate in the $Q_{\beta\beta}$-value region. As mentioned above, the 3 processes are expected as the backgrounds in the $Q_{\beta\beta}$-value region. The background rate from process (a) and (b) was estimated by radioactivities of the CaF_2(pure) scintillators. The background rate was ∼ 1 event/4987 kg·days. In the CANDLES system, the other background candidate is γ-rays from neutron capture in the surrounding materials of the detector (process (c)). In order to estimate the background rate from neutron capture γ-rays, we performed a

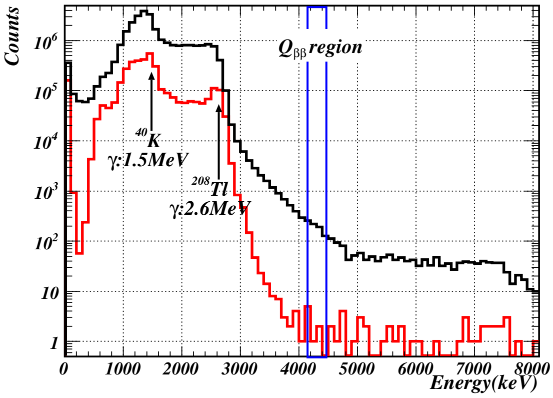

Figure 2: Energy spectra with/without the event selection. Black line represents an experimental data without the event selection. After the event selection, 6 events are seen in the $0\nu\beta\beta$ window.

special run using a ^{252}Cf neutron source. Based on the result of the special run and Monte-Carlo simulation, we estimated that the event rate from the γ-rays is 3.4 event/4987 kg·days. By using the expected background rate, we present an experimental sensitivity. The sensitivity with the 90 % C.L. is 0.8×10^{22} year.

5 Future perspective

In order to reduce the γ-rays from neutron capture, we plan to install a shielding system in the CANDLES III system in early 2015. The shielding system consists of boron/cadmium sheet and Pb blocks. We estimate to reduce the γ-ray rate by $\sim$ 2 orders of magnitude.

Other improvement for the CANDLES III system is a cooling system. The CaF_2(pure) scintillator is known that amount of light output increases with low temperature. The increasing rate of the light yield is 2%/°C. We have already installed the cooling system and will start operation of the system. We estimate to increase the light yield by 30%.

6 Conclusion

Now the CANDLES III system was installed at the Kamioka underground laboratory. By improvement of the detector system and the pulse shape analyses, we can reduce the background events from Bi $\rightarrow$ Po and ^{208}Tl. We performed the pilot run in order to check the background rate. The sensitivity of the $0\nu\beta\beta$ half-life is 0.8×10^{22} year with the pilot run . In near future we will upgrade the CANDLES III system to reduce the background rate. After the upgrade the sensitivity will be $\sim 10^{24}$ year for the $0\nu\beta\beta$ half-life.

References

[1] T. Kishimoto et al. In *Proc. of 4th Workshop on Neutrino Oscillations and their Origin*, page 338, 2003.

[2] S. Umehara et al. *Phys. Rev. C*, 78:058501, 2008.

[3] S. Umehara et al. *Physics Procedia*, in press.

[4] S. Umehara et al. *EPJ Web of Conferences*, 66:08008, 2014.

[5] K. Suzuki et al. *IEEE 19th REAL-TIME conference proceeding*, in press.

Precision measurement of ν_μ disappearance by T2K

Erez Reinherz-Aronis

Colorado State University, Fort Collins, Colorado, USA

DOI: http://dx.doi.org/10.3204/DESY-PROC-2014-04/165

T2K is a long-baseline neutrino oscillation experiment, where a muon neutrino beam is produced at the J-PARC facility and after traveling 295 km it is detected by Super-Kamiokande, a water Cherenkov detector with a 22.5 kton fiducial mass. One aim of the experiment is to precisely determine the mixing angle θ_{23} and the mass squared difference Δm^2_{23} using a measurement of muon neutrino disappearance. The T2K accumulated dataset is 6.57×10^{20} protons on target, which is 8% of the experimental goal. Here we present an analysis of the T2K muon neutrino disappearance data and the worlds best constraint on the value of the mixing angle θ_{23} obtained by this analysis.

1 Introduction

Neutrinos can be characterized by two different eigenstates states: Flavor eigenstates and Mass eigenstates. On one hand neutrinos production and detection is described by their flavor eigenstates, on the other hand neutrinos propagation through space is determined by their mass eigenstates. The relation between the flavor and mass states is given by the PMNS matrix [1, 2, 3, 4], which is a 3×3 unitary matrix, parametrized by 3 mixing angles and one phase. Moreover, it can be written as a multiplication of three 2D rotation matrixes. This commonly representation have been driven by the challenge to detect neutrinos.

The PMNS matrix has been tested by various experiments, different techniques, with different neutrino sources (such as solar, atmospheric, accelerator/reactor) and has been found to describe the relation between Flavor and Mass states to a good accuracy.

The probability of a muon neutrino with energy E_ν to remain a muon neutrino after traveling a distance L is given by

$$P(\nu_\mu \to \nu\mu) \simeq 1 - 4\cos^2\theta_{13}\sin^2\theta_{23} \cdot \left[1 - \cos^2\theta_{13} \cdot \sin^2\theta_{23}\right] \cdot \sin^2(1.267\Delta m^2 L/E_\nu) \qquad (1)$$

where θ_{13} and θ_{23} are the PMNS mixing angles and $\Delta m^2 (eV^2/c^4)$ is the neutrino mass-squared splitting. We note that the PMNS matrix depends on the difference between the neutrino masses (Δm^2) not on their absolute masses. Hence the absolute neutrino mass ordering is unknown. This is called the mass hierarch problem in neutrinos. In the case of three neutrinos there are two ways to order the masses, i.e the Normal Hierarchy (NH) and the Inverted Hierarchy (IH). In Eq. (1) the mass-squared split depends on the mass order and is $\Delta m^2_{32} = m^2_3 - m^2_2$

for the NH and $\Delta m^2_{13} = m^2_1 - m^2_3$ for the IH.

In these proceedings we present the recent T2K muon neutrino disappearance oscillation measurement with an accumulated data of 6.57×10^{20} protons on target (POT). This data has doubled since our previous measurement [5] and utilized the new near-detector selections samples which better constrain the measured neutrino charged current (CC) interactions.

2 T2K

Tokai-to-Kamioka (T2K) [6] is a neutrino oscillation experiment, located in Japan, with a baseline of 295 km. The experiment consists of a neutrino beam produced by the J-PARC lab, a near detector complex 280 m downstream of the target (ND280), and the well known Super-Kamiokande (SK) as its far detector (Figure (1) shows a profile of the T2K experiment setup) The neutrino beam is produced by colliding 30 GeV protons with a thick graphite target, creating charged mesons. The charged pions and kaons are then focused towards the axis of the proton beam by three magnetic horns and are directed into a decay volume, where they decay in-flight to muon neutrinos.

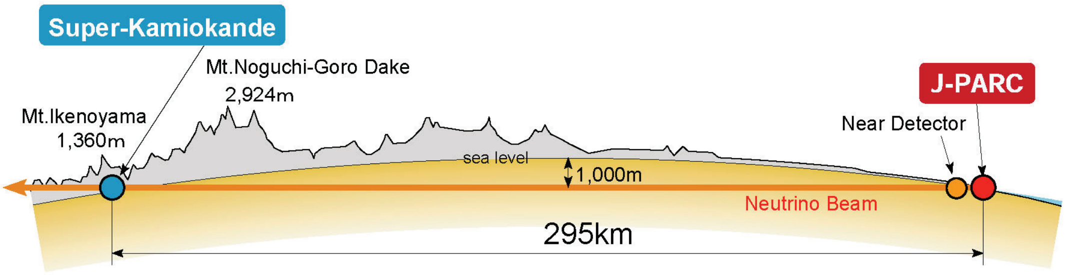

Figure 1: A schematic of a neutrinos traveling from the neutrino beamline at J-PARC, through the near detectors (green dot) which are used to determine the properties of the neutrino beam, and then 295 km underneath the main island of Japan to Super-Kamiokande.

T2K is an off-axis experiment, where its beam is directed 2.5˙ away from the target-SK line, this results and with neutrino energies that are peaked around the oscillation maximum (∼650 MeV) [7] and a smaller high energy tail, which are one of the main sources of backgrounds.

In the near detector complex the direction and stability of the beam is monitored by the on-axis INGRID detector [8]. The ND280 off-axis detectors [6], which have a similar opening angle as SK from the beam, are design to measure the unoscillated beam flux and energy spectrum for the SK (far detector) oscillation measurements.

3 Oscillation Analysis

The T2K analysis extracts the oscillation parameters using the near and far detector measurements. The near detector primarily measures and constrains the produced neutrino flux in order to predict the unoscillated neutrino rate at the far detector. Then the neutrino disappearance is determined by comparing the observed far detector neutrino rates to the predicted unoscillated neutrino rates. Fig. 2 shows the unoscillated expected numbers of events (blue) and the measured number of events (black) as a function of the neutrino energy. The far detector predictions depend on the input oscillation parameters, the unoscillated incident neutrino flux, the neutrino interaction cross sections and the detector response. A measurement of ν_μ CC events in ND280 is used to tune both the initial flux estimates and parameters of the neutrino interaction models. The measurement also estimates the uncertainties in the predicted neutrino spectrum at the far detector.

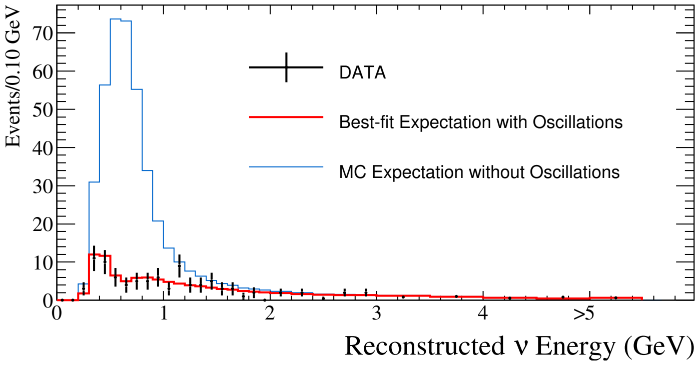

Figure 2: Reconstructed ν energy spectrum at the far detector for data (black), best-fit MC spectrum (red), and spectrum without oscillations (blue).

In this analysis, the ND280 measurement provides better constraints on the flux and interaction model parameters by using improved event selections, reconstruction, and higher ND280 statistics. This enhanced was achieved by dividing CC events into three categories based on the number of pions in the final state (for more detailed please see J. Perkin in these proceedings).

Source of uncertainty (number of parameters)	$\delta n_{SK}^{exp}/n_{SK}^{exp}$
ND280-independent cross section (11)	4.9%
Flux and ND280-common cross section (23)	2.7%
SK detector and FSI+SI systematics (7)	5.6%
$\sin^2\theta_{13}, \sin^2\theta_{12}, \Delta m^2_{21}, \delta_{CP}$	0.2%
Total (45)	8.1%

Table 1: The effect of 1 σ systematic parameter variation on the number of μ-like events, computed for oscillations with $\sin^2\theta_{23} = 0.5$ and $|\Delta m^2_{32}| = 2.40 \times 10^{-3}$ eV^2/v^4.

We estimated oscillation parameters using an unbinned maximum likelihood fit to the SK spectrum for the parameters $\sin^2\theta_{23}$ and either Δm^2_{32} or Δm^2_{13} for the NH and IH respectively. Oscillation probabilities are calculated using the full three-flavor oscillation framework with the other oscillation parameters are fit with constraints $\sin^2\theta_{13} = 0.0251 \pm 0.0035$, $\sin^2\theta_{12} = 0.312 \pm 0.016$, and $\Delta m^2_{21} = (7.50 \pm 0.20) \times 10^{-5}\mathrm{eV}^2/\mathrm{c}^4$ [9]. In addition, we have fitted 45 nuisance parameters (systematic uncertainties related to flux, cross section, final state nuclear effects and detector performance) which are summarized in Table 1 for the different uncertainties categories. Fig. 3 presents the ratio of the observed spectrum (points) to the unoscillation hypothesis, and our best fit (solid red line) to the data.

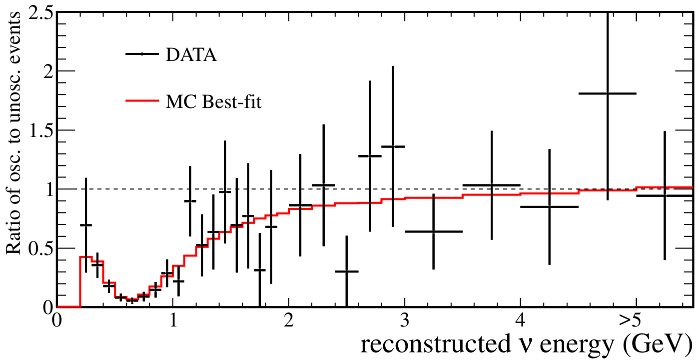

Figure 3: Ratio of far detector neutrino rates over the unoscillated neutrino rates as a function of neutrino energy for data (points) and MC expectations (red line) using the best-fitted neutrino parameters.

In Fig. 4 we present both the 68% and 90% C.L. confidence regions which were achieved using a Feldman-Cousins [12] and Cousins-Highland [13] alike methods which marginalizes over the second oscillation parameter. These limits are overlaid and compared to both MINOS [11] (hatch brown) and SK-atmospheric [10] (hatch blue) disappearance results.

4 Conclusion

T2K has made the most precise measurement of $\sin^2\theta_{23}$ using a data set based on 6.57×10^{20} POT. This measurement of $\sin^2\theta_{23} = 0.514^{+0.055}_{-0.056}$ ($\sin^2\theta_{23} = 0.511 \pm 0.055$) for the NH (IH) is consistent with maximal mixing. The best-fit mass-squared splitting is $\Delta m^2_{32} = 2.51 \pm 0.10$ ($\Delta m^2_{32} = 2.48 \pm 0.10$) $\times 10^{-3}\mathrm{eV}^2/\mathrm{c}^4$ for the case of the NH (IH).

References

[1] B. Pontecorvo, Sov. Phys. JETP **6**, 429 (1957) [Zh. Eksp. Teor. Fiz. **33**, 549 (1957)].

[2] B. Pontecorvo, Sov. Phys. JETP **7**, 172 (1958) [Zh. Eksp. Teor. Fiz. **34**, 247 (1957)].

[3] B. Pontecorvo, Sov. Phys. JETP **26**, 984 (1968) [Zh. Eksp. Teor. Fiz. **53**, 1717 (1967)].

[4] Z. Maki, M. Nakagawa and S. Sakata, Prog. Theor. Phys. **28**, 870 (1962).

[5] K. Abe *et al.* [T2K Collaboration], Phys. Rev. Lett. **111**, no. 21, 211803 (2013) [arXiv:1308.0465 [hep-ex]].

[6] K. Abe *et al.* [T2K Collaboration], Nucl. Instrum. Meth. A **659**, 106 (2011) [arXiv:1106.1238 [physics.ins-det]].

[7] K. Abe *et al.* [T2K Collaboration], Phys. Rev. D **87**, 012001 (2013) [arXiv:1211.0469 [hep-ex]].

[8] K. Abe, N. Abgrall, Y. Ajima, H. Aihara, J. B. Albert, C. Andreopoulos, B. Andrieu and M. D. Anerella *et al.*, Nucl. Instrum. Meth. A **694**, 211 (2012) [arXiv:1111.3119 [physics.ins-det]].

[9] J. Beringer *et al.* [Particle Data Group Collaboration], Phys. Rev. D **86**, 010001 (2012).

[10] A. Himmel [Super-Kamiokande Collaboration], AIP Conf. Proc. **1604**, 345 (2014) [arXiv:1310.6677 [hep-ex]].

[11] P. Adamson *et al.* [MINOS Collaboration], Phys. Rev. Lett. **112**, 191801 (2014) [arXiv:1403.0867 [hep-ex]].

[12] G. J. Feldman and R. D. Cousins, Phys. Rev. D **57**, 3873 (1998) [physics/9711021 [physics.data-an]].

[13] R. D. Cousins and V. L. Highland, Nucl. Instrum. Meth. A **320**, 331 (1992).

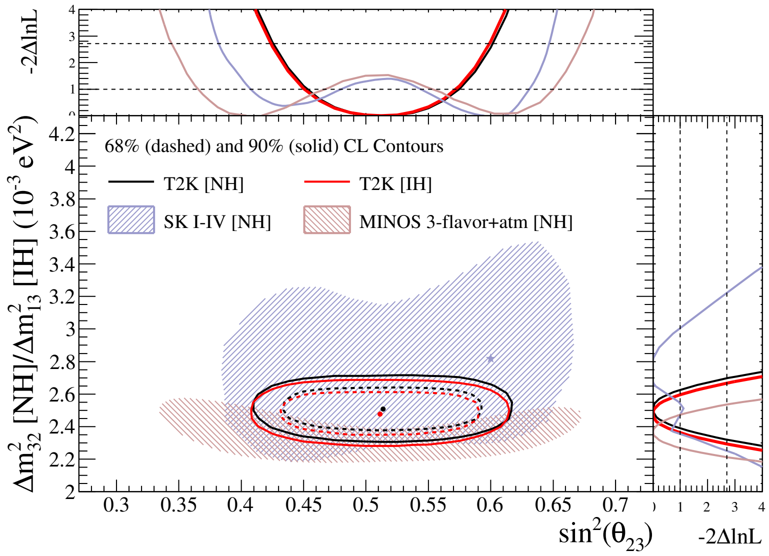

Figure 4: The 68% and 90% C.L. confidence regions for $\sin^2\theta_{23}$ and Δm^2_{32} (NH) or Δ^2_{13} (IH). The SK [10] and MINOS [11] 90% C.L. regions for NH are shown for comparison.

Recent Results from the T2K ND280 Detector

Jonathan Perkin[1] on behalf of the T2K collaboration

[1]The University of Sheffield, Department of Physics and Astronomy, Sheffield, S3 7RH, England

DOI: http://dx.doi.org/10.3204/DESY-PROC-2014-04/166

The T2K near detector complex, ND280, is located at the J-PARC accelerator facility in Tokai, Japan, 280 m downstream from the target. These proceedings will summarise recent physics results from ND280.

1 Introduction

T2K is a long-baseline neutrino oscillation experiment based in Japan designed to look for $\nu_\mu \to \nu_\mu$ disappearance and $\nu_\mu \to \nu_e$ appearance. In 2013 T2K reported [1] the discovery of ν_e appearance from a pure ν_μ beam. The beam is produced from the in-flight decay of pions and exploits the pion decay kinematics by positioning its detectors 2.5° off the beam axis. This improves the monochromaticity of the resulting ν_μ energy spectrum, reduces its high energy tail and selects a peak energy close to the ν_μ oscillation maximum for the 295 km T2K baseline. In order to quantify oscillations one must first predict the expected neutrino interaction rate and flavour composition, in the absence of oscillations, at some fixed baseline from the beam origin. In T2K this is facilitated by a near detector complex at 280 m from the graphite target used to produce the ν_μ beam. The off-axis near detector, ND280 and on-axis near detector, INGRID are used to constrain the neutrino flux and cross section parameters of the JPARC neutrino beam. Additionally, due to the large number of target materials present in the ND280 complex, it can provide information on neutrino-nucleon cross sections at energies around 1 GeV.

2 Off-axis near detector: ND280

The near detector at 280 m, ND280, illustrated in Figure 1, sits 2.5° from the beam axis and comprises a dedicated upstream, scintillator-based, π^0 detector (P0D) followed by a tracker region composed of three gaseous time projection chambers (TPCs) interleaved with two 0.8 ton fine grained scintillator detectors (FGDs). The P0D, TPCs and FGDs are surrounded by hermetic electromagnetic lead/scintillator sampling calorimeters (ECALs). A large electromagnet surrounds these sub-detectors, providing a 0.2 T field. The gaps in the flux-return are instrumented with scintillating paddles for muon tagging and constitute the side muon-range detector (SMRD). The P0D can be operated with or without a passive water target in order to permit on-water or on-carbon rate and cross section measurements. Additional target materials can be found in the two scintillator/brass sampling calorimeter sub-modules either side of the central P0D fiducial volume. The FGDs are scintillator based calorimeters with FGD1 having a pure hydrocarbon target mass and FGD2 containing a passive water target, again permitting on-carbon and on-water rate and cross section measurements. The large fiducial mass of lead in the ECALs can further be exploited for cross section studies, investigations into interactions on gaseous argon atoms in the TPC are currently underway.

3 T2K near detector constraint

Before ND280 can constrain the neutrino flux and cross section parameters, models of each must first be constructed. The T2K flux prediction [2] is derived from *in-situ* measurements of the proton beam and on-axis measurements of the neutrino beam, coupled with Monte Carlo (MC) simulations of the neutrino flux. The GEANT3/FLUKA based flux simulation is itself tuned using external data from hadron production experiments including NA61/SHINE. The official T2K MC event generator (NEUT) takes the flux prediction as an input and is subsequently used to predict neutrino interaction rates and flavour composition at the near and far detectors. NEUT cross section models are tuned to external lepton and pion scattering data. Uncertainties on NEUT cross section models are calculated [1] by varying model parameters such as axial-mass, fermi-momentum and binding energy (and their respective shapes and normalisations) in fits to external data from experiments such as MiniBooNE.

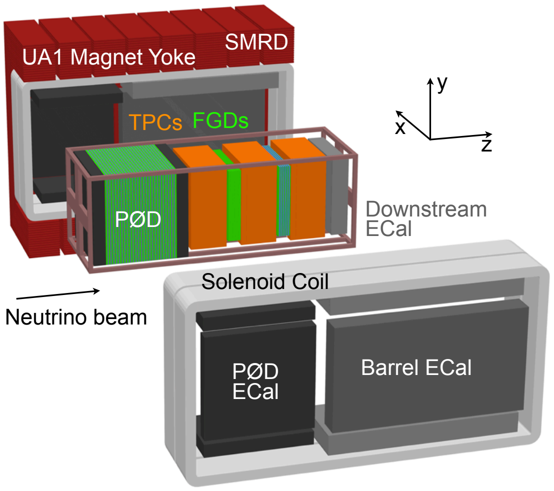

Figure 1: ND280: the T2K off-axis near detector at 280 m.

The ND280 constraint makes use of an inclusive charged current (CC) event sample which is classified according to three final state topologies: CC0π, CC1π^+ and CCOther. The CC0π subsample is predominantly composed of CC quasi-elastic (CCQE) events (i.e. the $\nu_l + n \rightarrow l^- + p$ signal channel at the far detector), the CC1π^+ sample is 40% resonant pion production ($\nu_l + p \rightarrow l^- + \pi^+ + p$) and CCOther, which is dominated by the deep inelastic scattering ($\nu_l + N \rightarrow l^- + N' + \pi^\pm + \pi^0 + ...$) component, covers all remaining toplogies. In each case the events require a reconstructed muon track in the fiducial volume of FGD1, which is identified by tagging the scattered lepton according to its energy loss in the TPCs. The efficiency (purity) of selecting CC0π, CC1π^+ and CCOther events are 50.1% (72.6%), 29.5% (49.4%) and 35.2% (73.8%) respectively. The inclusive CC selection, measured by ND280, is subsequently used to reweight the flux prediction at the far detector. The effect of applying the ND280 constraint on T2K systematic uncertainties is shown in Table 1. Contributions to the flux and cross section uncertainty that are correlated between near and far detectors are constrained by ND280. Systematics arising from differences in near and far detector target nuclei and hadronic interactions are not. In total there are 25 beam parameters, 21 cross section parameters and 210 ND280 systematic parameters in the fit. The far detector systematic is independent of the ND280 constraint. The ND280 constraint reweights 22 far detector flux parameters and 5 shared cross section parameters. After applying the ND280 constraint, the uncorrelated flux and cross section uncertainties remain the dominant contribution to the total T2K systematic.

Source	$\delta N_{\nu_\mu}/N_{\nu_\mu}$	$\delta N_{\nu_e}/N_{\nu_e}$
ND280 constrained flux + cross section	21.8%(2.7%)	26.0%(3.1%)
Uncorrelated flux + cross section	5.0%	4.7%
Hadronic interactions	3.0%	2.4%
Far detector systematic	4.0%	2.7%
Total	23.5%(7.7%)	26.8%(6.8%)

Table 1: Fractional error ($\delta N/N$) of the predicted number of ν_μ and ν_e events at the T2K far detector without (with) the near detector constraint.

4 Measuring the intrinsic ν_e component of the beam

There is an irreducible ν_e contamination of the JPARC ν_μ beam arising from muon and kaon decays. It is important to measure and constrain this effect using ND280 as it affects the predicted ν_e rate at the far detector. The CC inclusive ν_e selection, using particle identification in the TPCs and ECALs, is split into two different event classifications: CCQE-like and CCnonQE-like, with a constraint imposed using *in-situ* $e^{\pm}$ control samples. The T2K MC prediction is of a 1.2% ν_e component in the ν_μ beam [3]. The number of measured ν_e events $N_{\nu_e}^{\text{meas}}$ compared to the number predicted by MC $N_{\nu_e}^{\text{MC}}$ gives a ratio $N_{\nu_e}^{\text{meas}}/N_{\nu_e}^{\text{MC}} = 1.01 \pm 0.10$. Electron neutrinos coming from muon and kaon decay are also measured separately, resulting in ratios of $N_{\nu_e}^{\text{meas}}/N_{\nu_e}^{\text{MC}} = 0.68 \pm 0.30$ and $N_{\nu_e}^{\text{meas}}/N_{\nu_e}^{\text{MC}} = 1.10 \pm 0.14$, respectively.

5 Cross section measurements

T2K has performed the first measurement of CC inclusive ν_μ interactions on carbon at neutrino energies of ~1 GeV [4]. The measurement is reported as a flux-averaged double-differential cross section, binned in muon momentum and angle. The data used were taken in 2010 and 2011, with a total of 10.8×10^{19} protons-on-target (POT). The analysis is performed on 4485 inclusive CC candidate events selected in FGD2. The flux-averaged total cross section is measured to be $\langle\sigma_{\text{CC}}\rangle_\Phi = (6.91 \pm 0.13(\text{stat}) \pm 0.84(\text{syst})) \times 10^{-39}\text{cm}^2/\text{nucleon}$ for a mean ν_μ energy of 0.85 GeV.

Additionally, ND280 has made the first differential cross-section measurements of CC inclusive ν_e interactions on carbon at neutrino energies of ~1 GeV [5]. The measurement is reported as a function of electron momentum, electron scattering angle and four-momentum transfer of the interaction. The flux-averaged total cross section measured to be $\langle\sigma_{\text{CC}}\rangle_\Phi = (1.11 \pm 0.09(\text{stat}) \pm 0.18(\text{syst})) \times 10^{38}\text{cm}^2/\text{nucleon}$ for a mean ν_e energy of 1.3 GeV. A data sample with a total of 5.90×10^{20} POT was analysed. The differential and total cross section measurements agree with the predictions of the NEUT and GENIE MC event generators. The NEUT prediction is 1.23×10^{38} cm^2/nucleon and the GENIE prediction is 1.08×10^{38} cm^2/nucleon. The total ν_e charged-current cross section result is in agreement with data from the Gargamelle experiment. The total flux-averaged cross sections for ν_μ and ν_e on carbon, along with their respective NEUT and GENIE MC expectations are plotted in Figure 2.

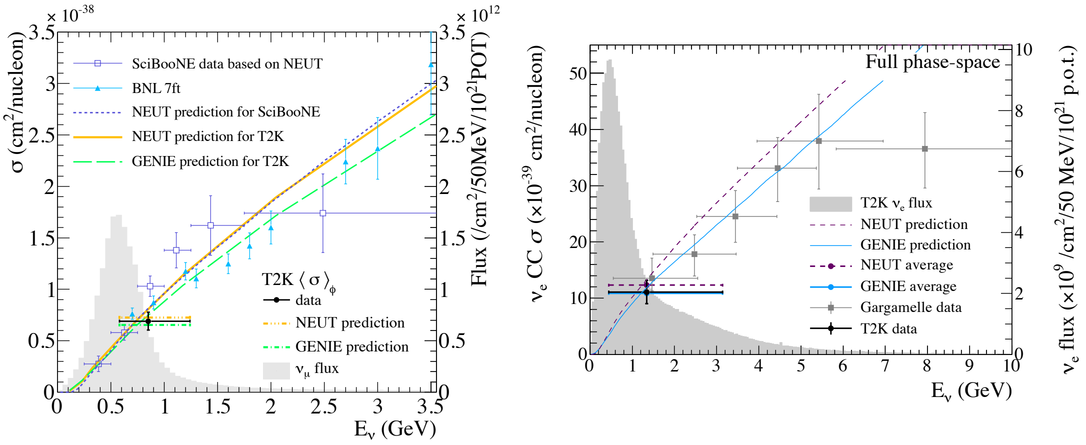

Figure 2: Total flux-averaged cross section for ν_μ *(left)* and ν_e *(right)* on carbon with MC expectations from NEUT and GENIE.

The on-axis interactive neutrino grid (INGRID), also located at the ND280 complex has measured the CC inclusive ν_μ cross section on iron and hydrocarbon [6] for a mean neutrino energy of 1.51 GeV. The flux-averaged total cross sections are $\langle\sigma_{\mathrm{CC}}\rangle_\Phi = (1.444 \pm 0.002(\mathrm{stat})^{+0.189}_{-0.157}(\mathrm{syst})) \times 10^{38}\mathrm{cm}^2/\mathrm{nucleon}$ and $\langle\sigma_{\mathrm{CC}}\rangle_\Phi = (1.379 \pm 0.009(\mathrm{stat})^{+0.178}_{-0.147}(\mathrm{syst})) \times 10^{38}\mathrm{cm}^2/\mathrm{nucleon}$ respectively, with a ratio of $1.047 \pm 0.007(\mathrm{stat}) \pm 0.035(\mathrm{syst})$.

6 Conclusions and outlook

The T2K near detector complex is essential to constrain the flux and cross section parameters that are correlated between the near and far detectors. Additionally, it provides an accurate measurement of the intrinsic, irreducable ν_e contamination. As more data are acquired, a rich sample of neutrino-nucleon cross section measurements are becoming accessible. Such measurements not only enhance the precision of T2K oscillation results, but also provide important constraints for other experiments in the field.

References

[1] K. Abe *et al.* (T2K Collaboration), Phys. Rev. Lett. **112**, 061802 (2014).

[2] K. Abe *et al.* (T2K Collaboration), Phys. Rev. D **87**, 012001 (2013).

[3] K. Abe *et al.* (T2K Collaboration), Phys. Rev. D **89**, 092003 (2014).

[4] K. Abe *et al.* (T2K Collaboration), Phys. Rev. D **87**, 092003 (2013).

[5] K. Abe *et al.* (T2K Collaboration), arXiv:1407.7389 (2014).

[6] K. Abe *et al.* (T2K Collaboration), Phys. Rev. D **90**, 052010 (2014).

Recent Results from MINERvA

Jonathan Miller[1] for the MINERvA Collaboration

[1]Departamento de Física Universidad Técnica Federico Santa María
Casilla 110-V, Valparaíso, Chile

DOI: http://dx.doi.org/10.3204/DESY-PROC-2014-04/158

MINERvA (Main INjector ExpeRiment for v-A) is a few-GeV neutrino nucleus scattering experiment at Fermilab using various nuclei as targets. The experiment provides measurements of neutrino and anti-neutrino cross sections off of nuclear targets which are important for neutrino oscillation experiments and the probing of the nuclear medium. Presented are recent results from MINERvA on quasi-elastic, inclusive charged-current neutrino scattering, and pion production processes.

The MINERvA physics program is a broad based particle and nuclear physics program to measure important cross sections and channels for other particle physics experiments like IceCube and NOvA, and to use the neutrino to probe the weak component of nucleon and nuclear structure. For both, measurements in the range of 1-20 GeV are necessary, as this is where the complementary electromagnetic and hadronic data exists from nuclear physics and is the energy range that many neutrino experiments are sensitive. The results presented in these proceedings are available [1, 2, 3], where more detail on the analysis and the results may be obtained.

These first results from MINERvA include coherent pion production [1], charged pion production [2], and inclusive charged current cross section ratios [3]. These results are relevant for the analyses of neutrino experiments such as T2K and provide important input into understanding the effects of nuclear structure.

MINERvA is an experiment situated at Fermilab, near Chicago in the United States. It utilises the NuMI beam line in order to measure neutrino-nuclear cross sections at neutrino energies of between 1.5 and 20 GeV. The results presented here include data from the Low Energy (LE) run with median energy of 3.5 GeV, future results will include data from the Medium Energy (ME) run with median energy of 5.7 GeV.

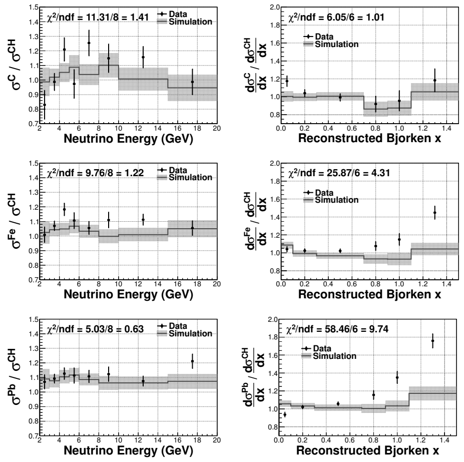

Figure 1: The ratios of the differential cross section per nucleon with respect to reconstructed bjorken x and of the cross section per nucleon depending on reconstructed energy (E_ν) for Pb, Fe, and C relative to CH. The error bars in data are statistical and in simulation are systematic. The calculation for χ^2 includes correlations. Events not shown with $x >$ 1.5.

The MINERvA detector[4] consists of a target region with 5 nuclear targets. Each target consists of a module with passive targets consisting of lead (Pb), iron (Fe), and graphite (C) and is separated by 4 active tracker modules. Downstream is an active tracker region. Active modules are made up of strips of plastic scintillator (CH) aligned in three orientations. Down stream of this region are the electromagnetic and hadronic calorimeters, with scintillator surrounded by iron and lead to induce energy loss. Downstream (2m) of the MINERvA detector is the MINOS near detector, a magnetised iron spectrometer.

The recent results from MINERvA have utilised charged current interactions in the neutrino and anti-neutrino datasets. The selection of charged current events are those where the muon travels from the interaction vertex through the MINERvA detector (leaving a minimum ionising track) and into the MINOS detector. MINOS serves as a muon spectrometer, and is used for a precise measurement of the muon momentum and charge. Two of the results presented here have charged pions in the final state. Charged pions may be identified using the deposited energy along the track, and by the observation of a Michel electron ($\pi \to \mu \to e$) at the end of the track in the tracker or electromagnetic calorimeter region. Details about basic tracking and vertex determination may be found in [4].

The charged current cross section, where a lepton (in MINERvA's case, a muon) is in the final state, are the most important cross sections to the neutrino physics program. Measuring the inclusive ratio of the cross sections of the main nuclear targets in MINERvA (0.628 tons of Fe, 0.711 tons of Pb, 0.159 tons of C, and 5.48 tons of CH), provides a flux independent probe of the structure of the nucleus. To have a well understood acceptance at all nuclear targets, the reconstructed neutrino energies are restricted to being above 2 GeV and the reconstructed muon angles to being less than 17°. The hadronic energy of the event E_h is calculated by the calorimetric sum not associated with the muon track. This allows the reconstruction of the kinematic variables $E_\nu = E_\mu + E_h$, $Q^2 = 4E_\nu E_\mu \sin^2(\theta_\mu/2)$, and $x = Q^2/(2M_N E_h)$. In this inclusive event selection, the GENIE sample is not dominated by any one process or classification (such as deep inelastic scattering (DIS)). The data used for this analysis consisted of $2.94e20$ protons on target (pot) in the neutrino configuration.

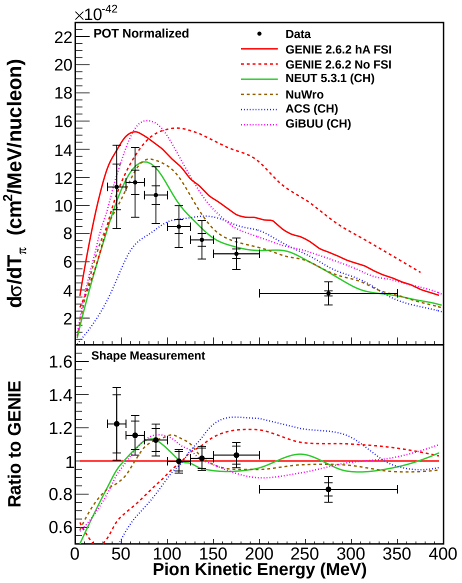

Figure 2: The charged pion differential cross section with respect to pion kinetic energy (top) and the ratio of this cross section to that predicted by GENIE with FSI normalised to the measured integral (bottom). Included are predictions from GENIE, ACS[7], NEUT[8], GiBUU[9] and NuWro[10]. Shown are the statistical uncertainty (inner error bars) and total uncertainty (outer error bars).

The results of this inclusive charged current ratios are shown in Fig. 1. The ratios of the cross section depending on reconstructed neutrino energy show broad agreement with the GENIE simulation, however, the differential cross section with respect to reconstructed bjorken x shows disagreement. This disagreement is a suppression at low x and enhancement at high

x, and the overall level changes as a function of the number of nucleons in the nucleus with the high x point showing agreement for the C over CH ratio and the low x point showing agreement for the Pb over CH ratio. The difference between data and simulation at low x may be due to poorly modelled nuclear shadowing effects. At high x most of the events are quasielastic, and so improvements in nuclear scaling models from the quasielastic to the deeply inelastic regime may be required.

A common case of charged current scattering is where a pion is produced. This is important to current and future long baseline experiments. Charged current pion production becomes convoluted with quasielastic scattering due to final state interactions (FSI) possibly causing the absorption of the pion in the nucleus causing the signature to appear quasielastic like. Models for the nuclear interactions which the produced pion may undergo are included in various generators/models including GENIE, ACS, NEUT, GiBUU and NuWro and the pion may undergo absorption, scattering, and charge exchange. The MiniBooNE measurement of this cross section shows agreement with the generators when they do not include FSI for pions with kinetic energy of 20 to 400 MeV (pions likely produced by delta decays)[5]. The charged current pion production differential cross section with respect to pion kinetic energy was measured by selecting events with a charged muon and at least one pion. The reconstructed pion provides the pion kinetic energy and the angle the pion travels with respect to the beam. To select events with only a single produced pion, a cut on the invariant mass (W) is used. The muon energy (E_μ), angle (θ_μ), and hadron energy (E_h) were used to reconstruct the invariant mass using the equations: $E_\nu = E_\mu + E_h$,$Q^2 = 2E_\nu(E_\mu - |\vec{p}_\mu|\cos\theta_\mu) - m_\pi^2$, and $W^2 = M_p^2 - Q^2 + 2M_pE_h$.

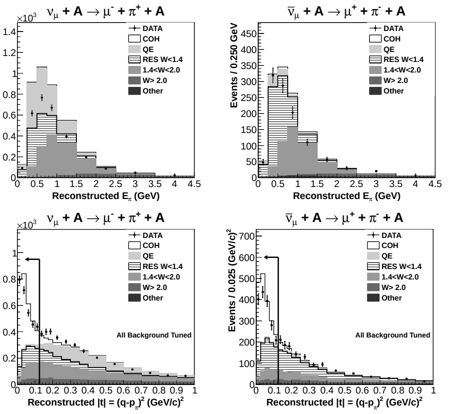

Figure 3: The top two plots show reconstructed energy in the $0.2 < t < 0.6$ (GeV/c)^2 sideband for the ν and $\bar{\nu}$ datasets. On the bottom is reconstructed t after background tuning. The shape in t near 0 is determined by the resolution.

The results of the measurement of charged pion production are shown in Fig. 2. Models of interactions within the nucleus cause pions to *migrate* to lower energies through scattering or be suppressed due to absorption or charge exchange. The shape is particular sensitive to such effects, and demonstrates that the models included in the favoured generators give broad agreement with the data when the generators include FSI for pions for pions with kinetic energy between 20 and 400 MeV. These results come from $3.04e20$ pot in the neutrino configuration.

Coherent pion production is the production of a pion after the neutrino scatters off the entire nucleus leaving the nucleus unchanged. It is characterised by a small momentum exchange between the nucleus and the system of the leptons and produced pion. The theory in this regime is not well understood, and many different approaches are included in neutrino event generators. This process is important in the analysis of accelerator neutrino experiments where this process is a background to the desired quasielastic signal, in these experiments the analyses use neutrino event generators to interpret their data and understand their background. A measurement of coherent charged pion production constrains the neutrino event generators for these processes and so improves the aforementioned analyses.

The coherent pion events were selected by requiring a charged pion and muon in the final state and little activity in the vertex region. The measured transferred four momentum (t) is required to be small. Other backgrounds are constained by use of a high t sideband. This provides a selection of model independent coherent pion production events and allows the study of the differential cross section with respect to pion angle and energy. As shown in Fig. 3, the background in the sideband region was tuned to the data correcting the incoherent background which was subtracted from the low t sample providing a sample of coherent pion events.

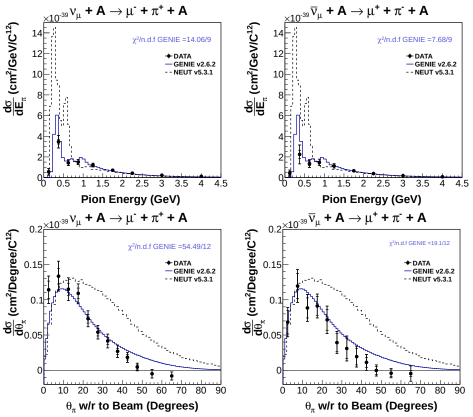

Figure 4: Shown is $\frac{d\sigma}{dE_\pi}$ on top and $\frac{d\sigma}{d\theta_\pi}$ on bottom with inner error bars showing the statistical uncertainty and outer error bars showing the total uncertainty. The χ^2 compares the data versus bin averaged cross sections from GENIE[6].

The coherent pion differential cross section is shown in Fig. 4 versus both pion angle and pion energy. Here the pion angle with respect to the beam is more forward than that of the commonly used Rein-Sehgal model in GENIE[6].

In conclusion, MINERvA has made important contributions to understanding the neutrino-nucleon interactions in the moderate energies (1-10 GeV) which are crucial to accelerator and atmospheric based neutrino experiments. Measurements of the pion production cross section and the ratio of the inclusive scattering cross section show broad agreement with the generators. The behaviour of the ratio of the cross section with respect to Bjorken x is not well modelled in the generator and requires theoretical input. Also, the pions produced in coherent pion production are more forward scattering than what exists within the generators. The start of the ME run has provided much larger statistics for future measurements studying nuclear structure and neutrino cross sections.

J.M. was supported by the National Science Foundation under Grant No. NSF PHY11-25915 and by PROYECTO BASAL FB 0821 CCT-Val and by Fondecyt (Grant No. 11130133) during the completion of this report.

References

[1] A. Higuera, A. Mislivec, L. Aliaga, O. Altinok, A. Bodek, A. Bravar, A. Butkevich and M. F. Carneiro *et al.*, arXiv:1409.3835.

[2] B. Eberly *et al.* [MINERvA Collaboration], arXiv:1406.6415.

[3] B. G. Tice *et al.* [MINERvA Collaboration], Phys. Rev. Lett. **112**, 231801 (2014) [arXiv:1403.2103].

[4] L. Aliaga *et al.* [MINERvA Collaboration], Nucl. Instrum. Meth. A **743**, 130 (2014) [arXiv:1305.5199].

[5] A. A. Aguilar-Arevalo *et al.* [MiniBooNE Collaboration], Phys. Rev. D **83**, 052007 (2011) [arXiv:1011.3572].

[6] C. Andreopoulos, A. Bell, D. Bhattacharya, F. Cavanna, J. Dobson, S. Dytman, H. Gallagher and P. Guzowski *et al.*, Nucl. Instrum. Meth. A **614**, 87 (2010) [arXiv:0905.2517].

[7] M. Sajjad Athar, S. Chauhan and S. K. Singh, Eur. Phys. J. A **43**, 209 (2010) [arXiv:0908.1443 [nucl-th]].

[8] Y. Hayato, Acta Phys. Polon. B **40**, 2477 (2009).

[9] U. Mosel, O. Lalakulich and K. Gallmeister, Phys. Rev. D **89**, 093003 (2014) [arXiv:1402.0297 [nucl-th]].

[10] T. Golan, C. Juszczak and J. T. Sobczyk, Phys. Rev. C **86**, 015505 (2012) [arXiv:1202.4197 [nucl-th]].

INO-ICAL detector sensitivity for the measurement of atmospheric neutrino mixing parameters

Daljeet Kaur, Md. Naimuddin, Sanjeev Kumar

Department of physics and Astrophysics, University of Delhi, Delhi, 110007, India

DOI: http://dx.doi.org/10.3204/DESY-PROC-2014-04/202

Neutrino oscillation physics is now enriched with various compelling evidences of neutrino oscillations and their masses from several experiments but measurement of correct neutrino mass hierarchy, octant of θ_{23} and determination of value CP violating phase δ_{CP} are still unknown puzzles. The recently measured substantially large third mixing angle θ_{13} from the reactor experiments [1, 2] has opened up new opportunities in the neutrino physics sector [3, 4]. Atmospheric neutrino experiments have potential to explain these unknown mysteries through their wide coverage of baseline and with energies in the range from MeV to TeV. The magnetised Iron CALorimeter detector (ICAL) at India-based Neutrino Observatory (INO) [5] is a proposed atmospheric neutrino experiment, located at Theni district in South India. The main goals of INO experiment is to measure the correct neutrino mass hierarchy and the precise measurement of neutrino mixing parameters through the observation of atmospheric ν_μ and $\bar{\nu}_\mu$ events. A 50 kton magnetised Iron CALorimeter (ICAL) detector will be the main detector at INO where Resistive Plate Chamber (RPC) will be used as an active detector to trace the particle tracks on their passage through the detector. The unique feature of ICAL is to separate the atmospheric ν_μ and $\bar{\nu}_\mu$ with its excellent charge identification capabilities. We have performed a χ^2 analysis for the precision measurement using the simulated neutrino data generated for the ICAL detector using NUANCE [6] neutrino generator. Here, we present INO-ICAL capability for measuring the atmospheric neutrino oscillation parameters $|\Delta m^2_{32}|$ and $\sin^2\theta_{23}$ using neutrino energy and muon direction as observables in presence of actual detector resolutions and efficiencies.

Interaction of atmospheric neutrinos with the detector produce associative lepton and hadrons through Quasi-Elastic (QE), Single pion production (Resonance) and Deep Inelastic scattering (DIS) processes. Muons are produced due to Charged Current interactions of muon neutrinos ant anti-neutrinos while single pion along with one lepton produced due to resonance interactions. Hadrons are produced due to deep inelastic scattering (DIS) at high energies. Muons create a long track on their passage through detector and their charge and momenta can be identified through the track bending and curvature in presence of magnetic field whereas hadrons produce bunch of hits in form of shower. The energy and direction resolutions of muons and hadrons based on GEANT4 detector [8] simulation are provided by the INO collaboration as a function of their true energies and true directions [7, 9]. Since the muon direction reconstruction is well known for ICAL we have used the reconstructed muon directions in the final analysis. In the present analysis, muon energy and angular resolutions are implemented by smearing true muon energy and direction of each μ^+ and μ^- event using the ICAL muon resolution functions [7]. True hadron energies are smeared using ICAL hadron resolution functions [9].

The neutrino energy can be reconstructed from reconstructed muon and hadron energy. We use reconstructed neutrino energy as the sum of reconstructed muon and hadron energy and muon direction as observables for binned χ^2 analysis.

For the analysis, we simulate 1000 year unoscillated NUANCE data generated using Honda et al. 3D flux [10]. The implementation of oscillation effects to these unoscillated data have been done using a well known re-weighting algorithm as presented in earlier ICAL analyses [11, 12]. We use the fixed values of solar mixing parameters $\sin^2(2\theta_{12}) = 0.86$, $\Delta m^2_{21} = 7.6 \times 10^{-5} eV^2$ and $\delta_{cp} = 0$ where as the atmospheric mixing parameters are marginalised within their 3σ range with the best fit values $\sin^2(\theta_{23}) = 0.5$ and $\Delta m^2_{32} = 2.4 \times 10^{-3} eV^2$. Here, we assume normal hierarchy is true. The oscillation re-weighted events with detector resolutions and efficiencies are then binned into neutrino energy and muon direction. The data is divided into neutrino energy bins in the range of 0.8 - 10.8 GeV. We use 15 bins in the range 0.8-5.8 GeV with bin size of 0.33 GeV and from 5.8-10.8 GeV 5 bins with bin size of 1 GeV. 20 $\cos\theta_\mu$ direction bins are used in the range of -1 to 1. Finally, for χ^2 estimation, the data has been scaled down for 10 years of exposure to minimising the statistical fluctuations. The definition of atmospheric mass square splitting as $|\Delta m^2_{eff}|$ following the Ref. [12] has been considered for the analysis. We have used the poissonian definition of χ^2 given as

$$\chi^2(\nu_\mu) = \sum_{min} \left(2N^{th'}_{ij}(\nu_\mu) - 2N^{ex}_{i,j}(\nu_\mu) + 2N^{ex}_{i,j}(\nu_\mu) \ln\left(\frac{N^{ex}_{i,j}(\nu_\mu)}{N^{th^{prime}}_{i,j}(\nu_\mu)} \right) \right) + \sum_k \zeta_k^2, \tag{1}$$

where

$$N^{th'}_{ij}(\nu_\mu) = N^{th}_{i,j}(\nu_\mu) \left(1 + \sum_k \pi^k_{ij} \zeta_k \right). \tag{2}$$

In Eq.(1), N^{ex}_{ij} is the observed number of the ν_μ events in i^{th} E_ν and j^{th} $\cos\theta_\mu$ bin generated using true values of the oscillation parameters. In Eq.(2), N^{th}_{ij} is the number of theoretically predicted events generated by varying oscillation parameters without including systematic errors, $N^{th'}_{ij}$ shows shifted events spectrum due to different systematic uncertainties, π^k_{ij} is the systematic shift due to k^{th} systematic error. A total five systematic uncertainties are considered for our analysis; these are 20% overall flux normalisation uncertainty, 10% cross-section uncertainty, 5% uncertainty on the zenith angle dependence of the flux. 5% energy dependent tilt error and 5% overall statistical uncertainty. All the systematic uncertainties are applied using the method of "pulls" as described in [11, 13]. ζ_k is the univariate pull variable corresponding to the π^k_{ij} uncertainty. An expression similar to Eq.(1) can be obtained for $\chi^2(\bar{\nu}_\mu)$ using reconstructed μ^+ event samples. We have calculated $\chi^2(\nu_\mu)$ and $\chi^2(\bar{\nu}_\mu)$ separately and then these two are added to get total χ^2_{total} as

$$\chi^2_{total} = \chi^2(\nu_\mu) + \chi^2(\bar{\nu}_\mu). \tag{3}$$

We impose a 10% prior while marginalising over $\sin^2\theta_{13}$ as

$$\chi^2_{ical} = \chi^2_{total} + \left(\frac{\sin^2\theta_{13}(true) - \sin^2\theta_{13}}{\sigma_{\sin^2\theta_{13}}} \right)^2. \tag{4}$$

Finally, in order to obtain the experimental sensitivity for θ_{23} and $|\Delta m^2_{eff}|$, we minimise the χ^2_{ical} function by varying oscillation parameters within their allowed ranges over all systematic uncertainties. The precision on the oscillation parameters can be defined as:

$$Precision = \frac{P_{max} - P_{min}}{P_{max} + P_{min}}, \tag{5}$$

where P_{max} and P_{min} are the maximum and minimum values of the concerned oscillation parameters at the given confidence level.

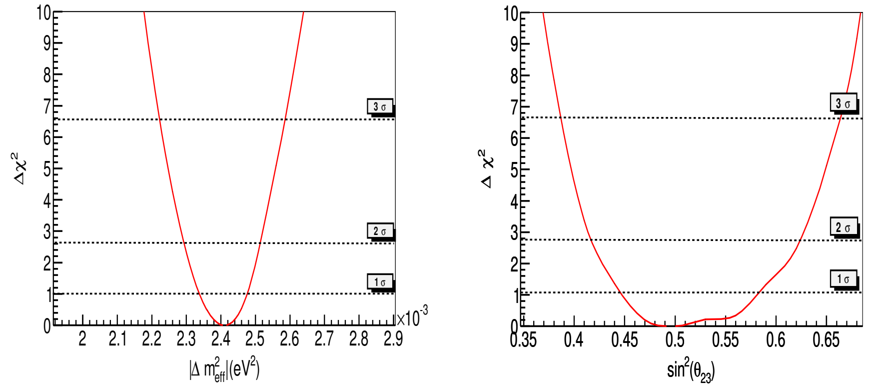

(a)

(b)

Figure 1: (a) $\Delta\chi^2$ as a function of $|\Delta m^2_{32}|$ (b) $\Delta\chi^2$ as a function of $\sin^2\theta_{23}$.

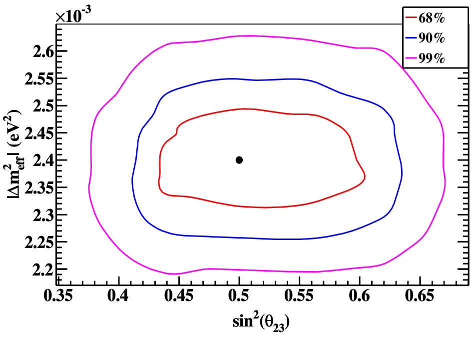

Figure 2: Contour plot for 68%, 90% and 99% confidence level for 10 years exposure of ICAL detector

The sensitivity for the measurement of test parameters $|\Delta m^2_{eff}|$ and for $\sin^2\theta_{23}$ at 1σ, 2σ and 3σ confidence intervals are shown in Figure 1(a) and Figure 1(b) respectively. The final contour plots in $|\Delta m^2_{eff}|$ and $\sin^2\theta_{23}$ plane assuming $\Delta\chi^2_{ical} = \chi^2_{min} + m$ has been obtained, where χ^2_{min} is the minimum value of χ^2_{ical} for each set of oscillation parameters and values of m are taken as 2.30, 4.61 and 9.21 corresponds to 68%, 90% and 99% confidence levels. The $(|\Delta m^2_{eff}|, \sin^2\theta_{23})$ contour plot is shown in Figure 2. We find that for 10 years of exposure of ICAL detector with detector resolutions and efficiencies, INO-ICAL is able to measure $|\Delta m^2_{32}|$ and $\sin^2\theta_{23}$ with a precision of 4.15% and 16% at 1σ confidence level using neutrino energy and muon direction binning. Present results show an imrovement of 18.62 % and 5 % on the precision of $|\Delta m^2_{32}|$ and $\sin^2\theta_{23}$ over the earlier ICAL analysis with muon energy and muon direction observables [11].

Acknowledgements

We thank INO physics and simulation group for continuous support throughout this work. We would also like to thank Department of Science and Technology (DST) and Council for Scientific and Industrial Research (CSIR) for providing us financial support for this research.

References

[1] F. P. An et al. [Daya-Bay Collaboration], Phys. Rev. Lett. 108, 171803 (2012), arXiv:hep-ex/1203.1669.

[2] J. K. Ahn et al. [RENO Collaboration], Phys. Rev. Lett. 108, 191802 (2012), arXiv:hep-ex/1204.0626.

[3] H. Minakata, Nucl. Phys. Proc. Suppl. 235-236, 173 (2013), arXiv:hep-ph/1209.1690.

[4] M C Gonzalez-Gracia, Physics of the Dark Universe **4**1-5 (2014).

[5] The Technical Design Report of INO-ICAL Detector (2006), http://www.ino.tifr.res.in/ino/.

[6] D. Casper, Nucl.Phys. Proc.Suppl. **112**, 161 (2002), arXiv:hep-ph/0208030.

[7] A. Chatterjee et al. [arXiv:1405.7243v1][physics.ins-det](2014).

[8] GEANT simulation toolkit wwwasd.web.cern.ch/wwwasd/geant/

[9] M. M. Devi et al., JINST **8** P11003 (2013).

[10] M. Honda et al., Phys. Rev. **D70**, 043008 (2004), arXiv:astro-ph/0404457.

[11] T. Thakore et al. JHEP **05**, 058 (2013).

[12] A. Ghosh et al., JHEP **04**, 009 (2013).

[13] M. C. Gonzalez-Garcia, M. Maltoni et al, Phys.Rev. **D70**, 033010 (2004), arXiv:hep-ph/0404085v1.

IsoDAR and DAEδALUS

Joshua Spitz

Massachusetts Institute of Technology, Cambridge, MA 02139, USA

DOI: http://dx.doi.org/10.3204/DESY-PROC-2014-04/124

The DAEδALUS collaboration seeks to construct a number of high-intensity cyclotrons for use throughout neutrino physics, including searching for a sterile neutrino, sensitivity to non-standard neutrino interactions, measurements of coherent neutrino-nucleus scattering and ultimately, a determination of CP violation in neutrinos. This proceedings focusses on the physics goals of the DAEδALUS project.

1 Introduction

We don't know if neutrinos obey Charge-Parity (CP) symmetry and we don't know how many neutrinos there are. Answers to these questions are vital for understanding the neutrino's place amongst the fundamental particles as well as its role in the evolution of the universe. The DAEδALUS collaboration has set out to produce cyclotron-based neutrino sources for, among other things, answering these questions. The experimental concept calls for two classes of cyclotrons in producing isotope and pion/muon decay-at-rest sources of neutrinos, an injector cyclotron and a Superconducting Ring Cyclotron (SRC). The injector cyclotron can be combined with a liquid scintillator based neutrino detector for trying to answer the question of how many neutrinos there are [1], and a set of SRC devices, located at various distances from an ultra-large free-proton-based detector, can be used to measure CP violation in neutrinos [2]. While there are a number of technological challenges associated with constructing these devices (e.g., see Ref. [3]), the focus of this work is on the physics capabilities of these unique experiments.

2 IsoDAR

The Isotope Decay-at-Rest experiment (IsoDAR), doubling as the injector cyclotron design for the DAEδALUS neutrino CP violation project, will use a 600 kW resistive cyclotron to accelerate 5 mA of 60 MeV/amu H_2^+. For IsoDAR, a dedicated experiment that will utilize this source, the ions will be directed onto a ^{9}Be target to produce a large flux of neutrons emanating from the target. These MeV-scale neutrons, produced at the level of $\sim$0.1 neutron per incoming proton [4], will slow down and eventually capture inside of a surrounding ^{7}Li ($\geq$99.99% isotopically pure) sleeve. The product of this capture, ^{8}Li, beta decays with a half-life of 840 ms to produce an electron antineutrino with energy in the 3-14 MeV range. There are about 15 $\overline{\nu}_e$ per 1000 protons on target expected. The cyclotron-target configuration can be placed within $\sim$10 m of a planned or existing liquid scintillator based detector, such as KamLAND [5], for

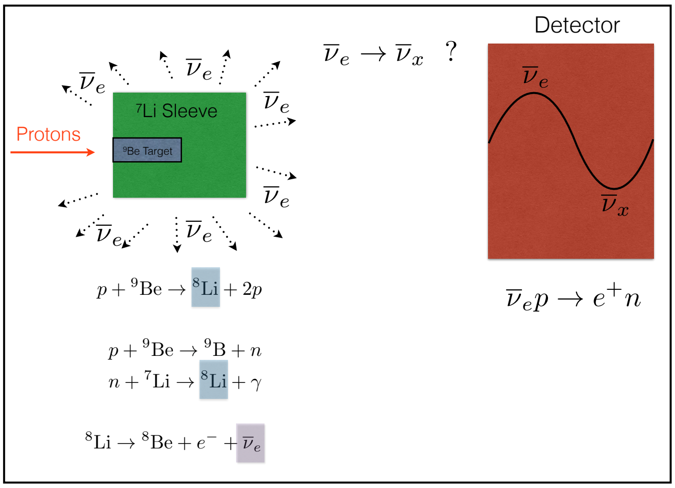

Figure 1: The IsoDAR idea for an intense source of electron antineutrinos source near a planned or existing liquid scintillator detector.

collecting electron antineutrino induced inverse beta decay (IBD) interactions ($\overline{\nu}_e p \rightarrow e^+ n$) and $\overline{\nu}_e$-electron elastic scatters ($\overline{\nu}_e e^- \rightarrow \overline{\nu}_e e^-$). The collected electron antineutrino IBD events can provide sensitivity to high-Δm^2 neutrino oscillations, a signal which would be indicative of the existence of at least one light sterile neutrino. The approximately 800,000 IBD events expected in 5 years running IsoDAR 16 m away from the 897 ton fiducial mass KamLAND detector would allow a sensitivity of $>10\sigma$ to electron antineutrino disappearance at $\Delta m^2 \sim 1$ eV^2. Such a large sample would even provide the ability to distinguish between the existence of one or two sterile neutrinos in many mixing scenarios [6]. Further, the $\approx$2500 $\overline{\nu}_e$-electron elastic events expected would provide a unique test of non-standard neutrino interactions and physics beyond the Standard Model in general [7]. The IsoDAR idea, with a focus on the oscillation concept, is shown in Figure 1.

3 DAEδALUS

The neutrino CP violating parameter δ_{CP} can be measured by studying $\overline{\nu}_\mu \rightarrow \overline{\nu}_e$ oscillations at medium baseline (tens of km for neutrino energies in the 20-50 MeV range). For DAEδALUS, the muon antineutrino flux is produced with 800 MeV protons striking a carbon target to create charged pions. The pions quickly come to rest in the target and decay to a muon and a muon neutrino ($\pi^+ \rightarrow \mu^+ \nu_\mu$). The positively charged muon subsequently comes to rest as well and decays to a positron and two neutrinos ($\mu^+ \rightarrow e^+ \nu_e \overline{\nu}_\mu$) with energies from 0-52.8 MeV. Electron antineutrino appearance from the muon antineutrino component of this source can be studied, via the IBD interaction at medium baseline, to provide a measurement of δ_{CP}. A set of cyclotrons, at distances of 1 km, 8 km, and 20 km away from a single ultra-large detector are envisioned by DAEδALUS for this purpose. In general, the near cyclotron will be used to constrain the initial flux via ν_e-electron scattering, the middle-distance cyclotron will constrain the rise probability, and the far cyclotron(s) will be used to power the fit for electron antineutrino appearance. Neutrinos from the different sources are differentiated at the single detector with pulse timing. DAEδALUS requires the power of the cyclotrons at each site to be 0.8, 1.6 and 4.8 MW, from near to far. These tentative requirements are set such that DAEδALUS can match the sensitivity of the Long Baseline Neutrino Experiment (LBNE) 2011 baseline design [8]. Notably, the contamination of intrinsic $\overline{\nu}_e$, from the source rather than from appearance, is at the $\sim 4 \times 10^{-4}$ level because almost all of the (grand)parent π^- capture on nuclei before they have a chance to decay. The DAEδALUS experimental concept, in consideration of the CP violation measurement, is shown in Figure 2.

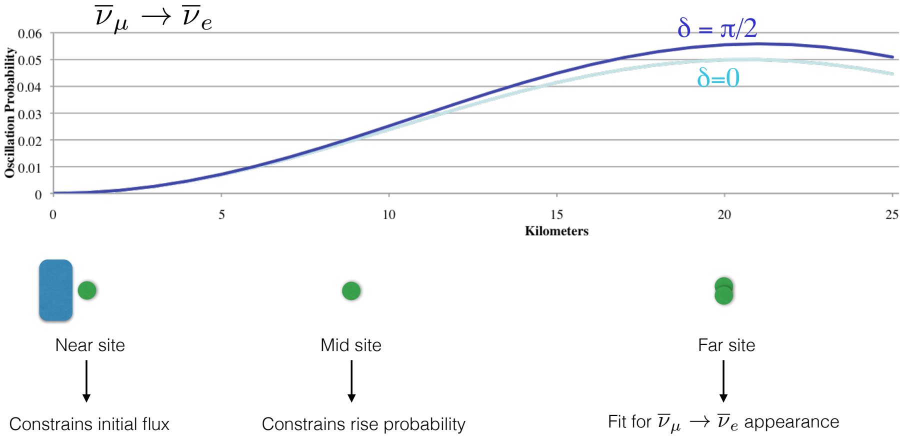

Figure 2: The DAEδALUS experimental concept, depicting the various accelerator locations and their general purposes, with respect to an ultra-large detector. A set of example oscillation probabilities, for two different values of δ_{CP}, is also shown.

Along with contributing information about the initial composition of the un-oscillated source, the first "near" cyclotron can be used for a set of of short-baseline measurements, especially when considered in combination with smaller detectors located near the accelerator. Specifically, a coherent neutrino-nucleus scattering experiment with a dark-matter-style detector sensitive to nuclear recoils at the keV-scale is possible [9]. Such a detector could be located tens of meters from the source in order to search for the well-predicted, but as-yet-unseen, coherent interaction of a neutrino with an entire nucleus. In case the accelerator is located at a deep underground lab, a dedicated dark matter experiment nearby could also make the discovery. Further, a multi-detector configuration could provide a unique neutral current based sterile neutrino oscillation search using the coherent events [10]. Such a neutral current based disappearance search would be uniquely sensitive to the sterile flavor component of the fourth neutrino mass eigenstate, a measurement which is not directly accessible using charged current based searches.

The near cyclotron can also be used to look for high-Δm^2 oscillations, $\overline{\nu}_\mu \rightarrow \overline{\nu}_e$ appearance as well as the disappearance of ν_e, in combination with the envisioned nearby ultra-large detector [11]. Both of these measurements can be considered complimentary to IsoDAR's low(er) energy electron antineutrino disappearance probe. In the case that a new oscillatory frequency consistent with a sterile neutrino is confirmed, we will want to measure its properties, including precise determinations of its characteristic mass splitting and mixing angles. Such measurements are best accomplished, of course, using multiple flavors in both appearance and disappearance modes and with both neutrinos and antineutrinos. It is also worth noting that the envisioned short baseline electron antineutrino appearance search with DAEδALUS can be considered a direct test of the LSND and MiniBooNE antineutrino anomalies [12, 13, 14].

4 Status and conclusion

DAEδALUS is working within a four-phase program for surmounting the technological obstacles associated with building and operating these megawatt-class cyclotrons and establishing their cost-effectiveness and ability. The currently underway Phase 1 aims to deploy and test an intense H_2^+ ion source; Phase 2 will demonstrate a full-scale version of the low energy beam transport and injector cyclotron systems, and use this system to definitively address the sterile neutrino; Phase 3 will continue with the production of an actual full superconducting ring cyclotron accelerator module at a near location from an ultra-large water or scintillator based detector for sterile neutrino and coherent neutrino-nucleus scattering physics; and Phase 4 involves the deployment of the complete DAEδALUS experiment featuring cyclotrons at three distances for a measurement of δ_{CP}. This program of research and development and measurements relevant for accelerator science, producing medical isotopes for industry [15], and neutrino physics is ongoing. Among other physics goals, this program will help to answer two of the most profound and important questions in physics today: 1) How many neutrinos are there? and 2) Do neutrinos and antineutrinos behave the same?

Acknowledgments

This work was done with support from the National Science Foundation under Grant Number PHY-1205175.

References

[1] A. Bungau *et al.*, Phys. Rev. Lett **109** 141802 (2012).

[2] J.M. Conrad and M.H. Shaevitz, Phys. Rev. Lett. **104** 141802 (2010).

[3] A. Adelmann, J. Alonso, W.A. Barletta, J.M. Conrad, M.H. Shaevitz, J. Spitz, M. Toups, and L.A. Winslow, Adv. High Energy Phys. **2014** 347097 (2014).

[4] A. Adelmann *et al.*, 1210.4454 [physics.acc-ph] (2012).

[5] S. Abe *et al.* [KamLAND Collaboration], Phys. Rev. Lett. **100** 221803 (2008).

[6] M. Sorel, J. M. Conrad, and M. H. Shaevitz, Phys. Rev. D **70** 073004 (2004).

[7] J.M. Conrad, M.H. Shaevitz, I. Shimizu, J. Spitz, M. Toups, and L. Winslow, Phys. Rev. D **89** 072010 (2014).

[8] V. Barger *et al.*, "Report of the US long baseline neutrino experiment study", arXiv:0705.4396 [hep-ph] (2007).

[9] A.J. Anderson, J.M. Conrad, E. Figueroa-Feliciano, K. Scholberg, and J. Spitz, Phys. Rev. D **84** 013008 (2011).

[10] A.J. Anderson, J.M. Conrad, E. Figueroa-Feliciano, C. Ignarra, G. Karagiorgi, K. Scholberg, M.H. Shaevitz, and J. Spitz, Phys. Rev. D **86** 013004 (2012).

[11] S.K. Agarwalla, J.M. Conrad, and M. Shaevitz, arXiv:1105.4984 [hep-ph] (2011).

[12] A. Aguilar *et al.* [LSND Collaboration], Phys. Rev. D **64** 112007 (2001).

[13] A.A. Aguilar-Arevalo *et al.* [MiniBooNE Collaboration], Phys. Rev. Lett. **105** 181801 (2010).

[14] A. A. Aguilar-Arevalo *et al.* [MiniBooNE Collaboration], Phys. Rev. Lett. **110** 161801 (2013).

[15] J.R. Alonso, arXiv:1209.4925 [nucl-ex] (2012).

Chapter 6

Dark matter and cosmology

XENON100 and XENON1T
Dark Matter Search with Liquid Xenon

Gaudenz Kessler on behalf of the XENON collaboration
Physics Department, University of Zurich

DOI: http://dx.doi.org/10.3204/DESY-PROC-2014-04/109

The XENON100 detector is a dual-phase (liquid-gas) xenon time-projection chamber for dark matter particle detection containing 161 kg liquid xenon and 242 photomultiplier tubes to detect the scintillation light produced by particle interactions with xenon nuclei.

XENON1T, the next generation dark matter experiment, is being under construction and will house a total amount of 3.2 t of xenon. The designed background level is 100 times lower than that in XENON100. It is surrounded by a water tank that acts as an active muon veto. It is planned to upgrade the experiment to XENONnT with 7 t of liquid xenon.

1 Particle Detection with a Dual-Phase Time-Projection Chamber

The XENON project aims to detect Weakly Interactive Massive Particles (WIMPs) with a dual-phase time-projection chamber (TPC) filled with liquid and gaseous xenon. There are two types of particle interaction with the xenon inside the TPC. Charged particles (like electrons or muons) or γ would interact electromagnetically with an electron of the xenon atom shell. This kind of interaction is referred to as electronic recoil (ER). WIMPs would scatter off the xenon nuclei and cause a nuclear recoil (NR). Neutrons as well interact via nuclear recoil.

Figure 1 shows a schematic description of particle detection in such a detector. An energy deposition due to a particle interaction inside the TPC causes both direct scintillation light and ionisation of the xenon atoms. The direct scintillation light (S1) is promptly detected by two arrays of photomultiplier tubes (PMTs) that are located at the top and at the bottom of the TPC. The ionised electrons are extracted upwards by an electric field. They drift with a constant velocity upwards until they reach the liquid-gas surface. After being extracted into the gas phase of the TPC they produce scintillation light (S2) that is proportional to the number of extracted electrons. Since the electron extraction into the gas phase is very close to the top PMT array, the xy position can be reconstructed using the hit-pattern of photons on the top PMTs. The z coordinate of the interaction can be calculated from the drift time between the S1 and the S2 signals. This allows for a full 3D event position reconstruction. Because the ionisation density is higher for NRs than for ERs, the recombination is stronger for NR. This leads to a different ratio between S2/S1 for NRs and ERs and can be used to discriminate between these types of interaction.

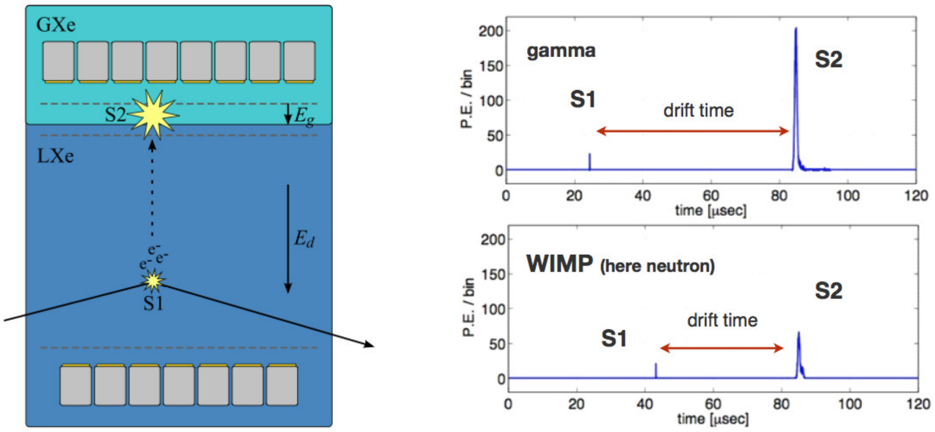

Figure 1: Working principle of a dual-phase time-projection chamber. Left: a particle interaction in the liquid xenon causes direct scintillation light (S1) and free electrons that drift to the gas phase and produce electroluminescence signal (S2). Right: the ratio between S1 and S2 is used to discriminate between ERs (electromagnetic background) and NRs (WIMPs or neutrons). The drift time between S1 and S2 peaks is used to determine the z position of the interaction.

2 XENON100

The XENON100 experiment is located at the Laboratori Nazionali del Gran Sasso (LNGS) in Italy, in which the flux of cosmic muons is reduced by a factor of 10^6 by 1400 meters of rock. The experiment consists of dual-phase time-projection chamber filled with 62 kg of liquid xenon (30 cm height × 30 diameter). The TPC is surrounded by other 99 kg of liquid xenon that act as an active veto. There are two arrays of PMTs on the top (in the gas phase) and the bottom of the TPC (242 in total). The drift field inside the liquid xenon is 530 V/cm and the field to extract drifting electrons into the gas phase is 12 kV/cm [1]

To probe the recoil behaviour of the background and signal high statistic calibrations have been performed. A ^{60}Co and a ^{232}Th source was used for the ER and an AmBe neutron source for the NR. For a good understanding of the background appearing in the experiment all components of the detector were screened for their radioactivity with high-purity Ge detectors. The obtained data was used to perform a full Monte Carlo simulation of all radioactive materials in all components of the experiment. The energy spectrum obtained in the Monte Carlo simulation fits very well to the background spectrum measured in the detector [2]. At the time of the publication, XENON100 is one of the experiments with the lowest background. The expected background rate in the signal region was determined to be only 1.0 ± 0.2 events for 224.6 live days, 0.79 ± 0.16 of which coming from γ events leaking to lower (S2/S1) values and $0.17^{+0.12}_{-0.07}$ coming from neutrons [3, 4]. In the signal region two events were observed, which means that there is no significant excess about the expected background due to a signal in the XENON100 data. There is a 26.4 % probability that the background fluctuates to two events. This result lead to the most stringent limit for the elastic spin-independent WIMP-nucleon cross-section at that time above 8 GeV/c^2, with a minimum of 2×10^{-45} cm^2 at 55 GeV/c^2 at 90% confidence

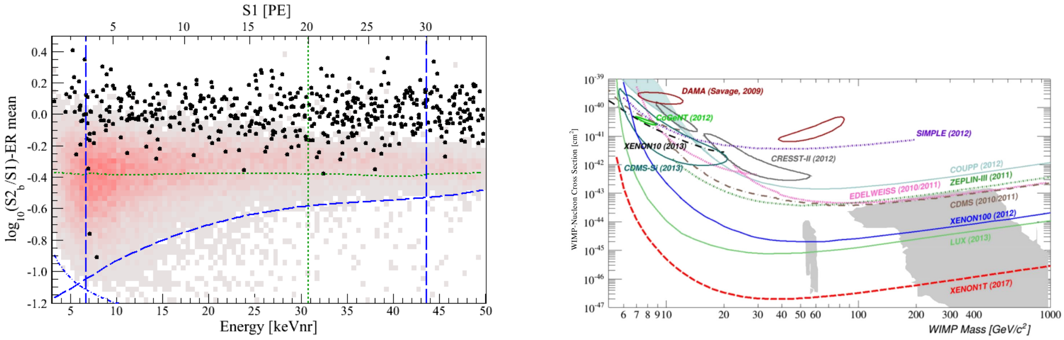

Figure 2: Left: event distribution observed during 224.6 live days using $\log_{10}(S2_b/S1)$ flattened by subtracting the ER band mean, as a function of NR energy. There are two events in the signal region, Right: exclusion limit on the WIMP-nucleon cross section obtained by XENON100 and expected sensitivity of XENON1T.

level [4]. Figure 2 shows the event distribution measured during 224.6 live days (left) and the limit for spin-independent WIMP-nucleon scattering that as achieved with XENON100 (right). 50% of the xenon nuclei have a non-zero spin. The natural abundance of ^{129}Xe and ^{131}Xe is 26.4% and 21.3%, respectively. XENON100 contains 26.2% ^{129}Xe and 21.8% ^{131}Xe. Hence also the spin-dependent elastic interaction was studied and XENON100 still holds the most stringent limit on the spin-dependent WIMP-neutron cross-section [5].

A search for axions and axion-like particles has been performed with the XENON100 data of 224.6 live days × 34 kg exposure. The axion-electric coupling constant, g_{Ae}, could be rejected for values larger than 7.7×10^{-12} (90% C.L.) [6].

An alternative way to directly detect Dark Matter is to observe inelastic WIMP-nucleus scattering, in which the nuclear recoil excites the nucleus to a low-level excited state [7]. There are two xenon isotopes for which this process is possible: ^{129}Xe has an excitation energy of 39.6 keV to the lowest-lying state, the excitation energy of ^{131}Xe is 80.3 keV. In the analysis of inelastic events ^{129}Xe is considered. The excited state has a lifetime of 0.97 ns which is too short for the nuclear recoil and the photon emission from the deexcitation to be distinguished in time. Hence the expected signal is a nuclear recoil simultaneous with a 40 keV photon. The expected sensitivity in the XENON100 detector is 5×10^{-38} cm^2 for a mass of 100 GeV/c^2 at 90% confidence level.

An annual modulation analysis and low-mass WIMP search are being performed. At the moment 154 live days of new data is available that will be unblinded soon. Currently the XENON100 detector is used to probe the recoil behaviour with various calibration sources.

3 XENON1T

The next generation detector, XENON1T, is currently under construction in Hall B of the Gran Sasso Underground Laboratory. It will house a total amount of 3.2 tons of liquid xenon with 2 tons inside the sensitive region of the TPC. The TPC is a cylinder of 1 meter diameter and 1 meter height and contains in total 248 3-inch PMTs that are designed to have an especially low radioactivity and to operate in liquid xenon environment [8] The experiment will have 100 times lower background than its predecessor XENON100. Therefore it is embedded inside a 10 meter diameter water shield that is instrumented with 84 8-inch PMTs and acts as a Cherenkov muon veto [9]. The sensitive volume is shielded by 10 cm of liquid xenon. The required level of ^{85}Kr will be below 0.5 ppt (a few ppt in XENON100), and the contamination of ^{222}Rn will be only 1 µBq/kg whereas it was 65 µBq/kg in XENON100. The goal is to achieve only 0.5 events per ton per year. The operation is planned to start in 2015. The expected sensitivity is 2×10^{-47} cm^2 for 55 GeV/c^2.

After two years of operation it is planned to upgrade XENON1T to XENONnT, the next stage with a total mass of 7 tons of liquid xenon, which would allow to increase the sensitivity by another order of magnitude. For a fast upgrade most of the systems XENON1T will be reused.

References

[1] E. Aprile et al. (XENON100), Astropart. Phys. 35, 573-590 (2012)

[2] E. Aprile et al. (XENON100), Phys. Rev. D 83, 082001 (2011).

[3] E. Aprile et al. (XENON100), J. Phys. G: Nucl. Part. Phys. 40, 115201 (2013)

[4] E. Aprile et al. (XENON100), Phys. Rev. Lett. 109, 181301 (2012).

[5] E. Aprile et al. (XENON100), Phys. Rev. Lett. 111, 021301 (2013)

[6] E. Aprile et al. (XENON100), Phys. Rev. D 90, 062009

[7] L. Baudis et al., Phys. Rev. D 88, 115014, (2013)

[8] L. Bauids et al., JINST 8 P04026 (2013)

[9] E. Aprile et al. (XENON100), arxiv:1406.2374

Current Status of the Dark Matter Search Experiment CRESST

Holger Kluck[1,2] for the CRESST Collaboration

[1]Institute of Atomic and Subatomic Physics, Vienna University of Technology, 1020 Wien, Austria
[2]Institute of High Energy Physics of the Austrian Academy of Sciences, 1050 Wien, Austria

DOI: http://dx.doi.org/10.3204/DESY-PROC-2014-04/240

CRESST is a cryogenic direct Dark Matter search experiment based on phonon-light technique. It is aiming for the detection of *weakly interacting massive particles* (WIMPs) via their scattering off nuclei in $CaWO_4$ target crystals. Significant improvements have been achieved with respect to previous measurement campaigns in terms of intrinsic radiopurity of $CaWO_4$ crystals and rejection of nuclear recoil events from alpha decays near surfaces. In this contribution, the related changes in the detector design will be discussed. Based on the first ~ 30 kg-live-days of data acquired by a single $CaWO_4$ detector module with a new design, we present limits for the spin-independent WIMP-nucleon cross section, which exclude new parameter space below $3\,\mathrm{GeV}/c^2$.

1 Introduction

Various observations point to the existence of particle-like Dark Matter [1]. However, the actual particle candidate, which may be a *weakly interacting massive particle* (WIMP), has not yet been discovered undoubtedly: Some experiments, e.g. LUX [2] and SuperCDMS [3], obtained null results, whereas other experiments, e.g. DAMA/LIBRA [4] and previously also CRESST [5], observed a potential signal.

CRESST recently published the result of a new search for WIMP-nucleon scattering based on a single upgraded detector module, *TUM40* [6]. After a short introduction of the CRESST experiment in sec. 2, we will present the improvements of this upgraded module (sec. 3) and the obtained result (sec. 4) before we conclude in sec. 5.

2 The CRESST experiment

The cryogenic Dark Matter search CRESST is looking for nuclear recoils induced by the elastic scattering of WIMPs off the nuclei in $CaWO_4$ targets. The energy deposited by a potential WIMP-nucleon scattering is only in the order of a few 10 keV, therefore a sufficient background suppression is crucial [5]. To discriminate e^-/γ background events, CRESST simultaneously reads out signals from two channels: the scintillation light emitted by the $CaWO_4$ crystal (*light signal*) and the non-thermal phonon excitation of the crystal lattice (*phonon signal*). The rejection of *near-surface α events* will be outlined in sec. 3. A detailed description of the experimental set-up, the data acquisition, and analysis can be found in earlier publications [7, 8].

The phonon signal, which is independent of the interacting particle type, is used to measure the deposited energy E. Contrary, for the same E, the light signal of nuclear recoils is suppressed with respect to the light signal of e^-'s/γ's, and decreases with the mass of the nucleus.

This *quenching effect* is evident in the plane of *light yield* (LY), i.e. the ratio of light signal over phonon signal, versus E as schematically shown in fig. 1: The e^-/γ-band is normalized to $LY = 1$ at 122 keV via calibration with a ^{57}Co source. At decreasing values of LY, bands for α recoils and recoils of the O, Ca, and W nuclei are located [9].

Due to the overlapping of the bands at low energies, see fig. 1, a low background activity and a low experimental threshold are necessary for dedicated low-mass WIMP searches. CRESST made progress in both aspects with an upgraded detector module, resulting in a WIMP sensitivity down to $\sim 1\,\mathrm{GeV}/c^2$ [6].

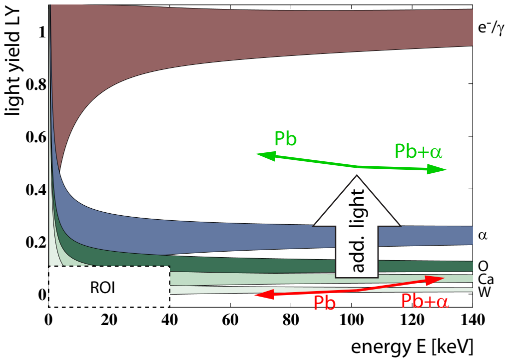

Figure 1: Illustration of the various bands in the light yield−energy-plane for a $CaWO_4$ detector and the region of interest (ROI) for the WIMP search with the TUM40 detector module. Additional scintillation light shifts near-surface α and Pb events out of the vicinity of the nuclear recoil bands [12], for details see text.

3 The upgraded detector module TUM40

CRESST runs with 18 detector modules of various designs and a total target mass of roughly 5 kg [6] in its current data taking period (CRESST-II Phase 2). Here, we will focus on 29.35 kg d recorded with only one module, *TUM40*, based on a $CaWO_4$ crystal with a mass of $\sim$ 250 g [6]. This module shows three improvements: a decreased intrinsic e^-/γ background, a fully efficient rejection of near-surface α background, and a high phonon resolution allowing to set a low trigger threshold.

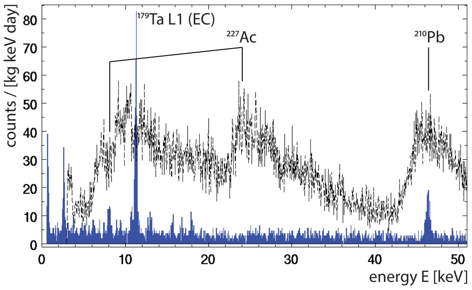

Figure 2: Background spectra for a commercial $CaWO_4$ crystal (*open black histogram*) and TUM40 (*filled blue histogram*). Prominent features are the beta decays of ^{227}Ac and ^{210}Pb, and the electron capture of cosmogenic ^{179}Ta [6, 11].

The intrinsic e^-/γ background is reduced by growing the crystal in a dedicated furnace at the TU Munich [10]. Figure 2 compares the background spectrum of TUM40 (*filled blue histogram*) with the one of a commercial $CaWO_4$ crystal (*open black histogram*). Whereas the spectrum of the commercial crystal is dominated by beta decays of internal ^{227}Ac and ^{210}Pb contaminations, these are strongly reduced in the TUM40 spectrum: The background rate of TUM40 is with ~ 3.5 counts/kg/d/keV up to 10 times lower than the one of a comparable commercial crystal. A detailed discussion of the remaining background of TUM40 can be found in [11].

Near-surface α decays are mostly $^{210}\mathrm{Po} \rightarrow {}^{206}\mathrm{Pb} + \alpha$ decays near surrounding surfaces and contribute to the background in two ways: If the resulting α particle hits the crystal after having already lost most of its energy, it can leak as *degraded* α into the nuclear recoil bands. In case the resulting ^{206}Pb nucleus hits the crystal, such an event can leak from its band closely below the W band to the ROI. To actively veto this α (Pb) background, already previously each crystal was encapsulated by a scintillating and reflecting foil which is hit by the remaining α particle. The additional scintillation light of the foil shifts the event to a higher LY value as illustrated in fig. 1. However, previously not the complete surrounding of the crystals was scintillating due to the bronze clamps that hold the crystal. This results in an unexpected high rate of non-vetoed near-surface α decays in the previous data taking period (CRESST-II Phase 1) [5]. The TUM40 module holds the target crystal by sticks made of scintillating $CaWO_4$, therefore it is nearly fully surrounded by scintillating surfaces, which strongly increase the veto efficiency against near-surface α events. So far, TUM40 found no near-surface α events which are not vetoed. A detailed evaluation of the *$CaWO_4$-stick-design* will be given in [12].

The TUM40 module features also an excellent trigger threshold: Measured with electronic calibration pulses, the trigger efficiency reaches 50 % already at ~ 600 eV. Furthermore, a very good energy resolution of ~ 100 eV has been achieved. This is validated by the widths of the γ lines in fig. 2 [6]. The good energy resolution together with the very low threshold predestines the TUM40 module for a low-mass WIMP search.

4 Results of a dedicated low-mass WIMP search

The TUM40 module alone collected an exposure of 29.35 kg d, before all cuts and corrections for detection efficiencies in 2013 [6]. The *region of interest* (ROI) for WIMPs on the $LY-E$-plane includes all events with a LY lower than the central LY of the O recoil band and within an energy interval starting at the trigger threshold of 600 eV and ending at 40 keV [6], see fig. 1.

Applying Yellin's optimum interval method [13] on the events in the ROI results in an exclusion limit at 90 % CL for elastic spin-independent WIMP-nucleon scattering as shown in fig. 3 (*red line*) [6]. We emphasize three features of this limit:

First, it is a leading limit and excludes new parameter space for $m_\chi \leq 3\,\mathrm{GeV}/c^2$. Second, compared to other

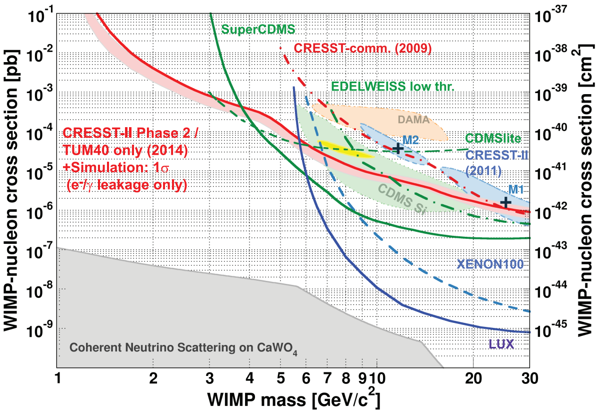

Figure 3: Limit on elastic spin-independent WIMP-nucleon scattering reported in [6] (red solid line) compared to selected results of current Dark Matter searches, see [6] for the references.

limits, this limit is relatively flat: Due to the multi-element target $CaWO_4$, CRESST is sensitive to the scattering of WIMPs at low and high masses via O ($A = 15.999\,\mathrm{u}$), and W ($A = 183.84\,\mathrm{u}$). Therefore, this limit is also relevant at higher WIMP masses. For instance, the TUM40 results exclude the low-mass maximum M2 and constrain the higher mass maximum M1 where CRESST-II Phase 1 previously reported an event excess over expected background [5]. Third, the experimental limit agrees with the expected 1σ limit due to the assumed leakage of e^-/γ background in the ROI (fig. 3, *light red region*). Therefore, no additional background component is necessary to explain the observed events [6].

5 Conclusion and outlook

With $\sim 30\,\mathrm{kg\,d}$ of data, CRESST could show the improved performance of the upgraded TUM40 detector module: a decreased intrinsic e^-/γ background by a factor of up to 10, an improved rejection power against near-surface α events, and a low trigger threshold of $\sim 600\,\mathrm{eV}$. Combined, these improvements result in a leading limit on elastic spin-independent WIMP-nucleon scattering below $3\,\mathrm{GeV}/c^2$ and in the exclusion of the M2 maximum of CRESST-II Phase 1.

It is planned to continue data taking with CRESST-II Phase 2 until reaching an exposure sufficient to clarify the nature of M1, probably mid of 2015. As all of the recent progress is well understood, projections based on reasonable further improvements indicate the possibility to reach $\sim 10^{-6}\,\mathrm{pb}$ at $\sim 3\,\mathrm{GeV}/c^2$. Therefore, CRESST is especially predestined to test new parameter space at low WIMP masses.

Acknowledgments

This work was supported by funds of the German Federal Ministry of Science and Education (BMBF), the Munich Cluster of Excellence (Origin and Structure of the Universe), the Maier-Leibnitz-Laboratorium (Garching), the Science and Technology Facilities Council (STFC) UK, and the Helmholtz Alliance for Astroparticle Physics. We gratefully acknowledge the work of Michael Stanger from the crystal laboratory of the TU Munich. We are grateful to LNGS for their generous support of CRESST, in particular to Marco Guetti for his constant assistance.

References

[1] G. Bertone, ed. *Particle Dark Matter.* Cambridge University Press, 2010.
[2] D.S. Akerib *et al.*, Phys. Rev. Lett. **112** 091303 (2013), arXiv:1310.8214[astro-ph.CO].
[3] R. Agnese *et al.*, Phys. Rev. Lett. **112** 241302 (2014), arXiv:1402.7137[hep-ex].
[4] R. Bernabei *et al.*, Eur. Phys. J. **C73** 2648 (2013), arXiv:1308.5109[astro-ph.GA].
[5] G. Angloher *et al.*, Eur. Phys. J. **C72** 1971 (2012), arXiv:1109.0702[astro-ph.CO].
[6] G. Angloher *et al.*, Eur. Phys. J. **C74** 3184 (2014), arXiv:1407.3146[astro-ph.CO].
[7] G. Angloher *et al.*, Astropart. Phys. **23** 325 (2005), arXiv:astro-ph/0408006.
[8] G. Angloher *et al.*, Astropart. Phys. **31** 270 (2009), arXiv:0809.1829[astro-ph].
[9] R. Strauss *et al.*, Eur. Phys. J. **C74** 2957 (2014), arXiv:1401.3332[astro-ph.IM].
[10] A. Erb and J.-C. Lanfranchi, Cryst. Eng. Comm. **15** 2301 (2013).
[11] R. Strauss *et al.*, arXiv:1410.4188[physics.ins-det] (2014), submitted to J. Cosmol. Astropart. Phys.
[12] R. Strauss *et al.*, arXiv:1410.1753[physics.ins-det] (2014), submitted to Eur. Phys. J. **C**.
[13] S. Yellin, Phys. Rev. **D66** 032005 (2002), arXiv:physics/0203002.